



**HAL**  
open science

# Modal analysis and flow control for drag reduction on a Sport Utility Vehicle

Stéphanie Edwige

► **To cite this version:**

Stéphanie Edwige. Modal analysis and flow control for drag reduction on a Sport Utility Vehicle. Mechanics [physics.med-ph]. Conservatoire national des arts et métiers - CNAM, 2019. English. NNT : 2019CNAM1233 . tel-02167243

**HAL Id: tel-02167243**

**<https://theses.hal.science/tel-02167243>**

Submitted on 27 Jun 2019

**HAL** is a multi-disciplinary open access archive for the deposit and dissemination of scientific research documents, whether they are published or not. The documents may come from teaching and research institutions in France or abroad, or from public or private research centers.

L'archive ouverte pluridisciplinaire **HAL**, est destinée au dépôt et à la diffusion de documents scientifiques de niveau recherche, publiés ou non, émanant des établissements d'enseignement et de recherche français ou étrangers, des laboratoires publics ou privés.

**ÉCOLE DOCTORALE DES SCIENCES DES METIERS DE L'INGENIEUR**

**Modélisation Mathématique et Numérique**

**THÈSE** présentée par :

**Stéphanie EDWIGE**

soutenue le : **14 Mars 2019**

pour obtenir le grade de : **Docteur du Conservatoire National des Arts et Métiers**

Discipline: Mathématiques appliquées et applications des mathématiques / Spécialité : Mécanique

**Modal analysis and flow control  
for drag reduction on a Sport Utility Vehicle**

THÈSE dirigée par :

**M. MORTAZAVI Iraj**

Professeur, CNAM, Paris

ENCADRANT INDUSTRIEL :

**M. GILOTTE Philippe**

Docteur, Chef de projet recherche, Plastic Omnium

RAPPORTEURS :

**M. SCHMID Peter**

Professeur, Imperial College, Londres

**M. EHRENSTEIN Uwe**

Professeur, Université d'Aix-Marseille

JURY :

**M. ROBINET Jean-Christophe**

Président du jury, Professeur, Arts et Métiers ParisTech

**Mme. MORGANS Aimée**

Professeur, Imperial College, Londres

**Mme. BRAZA Marianna**

Directeur de recherche, Institut de Mécanique des Fluides de Toulouse

**M. OTHMER Carsten**

Docteur, Chef de projet recherche, Volkswagen

**M. GILOTTE Philippe**

Docteur, Chef de projet recherche, Plastic Omnium

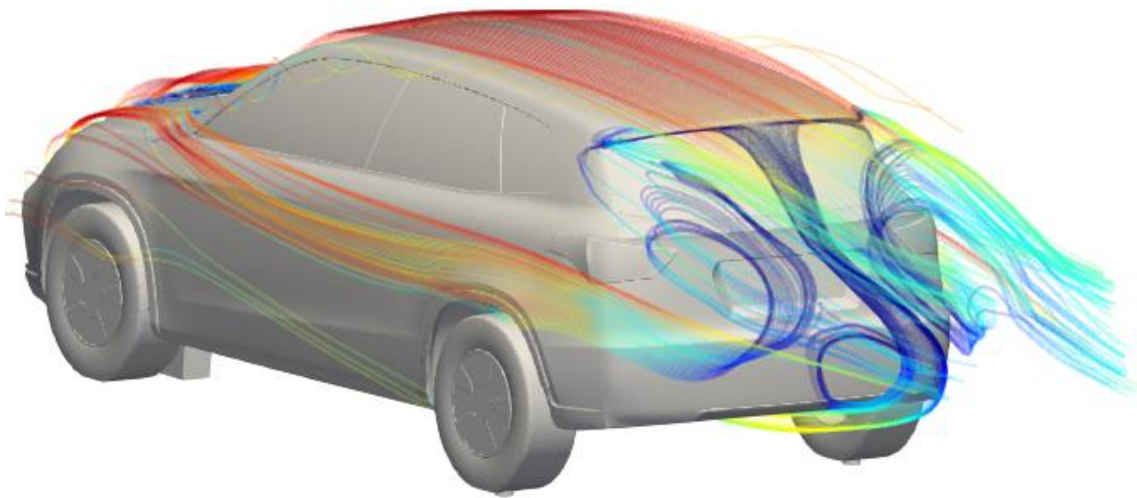
**M. MORTAZAVI Iraj**

Professeur, CNAM, Paris

**M. NAYERI Christian Navid**

Membre invité, Docteur, Chargé de recherche, Université de Berlin

*“La vraie science est une ignorance qui se sait.”*  
Michel de Montaigne.



## Remerciements

Au terme de cette thèse, l'aboutissement de ce travail n'aurait pas été possible sans les personnes qui m'ont entourée au cours de ces trois dernières années et que je tiens à remercier chaleureusement ici.

Ce projet est né de l'étroite collaboration entre Plastic Omnium et le Conservatoire National des Arts et Métiers. C'est pourquoi je tiens à remercier mon directeur de thèse Iraj Mortazavi, pour la confiance qu'il m'a accordée depuis notre rencontre à Bordeaux. Il a su répondre avec diligence et efficacité à toutes mes sollicitations. Aussi, j'adresse mes plus chaleureux remerciements à mon encadrant Philippe Gilotte, pour sa patience, pour avoir pris le temps de m'aiguiller et qui m'a poussée à aller toujours plus loin dans mes travaux. A tous deux, je leur exprime ma reconnaissance pour leurs soutiens et leurs conseils qui m'ont permis de mener à bien mon travail.

J'aimerais également remercier l'Association Nationale de la Recherche et de la Technologie qui a rendu possible ce projet CIFRE.

De très nombreuses personnes ont contribué à ce projet. J'associe donc à mes remerciements l'équipe de recherche de l'Université de Berlin qui m'a accompagnée au cours des campagnes expérimentales : Christian Nayeri et David Holst pour leur soutien technique et leur suivi. Je n'oublie pas Alexander Schoenmeier avec qui j'ai affronté de nombreuses épreuves aux cours des campagnes ; Je le remercie pour sa motivation et sa persévérance à toute épreuve. Je salue également Elliott Varon et Jean-Luc Aider de l'ESPCI qui m'ont introduit à la programmation de l'algorithme génétique.

Sur le plan numérique, je remercie ALTAIR et plus particulièrement Robert Sandboge pour ses conseils sur le calcul LES. Je remercie Olivier Wilk, Philippe Razac et Alexandre Malhomme qui m'ont de très nombreuses fois apporté leur support technique. Je ne peux omettre Yoann Eulalie qui m'a passé le flambeau de ce projet de recherche en 2015 et qui a gardé un œil attentif sur mes avancés durant toute ma thèse.

Je remercie vivement mes collègues de Plastic Omnium avec qui j'ai partagé le quotidien pendant ces trois années et que je suis heureuse de rejoindre au sein du département Innovation.

J'adresse mes plus vifs remerciements aux rapporteurs, Uwe Ehrenstein et Peter Schmid d'avoir accepté de lire, d'évaluer et de juger ce travail de thèse, qu'ils soient assurés de ma plus grande reconnaissance. J'associe à mes remerciements l'ensemble des examinateurs pour avoir accepté d'être dans le jury : Aimée Morgans, Marianna Braza, Jean-Christophe Robinet, Carsten Othmer. J'aimerais souligner les précieux conseils que m'ont apportés Peter et Jean-Christophe tout au long de la thèse et qui m'ont orientée à des moments décisifs.

J'exprime enfin mes sentiments envers les personnes qui comptent pour moi et qui ont eu la patience de supporter mes aléas ces dernières années. Mes pensées vont notamment à mes amies de longues dates Clarence et Naïma. Une petite dédicace à mon professeur de yoga, Aurélie, qui en « back stage » m'a aidée à développer mon self-control en toute circonstance et m'a soutenue pour garder le cap dans les moments difficiles.

Ce jour, ma pensée va plus particulièrement à mes parents, sans qui, je ne serais pas arrivée jusqu'ici. Ils ont toujours su m'écouter, m'encourager, me guider, me soutenir jusqu'au bout et surtout me donner les moyens dont j'ai eu besoin pour atteindre mes objectifs. Un grand merci à mon père, ma mère, ma sœur et mon beau-frère pour ce soutien indéfectible et sans quoi rien n'aurait été possible.

Aussi à tous ceux que j'ai oubliés ici mais qui ont partagé avec moi des moments inoubliables.

Merci à tous !

## Résumé

L'industrie automobile fournit de plus en plus d'effort pour optimiser l'aérodynamique externe des véhicules afin de réduire son empreinte écologique. Dans ce cadre, l'objectif de ce projet est d'examiner les structures tourbillonnaires responsables de la dégradation de traînée et de proposer une solution de contrôle actif permettant d'améliorer l'efficacité aérodynamique d'un véhicule SUV. Après une étude expérimentale de la maquette POSUV échelle réduite, une analyse modale croisée permet d'identifier les structures périodiques corrélées de l'écoulement qui pilotent la dépression sur le hayon. Une solution de contrôle optimale par jets pulsés sur le parechoc arrière, est obtenue avec un algorithme génétique. Celle-ci permet de réduire la dépression du hayon de 20% et l'analyse croisée des résultats instationnaires avec contrôle montre un changement significatif de la distribution spectrale. Après deux études préliminaires sur la rampe inclinée à 25° et sur le Corps d'Ahmed à 47°, la simulation de POSUV à partir d'un solveur LES, en éléments finis, est validé par rapport aux résultats expérimentaux. L'approfondissement des résultats 3D permet de comprendre les pertes aérodynamiques. La simulation de l'écoulement contrôlé permet également d'identifier les mécanismes du contrôle d'écoulements.

**Mots-clés:** Aérodynamique externe, Réduction de traînée, Contrôle d'écoulement, Décomposition Modale Dynamique, Analyse modale, Simulation LES, Écoulements détachés, Sillage turbulent, algorithme génétique

## Abstract

The automotive industry dedicates a lot of effort to improve the aerodynamical performances of road vehicles in order to reduce its carbon footprint. In this context, the target of the present work is to analyze the origin of aerodynamic losses on a reduced scale generic Sport Utility Vehicle and to achieve a drag reduction using an active flow control strategy. After an experimental characterization of the flow past the POSUV, a cross-modal DMD analysis is used to identify the correlated periodical features responsible for the tailgate pressure loss. Thanks to a genetic algorithm procedure, 20% gain on the tailgate pressure is obtained with optimal pulsed blowing jets on the rear bumper. The same cross-modal methodology allows to improve our understanding of the actuation mechanism. After a preliminary study of the 25° inclined ramp and of the Ahmed Body computations, the numerical simulation of the POSUV is corroborated with experiments using the cross-modal method. Deeper investigations on the three-dimensional flow characteristics explain more accurately the wake flow behavior. Finally, the controlled flow simulations propose additional insights on the actuation mechanisms allowing to reduce the aerodynamic losses.

**Keywords:** External aerodynamic, Drag reduction, Flow control, Dynamic Modal Decomposition, Modal analysis, Large Eddy Simulation, Detached flow, Turbulent wake, Genetic algorithm

# Résumé étendu

## Introduction

L'optimisation aérodynamique des véhicules terrestres est un défi majeur pour l'industrie automobile pour réduire son impact écologique.

Dans ce contexte, l'objectif de ce projet de thèse est d'améliorer notre compréhension des mécanismes responsables des pertes aérodynamiques sur un véhicule réaliste de type « Sport Utility Vehicle », sujet à un détachement massif induit par le design du hayon avec une lunette à  $47^\circ$ . Il s'agira aussi de proposer une solution de contrôle actif permettant de réduire efficacement les efforts de traînée inhérent à ce type de design.

Cette étude se concentre sur une maquette générique communément appelé « POSUV » reproduisant les caractéristiques moyennes des différents SUV existant dans la rue. Celle-ci a été réalisée à partir de l'exploration expérimentale et numérique de l'écoulement autour de cette géométrie en passant par des études corolaires sur les cas simplifiés de la rampe inclinée à  $25^\circ$  et le Corps d'Ahmed avec une lunette inclinée à  $47^\circ$ .

## I. Etats de l'art

Le premier chapitre est consacré à un état de l'art autour du contrôle d'écoulement pour la réduction de traînée sur un véhicule terrestre.

L'optimisation d'un véhicule SUV nécessite la compréhension de mécanismes complexes qui se développent autour d'une maquette donnée. De manière générale, les pertes aérodynamiques sont dues aux efforts de pression, aux frottements visqueux mais également due aux pertes de charges générées par l'écoulement sous capot ainsi qu'aux pertes créées par les structures turbulentes au niveau des roues, des rétroviseurs et du plancher du véhicule. Le bilan intégral de ces efforts permet de quantifier le coefficient de traînée associé à une maquette donnée par rapport à une surface frontale et une vitesse d'écoulement lointain. Les relevés effectués sur des voitures montrent que la catégorie des « Sport Utility Vehicle », appelé plus communément SUV sont associé à un coefficient de traînée autour de 0.32 (Eulalie et al., 2018a; Grandemange, 2013; I. Heft et al., 2012; Wieser et al., 2014; Wolf, 2018). Des études plus approfondies mettent en évidence l'importance de l'angle de la lunette sur le détachement de sillage (Hucho, 1987). Les véhicules de la catégorie SUV majoritairement associés à des lunettes inclinées à  $45^\circ$  sont donc soumis à un large détachement tourbillonnaire associé à une forte zone dépressionnaire dans le sillage. Parallèlement, les détachements tourbillonnaires pouvant avoir lieu sur un design réaliste participent à la complexité de l'écoulement turbulent avec entre autre les tourbillons du « A-pillar », ainsi que les instationnarités générées par l'écoulement de soubassement (Theissen, 2012; Wojciak, 2012; Yuan et al., 2018).

Les fondamentaux de la mécanique des fluides et des écoulements turbulents permettent de mettre en lumière les différents phénomènes intervenant dans ce type d'écoulement détaché à haut Reynolds. Le régime d'écoulement turbulent induit notamment une dissipation régit par la cascade turbulente en  $-5/3$  dans la zone inertielle où s'opère la turbulence homogène isotrope. Le développement de la couche limite, région soumise aux effets d'adhérence à la paroi, est également fortement régi par l'énergie cinétique turbulente transportée, ce qui favorise le fort gradient à la paroi. L'apparition d'un fort gradient de pression adverse ou d'un fort effet de courbure de la surface entraîne la séparation de la couche limite et le développement de la couche de cisaillement dont le fort gradient de vitesse génère des

instabilités de Kelvin-Helmholtz. La dynamique de l'écoulement de sillage qui se forme derrière l'obstacle est pilotée par des fréquences caractéristiques identifiées par le nombre de Strouhal. L'interaction entre ces mécanismes turbulents a été mise en évidence à partir de différents cas tests. L'étude de l'écoulement détaché sur une rampe inclinée effectuée par (Kourta et al., 2015; Stella et al., 2017a; Thacker, 2010) à 25° et (Creusé et al., 2009; Heenan and Morrison, 1998; Spazzini et al., 2001; Varon, 2017) à 90°, montre entre autre l'influence de la quantité de mouvement portée par la couche limite sur le développement de la couche de cisaillement et sur la longueur de la zone de recirculation résultante. Dans le cas plus complexe du Corps d'Ahmed proposée pour la première fois dans l'étude de (Ahmed et al., 1984a), la topologie du sillage pour un véhicule simplifié est gouverné par le détachement sur la lunette, attaché jusqu'à 10°, partiellement détaché entre 10 et 30° et entièrement détaché au-delà de 30°. Dans le cas spécifique du Corps d'Ahmed à 90°, la dynamique du sillage est gouvernée par le phénomène de bi-stabilité décrit par (Bonnaïon, 2018; Grandemange, 2013; Li, 2017a; Varon et al., 2017a; Volpe et al., 2015).

Diverses stratégies ont été adoptées afin de réduire les pertes aérodynamiques. Parmi les solutions existantes, l'intégration de systèmes type passifs tels que les déflecteurs (Bonnaïon, 2018; Grandemange, 2013), l'effet de rétreint (Beaudoin and Aider, 2008; Perry et al., 2016), les milieux poreux (Bruneau et al., 2014, 2010; Mimeau et al., 2017) ou les générateurs de vortex montrent l'impact du contrôle de la séparation de la couche limite sur l'arrière corps pour réduire la dépression du sillage. En outre, les solutions de contrôle actifs comme le plasma (Boucinha et al., 2010; Khalighi et al., 2016; Shadmani et al., 2018; Vernet et al., 2018), les jets stationnaires (Aubrun et al., 2011; McNally et al., 2015; Wassen et al., 2010), les oscillateurs fluidiques (Arwatz et al., 2008; Metka and Gregory, 2015; von Gosen et al., 2015), les jets synthétiques (Eulalie, 2014; Leclerc, 2008; Minelli et al., 2018) ou les jets pulsés montrent un fort potentiel pour la réduction de traînée mais permettent également d'approfondir la compréhension du mécanisme de séparation de la couche limite et comment il impact la zone dépressionnaire du sillage. Une analyse approfondie proposée par (Parezanovic et al., 2014) souligne l'importance des fréquences d'actionnement dans le contrôle de la couche de cisaillement.

Il apparaît ainsi judicieux d'implémenter des lois de contrôle permettant d'identifier les paramètres des actionneurs en vue d'optimiser l'efficacité du système. On peut mentionner les stratégies de contrôle boucle fermée en temps réel telles que l'opposition (Bruneau et al., 2010), la recherche d'extremum, la recherche de pentes (Parezanovic et al., 2014; Pastoor et al., 2008), les observateurs dynamiques (Pastoor et al., 2008; Tadmor, 2004, Varon, 2017). L'intérêt des méthodes d'apprentissage pour la recherche d'un point de fonctionnement optimal doit également être mentionné avec en temps réel des algorithmes tel que « Learning Genetic Programming Control » (Li, 2017b; Li et al., 2017a).

Dans le cadre de l'analyse de la sensibilité de l'écoulement au contrôle, il apparaît nécessaire d'introduire des outils mathématiques permettant d'extraire les structures cohérentes ainsi que les phénomènes périodiques qui gouvernent le sillage. La décomposition orthogonale en mode propre introduite par (Lumley, 1981, 1967), a été largement utilisée pour mettre en évidence les cohérences de l'écoulement. Parallèlement, on fait mention de l'intérêt de la Décomposition Modale Dynamique (Schmid, 2012) comme méthode permettant d'extraire les périodicités de l'écoulement. L'algorithme basé sur une étape préliminaire de décomposition en valeur singulière puis l'application combiné avec l'algorithme de sélection « Sparse Promoting » (Jovanović et al., 2014a) apparaît pertinent pour l'identification des fréquences caractéristiques de l'écoulement.

Enfin, l'exploration des méthodes numériques utilisées pour l'étude de ce type problème fait apparaître un large panel de potentielles stratégies. Cela passe par un choix sur le niveau de

résolution des échelles de la turbulence, allant de l'approche « Reynolds-Average Navier-Stokes » où l'intégralité des fluctuations turbulentes est modélisée jusqu'à la « Direct Navier-Stokes » où l'intégralité des fluctuations turbulentes est résolue, en passant par les approches hybrides « Detached Eddy Simulation », « Partially Average Navier Stokes » ou « Large Eddy Simulation ». Après exploration des différentes approches, il est convenu de se concentrer sur l'approche LES comme étant un compromis pertinent afin de résoudre les échelles de la turbulence nécessaire pour l'étude de l'écoulement sur une maquette à échelle réduite couplé avec le modèle de sous-maille Dynamique Smagorinsky (M Germano et al., 1991). De plus, la robustesse et la précision apportée par la méthode des éléments finis avec la technique d'approximation Galerkin moindre carrés (Shakib, 1991) est discutée par rapport à d'autres stratégies tels différences finies ou volumes finies qui sont très coûteuses et moins dissipatives. Notons toutefois qu'une méthode Lattice Boltzmann aurait également pu être adoptée compte tenu des hautes capacités de parallélisation de cette technique.

Tous les éléments explorés dans ce paragraphe permettent de poser les fondements des travaux effectués.

## II. Etudes expérimentales et contrôle d'écoulement sur un véhicule SUV échelle réduite

Les travaux expérimentaux ont été effectués sur une maquette échelle 1/6 par rapport à un véhicule réaliste avec une lunette inclinée à  $47^\circ$  comme illustré en Fig. 1. La longueur de référence est définie par rapport à la hauteur du véhicule égale à 200mm et la surface de référence associée à l'aire frontale du véhicule est égale à  $0.06\text{m}^2$ .

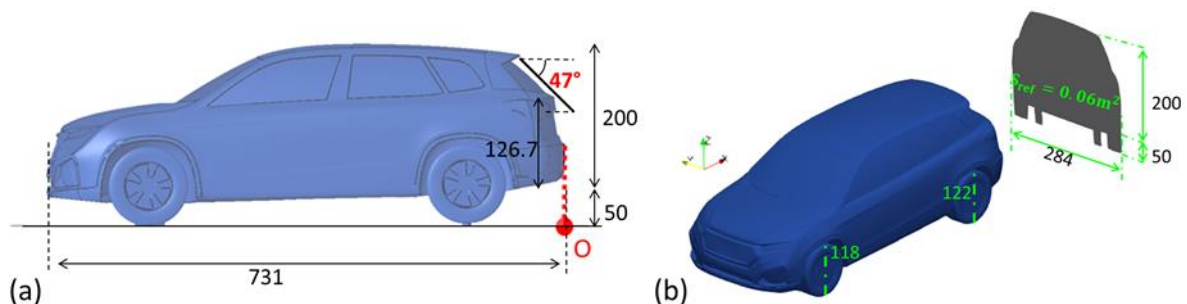


Fig. 1: Géométrie de la maquette du SUV générique à l'échelle réduite avec les dimensions caractéristiques en millimètres: (a) Vue latérale; (b) Vue 3D avec une projection montrant la surface frontale.

La maquette est placée dans le tunnel de la soufflerie de Berlin de section 1.4m de hauteur sur 2m de largeur ce qui correspond à un taux de blocage de la maquette de 2%. L'écoulement externe est caractérisé par un tube de Pitot où la pression de référence est mesurée. Le débit passant dans le convergent est calibré de façon à avoir une vitesse de référence au tube de Pitot de 30m/s. Ceci permet d'établir un écoulement associé à un nombre de Reynolds de 400 000 par rapport à la hauteur de la maquette ce qui correspond à un régime de vitesse de 110km/h sur autoroute. De plus, une intensité turbulente de 0.5% est injectée en entrée de convergent de la soufflerie. Enfin, la campagne a été effectuée avec des roues fixes et un sol non défilant.

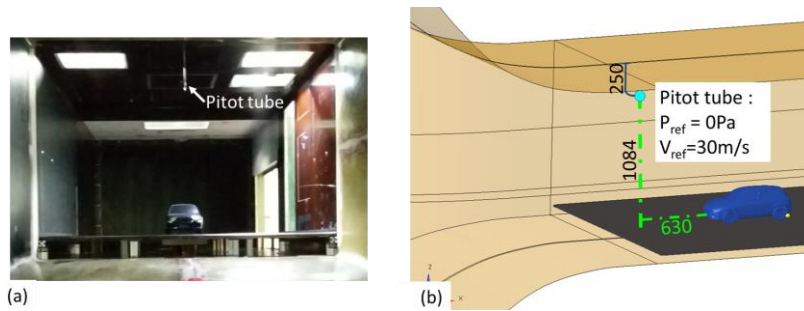


Fig. 2: (a) Photo de la maquette du POSUV placée dans le tunnel principal de la soufflerie de Berlin de section 1.4m x 2m avec le tube de Pitot où la pression de référence et la vitesse de référence sont prises. (b) Schéma de la maquette du SUV avec la position du Pitot par rapport au nez du véhicule.

L'analyse expérimentale est effectuée à partir de 48 capteurs de pression distribués sur l'arrière du véhicule. La pression statique est ainsi capturée avec un échantillonnage de 2000Hz sur une période d'acquisition de 1 minute. Des mesures PIV complémentaires ont permis de compléter l'analyse de l'écoulement de référence non contrôlé.

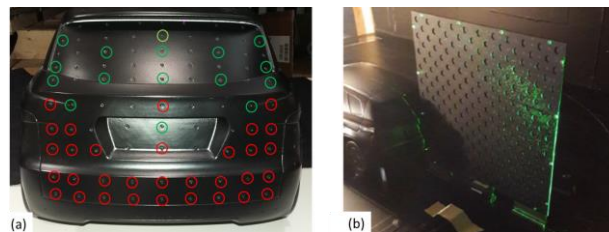


Fig. 3: (a) Photo des capteurs de pression distribués sur le hayon; (b) Photo du système PIV utilisé pour caractériser la dynamique du sillage.

Les actionneurs de type jets pulsés ont été placés sur les côtés latéraux et inférieur du parechoc arrière de la maquette comme illustré en Fig. 4. Les fentes, de dimension 0,5mm sur 2,5mm sont distribuées avec un espacement de 14mm.

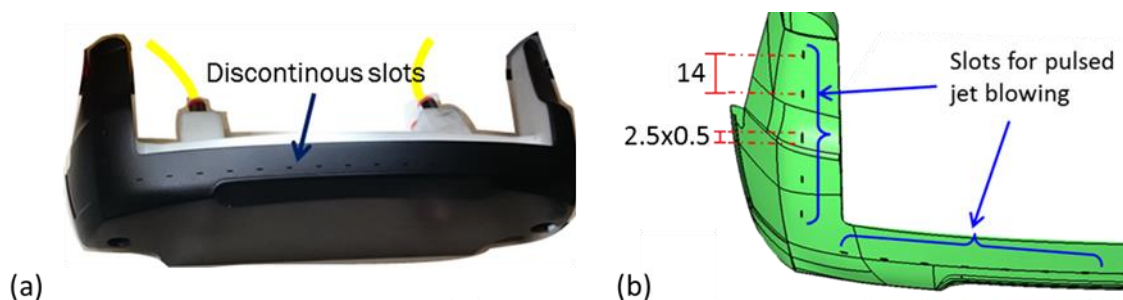


Fig. 4: Photo de la pièce parechoc arrière intégrant les jets discontinus; (b) Schéma illustrant les caractéristiques géométriques des fentes en millimètre. Celles-ci sont distribuées sur les côtés latéraux et sur la partie inférieure du parechoc avec un espacement de 14mm. Chaque fente fait 2,5mm de large sur 0,5mm de long.

En outre, les circuits d'alimentation du système pneumatique ont été mis en place de façon à ce que les débits dans les fentes latérales soient égaux et les débits dans les fentes en partie basse soient égaux. De plus quatre électrovannes ont été intégrées au circuit afin d'appliquer quatre fréquences différentes de façon à avoir une fréquence par groupe de fentes respectivement sur les côtés droit et gauche pour les fentes latérales et sur les moitiés droite et gauche des fentes inférieures. Ceci permet de définir des actionneurs pilotés par 4 fréquences,

4 phases et 2 débits. L'espace du plan d'expérience est donc défini par 10 paramètres de contrôle. Une caractérisation à l'aide de débitmètre permet de caractériser les débits équivalents en sortie de buses en fonction de la fréquence et du pourcentage d'ouverture de vanne.

Les capteurs et actionneurs sont connectés à une carte pilote  $\mu$  – Dacq gérée par Labview. Ce programme est en communication avec Matlab sur lequel a été implémenté l'outil d'optimisation.

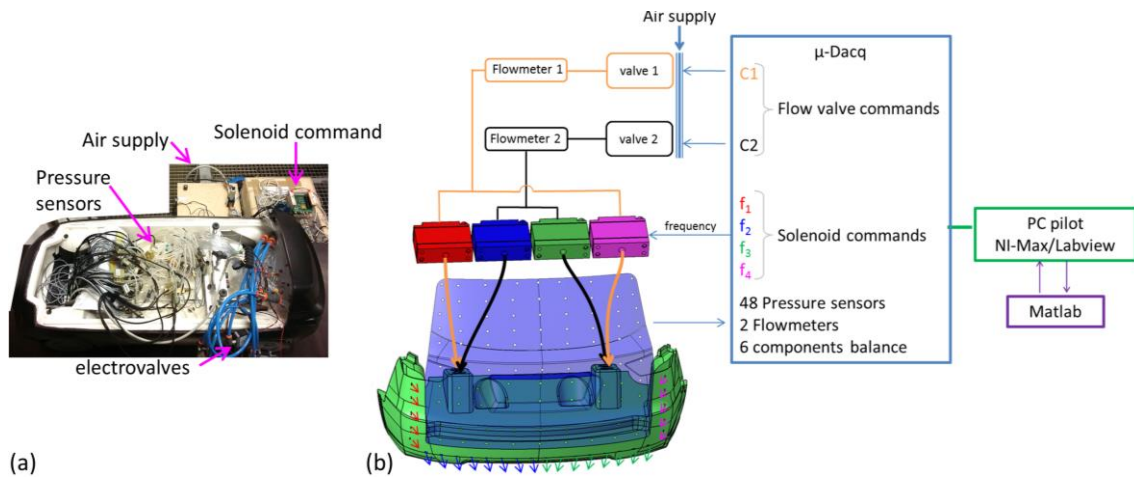


Fig. 5: (a) Photo des actionneurs et capteurs à l'intérieur de la maquette; (b) Diagramme du système de commande et d'acquisition pilotant les actionneurs et les capteurs sur Labview et Matlab.

L'algorithme de recherche de type contrôle réactif est une adaptation du programme « Machine Learning Control » proposé par (Gautier et al., 2015). Il s'agit d'une méthode de recherche, n'impliquant pas de modèle de comportement qui consiste à identifier la meilleure combinaison de paramètres de contrôle permettant de minimiser une fonction coût. Dans la logique de l'algorithme génétique, l'algorithme de recherche consiste à faire évoluer une population d'individus auxquels on attribue des caractères (4 fréquences et 2 débits) de façon à sélectionner les meilleurs individus. Un taux de mutation permet d'introduire de nouveaux caractères aléatoires ce qui assure le caractère global de l'algorithme de recherche. Outre la mutation, le processus d'évolution fait intervenir les mécanismes d'élitisme qui duplique le meilleur individu, de « cross-over » qui crée un nouvel individu en croisant les caractères de deux individus de la génération précédente et de réplication qui applique une redondance sur certains individus de la génération précédente (Fig. 6).

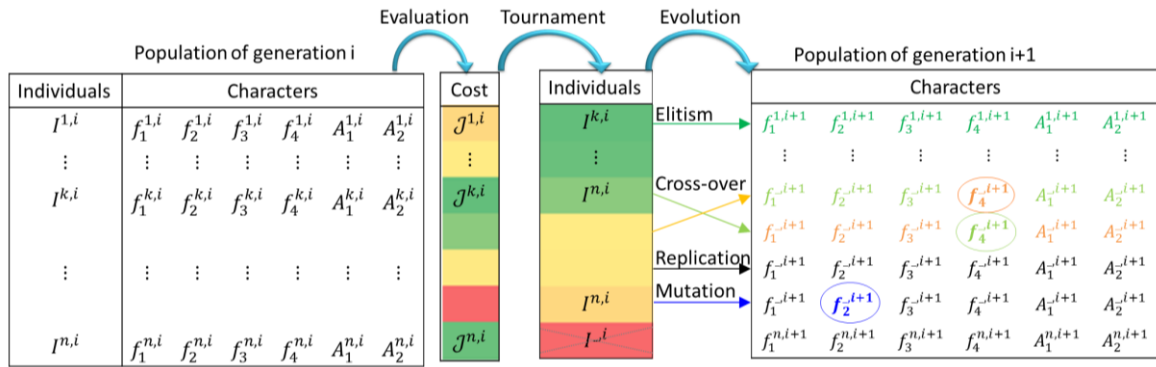


Fig. 6: Processus d'évolution intégré dans l'algorithme génétique, permettant de générer une nouvelle population d'individus associée à la génération i+1 (un ensemble de combinaison de paramètres) à partir des gains obtenus au sein de la population de la génération i.

Ainsi, à partir d'un plan d'expérience initial, les fréquences des jets pulsés et leur amplitudes sont optimisés afin maximiser la pression moyenne s'exerçant sur les capteurs du Hayon comme illustré en Fig. 7. Pendant cette campagne expérimentale, le processus d'évolution par algorithme génétique est exécuté sur une population de 51 individus par génération évoluant sur 16 générations correspondant à un total de 816 acquisitions. Le processus d'évolution est pondéré par 19% de mutations, 69% de « cross-over », 10% de réplifications et 2% d'élitisme.

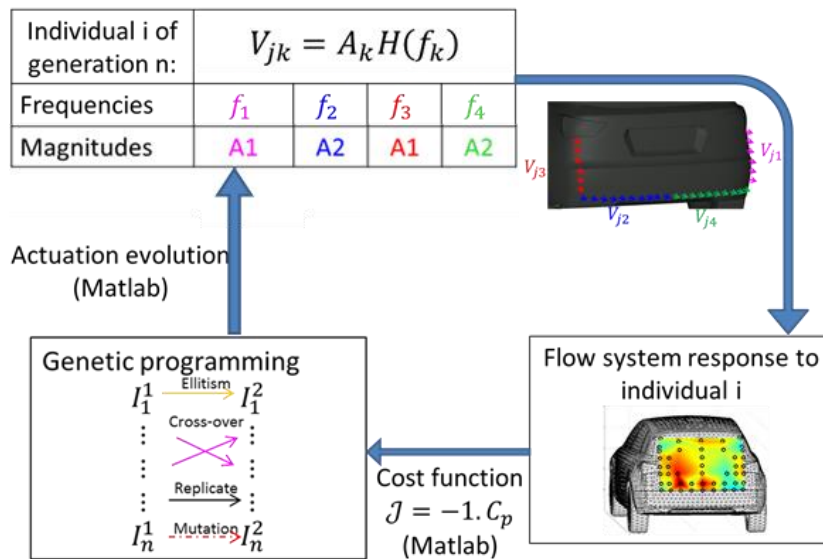


Fig. 7: Schéma de l'algorithme de contrôle implémenter afin d'identifier le meilleur point de fonctionnement sur les paramètres de fréquences et de débits des actionneurs.

Après ces 16 générations, le meilleur individu a été sélectionné et comparé à l'écoulement non contrôlé. Au-delà du gain obtenu, le but de l'étude vise à comprendre comment le contrôle actif modifie le comportement de l'écoulement comparé à l'écoulement non contrôlé.

- Topologie moyenne de l'écoulement avec et sans contrôle

La distribution du coefficient de pression moyen sur le hayon pour l'écoulement non contrôlé est caractérisée par une zone de basse pression en partie basse et une zone de haute pression sur la lunette comme illustré sur la Fig. 8a. Le coefficient de pression moyen appliqué sur cette surface est égal à  $C_p = -0,23$ . Le coefficient de traînée sur le véhicule mesuré par la

balance est égal à  $C_d = 0.36$ . En outre, la zone de basse pression mesurée en partie basse du hayon se superpose avec la zone marquée par d'importante fluctuation de pression illustré par la distribution de RMS de  $C_p$  en Fig. 8b.

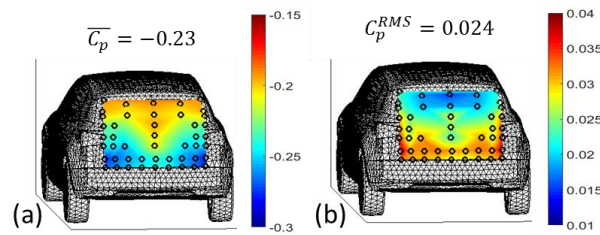


Fig. 8: (a) Distribution moyenne du coefficient de pression de l'écoulement non contrôlé; (b) Distribution de la RMS du coefficient de pression de l'écoulement non contrôlé.

L'amplitude des pertes aérodynamiques apparaît être élevée comparée aux mesures usuelles autour de  $C_d = 0.32$  ainsi que l'intensité de la dépression s'exerçant sur le culot qui s'élève à 64% de l'effort total. Notons cependant que le sol fixe de la soufflerie induit un taux de blocage plus important dans le sous-bassement de la maquette, ce qui modifie de façon significatif le gradient de pression adverse et par conséquent le détachement sur le parechoc arrière. En réduisant la section efficace de l'écoulement du sous-bassement, l'effet du diffuseur du parechoc arrière est accru et la dépression du sillage est plus accentuée. Ceci ne modifie pas la topologie générale de l'écoulement qui est en accord avec les observations à l'échelle 1 et sur route vue dans la section de l'étude bibliographique.

Des mesures de Vélocimétrie par Images de Particules (PIV) dans les plans 2D du sillage, ont permis d'approfondir la compréhension de la topologie de l'écoulement de référence. La figure Fig. 9a présente la distribution moyenne de vitesse dans le plan vertical  $Y0$  et la figure Fig. 9b présente le champs de vitesses moyen dans le plan horizontal placé à 140mm du sol ( $Z140$ ). Les champs moyens mettent en évidence une zone de recirculation marquée par une symétrie selon le plan vertical  $Y0$ .

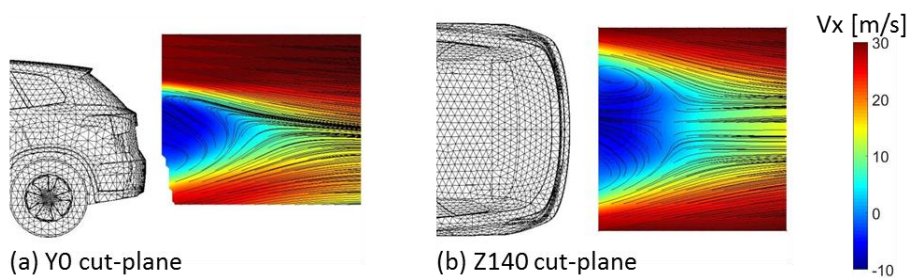


Fig. 9: Distribution moyenne de vitesse dans: (a) le plan vertical en  $Y0$ ; (b) le plan horizontal à 140mm du sol.

Les fluctuations de vitesses mesurées par la caméra rapide soulignent également l'intensité des fluctuations de vitesses particulièrement marquée au niveau des couches de cisaillement induit par les détachements du becquet en partie haute et sur le parechoc en partie basse dans le plan  $Y0$  (Fig. 10a). Ces fluctuations turbulentes sont également mesurées dans les couches de cisaillement induit par les détachements latéraux du parechoc (Fig. 10b).

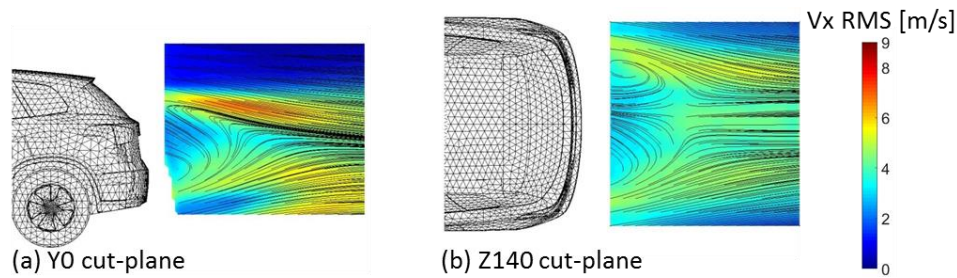


Fig. 10: Distribution de la RMS de vitesse : (a) le plan vertical en Y0; (b) le plan horizontal à 140mm du sol.

Ces observations permettent de pressentir l'interaction entre les mécanismes de détachements, de cisaillements et de recirculation dans le cas de l'écoulement non contrôlé.

La comparaison avec les résultats obtenus avec le contrôle a été effectuée à partir du point de fonctionnement le plus efficace identifié à l'aide de l'algorithme de recherche détaillé précédemment. Les paramètres de fréquences et débits associés sont illustrés en Fig. 11. En effet, l'algorithme de recherche a identifié une augmentation du niveau de pression moyen avec une combinaison de hautes fréquences à 294Hz et 93Hz sur les fentes latérales et à 430Hz et 374Hz sur les fentes en partie basse. Les jets pulsés sont pondérés par un faible débit à 15% d'ouverture de vanne en latéral et de 50% d'ouverture de vanne en partie basse. Selon l'abaque caractérisant le débit équivalent en fonction du pourcentage d'ouverture et de la fréquence d'actionnement, ces pourcentages d'ouverture correspondent à des débits de 15L/min sur les côtés et de 30L/min en partie basse.

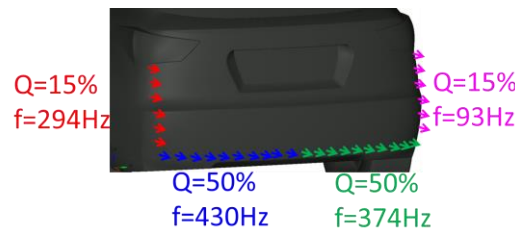


Fig. 11: Meilleur point de fonctionnement identifié à la fin de l'algorithme génétique.

Ce point de fonctionnement permet d'obtenir une pression moyenne sur le hayon de  $C_p = -0.19$ , correspondant à un gain de 20% par rapport au niveau de pression du hayon sans contrôle. La distribution moyenne du coefficient de pression est tracée sur Fig. 12a et la RMS en Fig. 12b. Similairement à la distribution de  $C_p$  moyen dans le cas sans contrôle, le champ de  $C_p$  moyen avec le contrôle est marqué par une zone de basse pression en partie basse. Si la topologie moyenne est conservée, l'intensité de la zone dépressionnaire a significativement été réduite. La RMS de  $C_p$  mesurée sur le hayon met en évidence un amortissement du niveau de fluctuations

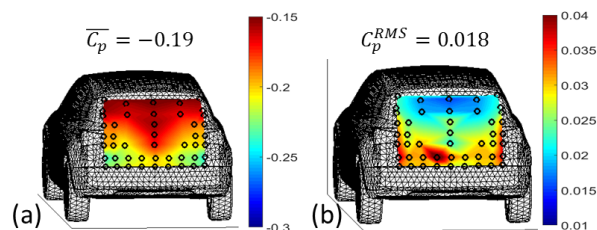


Fig. 12: (a) Distribution moyenne du coefficient de pression de l'écoulement contrôlé ; (b) Distribution de la RMS du coefficient de pression de l'écoulement contrôlé.

- Analyse modale et mise en évidence de la dynamique de l'écoulement avec et sans contrôle

L'outil d'analyse utilisé ici pour extraire la dynamique de l'écoulement est basé sur la méthode de Décomposition Modale Dynamique (DMD). Cet algorithme permet d'isoler des motifs se propageant de façon périodique dans l'écoulement. Il est basé sur une hypothèse de linéarité de l'information transmise d'un instantané à l'autre dans une base de données caractérisant l'évolution espace-temps d'un système dynamique. La matrice rassemblant ces déphasages entre instantanés est dénommée  $A$ , matrice carré de taille égal au nombre de capteurs / nœuds (Fig. 13). Les périodicités de l'écoulement sont extraites à partir des valeurs propres et modes propres de  $A$ .

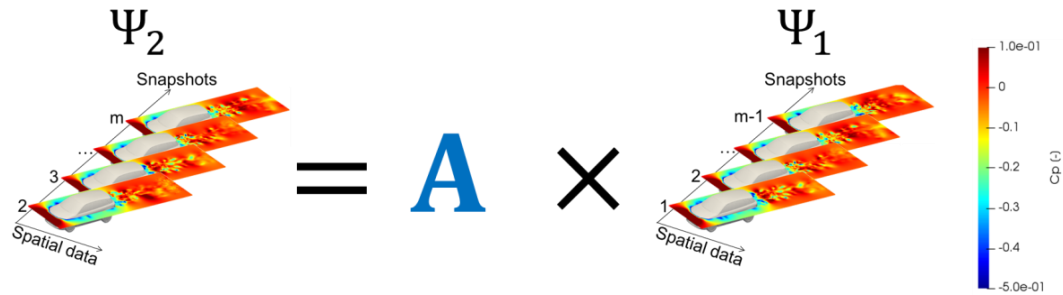


Fig. 13: Formulation matricielle de l'hypothèse de linéarité permettant de définir la matricide  $A$  contenant les déphasages d'un instantané à l'autre.

La matrice  $A$  étant dense et non-symétrique, la résolution des modes propres nécessite une projection préliminaire dans la base des modes propres orthogonaux (matrice  $U$ ), obtenu après décomposition en valeurs singulières de  $\Psi_1$ . La résolution des valeurs propres  $\mu$  et vecteurs propres  $Y$  de la matrice réduite  $\tilde{A}$ , issue de cette projection, sont à valeur complexe et contiennent les composantes spectrales de l'écoulement. Les modes DMD  $\Phi$  sont ensuite obtenus par projection des vecteurs propres  $Y$  sur les modes propres orthogonaux  $U$ .

$$\begin{aligned}
 \Psi_1 &= U\Sigma V^* & (a) \\
 A &= \Psi_2 \Psi_1^{-1} = \Psi_2 V \Sigma^{-1} U^* & (b) \\
 \tilde{A} &= U^* A U = U^* \Psi_2 V \Sigma^{-1} & (c) \quad \text{Eq.1} \\
 \tilde{A} Y &= Y D_\mu & (d) \\
 \Phi &= U Y & (e)
 \end{aligned}$$

Avec

$U$  matrice unitaire des vecteurs propres gauches de  $\Psi_1$

$$(U^* U = I_n)$$

$V^*$  matrice unitaire, adjointe de  $V$ , contenant les vecteurs propres à droite de  $\Psi_1$

$$(V^* V = I_n)$$

$\Sigma = \text{diag}(\sigma_1, \sigma_2, \dots, \sigma_r)$  la matrice diagonal des valeurs singulières de  $\Psi_1$ ,  
avec  $r = \text{rang}(\Psi_1)$

$\tilde{A}$  la matrice DMD réduite obtenu par projection sur  $U$

$D_\mu$  la matrice diagonale is the diagonal matrix of complex eigenvalues  $\mu_k$  of  $\tilde{A}$

$Y$  are the complex eigenvectors of  $\tilde{A}$ .

Cette décomposition permet de reconstruire l'écoulement à partir d'une suite de composantes périodiques auxquelles on associe des fréquences caractéristiques et des taux de croissance ou décroissance  $\sigma$  (Fig. 14). Les amplitudes  $\alpha$  associées aux modes DMD dans l'écoulement est calculé à l'aide de l'algorithme « Sparse Promoting » (Jovanović et al., 2014a) visant à

minimiser le résidu entre la base de données reconstruite et la base de données initiale, sous contrainte de minimiser le nombre de modes permettant de décrire la dynamique du système. Cette technique permet de réduire la dimension du système, ce qui est particulièrement pertinent pour des écoulements de sillages turbulents.

$$P_k = \sum_{j=1}^{m-1} e^{k \cdot \sigma_j \cdot \delta t} \cdot [\cos(2\pi f_j \cdot k \cdot \delta t) \times \Re(\alpha_j \Phi_j) - \sin(2\pi f_j \cdot k \cdot \delta t) \times \Im(\alpha_j \Phi_j)] \quad \text{Eq.2}$$

Avec :

$f_i = \frac{\Im(\ln(\mu_i))}{2\pi \cdot \delta t}$  la fréquence associée à la valeur propre  $\mu_i$

$\sigma_i = \frac{\Re(\ln(\mu_i))}{\delta t}$  le taux de croissance/décroissance associé à la valeur propre  $\mu_i$

$\alpha_i$  l'amplitude associée au mode  $\Phi_i$

$\delta t$  le pas de temps séparant deux instantanés.

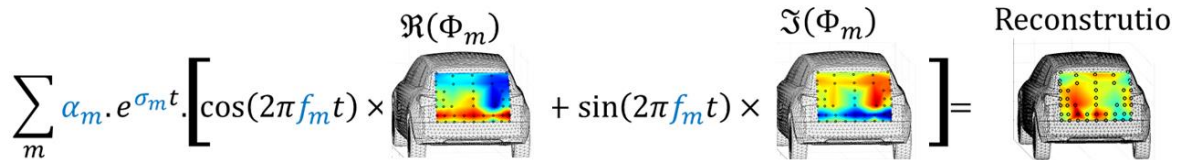
$$\sum_m \alpha_m \cdot e^{\sigma_m t} \left[ \cos(2\pi f_m t) \times \Re(\Phi_m) + \sin(2\pi f_m t) \times \Im(\Phi_m) \right] = \text{Reconstruction}$$


Fig. 14: Equation de la reconstruction des champs instantanés de pression à partir de la décomposition modale.

Cette méthode d'analyse modale a été appliquée afin de caractériser la dynamique du sillage. Après exploration des comportements périodiques caractéristiques impactant le hayon de la maquette, une analyse croisée a été appliquée pour identifier quels sont les mouvements de circulation du sillage régissent ces même fréquences. Puis une analyse modale croisée avec les résultats obtenus avec le contrôle a été effectué afin de mettre en évidence quels sont les phénomènes atténués et quels sont ceux qui ont été accrus par les jets. Cette démarche a pour but d'identifier les mécanismes turbulents qui accentuent les pertes aérodynamiques afin d'affiner la compréhension du contrôle d'écoulement.

Dans un premier temps, l'étude basée sur la dynamique des capteurs de pression sur le hayon (Fig. 15) dans le cas de l'écoulement non contrôlé, a permis d'identifier la signature spectrale de mouvements oscillants à 4.3Hz ainsi qu'à 8.2Hz, couplé à des phénomènes de pulsations de fluctuations de pression réparties de façon homogène sur le culot à 1.8 et 9.3Hz. De plus, la décomposition modale a mis en évidence une composante statique, associé à un mode à 0Hz dont l'amplitude représente 95% de l'ensemble des caractéristiques modales.

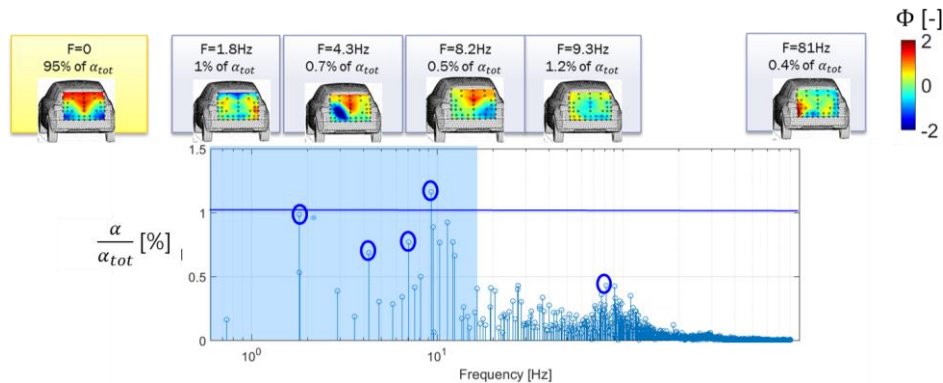


Fig. 15: Distribution d'énergie des composantes DMD en fonction de la fréquence.

Ensuite une analyse DMD croisée avec les mesures PIV rapides dans les plans Z140 et Y0 a été proposée afin d'identifier l'interaction entre la dynamique du sillage et la zone dépressionnaire agissant sur le culot.

En outre, l'application de cette méthodologie pour approfondir les changements de répartition d'énergie opérée par le contrôle d'écoulement permet de conclure sur l'interaction du jet pulsé à haute fréquence sur les structures énergétiques basses fréquences.

### III. Etudes numériques et contrôle d'écoulement

L'étude expérimentale a permis d'extraire les caractéristiques principales de la topologie de l'écoulement de sillage l'impact sur le hayon. L'étude numérique effectuée conjointement a ainsi été validée grâce à ces éléments et l'exploration du comportement 3D à haute fréquence a été effectuée en vue d'approfondir la compréhension des phénomènes en jeu.

Dans cette optique, des simulations préliminaires ont été mise en place pour le dimensionnement du modèle numérique. Dans un premier temps, la simulation de l'écoulement au-dessus d'une rampe inclinée à  $25^\circ$  a été utilisée pour appréhender les mécanismes turbulents intervenant dans la couche de cisaillement et l'interaction avec la zone de recirculation. Dans un second temps, la simulation de l'écoulement autour d'un corps d'Ahmed avec un culot à  $90^\circ$  a été utilisée pour calibrer les phénomènes périodiques du sillage. Ces cas d'études ont parallèlement été exploités avec la méthode de Décomposition Modale Dynamique afin de valider une méthodologie efficace pour l'analyse d'écoulements turbulents complexes.

Après ces études préliminaires, la simulation de l'écoulement autour de la maquette SUV générique placée dans la soufflerie de l'Université de Berlin a été mise en place conformément aux conclusions ressortant des études préliminaires. Après un travail de validation et de critique des résultats obtenus, une étude du comportement de l'écoulement été effectué avec et sans contrôle.

- Modèles mathématiques et techniques d'approximations pour la simulation des grandes échelles (LES)

Les travaux effectués au cours de cette étude sont basé sur le solveur AcuSolve de la suite ALTAIR. Il s'agit d'un code éléments finis qui propose une approche LES largement détaillé dans la publication de (Shakib, 1991). Les équations de Navier-Stokes sont résolus jusqu'à la fréquence de filtrage du maillage. Les contributions de sous mailles sont modélisées avec le modèle de Smagorinsky Dynamique qui quantifie l'énergie turbulente à modéliser localement et à tout instant, à partir l'énergie résolue entre un filtre numérique et le filtre du maillage (Fig. 16). Cette technique garantit une estimation adaptée de la dissipation turbulente contrairement à la version du modèle de Smagorinsky classique dont la dissipation turbulente est pondérée par un facteur fixé de façon empirique.

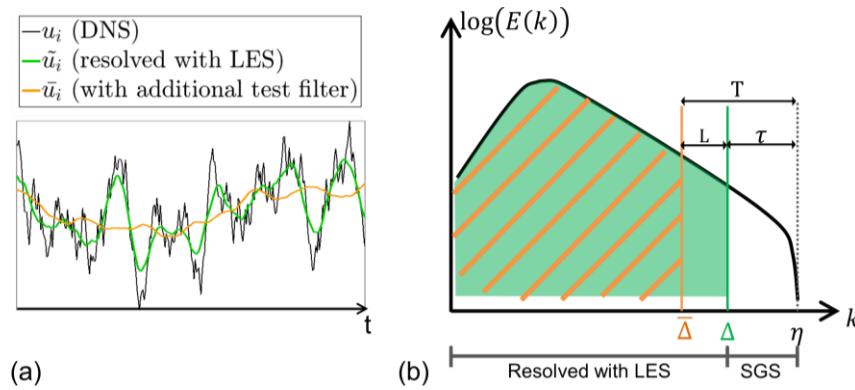


Fig. 16: (a) Illustration des signaux de vitesses en DNS comparés avec les signaux filtrés utilisés en LES avec et sans le filtre numérique. (b) Graphique schématisant la répartition d'énergie turbulente totale (surface sous la courbe noire), résolue en LES (surface verte) et l'écart d'énergie turbulentes entre le filtre du maillage et le filtre numérique permettant de dimensionner le taux de dissipation dans le modèle de Smagorinsky dynamique.

De plus, un modèle de traitement à la paroi est utilisé pour reproduire le profil de couche limite turbulent basé sur un modèle linéaire lorsque la première maille à la paroi se situe dans la sous-couche visqueuse ( $y^+ < 5$ ) et une loi logarithmique lorsque la première maille à la paroi se situe dans la couche externe ( $y^+ > 30$ ). Entre ces deux régions, une fonction pont est utilisée. Une modélisation de la sous-couche visqueuse est préconisée afin de garantir une bonne reproduction de la quantité de mouvement dans la couche limite.

Les équations de Navier-Stokes filtrées sont ensuite résolues à l'aide de la méthode d'approximation Galerkin moindre carré, qui consiste à minimiser le résidu. L'algorithme de minimisation est basé sur une combinaison d'un terme de Galerkin qui garantit la précision de la solution avec un terme moindre carré qui permet d'amortir les instabilités potentiellement générés par les éléments distordus. Ce terme est notamment particulièrement nécessaire afin d'assurer la robustesse des simulations des écoulements autour de géométries complexes tel que le SUV réaliste. Une attention particulière doit cependant être portée dans les zones à faible vitesse mais fortement turbulentes ou la contrainte du terme moindre carré est très restrictive (Fig. 17). C'est notamment le cas dans la zone « d'eau morte » du sillage et la zone de la couche de cisaillement où une nappe à vitesse nulle se développe.

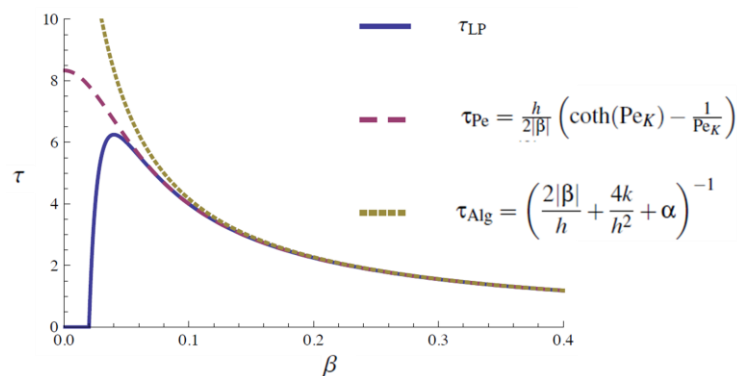


Fig. 17: Relation entre le rayon spectral de la matrice moindre carré  $\tau_{Pe}$  qui pondère le terme de régularisation en fonction de la vitesse de convection mesurée sur la base d'un problème 1D.

Enfin, le solveur intègre un schéma d'ordre 2 en espace sur toutes les variables avec un algorithme semi-discret d'ordre 2 en temps.

- Etudes préliminaires sur la rampe inclinée à 25°

La simulation de l'écoulement au-dessus de la rampe a été effectuée et validée à partir des résultats expérimentaux disponibles dans les publications de (Kourta et al., 2015; Stella et al., 2017a; Thacker, 2010). Le domaine de simulation 3D a été restreint à une zone de 4h en amont de la rampe, 12h en aval, 6h en hauteur et 4h en profondeur. En prenant en compte les critères de qualité de la discrétisation de la couche limite, et résolution de la turbulence avec l'approche LES, plus le modèle de Smagorinsky dynamique, un maillage final de 60 millions d'éléments et 9 millions de nœuds a été généré.

L'analyse comparative des résultats avec les mesures expérimentales de la littérature a fait apparaître plusieurs points importants. En effet, en dépit d'une sous-évaluation des fluctuations de vitesse en amont de la rampe dû à l'absence de condition limite avec injection de turbulence synthétique, le profil moyen de la couche limite a montré une bonne reproduction du comportement expérimental associé à une bonne qualité de résolution du phénomène de séparation sur le bord de la rampe. L'écart d'énergie cinétique turbulente en amont de la rampe entraîne une différence sur l'épaisseur de la couche de cisaillement très localement au niveau du bord. La courbe de tendance définissant l'évolution de l'épaisseur de quantité de mouvement  $\theta_{SH}$  en fonction de  $x$  est en accord avec les observations de la littérature.

De plus, les topologies moyennes de la zone de recirculation en numérique et en expérimental, en terme de champ de vitesses moyennes, ainsi que de pression à la paroi (Fig. 18 a et b) permettent de valider l'écoulement non contrôlé.

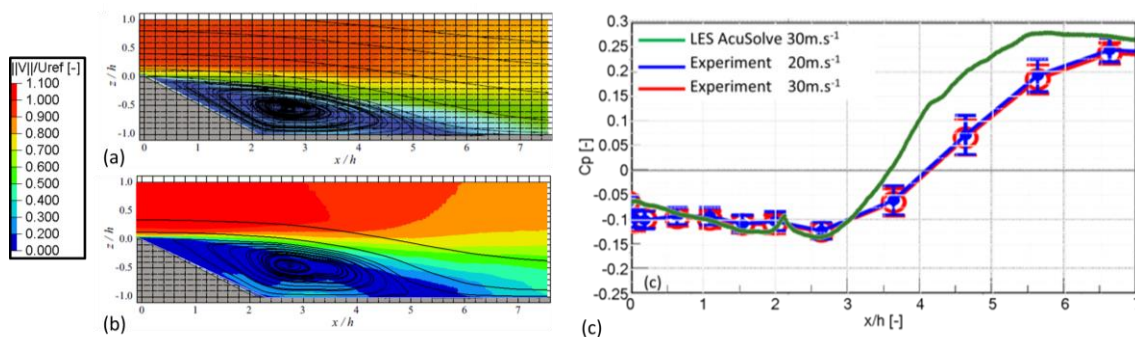


Fig. 18: Comparaison des champs moyens de vitesses: (a) en expérimental (Kourta et al., 2015b); (b) en numérique; (c) Comparaison du profils de pression montrant une zone dépressionnaire jusqu'à 3h suivie d'une zone de recompression qui s'opère de façon plus violente en calcul par rapport aux mesures expérimentales.

La simulation de l'écoulement avec du contrôle actif par jet synthétique a ensuite été effectuée et validée conformément aux observations expérimentales. La physique du contrôle a donc ainsi pu être capturée par le modèle numérique. Ceci a été vérifié grâce au meilleur point de fonctionnement proposé dans l'étude de expérimental (Kourta et al., 2015) avec un soufflage correspondant à un nombre de Strouhal de 0,6 (adimensionné avec la hauteur de la rampe de 0,1m et la vitesse infinie de 30m/s). La visualisation des champs de fluctuations de vitesses (Fig.19), suggère une injection de quantité de mouvement par les jets qui modifie le comportement de la couche de cisaillement.

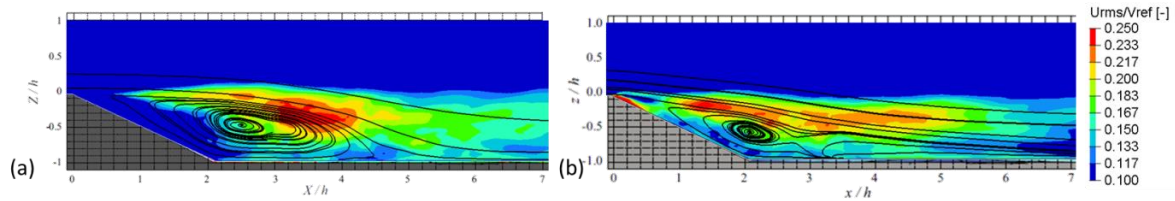


Fig. 19: Comparaison des champs RMS de vitesses dans le plan  $Y0$ : (a) écoulement non contrôlé; (b) écoulement contrôlé.

Une analyse plus approfondie avec la Décomposition Modale Dynamique a permis de mettre en évidence ce phénomène et l'interaction avec la longueur de la zone de recirculation (Fig. 20). En effet, un amortissement des caractéristiques spectrales à basse fréquences ( $St=0,02$  ;  $St=0,08$ ) a été montré entre l'écoulement non contrôlé et celui avec contrôle. La répartition spectrale de l'énergie suggère un apport accru de l'énergie sur le mode à  $St=0,6$  qui favorise le mécanisme de mélange turbulent et de dissipation. Ainsi les structures à échelle intégrale portent moins d'énergie expliquant la diminution de la longueur caractéristique de la zone de recirculation.

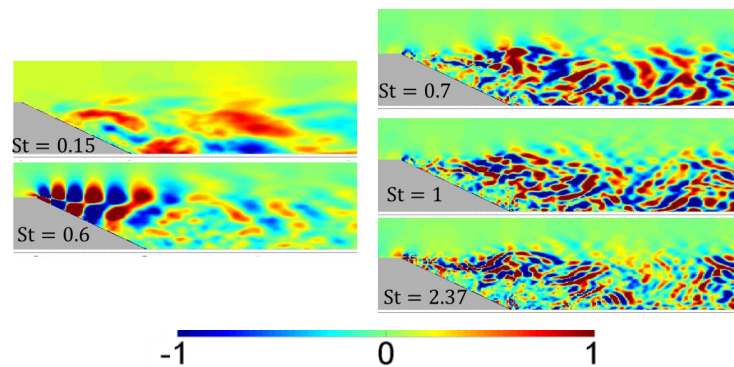


Fig. 20: Modes DMD participant au mécanisme de dissipation turbulente favorisé par l'actionnement.

- Etudes préliminaires sur le corps d'Ahmed avec un culot à  $47^\circ$

Les travaux ont été effectués sur une version modifiée du Corps de Ahmed à  $47^\circ$  afin de reproduire les principaux rapports d'aspect d'un véhicule SUV (Fig. 21) par rapport à la version originale proposée par (Ahmed et al., 1984b). Cette étude a pour objectif de dimensionner une simulation 3D LES d'une maquette équivalente au SUV dans une soufflerie à un nombre de Reynolds de 420 000.

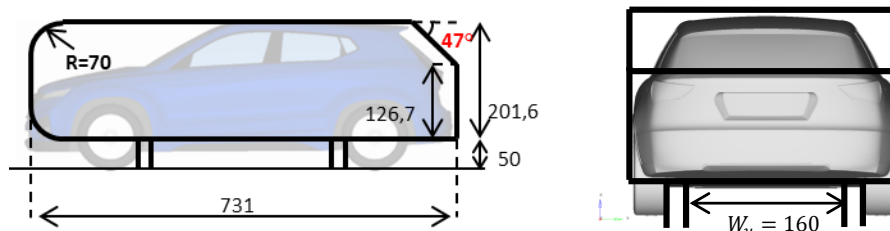


Fig. 21: Comparaison des géométries du SUV générique avec le Corps d'Ahmed avec une lunette inclinée à  $47^\circ$ .

Sur la base d'un maillage à 160 millions d'éléments, la simulation de l'écoulement non contrôlé a permis de retrouver le coefficient de traînée de 0,272 correspondant à un écart de 3% par rapport à ce qui a été obtenu expérimentalement dans les études de (Metka, 2013).

Après analyse de la topologie de l'écoulement (Fig. 22), l'application de la SPDMD, a permis de faire ressortir les structures caractéristiques du sillage et notamment un mode particulièrement énergétique à  $St=0,22$  associé à un mouvement de balancier asymétrique impactant la dépression du culot.

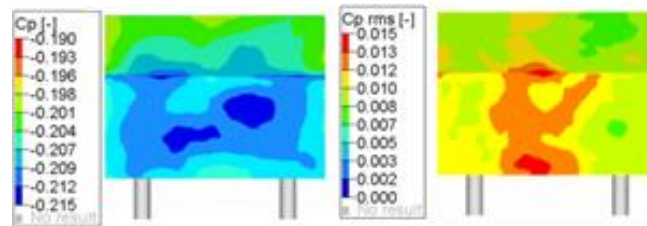


Fig. 22: Distribution moyenne et RMS de  $C_p$  de l'écoulement non contrôlé.

Sur cette base, une loi de contrôle boucle fermée a été proposée afin de suivre la dynamique de ce mode énergétique. Ce contrôle d'écoulement a permis de modifier de façon significative la topologie de la zone dépressionnaire sur le culot (Fig. 23).

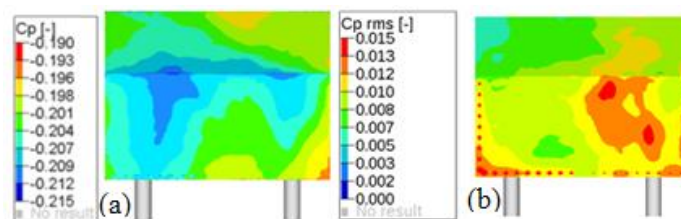


Fig. 23: Distribution moyenne et RMS de  $C_p$  de l'écoulement avec le contrôle d'écoulement par jets discontinus.

Cette étude a permis de mettre en lumière le potentiel d'une loi de contrôle basée sur un modèle DMD intégrant une loi physique sur la dynamique de l'écoulement.

- Etude numérique de l'écoulement non contrôlé autour du SUV générique

La mise en place de la simulation de l'écoulement autour de la maquette du SUV a abouti à un maillage de 300 millions d'éléments, et 53 millions de nœuds de façon à avoir une résolution spatiale dans le sillage de 2mm et une première couche de maille à 0,05mm sur les parois du SUV. L'analyse des résultats a été effectuée sur 1,2 secondes de simulation échantillonnées à 2000Hz, après 0,3secondes de convergence.

A partir de ce modèle numérique, les comparaisons des caractéristiques aérodynamiques simulées avec les observations obtenues expérimentalement ont permis de valider la pertinence et la représentativité de l'écoulement moyen sur le hayon (Fig. 24), le sillage (Fig. 25) et le coefficient de traînée de 0,36.

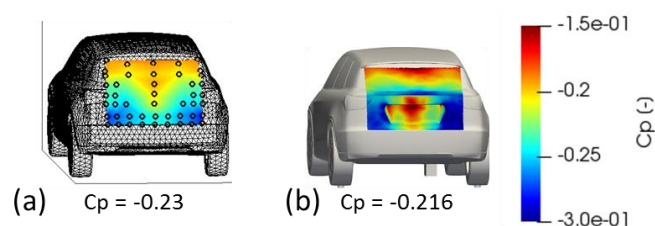


Fig. 24: Comparaison des champs moyens de pression sur le hayon: (a) expérimental, (b) calcul.

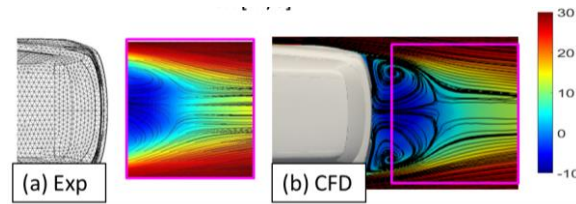


Fig. 25: Comparaison des champs de vitesses moyennes  $V_x$  (m/s) dans le plan Z140 en (a) expérimental et (b) calcul.

Pour aller plus loin, l'analyse de l'écoulement moyen 3D a permis de mettre en évidence les structures 3D expliquant les distributions 2D des plans de coupes PIV. On peut mentionner notamment les deux tourbillons latéraux qui semblent impacter considérablement la zone dépressionnaire en partie basse du hayon et le tourbillon horizontal impactant la dépression du parechoc (Fig. 26).

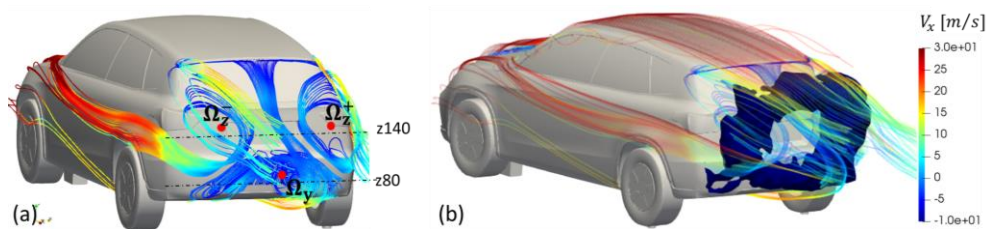


Fig. 26: Lignes de courant moyenne mettant en évidence les 3 principaux tourbillons du sillage; (b) Superposition avec l'iso-contour à  $C_p$  égal à  $-0,1$ .

L'examen des grandeurs turbulentes et fluctuantes a cependant fait apparaître des niveaux d'énergie surévalué notamment dans les couches de cisaillement (Fig. 27). De plus, la cascade de dissipation turbulente qui s'exerce dans le sillage a mis en évidence une surestimation des structures basses fréquences associées à une pente de décroissance plus forte comparé à la loi en  $-5/3$  mesurée en essais.

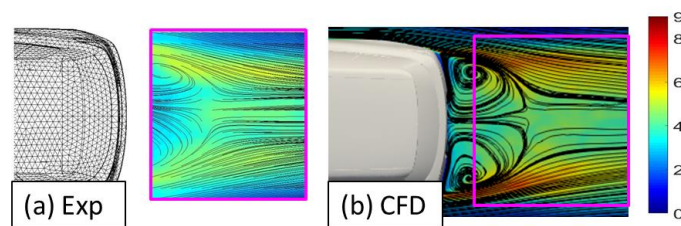


Fig. 27: Comparaison de la RMS de  $V_x$  (m/s) dans le plan Z140 en (a) expérimental et (b) calcul.

Après une exploration des restrictions du modèle numérique (modèle de turbulence, loi de paroi, maillage), l'impact du terme de régularisation inhérent à la formulation éléments finis a été démontré au niveau de la nappe de la couche de cisaillement englobant le sillage.

Un estimateur exact des différences de dynamique de l'écoulement entre les résultats expérimentaux et les résultats numériques grâce à l'application de la DMD croisée sur les champs PIV avec les plans de coupe du calcul. Ceci a permis de mettre en évidence l'écart d'énergie portée par la structure associée au Strouhal de 0,2 dans le sillage. Le mécanisme de détachement tourbillonnaire porté par la fréquence naturelle de l'écoulement a donc été surévalué.

En dépit de cette différence d'énergie, la représentativité de l'écoulement moyen, et de la dynamique du sillage a permis d'approfondir l'analyse d'écoulement étendue tout autour de la maquette, entre autre avec la SPDMD.

L'analyse modale des résultats numériques appliquée sur la pression tout autour du SUV avec les plans de coupe Y0 et Z140 englobant le véhicule, a pu faire ressortir entre autre l'importance du phénomène au Strouhal 0,12 dues aux détachements sur les pièces de carrosseries latérales (ailes avant, portes et arche de roues) avec les structures turbulentes portées dans les couches de cisaillement. Ces structures ont pu être identifiées comme des termes sources de turbulence qui interagissent avec le détachement tourbillonnaire au Strouhal 0,2 et avec la dynamique du sillage au Strouhal 0,04 associée à une forte zone dépressionnaire (Fig. 28).

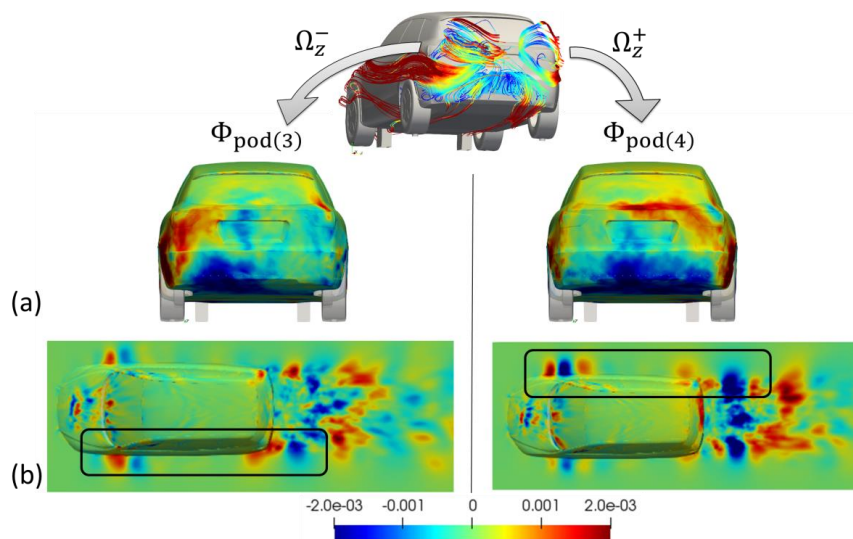


Fig. 28: 3ème et 4ème modes POD montrant les corrélations entre (a) les fluctuations de pression sur le parechoc arrière et sur le hayon avec (b) les fluctuations de vitesses dues aux détachements sur les flancs du véhicule.

Ces observations permettent de converger vers l'intérêt d'une solution de contrôle permettant soit de limiter la propagation des structures émises les flancs du véhicule soit de lisser l'énergie turbulente des couches de cisaillement issues de la séparation sur le parechoc arrière.

- Etude numérique de l'écoulement contrôlé autour du SUV générique

La simulation intégrant le contrôle d'écoulement à partir du jeu de paramètres de contrôle identifié expérimentalement a été réalisée. Des difficultés ont été rencontrées pour reproduire l'action du contrôle actif par jet pulsé à hautes fréquences. Si une modification des centres tourbillonnaires du sillage a pu être identifiée (Fig. 29), les gains n'atteignent pas les performances relevées expérimentalement.

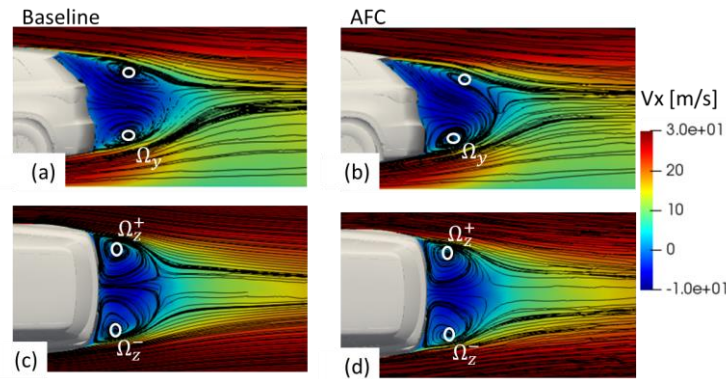


Fig. 29: Champs moyen de vitesses: (a) écoulement non contrôlé en Y0; (b) écoulement contrôlé en Y0; (c) écoulement non contrôlé en Z140; (d) écoulement contrôlé en Z140.

Des hypothèses ont été proposées pour expliquer ces écarts avec les résultats expérimentaux notamment sur la précision de la résolution des mécanismes de turbulence en sortie de buses nécessaire pour reproduire l'interaction avec les couches de cisaillement et la zone de recirculation.

## Conclusions et perspectives

Dans un contexte environnemental où l'industrie automobile a une empreinte écologique majeure, la question de l'optimisation aérodynamique des véhicules urbains est prépondérante. Dans ce cadre, l'objectif de cette thèse a été d'intégrer une stratégie de contrôle d'écoulement permettant de réduire l'effort aérodynamique sur une maquette SUV générique à échelle réduite.

Les travaux effectués ont permis de mettre en exergue les mécanismes de contrôle d'écoulement permettant de réduire les pertes aérodynamiques.

Dans un premier temps, grâce à l'étude expérimentale réalisée, la topologie de l'écoulement non contrôlé a pu être appréhendée de façon précise. Après identification d'un point de contrôle efficace issu du résultat de l'algorithme génétique, l'analyse modale a permis de mettre en lumière le mécanisme de contrôle d'écoulement permettant de réduire significativement la dépression agissant sur le hayon.

Après études préliminaires sur les cas simplifiés de la rampe inclinées à  $25^\circ$  et le Corps d'Ahmed avec une lunette inclinée à  $47^\circ$ , les simulations numériques de l'écoulement autour du SUV générique ont pu être validées conformément aux mesures expérimentales. La méthodologie d'analyse modale croisée a été reprise dans le cadre de l'analyse comparative entre les résultats de pression et PIV mesurés en expérimental et la simulation numérique afin de corroborer la dynamique de l'écoulement simulé. Enfin une étude approfondie de l'écoulement tout autour du véhicule a été proposée et a permis de mettre en évidence l'importance des interactions entre les différents mécanismes de turbulence en jeu et responsables des pertes aérodynamiques.

Enfin, des difficultés ont été rencontrées pour la simulation de l'écoulement contrôlé, ce qui a mis en exergue la complexité des mécanismes de contrôle d'écoulement et leur simulation.

Pour terminer, une discussion a été proposée sur les potentielles nouvelles pistes à explorer qui permettraient d'aller plus loin dans la recherche de stratégies de contrôle d'écoulement pour la réduction de traînée de véhicules SUV.

# Table of contents

Remerciements .....	2
Résumé .....	4
Abstract .....	4
Résumé étendu .....	5
Table of contents .....	24
List of tables .....	27
List of figures .....	28
Nomenclature .....	37
Introduction .....	1
Chapitre 1: Literature survey .....	5
1.1. Aerodynamic loss identification on realistic cars .....	6
1.1.1 Flow characteristics of realistic cars .....	8
1.1.2 Flow detachments for a realistic SUV .....	11
1.2. Description of detached flow mechanisms .....	14
1.2.1 Fundamentals of turbulence .....	15
1.2.2 Detachments and vortex shedding of the wake flow past an inclined ramp .....	20
1.2.3 Detachments and vortex shedding of the wake flow past the Ahmed Body .....	22
1.3. Flow control and optimization techniques .....	26
1.3.1 Flow control solutions .....	26
1.3.1.1 Passive flow control solutions .....	26
1.3.1.2 Active flow control solutions .....	28
1.3.2 Closed-loop and automatic control/optimization methods .....	34
1.3.2.1 Strategies for active flow control .....	34
1.3.2.2 Shape optimization with sensitivities .....	37
1.4. Modal decompositions .....	39
1.4.1 Orthogonal Decompositions .....	39
1.4.2 Dynamic Modal Decomposition .....	41
1.5. Numerical methods .....	46
1.5.1 Numerical approaches .....	46
1.5.2 Large Eddy Simulation .....	48
1.5.3 Numerical approximation techniques .....	50
1.6. Partial conclusions .....	52
Chapitre 2: Experimental investigation and control on a reduced scale generic SUV .....	53

2.1	Experimental setup of the POSUV .....	54
2.1.1	Wind tunnel characteristics and POSUV mockup .....	54
2.1.2	Pressure sensors, PIV and actuators setup .....	55
2.1.3	Reactive flow control by machine learning with a genetic evolution process .....	58
2.2	Comparison of the time averaged flow topology .....	60
2.2.1	Topology of the time averaged baseline flow .....	60
2.2.2	Time averaged results of the active flow control .....	62
2.3	Modal cross-analysis .....	63
2.3.1	Hypothesis and method .....	63
2.3.2	Pressure-velocity cross-analysis of the baseline flow .....	68
2.3.3	AFC and baseline pressure cross-analysis .....	72
2.4	Partial conclusions.....	78
Chapitre 3: Numerical investigations and wake flow control on different test cases .....		80
3.1.	Numerical simulations with Large Eddy Simulation .....	81
3.2.	First Preliminary study: Detached flow over a 25° inclined ramp.....	84
3.2.1	Numerical setup and convergence according to experimental conditions .....	84
3.2.2	Analysis of the baseline wake flow compared to literature .....	88
3.2.3	Physics of periodic jet actuation.....	90
3.2.4	Partial conclusions and guidelines for detached flow simulation .....	97
3.3.	Second preliminary study: The Ahmed body with 47° slant angle.....	97
3.3.1	Introduction .....	97
3.3.2	Numerical setup.....	98
3.3.3	Baseline flow.....	99
3.3.4	Modal analysis.....	104
3.3.5	Controlled flow .....	109
3.3.6	Discussion .....	112
3.4.	Numerical investigation of the reduced scale generic SUV.....	112
3.4.1	Numerical setup and convergence according to turbulent model .....	113
3.4.2	Time averaged flow topology compared with experiment.....	115
3.4.3	Validation of the wake flow dynamics compared to experiments .....	122
3.4.4	Boundary layer and detachments correlations with the wake flow.....	134
3.4.5	Flow control simulations with Large Eddy Simulation .....	146
3.4.6	Partial conclusions.....	153
Concluding remarks, discussion and perspectives .....		154
Bibliography.....		159

Table of contents	25
-------------------	----

---

Appendices .....	167
Résumé .....	173
Résumé en anglais .....	173

## List of tables

<b>Table 1: Time averaged forces and torques coefficients. ....</b>	<b>100</b>
<b>Table 2: Torques coefficients and RMS at rear center. ....</b>	<b>101</b>
<b>Table 3: Torques coefficients for the uncontrolled flow computed at the of the cut plane.....</b>	<b>103</b>
<b>Table 4: Time averaged and RMS of forces on the Ahmed Body and difference with uncontrolled flow. ....</b>	<b>111</b>
<b>Table 5: Dimensional analysis of the turbulent quantities applies to the POSUV wake flow. ....</b>	<b>114</b>

## List of figures

Figure I.1: (a) European CO <sub>2</sub> emissions from fuel combustion by sector, 2015 from (“CO <sub>2</sub> Emissions from Fuel Combustion 2017 Highlights,”.); (b) CO <sub>2</sub> emission breakdown in transport industry. ....	2
Figure I.2: Evolution of worldwide automotive production per region using data from (“CO <sub>2</sub> Emissions from Fuel Combustion 2017 Highlights,”.) and (Gao et al., n.d.). ....	2
Figure I.3: (a) Reduced scale POSUV mockup in TU-Berlin wind tunnel; (b) Different modules in green can be changed on the basis of the mockup in blue. ....	3
Figure I.4: Aerodynamic loss components observed on a real car. The theory of the quantity momentum integration on a fluid stream tube surrounding the car quantifies the aerodynamic loss. ....	7
Figure I.5: Drag coefficient measured for different obstacle from the flat plate with high drag coefficient to the profiled body with an optimal drag coefficient. ....	8
Figure I. 6: Influence of the design on the drag coefficient: (a) Illustration of rear end types; (b) Drag coefficient as a function of the rear slant angle $\alpha$ (Hucho, 1987); ....	9
Figure I.7:(a) Hatchback versions of the SUV with a rear window inclined at 45°; (b) New SUVs with a rear window inclined at 22°;.....	9
Figure I.8: Drivaer model and drag coefficient depending on the rear end geometry, measured by (I. Heft et al., 2012a). ....	10
Figure I.9: Picture of experimental campaign presented in (Wolf, 2018) to characterized the impact of the rear end slant angle on a Porsche Cayenne mockup at 1/6 scale.....	10
Figure I.10: Drag coefficient measurements on the reduced scale Porsche Cayenne as a function of the slant angle $\varphi$ . The critical angle at 32° with the worst drag coefficient is highlighted with a pink circle. The two generic configurations at 22° and 45° are highlighted respectively with the green and blue circles. ....	10
Figure I.11: Time averaged pressure coefficients distribution measured on (a) the rear end and (b) transverse vertical Y0 cut-plane of a full scale 3008 mockup (Grandemange, 2013). ....	11
Figure I.12: Numerical results of a full scale BMW X5 model from (Eulalie et al., 2018): (a) Time averaged pressure distribution on the rear end; (b) in the wake in the Y0 cut-plane;(c) in a horizontal cut section. ....	11
Figure I.13: Turbulent structures participating to the excrescence drag observed on the body panel proposed by (Hucho and Sovran, 1993). ....	12
Figure I.14: (a) Forces and torques defined in automotive coordinates; (b) Normalized forces coefficients defining handling and stability criteria. ....	12
Figure I.15: (a) Turbulent structures simulated on a realistic underbody from (“Audi Technology Portal - Underbody,”); (b) Underbody flow through a complex car floor design, subjected to a yaw deviation of 3.3° (Wojciak, 2012); ....	13
Figure I.16: Experimental measurements performed by (Eulalie et al., 2018): (a) Full scale BMW X5 prototype; (b) Sensitivity of the rear end pressure to yaw angle deviation. ....	13
Figure I.17: Streamlines in the underbody flow and around the body panels propagating in the wake: (a) at 0° yaw angle; (b) 6° yaw angle (Yuan et al., 2018). ....	14
Figure I.18: Some classical structures observed in fluid mechanics: (a) Tollmien-Schlichting instability developing in a laminar boundary layer; (b) Horseshoes and turbulent boundary layer pattern; (c) Kelvin-Helmholtz of the shear layer and Karman vortices .....	14
Figure I.19: (a) Scheme of eddies in turbulent flow and (b) turbulent kinetic energy occurring in homogeneous isotropic turbulent flow. ....	15
Figure I.20: Sketch of a boundary layer profile developing over a plate plane.....	16
Figure I.21: Boundary layer development from laminar to turbulent on a flat plate: (a) Emergence of horseshoes in the transition region, impacting the averaged velocity profile and leading to the turbulent burst (Hinze, 1975); (b) Friction coefficient as a function of the Reynolds number. ....	17
Figure I.22: (a) Sketch of a boundary layer profile developing over a flat plate. The transition is triggered at a critical position $x_c$ leading to a turbulent boundary layer; (b) Normalized boundary layer velocity profile as a function of the normalized wall distance $y^+$ . ....	18
Figure I.23: (a) Contour maps of velocity spectra with wall normal at Reynolds number 7300 from DNS computation of (Hutchins and Marusic, 2007; Smits et al., 2011); (b) Blocking effect highlights with	

velocity spectra in outer region of the boundary layer as a function of the wall distance $z$ from (Hunt and Morrison, 2000).....	18
Figure I.24: Sketch of (a) flow separation on a curved surface (Epifanov, n.d.) and (b) interaction between the boundary layer and the shear layer as proposed in (Varon, 2017b). .....	19
Figure I.25: Flow pattern captured experimentally behind a circular cylinder by (Van Dyke, 1982): (a) Laminar wake flow at Reynolds number 26; (b) Von Karman vortex street observed at $Re = 140$ ; (c) Turbulent wake flow observed at $Re = 10\ 000$ . .....	20
Figure I.26 : Spectral signatures measured in the turbulent flow past a cylinder at Reynolds number $4.7 \cdot 10^4$ : (a) at the center in the wake ; (b) in the shear layer past the cylinder from (Boudet et al., 2016). .....	20
Figure I.27: Sketch of the turbulent structures observed in the flow over a backward facing step: the turbulent boundary layer evolved in a shear layer leading to Kelvin-Helmholtz instabilities. The roll-up of the shear layer generate vortex structures sheds downstream the recirculation area. ....	21
Figure I.28: Influence of the upstream boundary layer quantity momentum on: (a) the shear layer characteristic thickness and (b) the recirculation length (Stella et al., 2017b). .....	22
Figure I.29: Geometry of the Ahmed Body according to (Ahmed et al., 1984a). .....	22
Figure I.30: (a) Variation of the drag coefficient as a function of the slant angle with the contribution of the vertical base $CB$ compared to the contribution of the slant area $CS$ ; (b) Horseshoe vortex in wake for slant angle below $10^\circ$ with low drag coefficient; (c) Partially detached flow observed for slant angle between $10^\circ$ and $30^\circ$ with high drag coefficient (Ahmed et al., 1984); (d) Fully detached flow for a slant angle beyond $30^\circ$ leading to a wake topology and a drag coefficient similar to the attached boundary layer configuration.....	23
Figure I.31: O-ring structure observed in time averaged pressure iso-value: (a) in the wake of a square back Ahmed Body (Eulalie, 2014a); (b) in the wake of an Ahmed Body with a $47^\circ$ slant angle. ....	24
Figure I.32: Flow structure in the separation zone of the front part: (a) Top view; (b) Side view from (Spohn and Gilliéron, 2002).....	24
Figure I.33: Identification of the bi-modal component from (Varon et al., 2017b): (a) From left to right, comparison of the left state averaged, total averaged and right state averaged on the rear end pressure and in the wake velocity from PIV measurements; (b) Normalized 2D Probability Function of pressure barycenter measured on the squared back Ahmed Body. ....	25
Figure I.34: Time scales of the bi-stability behavior measured on pressure transversal gradient on the square back correlated with the PDF highlighting the characteristics 2 disjointed Gaussian distributions (Grandemange et al., 2013b).....	25
Figure I. 35: (a) Picture of a boat tailing appendices integrated on a reduced scale Ahmed Body, (b) Picture of the lateral deflectors integrated on the full scale Peugeot Partner (Bonnavion, 2018).....	26
Figure I.36: Wake topologies past a Citroën C4 (a,b) without spoiler and (c, d) with roof spoiler (Grandemange, 2013). .....	27
Figure I.37: Two configurations of porous media control integrated on a square back Ahmed Body from (Bruneau et al., 2010b).....	27
Figure I.38: Vortex generator used on a round rear end Ahmed Body: (a) Picture of the device mounted on the mockup, (b) Baseline flow with a short recirculation bubble close to the rear end; (b) Controlled flow with a larger recirculation bubble and vortex center shifted away from the rear end. ....	28
Figure I.39: (a) Picture of a full scale PSA C4 characterized with a $35^\circ$ rear window; (b) PIV measurements of the baseline flow; (c) PIV measurements of the controlled flow with vortex generator from (Aider et al., 2014).....	28
Figure I.40: Pattern of the flow passing through the $25^\circ$ Ahmed Body behind the model at 10m/s: (a) Baseline wake flow; (b) Steady plasma actuation leading to a drag reduction of 7.3%; (c) Unsteady plasma actuation leading to a drag reduction of 4.88% (Shadmani et al., 2018).....	29
Figure I.41: (a) Picture of the reduced scale truck mockup with the unactive DBD actuators, (b) Focus on the A-pillar with the active DBD actuators. ....	29
Figure I.42: (a) 3D view of the blowing jets integrated on the square back Ahmed body; (b) Interaction of micro-jet quantity momentum with the shear layer observed with iso-Qcriterion. ....	29
Figure I.43: PIV measurements of the (a) baseline and (b) controlled flow behind a $25^\circ$ Ahmed Body in (Aubrun et al., 2011). .....	30
Figure I.44: The flow in a fluidic oscillator: (a) with air; (b) with water (von Gosen et al., 2015).....	30
Figure I. 45: Comparison of baseline and controlled flow measured in the PIV transverse vertical cut-plane $Y0$ by (Metka and Gregory, 2015).....	30

Figure I.46: (a) Synthetic jet system; (b) PIV snapshots close to the synthetic jets at the maximum blowing phase ( $\Phi = 90^\circ$ ), the zeros blowing phase ( $\Phi = 0^\circ$ ) and at the maximum suction phase ( $\Phi = 270^\circ$ ) measured by (Leclerc, 2008b).....	31
Figure I.47: iso-contour of Qcriterion for (a) baseline flow; (b) Controlled flow; (c) Vortex rings blown on the top edge of the square back Ahmed Body (Eulalie, 2014b).....	31
Figure I.48: (a) Pictures of Volvo front Truck cabin; Time averaged streamlines and transient snapshot of velocity field of PIV measurements: (b) Baseline, (c) Synthetic control at the shear layer frequency (Minelli et al., 2018). ....	32
Figure I.49: Comparison of iso-contour of second invariant of the velocity for : (a) Baseline flow around a the Volvo Truck cabin; (b) with synthetic jets on the A-pillar of the Front cabin (Minelli et al., 2018). ....	32
Figure I.50: Comparison of the (a) baseline and (b) controlled flow at 500Hz behind a 35° Ahmed Body from (Bideaux et al., 2011). ....	33
Figure I.51: (a) Pulsed jet actuators integrated on a full scale C6 car; (b) Pressure coefficient profiles measured over the rear end (Aider et al., 2014). ....	33
Figure I.52: Smoke laser visualization of the mixing layer after a splitter plate: (a) Baseline flow; (b) 10Hz low frequency control configuration; (c) 400Hz high frequency control configuration from (Parezanovic et al., 2014). ....	33
Figure I. 53: Block diagram of a closed-loop control system using automation terminology (Bewley and Liu, 1998).....	34
Figure I.54: Block diagram of the slope seeking algorithm using high-pass and low-pass filters for the identification of the dynamic model (Pastoor et al., 2008). The arrow on the left indicates the feedback between the sensor $\langle Cp \rangle$ toward the controller blocks and the arrow on the right indicates the input control signal $C\mu$ used to the physical system. ....	35
Figure I.55: (a) Sketch of the opposition closed-loop control law based on the detection of the horizontal position of the recirculation barycenter (white diamond) integrated from the transient wake PIV measurement; (b) 2D Power Density Function of the rear end pressure barycenter: the blue distribution corresponds to the baseline mapping, the yellow contour corresponds to the closed-loop control of the pulsed jet magnitude (St=0.2) (Varon, 2017).....	36
Figure I.56: Linear Genetic Programming Control (LGPC) algorithm: (a) closed loop control with a real time feedback combined with a phase averaged learning loop. (b) Genetic algorithm learning process (Li et al., 2017a). ....	37
Figure I.57: Comparison of RANS and DES sensitivities to compute the optimal morphing of lateral tapering of the rear end on the Audi A7. ....	38
Figure I.58: Drag force sensitivities to active flow control blowing symmetrically in the region of the pink circle. ....	38
Figure I.59: Classification optimization methods as a function of model requirements and of the time scale consideration. The purple, blue and green colored boxes refer respectively to method used in experiment, CFD or both. ....	39
Figure I.60: Sketch of the snapshot sequence for a (a) temporal (b) spatial modal analysis (Schmid, 2012). ..	40
Figure I.61: POD results of pressure measurements on square back Ahmed Body and comparison of the baseline decomposition with the closed loop continuous blowing and with the closed-loop high frequency pulsed jet from (Varon et al., 2017a). ....	41
Figure I. 62: Sparsity promoting DMD algorithm from (Jovanović et al., 2014b) source code. ....	43
Figure I.63: Illustration of the rank of the phase shift matrix A in experiments with (a) DMD, (b) High Order DMD. ....	44
Figure I.64: Results of classical DMD obtained on transient rear end pressure on a full scale BMW X5 mockup (Eulalie et al., 2018). ....	44
Figure I.65: DMD results obtained on a controlled blunt body wake: (a) DMD spectra on continuous blowing jet with main mode iso-contour; (b) DMD spectra of obtained on best actuation frequency from (Tu, 2013; Tu et al., 2014).....	45
Figure I.66: scheme of periodic decomposition obtained with the DMD with control. ....	45
Figure I.67: Sketch of the resolved turbulent energy as a function of the length scale depending on the numerical approaches.....	47
Figure I.68: (a) Illustration of filtered velocities used in LES; (b) Scheme of the turbulent energy distribution with the subgrid stress tensors contribution used to model the filtered dissipated energy according to the dynamic Smagorinsky subgrid scale model. ....	49

Figure II.1: Geometric features of the reduced scale generic SUV in millimeter: (a) Side view; (b) 3D view with a projected frontal area visualization.....	54
Figure II.2: (a) Picture of TU-Berlin wind tunnel; (b) Sketch of the wind tunnel dimensions. ....	55
Figure II.3: (a) Picture of the POSUV mockup placed in the main section with the Pitot tube probe; (b) Sketch of the main section of the wind tunnel with a highlight on the Pitot tube located at 63cm from the nose of the mockup and 1.08m from the floor. ....	55
Figure II.4: (a) Picture of experimental 48 pressure sensors distributed on the rear tailgate; (b) Time resolved 2D PIV acquisitions.....	56
Figure II.5: (a) Pictures of the rear end module with the discontinuous slots; (b) Sketch of the geometry of the slots in millimeter. ....	56
Figure II.6: (a) Picture of actuators and sensors system; (b) Diagram of command-acquisition system. ....	57
Figure II.7: Surface distribution of flowmeter measurements in each pneumatic circuit: (a) Bottom circuit, (b) Lateral circuit. ....	57
Figure II.8: System diagram of potential application of the DMDc for closed loop control. ....	58
Figure II.9: Reactive flow control algorithm used for the research of an efficient operating point for the reduction of the rear end pressure.....	59
Figure II.10: Evolution process implemented in the genetic program. ....	60
Figure II.11: Time averaged rear end pressure coefficient distribution corresponding to a mean value of $C_p = -0.23$ .....	61
Figure II.12: Time averaged PIV measurements of the stream wise velocity in: (a) Y0 cut-plane; (b) Z140 cut-plane.....	61
Figure II.13: RMS of PIV measurements of the stream wise velocity in: (a) Y0 cut-plane; (b) Z140 cut-plane. ....	62
Figure II.14: Best operating point identified with the machine-learning algorithm. ....	62
Figure II.15: (a) Time averaged pressure coefficient and (b) RMS of the pressure coefficient of the controlled flow.....	63
Figure II.16: Linear decomposition formulation used for DMD analysis; the matrix A corresponds to the phase shift matrix measured between each snapshot.....	64
Figure II.17: Scheme of the SVD of a database decomposed into POD modes associated to an energy level and a dynamic signal. ....	65
Figure II.18: Interpretation of the database reconstruction based on the DMD decomposition. ....	67
Figure II.19: Sparsity optimization convergence. ....	68
Figure II.20: Energy distribution as a function of the frequency obtained on the Dynamic Modal Decomposition of the rear end pressure sensors distributed on the tailgate on the database of the uncontrolled flow sampled at 2000Hz during one minute of acquisition. Main DMD components are highlighted and the associated DMD modes are plotted. (See Appendix 1 for a larger view).....	69
Figure II.21: Projection of the cross modal decomposition as a function of the frequency on the horizontal Z140 cut-plane synchronized with the rear end pressure. (See Appendix 2 for a larger view). ....	70
Figure II.22: Reconstruction of the cross-DMD pressure coefficient correlated to the wake velocity based on the DMD modes below 10Hz.....	70
Figure II.23: Projection of the cross modal decomposition on the vertical Y0 cut-plane. (See Appendix 3 for a larger view). ....	71
Figure II.24: Periodic vertical motion observed on the reconstruction of the 2Hz DMD mode.....	71
Figure II.25: DMD spectra of the rear end pressure for the controlled flow. (See Appendix 4 for a larger view). ....	72
Figure II.26: Synchronized periodic components emerging from the cross-DMD analysis. ....	73
Figure II.27: Result of cross DMD between baseline and controlled rear end pressure database. The components highlighted in blue in the background correspond to the frequencies, which were vanished with control. ....	74
Figure II.28: (a) Correlated POD energy distribution obtained on the concatenated baseline and controlled rear end pressure; (b) ratio of the controlled flow energy compared to the baseline modal energy ....	74
Figure II.29: Correlated periodic mechanisms model associated to each POD mode and based on the transfer matrix coefficient.....	76
Figure II.30: Logarithm of the weight matrix W highlighting the energy production and decay as a function of the POD index and of the DMD frequency. ....	76
Figure II.31: Correlations with the 0Hz static DMD mode showing the influence of the 2nd, the 4th, and the 8th POD modes. ....	77

Figure II.32: (a) Spatial distribution of the POD modes affecting the 0Hz static DMD component; (b) Correlated spectra obtained with the row vectors of the transfer matrix. In green, the controlled flow contributions and in blue the baseline contributions. (See Appendix 5 for a larger view). .....	77
Figure III.1: Dependency of the least square term as a function of the convective velocity $\beta$ measured for a 1D problem. The curve shows the impact of the regularization term in the low velocity regions ( $\beta < 0.2$ ).....	83
Figure III.2: Scheme of the experiments of the 25° inclined ramp model presented in (Kourta et al., 2015b) .	84
Figure III.3: (a) Boundary layer profile imposed at inlet boundary condition; (b) Scheme of the domain dimensions and boundary condition. ....	85
Figure III.4: Domain discretization corresponding to 60 million cells mesh.....	86
Figure III.5: Boundary layer velocity profile: (a) at $x=-4h$ , (b) at $x=-2.5h$ and (c) and turbulence intensity measured by PRISM compared to CFD results.....	86
Figure III.6: (a) Normalized averaged velocity profile in the boundary layer as a function of the normalized wall distance; (c) Normalized turbulent intensity profile in the boundary layer. ....	87
Figure III.7: (a) Comparison of a the resolved turbulent kinetic energy with the constant Smagorinsky subgrid scale model; (b) Comparison of the PSD downstream of the recirculation (white circle on the tke field). ....	87
Figure III.8: (a) Scheme of the PIV system capturing the separated flow in the Y0 cut plane; (b) the pressure sensors on the ramp wall used in experiments of (Kourta et al., 2015b). ....	88
Figure III.9: Time averaged velocity in central cut plane: (a) Experiments (Kourta et al., 2015b); (b) CFD; (c) Profile measured on wall ramp monitoring point and comparison with experiments (Kourta et al., 2015b).....	88
Figure III.10: Shear layer quantity momentum profile along the x axis compared with experiments (Stella et al., 2017b). ....	89
Figure III.11: (a) Comparison of the turbulent intensity between experiments and resolved velocity fluctuations. The white circle indicates the probe location for the spectral analysis; (b) PSD comparison at the reference probe in the wake flow, the blue curve is the numerical results, the red curve is the experimental results. ....	89
Figure III. 12: (a) Description of the active flow control boundary condition; (b) Design of experiments explored in literature. The star indicated the best operating point based on the pressure coefficient. .	91
Figure III.13: Comparison of the time averaged pressure coefficient profile along the ramp wall for baseline and AFC: (a) in experiment; (b) in CFD.....	92
Figure III.14: Time averaged recirculation streamlines colored by pressure coefficient for (a) Baseline flow; (b) AFC flow; (c) Pressure coefficient profiles along the normal axis of the ramp and going through the vortex center $Om$ . ....	92
Figure III.15: Transient iso-contour of zeros velocity in the baseline flow. ....	93
Figure III.16: Comparison of turbulent intensity in the Y0 cut-plane: (a) Baseline flow; (b) Controlled flow. ..	93
Figure III.17: Visualization of transient iso-contour of zero velocity: (a) baseline; (b) AFC.....	93
Figure III. 18: Comparison of the DMD spectra obtained with the baseline flow and the controlled flow. The low frequency components are damped with the actuation while a high frequency peak at $St = 0.6$ emerges. The remaining low frequency peaks identified in the controlled flow are at $St = 0.02$ and $St = 0.08$ .....	94
Figure III.19: Vx DMD modes showing of the frequencies highlighted in the DMD spectra.....	95
Figure III.20: Weight matrix between DMD base and POD base. The low frequency modes are strong within the POD components below 10.....	95
Figure III.21: Spectral projection of the correlated mechanisms associated with POD(4). The dissipation process triggered by the actuation frequency is identified by the logarithmic energy decay between $St = 0.6$ , $St = 0.9$ , $St = 1$ , $St = 2.37$ . ....	96
Figure III.22: DMD modes participating to the 4 <sup>th</sup> POD mode displaying the actuation dissipation process. ..	96
Figure III. 23: Geometry comparison of a generic SUV and the 47° Ahmed Body (in mm).....	98
Figure III.24: (a) Ahmed body tetrahedral mesh with active flow control refinement; (b) turbulent kinetic energy PSD in wake flow. ....	99
Figure III.25: Computed time averaged drag coefficient per surface and comparison with experimental results of literature marked by * .Rear end surface contributes to 75% of total drag .....	99
Figure III.26: Time averaged Cp mean value of -0.21 (75% of total Cd and its RMS of 0.007; .....	100

Figure III.27: Axes orientation for forces and torques definition at center of rear.....	100
Figure III. 28: PSD forces on Ahmed body as a function of Strouhal $StW$ .....	101
Figure III.29: PSD of rear pressure (a) and torques (b) coefficients at the rear center as a function of Strouhal $StW$ .....	101
Figure III. 30: PSD of normal velocity in the boundary layer detachment at 3mm to wall, as a function of Strouhal $StW$ : (a) On vertical edge; (b) On horizontal edge. ....	102
Figure III.31: Pressure minima distribution in wake flow during simulation time. ....	102
Figure III.32: Time averaged pressure coefficient and RMS transversal cut-plane at 250mm from rear.....	103
Figure III.33: PSD of virtual torques $C_{my} S_x$ $C_{mz} S_x$ computed in this cut plane as a function of Strouhal $StW$ .....	104
Figure III.34: DMD modes energy and growth rate.....	105
Figure III.35: Residual between reconstructed field and real snapshots. ....	105
Figure III.36: (a) Reconstruction based on averaged mode with time averaged reconstructed $C_p$ on rear of -0.200; (b) Reconstruction based on fluctuating modes highlighted in Figure III.34 with time averaged reconstructed $C_p$ of -0.01. ....	106
Figure III.37: Modes contributions in rear pressure fluctuations. Highlighted modes at $StW$ =[0.13; 0.15; 0.22; 1.16].....	106
Figure III.38: Mode at Strouhal 0.13 projected on rear with time averaged $C_p$ =-0.0079: (a) Real (b) Imaginary (c) Conjugate imaginary parts; .....	107
Figure III.39: Mode at Strouhal 0.22 projected on rear with time averaged $C_p$ =0.0001: (a) Real (b) Imaginary (c) Conjugate imaginary parts; .....	107
Figure III.40: Mode at Strouhal 1.16 projected on rear end with time averaged $C_p$ =-0.0014: (a) Real (b) Imaginary (c) Conjugate imaginary parts; .....	107
Figure III.41: modes contribution to the rear torques especially at $StW$ = 0.22 on pitch and yaw.....	108
Figure III.42: Mode contribution on the virtual torques in wake flow especially at $StW$ = 0.22 on pitch and yaw. ....	108
Figure III.43: Mode at Strouhal 0.22 in wake in $Y_0$ and at $Z=150$ mm cut sections: (a) Real (b) Imaginary (c) Conjugate imaginary parts; .....	109
Figure III.44: Dimensions and positions of jets located on lateral and bottom edges of the basis. ....	109
Figure III.45: Closed-loop control law. ....	110
Figure III.46: (a) Jets signals PSD as a function of Strouhal $StW$ ; (b) Sensor PSD as a function of Strouhal $StW$ .....	110
Figure III.47: PSD of pressure coefficients on rear end as a function of Strouhal $StW$ .....	111
Figure III.48: Time averaged pressure (a) and RMS (b) of the controlled flow with $C_p$ = -0.20. ....	111
Figure III.49: Simulation domain defining the wind tunnel environment around the POSUV. A monitoring point captures the reference zero pressure and the reference velocity of 30m/s at the Pitot tube.....	113
Figure III.50: Refinement boxes dimensions with the final mesh discretization.....	114
Figure III. 51: Mesh discretization in the $Y_0$ cut plane with a focus on the boundary layer definitions. ....	115
Figure III.52: Mesh convergence based on the error on the drag coefficient as a function of the number of nodes. ....	115
Figure III.53: Picture of experimental sensors: (a) 47 rear end pressure sensors; (b) Time resolved 2D PIV acquisitions.....	116
Figure III.54: (a) Breakdown of the body panels;(b) Forces breakdown per body panel. Simulated total drag force and tailgate contribution are in agreement with experiments. In both cases, the tailgate generates 55% of the total aerodynamic loss.....	116
Figure III.55: Comparison of the time averaged pressure coefficient obtained in (a) experiments; (b) CFD. .	117
Figure III. 56: Comparison of time averaged velocity components $V_x$ and $V_z$ in the $Y_0$ cut-plane: (a) and (c) experiments; (b) and (d) CFD; .....	117
Figure III. 57: Comparison of time averaged velocity components: (a) $V_x$ in experiment; (b) $V_x$ in CFD, (c) $V_y$ in experiments, (d) $V_y$ in CFD. ....	118
Figure III.58: (a) Time averaged velocity streamlines showing one horizontal vortex denoted by $\Omega_y$ on the bottom of the rear bumper, and 2 lateral vortices $\Omega_z^-$ and $\Omega_z^+$ on each side of the tailgate; (b) Superposition of the streamlines with the iso-contour of $C_p$ at -0.1. ....	119
Figure III. 59: Time averaged pressure coefficient in (a) the $Y_0$ cut plane and (b) in the $Z_{140}$ cut-plane superposed with the time averaged velocity streamlines. ....	119
Figure III.60: Q-criterion of the time averaged field: (a) $Y_0$ cut-plane; (b) Focus on the separation at the rear bumper. ....	120

Figure III.61: Q-criterion of the time averaged field: (a) Z140 cut-plane; (b) Focus on the separation on the lateral corner of the rear bumper. ....	120
Figure III.62: (a) Time averaged skin friction velocity streamlines on the rear end wall highlighting the backflow path on the rear end. The black dot circles indicate the 3 stagnation points with low velocity and diverging streamlines. ....	121
Figure III.63: RMS of pressure coefficient on the tailgate in (a) experiments and (b) CFD. ....	122
Figure III.64: Power spectra density of the pressure measured at the probe highlighted in Figure III.63. The black curve associated to experimental results is plotted on the left axis and the blue curve associated to CFD, is plotted based on the right axis. ....	123
Figure III.65: RMS of pressure measured in the wake flow: (a) in the Y0 cut-plane, (b) in the Z140 cut plane. ....	123
Figure III.66: Comparison of velocity fluctuations in the Y0 cut-plane: (a) stream wise velocity in experiment, (b) in CFD, (c) vertical velocity component in experiment, (d) in CFD. The white circle indicates the position of the maximum velocity fluctuation. ....	124
Figure III.67: Comparison of velocity fluctuations in the Z140 cut-plane: (a) Vx RMS in experiments, (b) Vx RMS in CFD, (c) Vy RMS in experiments, (d) Vy RMS in CFD. ....	124
Figure III.68: (a) Focus on the velocity RMS downstream the roof spoiler superposed with the mesh grid; (b) PSD of PIV velocity magnitude and simulation velocity magnitude at the maximum turbulence intensity in Y0 vertical cut-plane. ....	125
Figure III.69: Estimation of the Least-Square regularization intensity: (a) Reference mesh showing the sensitivity to the recirculation bound to the regularization term; (b) Zonal mesh refinement showing the reduction of the Least-Square matrix around the recirculation. ....	126
Figure III.70: Illustration of the database assembly for cross-dmd analysis between CFD results and experiments. ....	127
Figure III.71: DMD energy intensity as a function of the DMD frequency. In this spectrum, peaks are outlined at 25Hz, 31H, 33Hz, 61Hz, 70Hz, 80Hz, 135Hz, 210Hz and 400Hz. ....	127
Figure III.72: Comparison of the synchronized DMD spectra on the rear tailgate between experiments and CFD. ....	128
Figure III.73: (a) CFD/Exp ratio measured in POD modes. An overestimation of the energy contained in the 2 <sup>nd</sup> and 3 <sup>rd</sup> POD modes, is measured in the numerical simulation. (b) Energy distribution per POD mode showing the ratio of the static component in the first POD mode at 97% of the total modal energy. .	129
Figure III. 74: Visualization of the transfer matrix measured between DMD modes and POD modes. ....	130
Figure III.75: DMD spectral projection per POD mode showing the change of energy distribution per frequency depending on the POD mode. The 2 <sup>nd</sup> POD mode is the most energetic components and mainly driven by low frequencies. The high frequencies have more impact on the low energy POD modes such as the 100 <sup>th</sup> and 1000 modes. ....	130
Figure III.76: Spatial correlated POD modes between CFD and experiments. If the POD mode 2 is associated to a large-scale structure, the characteristic lengths decrease as the associated POD energy decreases. ....	131
Figure III.77: Cross-POD mode 2: (a) Y0 cut-plane experiment; Y0 cut-plane CFD; (c) Z140 cut-plane experiment; Z140 cut-plane CFD. ....	131
Figure III.78: DMD weights in the 2 <sup>nd</sup> POD mode showing the numerical contribution compared to experiments. The frequencies at 25Hz and 30Hz appear to be too energetic in CFD. ....	132
Figure III.79: Comparison of the velocity RMS: (a) in experiment, (b) in CFD, (c) in CFD after the application of the cross-modal correction. The white dot is a monitoring point used for spectral analysis. ....	133
Figure III.80: Comparison of the velocity PSD computed at the white dot monitoring point of Figure III.79. The low frequencies of the CFD spectra corrected with the modal penalty term were adjusted at the level of the experimental spectrum. ....	133
Figure III.81: (a) Picture of the hot-wires setup measured with the horizontal arm; (b) location of the measured profiles on the front fender; (c) location of the measured profiles on the rear fender. ....	135
Figure III.82: Comparison of hot-wires and computed time averaged normalized boundary layer velocity magnitude profiles along the body panel in the Z80 cut-plane for the first 2 profiles and in the Z140 cut-plane for the last 3 profiles. ....	135
Figure III.83: Comparison of hot-wires and computed velocity fluctuations along the lateral body panel in the Z80 cut-plane for the first 2 profiles and in the Z140 cut-plane for the last 3 profiles. ....	136
Figure III.84: Time averaged 3D structure responsible for the turbulent kinetic energy in the boundary layer of the front bumper. ....	136

Figure III.85: Time averaged velocity streamlines of the flow around the POSUV: the circles indicate the monitoring points used to correlate the lateral detachments with the wake vortices .....	137
Figure III.86: Cross correlation between A1 and A2 in the Z80 cut-plane showing the synchronized characteristic at 16Hz. ....	137
Figure III.87: Spatial data used for the 3D modal analysis. ....	137
Figure III.88: DMD velocity X modes in the Z140 cut-plane at 16Hz in the Z140 and Z180 cut-planes. ....	138
Figure III.89: Snapshots of the reconstruction in Z140 and Z80 cut-planes with the dynamic behavior of the periodic component at 17Hz during the phase ( $t=0s$ ) and the opposition ( $t=0.028s$ ). ....	138
Figure III.90: Transfer matrices between POD and DMD matrices: (a) wake velocity transfer matrix; (b) SUV pressure transfer matrix. ....	140
Figure III.91: (a) Projection of the velocity and pressure POD contributions into the 0Hz static component. The POD modes 3, 4 and 6, highlighted by the green box, are the main fluctuations correlated with the 0Hz static component; (b) POD modes 3, 4 and 6 correlated with the static 0Hz DMD modes. ....	140
Figure III.92: 2 <sup>nd</sup> and 6 <sup>th</sup> POD modes of the modal pressure fluctuations on the rear tailgate and of the associated modal wake velocity. ....	141
Figure III.93: (a) DMD weight corresponding to the 2 <sup>nd</sup> column vector of the transfer matrix between periodic decomposition and POD. Velocity DMD modes in the Z140 cut-plane associated to the correlated mechanisms identified $\Phi_{pod2}$ at (b) 6.4Hz, (c) 23Hz, (d) 31Hz. The frequencies in bold indicate common features with $W3$ , $W4$ and $W6$ . ....	142
Figure III.94: (a) DMD weight corresponding to the 6 <sup>th</sup> column vector of the transfer matrix between periodic decomposition and POD. Velocity DMD modes in the Y0 cut-plane associated to the correlated mechanisms identified $\Phi_{pod6}$ at (b) 23Hz, (c) 31Hz. The frequencies in bold indicate common features with $W2$ , $W3$ and $W4$ . ....	142
Figure III.95: 3 <sup>rd</sup> and 4 <sup>th</sup> POD modes showing the correlation of (a) pressure modes on the tailgate and (b) velocity modes in Z140 cut-plane. ....	143
Figure III.96: (a) DMD weight corresponding to the 3 <sup>th</sup> column vector of the transfer matrix between periodic decomposition and POD. Velocity DMD modes in the Z140 cut-plane associated to the correlated mechanisms identified $\Phi_{pod3}$ at (b) 23Hz, (c) 31Hz, (d) 63Hz, (e) 106Hz, (f) 148Hz, (g) 168Hz. The frequencies in bold indicate common features with $W4$ . ....	144
Figure III.97: (a) DMD weight corresponding to the 4 <sup>th</sup> column vector of the transfer matrix between periodic decomposition and POD. Velocity DMD modes in the Z140 cut-plane associated to the correlated mechanisms identified $\Phi_{pod4}$ at (b) 23Hz, (c) 31Hz, (d) 63Hz, (e) 146Hz, (f) 168Hz, (g) 182Hz. The frequencies in bold indicate common features with $W4$ . ....	144
Figure III.98: Time averaged skin friction velocity computed on the generic SUV body panels with focus on separated flow vortices observed on time averaged velocity streamlines. Main detachment regions are located on (a) front end, (b) Hood-windshield junction, (c) A-pillar, (d) Spoiler, (e) Rear bumper edges, (f) Front corners, (g) Lower front bumper. ....	145
Figure III.99: (a) Geometry of the discontinuous slots in millimeter; (b) Optimal set of parameters identified in experiments with the machine-learning algorithm. A flowrate of 15L/min is distributed on the lateral boundary conditions and a flowrate of 30L/min is distributed between the bottom boundary conditions. ....	146
Figure III.100: Time averaged tailgate pressure coefficient in (a) baseline flow, (b) controlled flow. ....	147
Figure III.101: Pressure coefficient RMS on the tailgate in (a) baseline flow, (b) controlled flow. ....	147
Figure III. 102: Time averaged flow showing a change of flow topology from the recirculation of $\Omega_y$ to the S-shape structure between: (a) Y0 Baseline, (b) Y0 AFC; (c) Z140 Baseline; (d) Z140 AFC. ....	147
Figure III.103: Time averaged velocity field focus in the region of the pulsed jets (a) left side, (b) right side. A velocity of 5m/s is obtained near the lateral jets in accordance with the flowrate of experiments. Actuation flux is evenly distributed between all the slots. ....	148
Figure III.104: Time averaged velocity field focus in the region of the bottom jets in the horizontal cut-plane going through the slots. A velocity of 4m/s is obtained near the bottom jets. Actuation flux is evenly distributed between each slot. ....	148
Figure III.105: Velocity RMS showing the increase of turbulent energy in the shear layers: (a) Y0 baseline; (b) Y0 AFC; (c) Z140 baseline; (d) Z140 AFC. The color map starts at 3m/s in order to capture the difference between the baseline and the controlled results. ....	149
Figure III.106: Longitudinal velocity fluctuations in the vertical transverse cut-plane going through the slots: (a) right jets, (b) left jets. The inlet boundary conditions associated to the pulsed blowing jets generate 9m/s velocity RMS near the slots. ....	149

---

Figure III.107: Longitudinal velocity fluctuations measured in the horizontal transverse cut-plane going through the bottom slots. The inlet boundary conditions associated to the pulsed blowing jets generate 5m/s velocity RMS near the slots. ....	149
Figure III.108: POD ratio comparing the energy of the correlated mechanisms in the baseline and the controlled simulations. ....	150
Figure III.109: Tailgate pressure POD modes obtained in the controlled simulation. The 8 <sup>th</sup> and 9 <sup>th</sup> POD modes can be related to the complementary paired modes $\Phi_{pod(3)}$ and $\Phi_{pod4}$ previously observed in the baseline flow.....	150
Figure III.110: DMD magnitude ratio between controlled and baseline flow in (a) CFD; (b) experiments. ....	151
Figure III.111: DMD modes enhanced by the actuation : (a) 243Hz in Z140 cut-plane, (b) 504Hz in Z140 cut-plane, (c) 243Hz in Z80 cut-plane, (d) 504Hz in Z80 cut-plane.....	152

## Nomenclature

### Aerodynamics:

$V_x$	Stream-wise velocity	[m/s]
$V_y$	Transverse velocity	[m/s]
$V_z$	Vertical velocity	[m/s]
$F_x$	Drag force	[N]
$F_y$	Side force	[N]
$F_z$	Lift force	[N]
$M_x$	Roll torque	[N.m]
$M_y$	Pitch torque	[N.m]
$M_z$	Yaw torque	[N.m]
$P_{stat}$	Static pressure	[Pa]
$P_{ref}$	Atmospheric pressure	[Pa]
$q$	Dynamic pressure	[Pa]
$P_t$	Total pressure	[Pa]
$\tau$	Shear stress tensor	[Pa]
$C_d$	Drag coefficient	[-]
$C_M$	Side force coefficient	[-]
$C_L$	Lift force coefficient	[-]
$C_l$	Roll coefficient	[-]
$C_m$	Pitch coefficient	[-]
$C_n$	Yaw coefficient	[-]
$C_p$	Pressure coefficient	[-]
$C_\mu$	Jet quantity momentum coefficient	[-]
$\Omega_z^-, \Omega_z^+$	Vertical vortices on the left and right sides of the tailgate	
$\Omega_y$	Horizontal vortex on the rear bumper	

### POSUV characteristics

$H$	Height	[m]
$W$	Width	[m]
$h_u$	Ground clearance	[m]
$S_{ref}$	Frontal area	[m <sup>2</sup> ]

---

$V_{ref}$	Far field velocity	[m/s]
$V_j$	Jet velocity	[m/s]
$f_j$	Jet forcing frequency	[Hz]

### Fluid mechanics and turbulence

$\rho$	Fluid density	[kg/m <sup>3</sup> ]
$\mu$	Dynamic viscosity	[Pa.s]
$\nu$	Kinematic viscosity	[m <sup>2</sup> /s]
$Re$	Reynolds number	[-]
$f$	Frequency	[Hz]
$\epsilon$	Dissipation rate	[m <sup>2</sup> /s <sup>3</sup> ]
$U$	Velocity of the integral scale	[m <sup>2</sup> /s]
$L$	Integral scale	[m]
$\tau_w$	Wall shear stress	[Pa]
$u_\tau$	Skin friction velocity	[m/s]
$C_f$	Friction coefficient	[-]
$y^+$	Normalized wall distance	[-]
$u^+$	Normalized boundary layer velocity	[-]
$\delta_1$	Boundary layer displacement thickness	[m]
$\delta_{99}$	Boundary layer thickness	[m]
$\theta$	Boundary layer momentum thickness	[m]
$\theta_{SL}$	Shear layer momentum thickness	[m]
$St$	Strouhal number	[-]
$L_r$	Recirculation length	[m]
$F^+$	Normalized frequency based on the recirculation length	[-]

### Numerical methods

$\bar{u}$	Averaged velocity	[m/s]
$u'$	Velocity fluctuation	[m/s]
$\tilde{u}$	Filtered velocity	[m/s]
$\bar{p}$	Averaged pressure	[Pa]
$p'$	Pressure fluctuation	[Pa]
$\tilde{p}$	Filtered pressure	[Pa]
$G$	Test filter	
$\tau'_{ij}$	Subgrid scale stress tensor	[Pa]

---

$\mu_s$	Turbulent viscosity	[Pa.s]
$C_s$	Smagorinsky coefficient	[-]
$\Delta$	Mesh grid cutoff	[m]
$\tilde{\Delta}$	Numerical test filter cutoff	[m]
$\widetilde{S}_{ij}$	Resolved strain rate tensor	
$L_{ij}$	Resolved stress tensor between $\Delta$ and $\bar{\Delta}$	[Pa.s]
$y^+$	Normalized wall distance	[-]
$u^+$	Normalized boundary layer velocity	[-]
$\mathcal{L}$	State equations	
$Q_n$	Discretized space -time domain	
$P_n$	Discretized space-time boundary	
$N_i$	Prescribed shape function	
$v$	Trial function	
$\varphi_i$	Unknown state value at the nodal points of the elements	
$w_i$	Prescribed weight function	
$\tau$	Least-Square matrix	
$Pe$	Element Peclet number	

### Optimization

$J$	Cost function
$F$	State equations
$\mathcal{L}$	Lagrangian functional

### Modal Decomposition

$\Psi$	Database of all snapshots
$\Psi_1$	Initial database
$\Psi_2$	Delayed database
$R^x$	Spatial correlation matrix
$R^t$	Temporal correlation matrix
$\Phi_{pod}$	POD modes
$C$	Companion matrix
$U$	Left singular vectors and POD matrix
$\Sigma$	Singular value diagonal matrix
$V$	Right singular vectors
$\mu$	Eigenvalues

---

$Y$	Eigenvectors	
$A$	Phase shift matrix	
$\tilde{A}$	Reduced phase shift matrix	
$\Phi$	Unit DMD mode	[-]
$f$	DMD frequency	[Hz]
$\sigma$	DMD growth rate	[s <sup>-1</sup> ]
$\delta t$	Time delay between snapshots	[s]
$V_{and}$	Vandermond matrix	
$\mathcal{L}$	Lagrangian functional	
$\alpha$	DMD modes magnitude	
$\beta$	Dual vector	
$\gamma$	Weight of sparsity constraint	
$\lambda$	Vector of Lagrange multipliers	
$\rho$	Quadratic penalty coefficient	
$\alpha_{static}$	DMD magnitude of the static mode	
$\alpha_{rms}$	DMD magnitude of the fluctuation modes	
$\alpha_{tot}$	Total DMD magnitude	
$\Phi_{ref}$	Modal block matrix of the baseline flow	
$\Phi_{afc}$	Modal block matrix of the controlled flow	
$\alpha_{ref}$	Modal contribution vector of the baseline flow	
$\alpha_{afc}$	Modal contribution vector of the controlled flow	
$r_{afc}$	Modal ratio vector of AFC against baseline contributions	
$W$	Transfer matrix between POD and DMD	
$w_{ij}$	Weight of each DMD mode I in the POD mode j	

## Abbreviations

SUV	Sport Utility Vehicle
POSUV	Generic SUV mockup
TKE	Turbulent Kinetic Energy
RMS	Root Mean Square
PSD	Power Spectra Density
PDF	Power Density Function
AFC	Active Flow Control
DOE	Design of Experiment
MLC	Machine Learning Control

---

ROM	Reduced Order Model
DMD	Dynamic Modal Decomposition
SPDMD	Sparsity Promoting Dynamic Modal Decomposition
DMDc	Dynamic Modal Decomposition with Control
SVD	Singular Value Decomposition
HODMD	High Order Dynamic Modal Decomposition
POD	Proper Orthogonal Decomposition
SPOD	Spectral Proper Orthogonal Decomposition
CFD	Computational Fluid Dynamic
DNS	Direct Numerical Simulation
RANS	Reynolds Average Navier-Stokes
LES	Large Eddy Simulation
DES	Detached Eddy Simulation
LBM	Lattice Boltzmann Method
FEM	Finite Element Method
PIV	Particle Image Velocimetry
WLTP	Worldwide Harmonized light vehicles Test Procedure

# Introduction

Despite the climate change awareness, the consumption of fossil resources still carries on to increase in order to answer to the energy demand in the world. This consumption depends on the local region and the last statistics show that effort done in Europe is already visible especially in electricity and heat production due to alternative energy. The transport industry is still a growing factor in CO<sub>2</sub> emission (Figure I.1): in Europe, despite a slowdown of the market growth; in North America, similar phenomenon exists; in Asia, automotive market is still highly increasing and becomes a major actor of CO<sub>2</sub> emissions (Figure I.2) as described in the European report (Biol, 2017).

This trend in automotive industry is related to the growth of vehicle sales but also to the increase of the mass and frontal area of road vehicles. Worldwide regulations enforced with the WLTP cycles still remain a challenge in order for the transport sector to reduce the fuel consumption. The regulation of 130gCO<sub>2</sub>/km, applied in Europe in 2015, is not visible on the 2017 statistics. This can be explained by an anticipation of vehicles consumption improvement before 2015. However, the future constraint of 95gCO<sub>2</sub>/km, starting in 2021, should have a statistic impact in the report of 2023 and after.

In this context, the contribution of the mass and the frontal area have to be reduced meanwhile the development of alternative energy modes such as fuel cells suitable for road vehicles. Thus, drag reduction is still a challenge in order to reduce aerodynamic loss characterized by the AC<sub>d</sub> property of each vehicle version especially for Sport Utility Vehicles (SUV) corresponding to the current growth market.

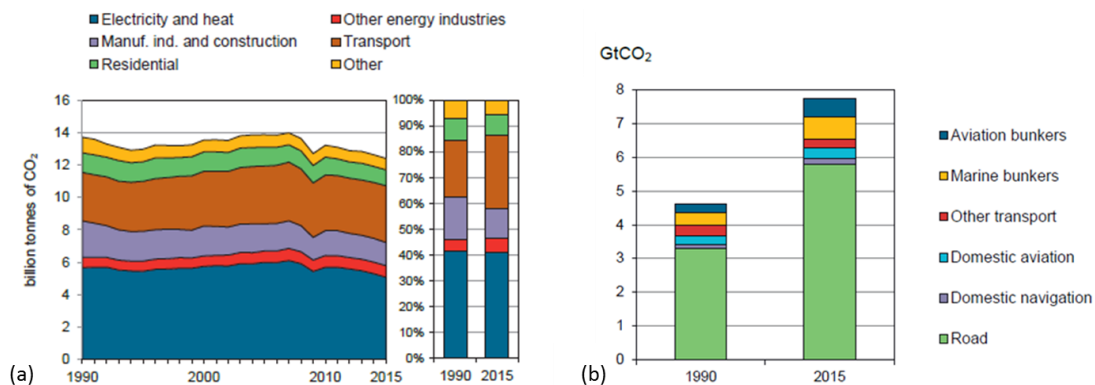


Figure I.1: (a) European CO<sub>2</sub> emissions from fuel combustion by sector, 2015 from (“CO<sub>2</sub> Emissions from Fuel Combustion 2017 Highlights,”); (b) CO<sub>2</sub> emission breakdown in transport industry.

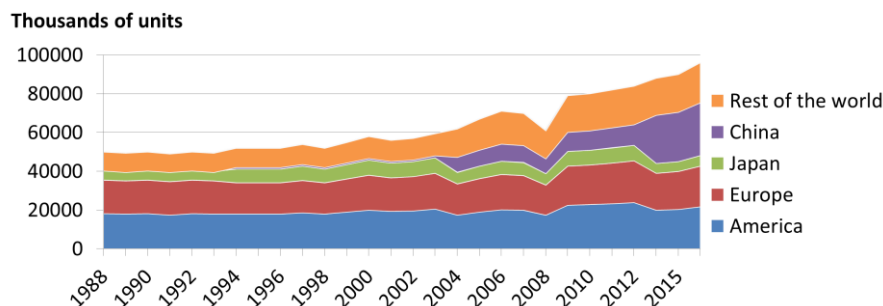


Figure I.2: Evolution of worldwide automotive production per region using data from (“CO<sub>2</sub> Emissions from Fuel Combustion 2017 Highlights,”) and (Gao et al., n.d.).

As an automotive supplier for exterior body panels such as bumpers and tailgate, Plastic Omnium is interested in flow control modules integration designed in order to improve the aerodynamical performances.

The work focuses on drag reduction of a reduced scale generic mockup dealing with a Sport Utility Vehicle (SUV) geometry. The objective is to identify the sources of aerodynamical losses by numerical simulations and to quantify the capability to reduce the pressure losses thanks to experimental measurements. The generic mockup proposed here has been designed in order to match realistic features of road SUVs (Figure I.a). The test of several modular parts (Figure I.b) has led to the definition of the generic version used in this work, commonly called POSUV.

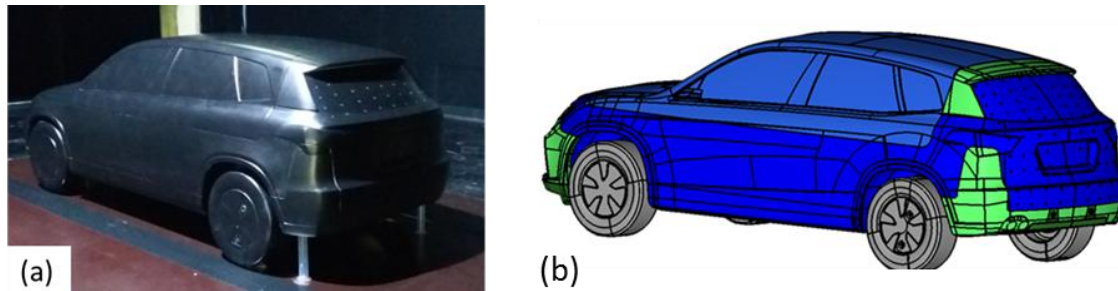


Figure I.3: (a) Reduced scale POSUV mockup in TU-Berlin wind tunnel; (b) Different modules in green can be changed on the basis of the mockup in blue.

Knowing that the aerodynamic losses are mostly concentrated in wake flow driven by the boundary layer separations, the detachment phenomena in the flow past the POSUV are targeted. In fact, the major part of drag forces is concentrated on the rear window and the back wall of the car model. Therefore, a good understanding of the near wake dynamics helps to think efficient flow control strategies. Interactions between shear layer developments and characteristic frequencies are captured with experimental flow measurements thanks to high sampling frequency acquisition of wall pressure and velocity planes and correlated to Computational Fluid Dynamics (CFD) results performed with a Large Eddy Simulation (LES) solver.

To better understand and manipulate the flow detachment and the near wake behaviour two numerical corollary studies are also performed to complement the POSUV wake analysis and control. First, the flow over a ramp is deeply analyzed and controlled as the ramp produces some main characteristics similar to the rear window detachment. Second the flow around a  $47^\circ$  Ahmed body is studied. This later geometry has some similarities with SUV cars and its understanding and control seemed to be a necessary path towards the car simulation and control. These studies are of course directly correlated to the POSUV experiments and simulations with or without control as common tools as Dynamic Mode Decomposition (DMD) are used to achieve straightforward results.

The PhD manuscript is structured around three chapters.

In the first chapter, an overview of the existing knowledge on the main topics mentioned in this domain of research is achieved. After a wide exploration of existing flow control studies on real car and simplified mockup aerodynamics, a reminder of most important fluid mechanics and turbulence involved in road vehicle will be explained. Then a focus will be done on mathematical techniques used for turbulent flow simulation, optimization, model reduction and modal analysis.

The second chapter is dedicated to experimental measurements performed on the reduced scale generic SUV mockup. The baseline flow will be fully analyzed focusing on the identification of the flow features responsible of aerodynamic loss. An original method will be proposed to highlight turbulence characteristics thanks to a Proper Orthogonal Decomposition (POD) with respect to flow periodical motion observed with Dynamic Modal Decomposition (DMD). After a presentation of the reactive optimization control achieved during the experimental campaign using machine learning, a deeper analysis of the best operating point is proposed using a multivariate modal decomposition. A first objective is to find a relation on the tailgate between averaged wall pressure level and the spectral information contained in the pressure fluctuations. A second objective is to demonstrate the change of energy transfer process depending on the actuation frequencies. According to this work, a discussion is proposed on the role of actuation frequencies used to damp periodical coherent structures emerging in the detachment zones.

The third and larger chapter of this work gathers the numerical investigations of the flow control performed in order to identify the origin of the aerodynamic losses. All bench simulations are validated with experiments and satisfy the numerical convergence needs.

The starting point of the numerical work relies on preliminary computations of a flow control benchmark dealing with a detached flow over a  $25^\circ$  inclined ramp. This test case allowed an understanding of the requirements for an accurate numerical simulation of detached flows. Criteria for a correct resolution of the boundary layer and the shear layer will be identified. In regards to experimental results from the literature, an analysis of the active flow control is proposed in order to improve our knowledge on the physics of periodic jets. This preliminary work will provide the guidelines for simulation and control of detached flows.

Then, a second numerical study of a flow control case around a 47 degrees Ahmed body will be performed in order to move closer to a simplified version of the SUV benchmark. The goal is to extend the knowledge obtained on the ramp into a 3 dimensional wake flow in order to extract the flow topology and the dynamic of the vortices. Premise of real-time closed loop control will be proposed using Dynamic Modal Decomposition.

It is in this framework that the numerical LES simulation of the flow around the reduced scale POSUV will be achieved. Energy transfer between coherent structures subjected to the turbulent cascade in the inertia zone is analyzed thanks to a Sparse Promoting Dynamic Modal Decomposition (SPDMD). Cross-correlations between experiments and CFD will help to quantify the periodical flow structures that have to be accurately reproduced in numerical LES simulations. These numerical results will enable to focus on the coupling mechanism between boundary layers separation and dynamic of the wake flow. Finally, the numerical simulation results obtained with boundary conditions reproducing the best experimental configuration of the active flow control case will be discussed.

To conclude, a discussion on the outlooks emerging from this study will be proposed. The prospects for future work and for the application on a full scale model will be examined.

# Chapitre 1: Literature survey

According to literature review, we will look at the regions of the flow responsible for energy losses and affecting the steady state topology of the recirculating zone on realistic car. This concerns regions such as the A-pillar, rear flow and underbody. This will give us some insight on the natural frequencies and the length scales of the vortices.

This first review will help to explain the passive solutions that were introduced in order to reduce the energy generates in these structures. However, drag reduction obtained with this steady state analysis is now limited and dynamical description of the flow need to be better understood in order to find some new optimization possibilities in this constraint environment. The second review will focus on the investigation on detached flow mechanics.

Application of flow control solutions will be then presented with an explanation of their impact on the flow mechanisms. Results obtained with control loop solutions used to stabilize large vortex structures position in symmetric state will be highlighted. This review will also help us to select active flow control solutions working on shear layers modification leading to energy decrease in the wake leading to drag reduction of a vehicle mockup.

Periodical behavior can be described with modal decomposition techniques such as POD, SVD and DMD. These methods will be detailed and discussed in the third section in order to select the most suitable algorithm appropriate for a coherent structure description of the turbulent wake flow.

Unsteady Navier-Stokes computation is an efficient way to describe the coherent flow structures in the wake. However, special care has to be taken in the inertia zones to ensure accurate energy transfer. Different simulation techniques will be review from literature in order to model the turbulent energy in the subgrid scale of the wake flow and in the turbulent wall boundary layer.

## 1.1. Aerodynamic loss identification on realistic cars

Analyses of the aerodynamic flow around vehicle are of prime interest in order to understand the physics of the flow. This knowledge will enable to define passive or active solutions for drag reduction in the main regions of detachment, thanks to a good description of these phenomena.

Several sources are responsible for the aerodynamic loss on a real car (Figure I.4) as described by (Hucho and Sovran, 1993). The main component is due to the pressure force coming from the detached wake flow and the stagnation point at the front. This is defined as the pressure drag contributing until 33% of the total aerodynamic loss according to the study of (Barnard, 2001). The skin friction is the results of the viscous stress applied by the flow on the car body panels, contribution to 27%. Additional aerodynamic contributions appear from the flow going through the engine and the radiator corresponding to the internal drag, contributing to 13%. The turbulent structures generate on wheels, wheelhouses and mirrors are assimilated to the excrescence drag, contributing to 27%.

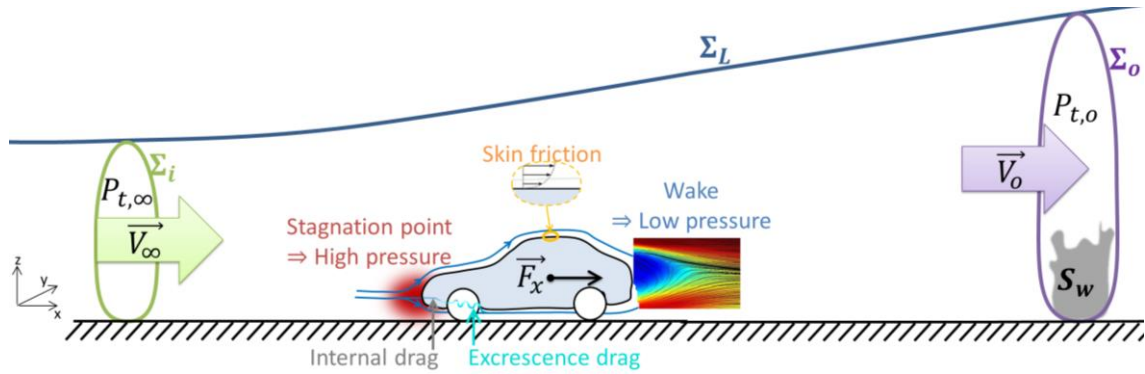


Figure I.4: Aerodynamic loss components observed on a real car. The theory of the quantity momentum integration on a fluid stream tube surrounding the car quantifies the aerodynamic loss.

The complete force is obtained by integration of the pressure and viscous stress on the car surface.

$$\vec{F} = \int_S P_{stat} \vec{n} \cdot d\vec{S} + \int_S \tau \vec{n} d\vec{S} \quad \text{Eq.3}$$

Where

- $P_{stat} = P - P_{\infty}$  is the static pressure in [Pa]
- $\tau = \mu(\partial u / \partial y)_{y=0}$  is the shear stress tensor [Pa].
- $\vec{n}$  is the unit normal vector to the surface

It is demonstrated in the work of (Onorato, 1984) that the overall aerodynamic loss can be evaluated thanks the momentum equation integration in a stream tube domain surrounding the mockup ( $\Sigma_i, \Sigma_L, \Sigma_o$  in Figure I.4). This leads to an aerodynamic force definition driven by total pressure difference (1<sup>st</sup> term in Eq.4), streamwise velocity deficit (2<sup>nd</sup> term in Eq.4), and a vortex drag quantified by the transverse velocities (3<sup>rd</sup> term in Eq.4).

$$F_x = \int_{\Sigma_o} (P_{t,\infty} - P_{t,o}) ds + \frac{\rho}{2} \int_{\Sigma_o} (V_{\infty} - u_o(y, z)) ds + \frac{\rho}{2} \int_{\Sigma_o} (v_o^2 + w_o^2) ds \quad \text{Eq.4}$$

Where:

- $P_t = P + 0.5\rho V^2$  is the total pressure in [Pa]
- $\Sigma_o$  is the downstream section of the fluid tube.
- $u_o, v_o, w_o$  are the velocity components of the flow  $\vec{V}_o$  going through  $\Sigma_o$
- $V_{\infty}$  and  $P_{t,\infty}$  are the farfield velocity and total pressure measured on the upstream section  $\Sigma_i$ .
- $\rho$  is the density.

Since the flow disturbances measured downstream of the bluff body contains the aerodynamic loss information (illustrated in the fictive surface  $S_w$  of Figure I.4), the aerodynamic efficiency of a car can be redefined as its imprint on the downstream flow. One can mention the transparency of a bluff body in the flow. This efficiency is calculated with the normalized drag force  $C_d$  and the normalized pressure contribution  $C_p$ .

$$C_d = \frac{F_x}{0.5\rho V_\infty^2 S_{ref}}; \quad C_p = \frac{P - P_\infty}{0.5\rho V_\infty^2 S_{ref}}; \quad \text{Eq.5}$$

Where:

$F_x$  is the drag force along respectively x axis  
 $\rho$  the fluid density with  $\rho_{air} = 1.225 \text{ [kg/m}^3\text{]}$   
 $S_{ref}$  the reference surface

Looking at synthesis presentation of French OEM (Parpais, 2015) and to the drag history of car of (Hucho and Sovran, 1993), the drag coefficients of ground vehicles are distributed between 0.42 for large SUV and 0.15 for concept cars depending on design features (Figure I.5).



Figure I.5: Drag coefficient measured for different obstacle from the flat plate with high drag coefficient to the profiled body with an optimal drag coefficient.

### 1.1.1 Flow characteristics of realistic cars

According to this classification, automotive geometric features can be categorized depending on the top geometry of the rear end (Figure I. 6a). Fastback shape relates to vehicle with a rear window slopes extending smoothly from the roof until the back tail. Notchback geometry has a smooth angle between the roof and the slant window connected to a square trunk. The hatchback geometry relates to vehicle with a rear end window merging with the trunk with a sharp angle between the roof and the window.

These geometrical features and especially the slant angle directly drive vortices appearing on the rear end between the roof and the rear window (Figure I. 6b). For Notchback and fastback, the flow tends to remain attached to the rear window and pressure loss developing in the wake flow will act only on the tail of the vehicle. These shapes will be associated to low drag coefficient.

For higher slant angle, vortices appear on the rear window leading to a pressure loss impacting all the rear end. The drag coefficient increases drastically with this type of vehicle due to an unsteady and partially detached flow above the rear window. Hatchback vehicles are associated to fully detached flow with a pressure loss acting on all the tailgate area.

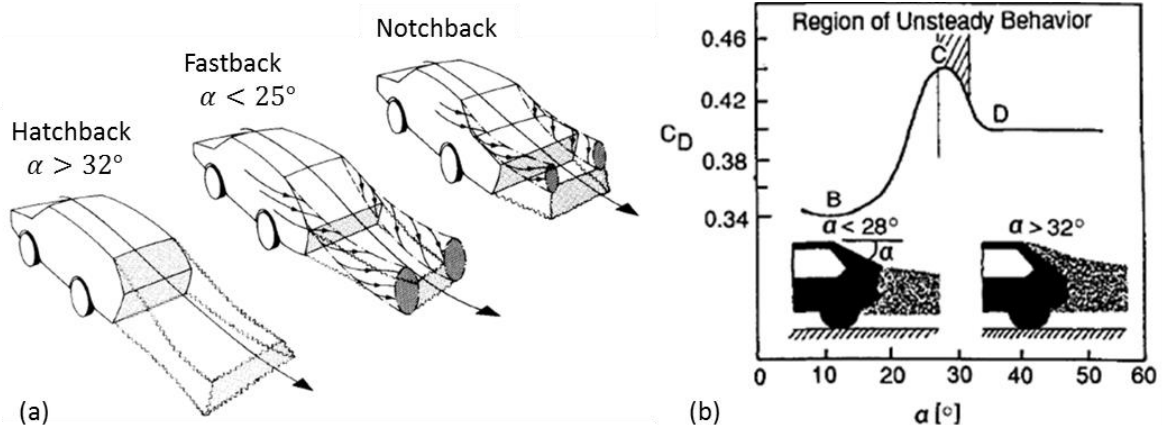


Figure I. 6: Influence of the design on the drag coefficient: (a) Illustration of rear end types; (b) Drag coefficient as a function of the rear slant angle  $\alpha$  (Hucho, 1987);

SUV vehicles correspond to the hatchback configuration with a rear window inclined at  $45^\circ$  (Figure I.7a). However, there is a new trend in SUV market dealing with big SUV designed as fastback with a rear window inclined at around  $25^\circ$  (Figure I.7b).



Figure I.7:(a) Hatchback versions of the SUV with a rear window inclined at  $45^\circ$ ; (b) New SUVs with a rear window inclined at  $22^\circ$ ;

There is similitude between these versions of SUV and the Hatchback/Fastback Drivaer versions proposed by (I. Heft et al., 2012; Wieser et al., 2014). The Drivaer is a 1/4 reduced scale mockup proposed by TU-Munich in order to compare the wake flow of Hatchback, Fastback and Notchback vehicle (Figure I.8). It should be mentioned that the dimension of the original fastback version of the Drivaer mockup is closer to sedan vehicle than SUV with  $22^\circ$  inclined rear window. Regardless, 14% drag difference is measured between the  $22^\circ$  and the  $47^\circ$  slant angle version of the Drivaer. The flow characteristic around this mockup was measured in the TU-Berlin. The measurement methods used for the pressure, velocity and forces acquisitions ensure our confidence on the quality of the measurements described in the PhD work of (Wieser et al., 2014). Additional flow measurement techniques to characterize more precisely the dynamics of the flow such as high speed PIV are presented in the work of (Martinat et al., 2008). This technique can be improve with flow optic method solved on GPU, allowing the tracking of dynamical structures in the wake as presented by (Varon, 2017).

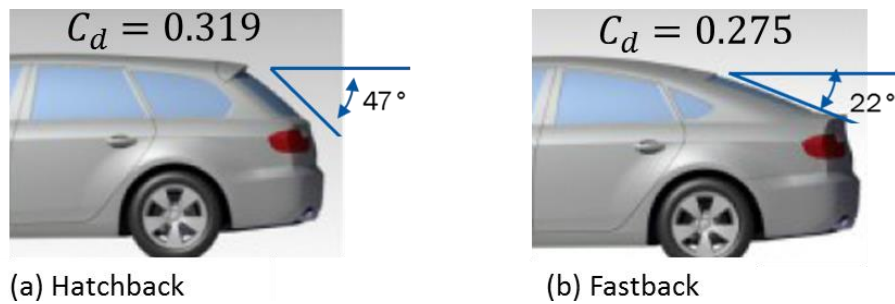


Figure I.8: Drivaer model and drag coefficient depending on the rear end geometry, measured by (I. Heft et al., 2012a).

Recently, influence of the slant angle was highlighted on the Porsche Cayenne at 1/6 scale model (Wolf, 2018). An appendix was added in order to vary the rear window slant angle (Figure I.9).

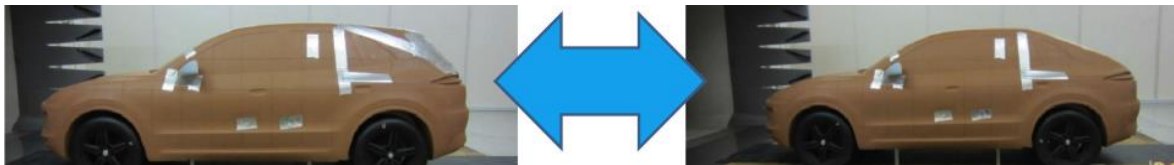


Figure I.9: Picture of experimental campaign presented in (Wolf, 2018) to characterized the impact of the rear end slant angle on a Porsche Cayenne mockup at 1/6 scale.

The result of this study (red line on Figure I.10) reveals that the 45° slant angle yields the best drag coefficient of 0.32 (blue circle). The critical slant angle associated to the worst drag coefficient is obtained at 32° (pink circle on Figure I.10). A difference of 6% aerodynamic loss compared to 45° angle is measured.

These measurements also give a comparison of the two generic slant angles at 22° (green circle) and 45° (blue circle). An increase of 4% drag coefficient is captured between these two configurations instead of 14% drag reduction measured between the fastback and the hatchback Drivaer mockup. Consequently, it seems that the benefit of the fastback SUV is not as obvious as it is commonly stated on simplified mockup.

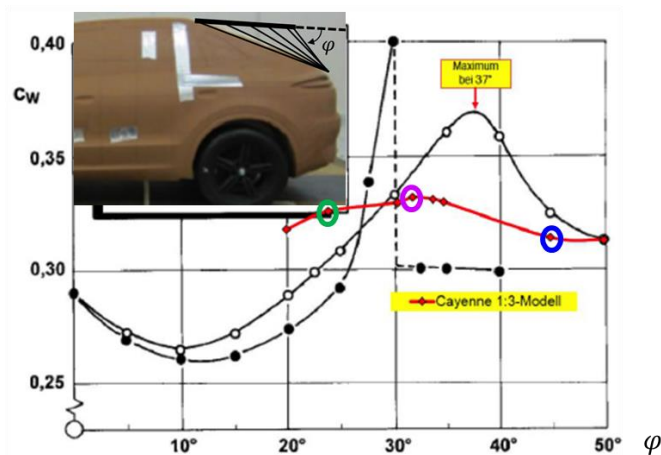


Figure I.10: Drag coefficient measurements on the reduced scale Porsche Cayenne as a function of the slant angle  $\varphi$ . The critical angle at 32° with the worst drag coefficient is highlighted with a pink circle. The two generic configurations at 22° and 45° are highlighted respectively with the green and blue circles.

It was decided for this work to focus on the  $45^\circ$  configuration, as it is still the most common design in the street. Moreover the fully detached flow brings more potential for an aerodynamic optimization. It is important to mention the experimental work of (Grandemange, 2013) on a full scale Peugeot 3008 model and the numerical study of (Eulalie et al., 2018a) on a full scale BMW X5 mockup. They proposed an exhaustive description of the flow past SUV model with a slant window at  $45^\circ$ . For both cases, the rear end pressure distribution reveals a higher pressure loss in the region of the rear bumper (Figure I.11a and Figure I.12a). Massive recirculation region in the wake flow is mainly responsible for the aerodynamic loss (Figure I.11b and Figure I.12b,c).

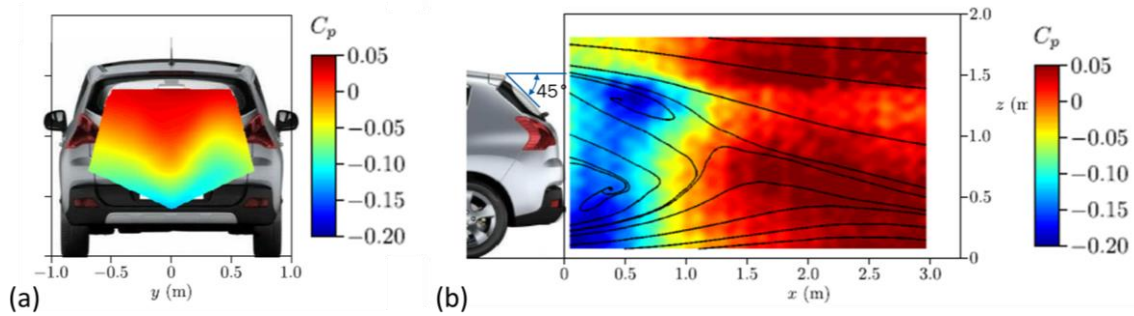


Figure I.11: Time averaged pressure coefficients distribution measured on (a) the rear end and (b) transverse vertical  $Y_0$  cut-plane of a full scale 3008 mockup (Grandemange, 2013).

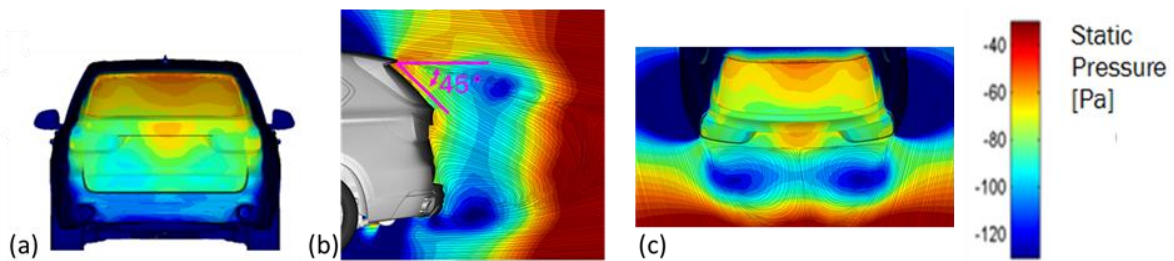


Figure I.12: Numerical results of a full scale BMW X5 model from (Eulalie et al., 2018): (a) Time averaged pressure distribution on the rear end; (b) in the wake in the  $Y_0$  cut-plane; (c) in a horizontal cut section.

To go further, several studies show the impact of flow detachments and unsteadiness in the aerodynamic loss of realistic cars.

### 1.1.2 Flow detachments for a realistic SUV

The turbulent structures generated on the body panel discontinuities assimilated to the excrescence drag, due to mirror, wheels and underbody flow, contributes to 27% of the aerodynamic loss. More generally, each curved discontinuities introduce disturbances in the fluid flow. Vortices are commonly observed in the region of the front bumper, hood-windshield junction, A-pillar, side window, and wheels (Figure I.13). One can question about the interaction between these structures. It would be particularly interesting to understand their impact on the detached wake flow.

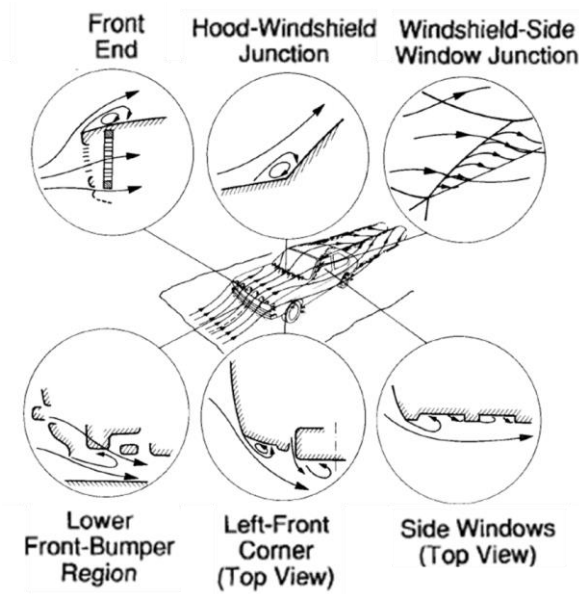
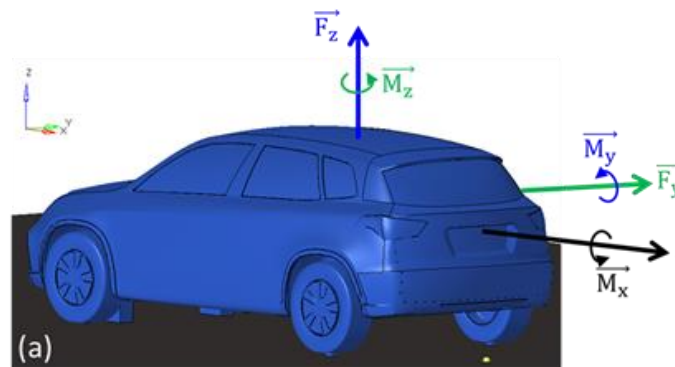


Figure I.13: Turbulent structures participating to the excrescence drag observed on the body panel proposed by (Hucho and Sovran, 1993).

The 3D complexity of the flow is important for the drag control but also for the definition of the vehicle behavior on road. This turbulent unsteadiness explains the interests of three directional forces and torques measurements to maintain car handling and stability features. Figure I.14a shows the lift force  $\vec{F}_z$  and pitch moment  $\vec{M}_y$  (in blue) characterizing the handling which is defined as the car sensitivity to external disturbances. The side force and yaw moment (in green) is associated to the stability which is defined as the sensitivity to cross wind and lateral unsteadiness. The corresponding normalized lift, pitch, side force and yaw coefficients are defined in Figure I.14b.



Handling		Stability	
$C_L = \frac{F_z}{q \cdot S_{ref}}$	$C_m = \frac{M_y}{q \cdot S_{ref} \cdot l}$	$C_M = \frac{F_y}{q \cdot S_{ref}}$	$C_n = \frac{M_z}{q \cdot S_{ref} \cdot l^2}$
Where:			
$C_L$ is the lift coefficient;		$C_M$ is the side force coefficient;	
$C_m$ is the pitch coefficient;		$C_n$ is the yaw coefficient;	
$q$ is the dynamic pressure; $S_{ref}$ is the reference surface; $l$ is the moment arm;			

Figure I.14: (a) Forces and torques defined in automotive coordinates; (b) Normalized forces coefficients defining handling and stability criteria.

In the following paragraph, we will focus first on the flow detachments impacting the handling and then on the turbulent structures impacting the stability.

The handling is mainly impacted by turbulent structures in the underbody flow since vertical ascending lift due to ground effect tends to decrease the load on the wheels. Moreover, the pitch  $\overline{M}_y$  is associated to the load distribution between the front wheels and the rear wheel. When it becomes negative, the nose of the vehicle tends to pitch downward, the load on the rear wheels is lightened and there is a risk to oversteer. In addition studies from reported 13% drag reduction can be obtained with suitable optimization of the underbody floor according to (“Audi Technology Portal - Underbody,” n.d.). Figure I.15a and b show the time averaged flow in a horizontal cut plane going through the underbody obtained on the Audi Q5 and on a complex car design obtained in the numerical simulation of (Wojciak, 2012). We can see the impact of the detachment around the wheels and the pressure loss induced by the exhaust.

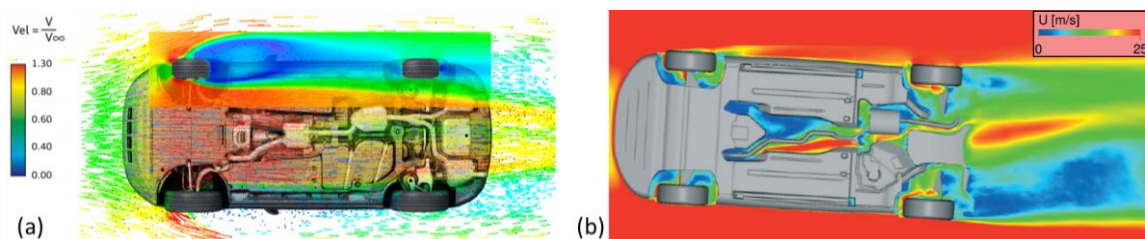


Figure I.15: (a) Turbulent structures simulated on a realistic underbody from (“Audi Technology Portal - Underbody,”); (b) Underbody flow through a complex car floor design, subjected to a yaw deviation of  $3.3^\circ$  (Wojciak, 2012);

The detachments affecting the car stability are highlighted thanks to the flow sensitivity to side effects. Figure I.16 shows the rear end pressure distribution and the drag force as a function of the yaw angle from the experimental study of a full scale BMW X5 model (Eulalie et al., 2018a). If the centered configuration exhibits high rear end pressure,  $2^\circ$  deviation on the yaw angle leads to 3% aerodynamic loss compared to the baseline flow associated to a decrease of the rear end pressure map.

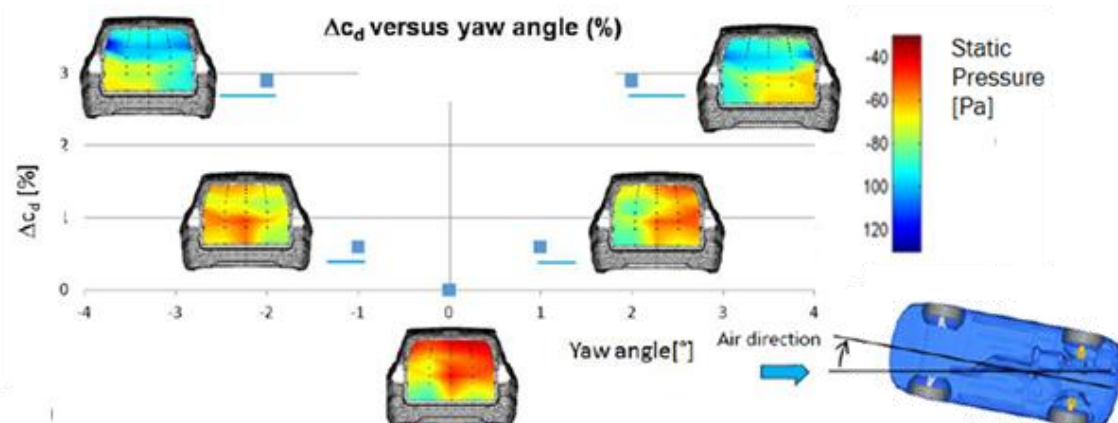


Figure I.16: Experimental measurements performed by (Eulalie et al., 2018): (a) Full scale BMW X5 prototype; (b) Sensitivity of the rear end pressure to yaw angle deviation.

Figure I.17 shows the influence of the yaw deviation on the wake flow topology from the numerical study of a simplified realistic car (Yuan et al., 2018). The streamlines track the importance of the underbody flow propagating in the wake while in  $6^\circ$  yaw deviation, the detachments on the fender and wheelhouses become dominant.

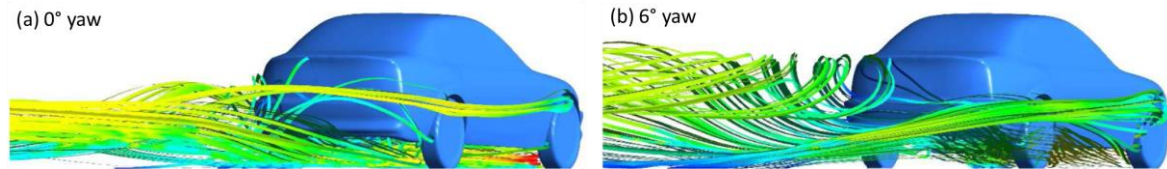


Figure I.17: Streamlines in the underbody flow and around the body panels propagating in the wake: (a) at  $0^\circ$  yaw angle; (b)  $6^\circ$  yaw angle (Yuan et al., 2018).

Additionally, the work of (Theissen, 2012; Wojciak, 2012) stresses out the impact of unsteady periodical crosswind fluctuations on the aerodynamic of a full scale BMW mockup especially on the natural vortex shedding in the wake flow. All these observations are significant especially in case of sudden crosswind gust for security matter.

We need to have a closer look on the physics of turbulent flows and separation mechanisms, which occur in the wake flow of realistic cars.

## 1.2. Description of detached flow mechanisms

The complexity of the flow surrounding a car in highway driving condition is mainly explained by a strong turbulence level. In this environment, the physics of the flow is governed by vortices with a wide range of length scales. In the following section, the flow pattern observed around a vehicle will be discussed based on the fundamentals of turbulent flows.

One can briefly remind some classical turbulent structures visible in complex flows. Figure I.18a illustrates the development of Tollmien-Schlichting wave instability emerging in laminar boundary layer and leading to turbulent transition burst. Figure I.18b shows the 3D breakdown of the wave instability into horseshoes decaying into complex flow pattern of the turbulent boundary layer. Figure I.18c exhibits the Kelvin Helmholtz instability created by the boundary layer separation on a cylinder and propagating in the shear layer. This instability is associated to high frequency signature. The wake dynamics of the flow past an obstacle is driven by the Karman vortex shedding, also visible in Figure I.18c, and is generally associated to low frequency pulsation.

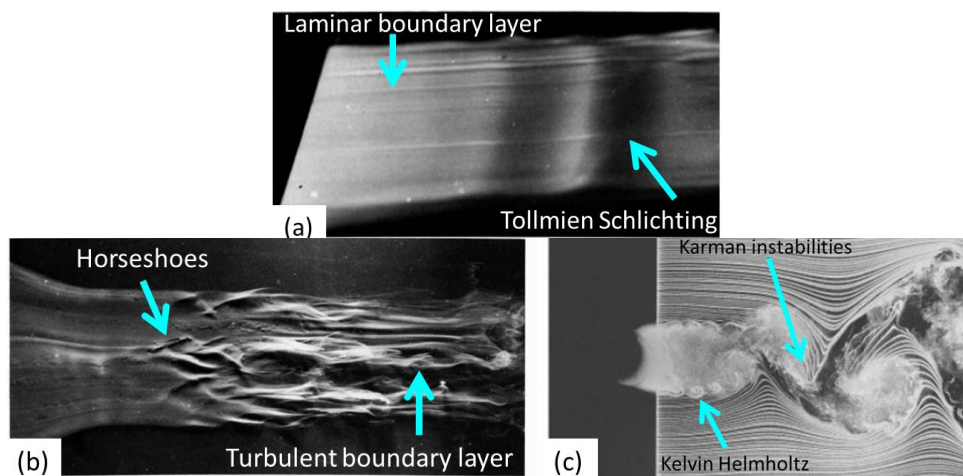


Figure I.18: Some classical structures observed in fluid mechanics: (a) Tollmien-Schlichting instability developing in a laminar boundary layer; (b) Horseshoes and turbulent boundary layer pattern; (c) Kelvin-Helmholtz of the shear layer and Karman vortices

The following section will go further in the description of the turbulent behavior in the detached flow past an obstacle. First a focus on the turbulent boundary layers developing on the body panels will be done. This part relies on observations from the boundary layers developing over a flat plate. External parameters responsible for the boundary layer separation will be investigated and the resulting disturbances propagating in the shear layers will be explored. The detachment will be more wisely described thanks to the test case of the flow past a circular cylinder for a better understanding of the wake dynamics driven by Karman vortex shedding at natural frequencies. The interactions between all these phenomena will be then investigated with the 25° inclined ramp benchmark. Finally, the correlation between the shear layer and the more complex 3D wake flow of the Ahmed Body will be examined.

### 1.2.1 Fundamentals of turbulence

- Turbulent flow

The pattern in turbulent flows is governed by inertia forces while the viscous effect is minimal contrary to what is observed in laminar flow. The scale of the turbulence level is estimated by the Reynolds number (Eq.6) corresponding to the normalized ratio between inertia effect and the viscous dissipation forces. It should be mentioned that the flow past a full scale car in high speed condition is at a Reynolds number of  $4 \cdot 10^6$  and for a 1/6 reduced scale model at a Reynolds number of  $4 \times 10^5$ .

$$Re = \frac{\rho U_{\infty} H}{\mu} = \frac{U_{\infty} H}{\nu} \quad \text{Eq.6}$$

where

$U_{\infty}$  the reference velocity [m/s]

$\rho$  the fluid density with  $\rho_{air} = 1.225$  [kg/m<sup>3</sup>]

$\mu$  the dynamic viscosity with  $\mu_{air} = 1.8e^{-5}$  [Pa.s]

$\nu = \mu/\rho$  the kinematic viscosity  $\nu_{air} = 1.5e^{-5}$  [m<sup>2</sup>/s]

Turbulent flows are described as a set of eddies associated to a large range of characteristic length scales, velocity scales and time scales (Figure I.19b). Large scale eddies observed in turbulent flows are submitted to unstable behavior leading to breakup of the structures. The kinetic energy carry by them are transfer to smaller eddies. This phenomenon is called the turbulent kinetic energy decay, illustrated in Figure I.19b. It occurs as long as the inertial forces are predominant on viscous forces. The turbulent kinetic energy of the smaller eddies are dissipated by heat dissipation.

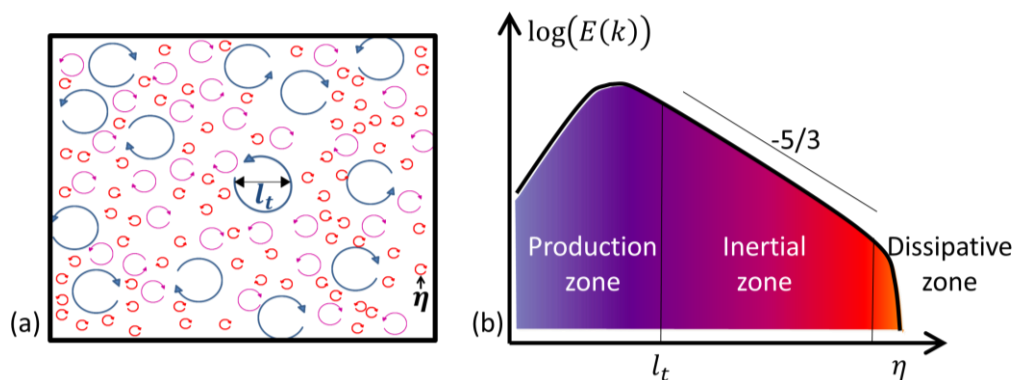


Figure I.19: (a) Scheme of eddies in turbulent flow and (b) turbulent kinetic energy occurring in homogeneous isotropic turbulent flow.

The Kolmogorov theory states that, at high Reynolds number, the small eddies are isotropic and determined only by the kinematic viscosity  $\nu$  and the dissipation rate. This gives the Kolmogorov length scale defined as in Eq.7 defining eddies dissipated by heat.

$$\eta = \left(\frac{\nu^3}{\epsilon}\right)^{1/4} \quad \epsilon = U^3/L \quad \text{Eq.7}$$

Where

- $\eta$  is the Kolmogorov scale [m]
- $\nu$  is the kinematic viscosity [ $\text{m}^2/\text{s}$ ]
- $\epsilon$  is the dissipation rate [ $\text{m}^2/\text{s}^3$ ]
- $L$  is the integral scale
- $U$  is the reference velocity of the integral scale.

In cases of Homogeneous Isotropic Turbulence hypothesis (HIT), where the statistical quantities are invariant by translations and under rotation, turbulent kinetic energy decay occurs according to a -5/3 law as shown in Figure I.19b.

- Turbulent boundary layer

The boundary layer is the thin fluid layer in the vicinity of a bounding surface where the flow expands from a zero velocity at the wall due to adherence effects until the freestream velocity. It is described by a flow stream, which is statistically tangential to the bounding surface with a strong gradient effect acting normally to the wall as shown in Figure I.20. Plus, this fluid layer is mainly driven by viscosity effect as it is associated to a really small characteristic scales.

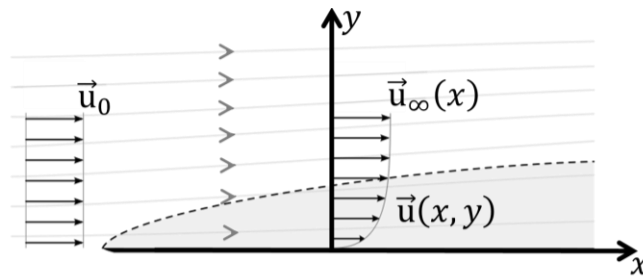


Figure I.20: Sketch of a boundary layer profile developing over a plate plane.

There are different ways to measure the boundary layer thickness. The length  $\delta_{99}$  is the distance between the wall and the point where the flow reaches 99% of the freestream values. The displacement thickness (Eq.8a) or the momentum thickness (Eq.8b) are also classically used to measure precisely the boundary layer thickness.

$$\delta_1 = \int_0^\infty \left(1 - \frac{U(x,y)}{U_\infty(x)}\right) dy \quad (a) \quad \theta = \int_0^\infty \frac{U(x,y)}{U_\infty(x)} \left(1 - \frac{U(x,y)}{U_\infty(x)}\right) dy \quad (b) \quad \text{Eq.8}$$

Where:

- $\delta_1$  is the displacement thickness.
- $\theta$  is the quantity momentum thickness.
- $x$  and  $y$  are respectively the tangential, normal direction to the wall
- $U_\infty(x)$  is the freestream velocity
- $U(x,y)$  is the tangential velocity

The gradient induced by the boundary layer on the wall leads to a wall shear stress  $\tau_w$  (Eq.9a) and the equivalent friction velocity  $u_*$  (Eq.9b).

$$\tau_w = \mu \left( \frac{\partial U(x,y)}{\partial y} \right)_{y=0} \quad (a) \quad u_* = \sqrt{\frac{\tau_w}{\rho}} \quad (b) \quad \text{Eq.9}$$

where :

- x and y are respectively the tangential, normal direction to the wall
- $\mu$  is the dynamic viscosity
- $\rho$  is the fluid density
- $U(x, y)$  is the tangential velocity
- $\tau_w$  is the wall shear stress
- $u_*$  is the friction velocity

The friction induced by a boundary layer is dimensioned thanks to the normalized friction coefficient  $C_f$ . The normalized wall distance  $y^+$  gives an estimation of the fluid flow thickness impacted by the wall roughness and the normalized velocity  $u^+$  gives an estimation of the velocity ratio in the shear gradient (Eq.10).

$$y^+ = \frac{u^* y}{\nu} \quad u^+ = \frac{u}{u_*} \quad C_f = \frac{\tau_w}{0.5 \rho U_\infty^2} \quad \text{Eq.10}$$

where :

- x and y are respectively the tangential, normal direction to the wall
- $U_\infty(x)$  is the freestream velocity
- $U(x, y)$  is the tangential velocity

Turbulent regimen changes the energy balance in the boundary layer. Turbulent boundary layer is statistically tangential to a bounding surface but additional eddies are involved. These eddies are the results of horseshoe structures developed in the transition region. They propagated until the turbulent burst where the flow is mainly driven by the inertia of these structures (Figure I.21a). Thus, the turbulent kinetic energy increases and reinforces the flow gradient at the wall, as well as the induced friction at the wall (Figure I.21b).

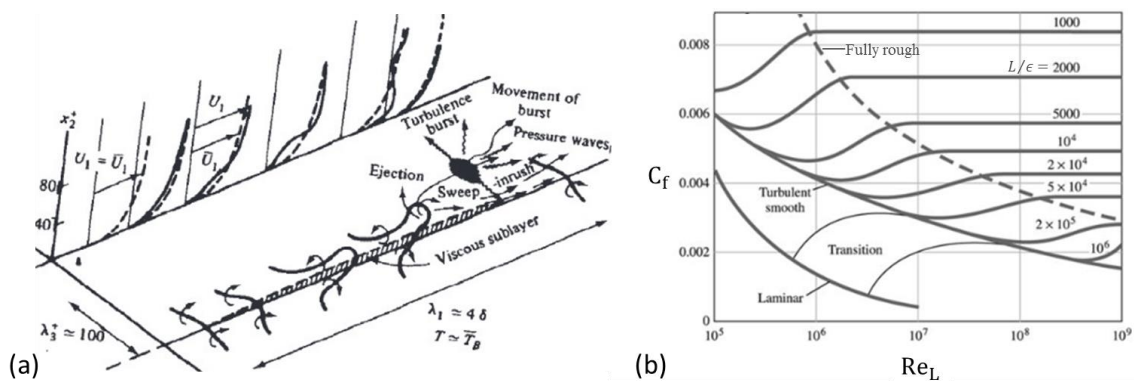


Figure I.21: Boundary layer development from laminar to turbulent on a flat plate: (a) Emergence of horseshoes in the transition region, impacting the averaged velocity profile and leading to the turbulent burst (Hinze, 1975); (b) Friction coefficient as a function of the Reynolds number.

The turbulent boundary layer is constituted of three layers (Figure I.22 a and b) identified by characteristics normalized wall distance: the viscous layer in the close vicinity of the wall

( $y^+ < 5$ ) where eddies are driven by viscous effect, the turbulent layer ( $y^+ > 60$ ) where eddies are driven by inertia and the buffer layer between them ( $5 < y^+ < 60$ ).

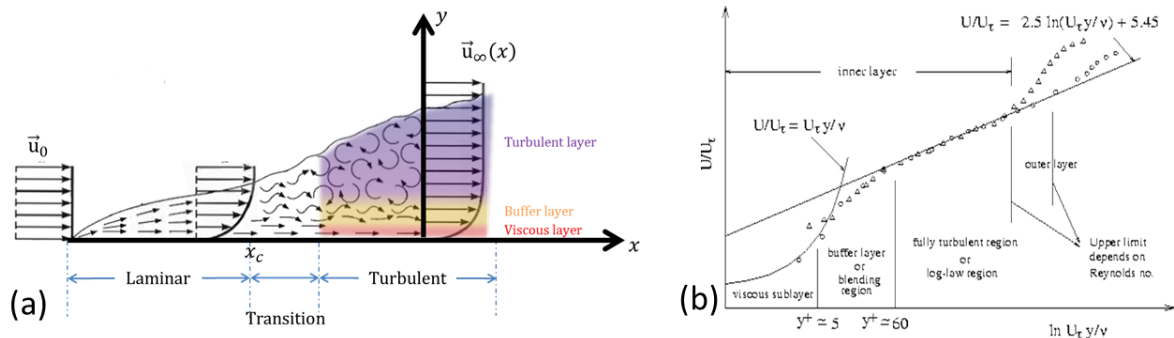


Figure I.22: (a) Sketch of a boundary layer profile developing over a flat plate. The transition is triggered at a critical position  $x_c$  leading to a turbulent boundary layer; (b) Normalized boundary layer velocity profile as a function of the normalized wall distance  $y^+$ .

Turbulent eddies embedded in the boundary layer are driven by important energy transfer. The studies of (Hutchins and Marusic, 2007; Smits et al., 2011) investigate on the power spectra density evolution along the wall normal in high turbulent boundary layers at Reynolds number of 7300. Figure I.23b displays the stream wise velocity spectrogram as a function of the normalized wall distance  $y/\delta$ . The wave number  $\lambda_x^+$  is computed as  $2\pi U/f$ . The spectrogram outlines two significant peaks. The first peak emerges in the inner layer. In this region, the turbulent production energy is driven by low wave lengths and high frequency eddies. Another peak arises in the outer layer with turbulent production energy at high wave lengths and low frequency eddies. In addition, (Hunt and Morrison, 2000) highlights the turbulent decay in the boundary impacted by the wall. The small eddies at high frequency are not disturbed nearby the wall so that the dissipation rate in the inertia zone is not altered. The larger eddies are subjected to a blockage effect between the freestream and the bounded surface. Thus, the turbulent production energy is reduced when the distance to the wall decreases as shown in Figure I.23b.

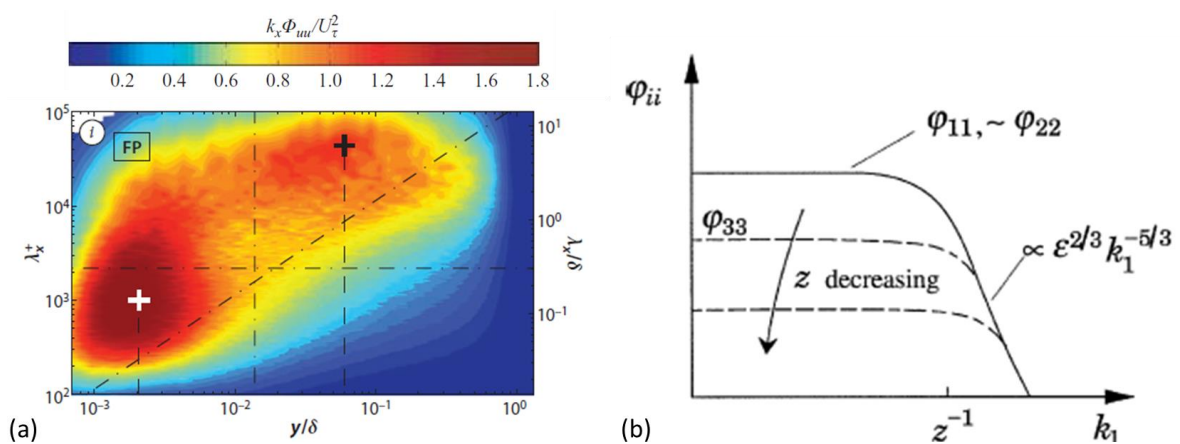


Figure I.23: (a) Contour maps of velocity spectra with wall normal at Reynolds number 7300 from DNS computation of (Hutchins and Marusic, 2007; Smits et al., 2011); (b) Blocking effect highlights with velocity spectra in outer region of the boundary layer as a function of the wall distance  $z$  from (Hunt and Morrison, 2000).

- Boundary layer separation and shear layer

Flow separation is the detachment of the boundary layer from the bounding surface. It is triggered when an adverse pressure gradient resisting to the fluid stream, tends to overcome the inertia of the boundary layer (Figure I.24a). It occurs in regions of curved walls or shape discontinuities. The induced suction effect tends to thicken the boundary layer and to weaken the shear stress acting in the viscous sublayer, until the flow close to the wall changes direction. The skin friction drops down to zero which defined the separation line (red dotted line on (Figure I.24b)). It should be noted that the kinetic energy contained in the boundary layer tends to delay the separation, meaning that laminar boundary layers are more willing to detach than turbulent boundary layers.

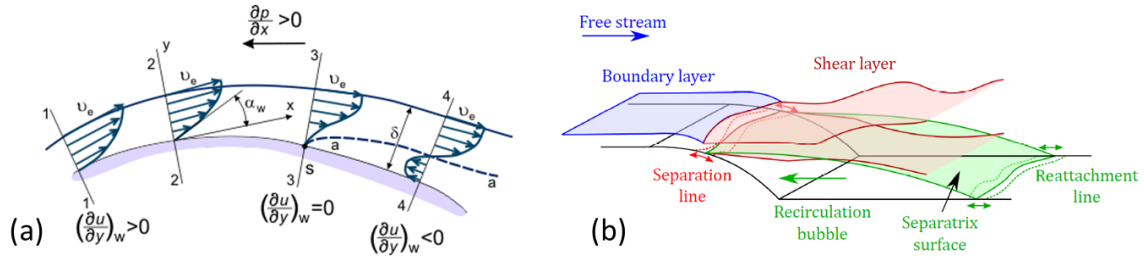


Figure I.24: Sketch of (a) flow separation on a curved surface (Epifanov, n.d.) and (b) interaction between the boundary layer and the shear layer as proposed in (Varon, 2017b).

The resulting flow evolved in a shear layer defined as an anisotropic flow with a strong velocity profile gradient. The shear layer thickness is defined in Eq.11, as a function of the velocity difference between the freestream and the recirculation bubble.

$$\theta_{sl} = \int_0^{\infty} \frac{U(x, y) - U_{min}(x)}{U_{\infty}(x) - U_{min}(x)} \left( 1 - \frac{U(x, y) - U_{min}(x)}{U_{\infty}(x) - U_{min}(x)} \right) dy \quad \text{Eq.11}$$

where :

- x and y are respectively the tangential, normal direction to the wall
- $U_{\infty}(x)$  is the freestream velocity
- $U_{min}(x)$  is a local minimum streamwise velocity
- $U(x, y)$  is the tangential velocity

- Vortex shedding and wake flow

In the test case of the flow past a cylinder, the flow separation is due to the obstacle shape curvature. The adverse pressure gradient required to enforce the separation depends on the energy contained in the upstream boundary layer. Thus, the wake vortex topology depends on the flow regimen. Figure I.25 shows the flow pattern observed behind a cylinder as a function of the Reynolds number. If in laminar configuration ( $Re < 40$ ), the wake flow tends to be stable and symmetric (Figure I.25a), for Reynolds number in the range of [40; 400], disturbances emerged and typical structures called Von Karman Vortex Street are observed (Figure I.25b). It is an alternating periodical vortices pattern due to the separated flow. The vortex shedding is characterized by a characteristic frequency only depending on the bluff body reference length and the free stream velocity. Thus, the Strouhal number, defining the normalized frequency in Eq.12, is constant and equal to 0.2 for this typical flow regimen. At higher Reynolds number ( $Re > 400$ ), the vortex shedding becomes fully complex and unstable and the flow pattern cannot be described anymore by a unique scale and a unique frequency (Figure I.25c). The flow behavior becomes a lot more difficult to predict.

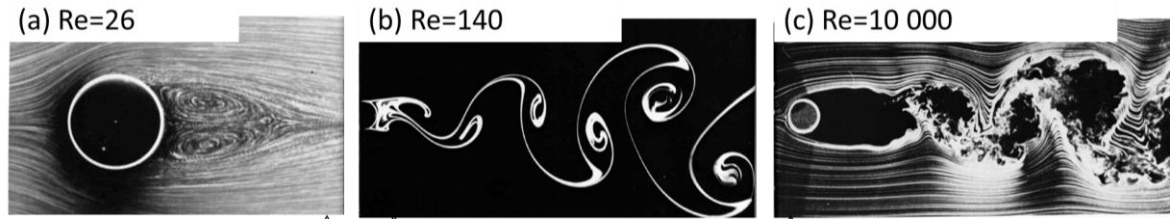


Figure I.25: Flow pattern captured experimentally behind a circular cylinder by (Van Dyke, 1982): (a) Laminar wake flow at Reynolds number 26; (b) Von Karman vortex street observed at  $Re = 140$ ; (c) Turbulent wake flow observed at  $Re = 10\,000$ .

$$St = \frac{fH}{V_\infty} \quad \text{Eq.12}$$

where

$f$  is the frequency

$V_\infty$  the freestream velocity

$H$  is the reference length

In turbulent wake flow, the shedding frequency is an additional production source term which is dissipated by the turbulence decay as shown in Figure I.26a. In this type of complex flow, the energy transfer between eddies measured at a monitoring point, is altered if the local flow condition differs from the Homogeneous Isotropic Turbulence. For instance, the dissipation at the center of the wake past the cylinder follows the  $-5/3$  rule but the energy transfer becomes more complex depending on the flow behavior. Characteristic scaling identified by (Boudet et al., 2016) highlights the action of the sheared turbulence in the dissipation rate according to  $f^{-1}$  law (Figure I.26b).

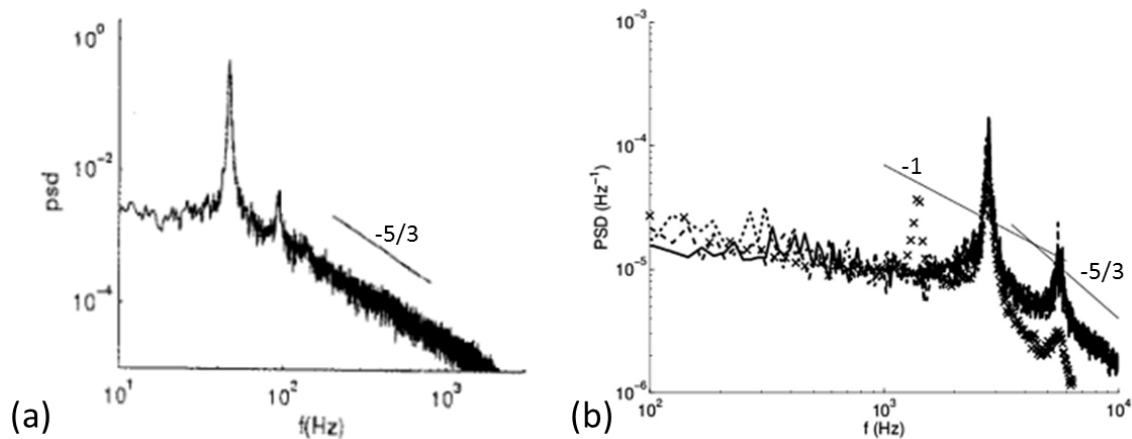


Figure I.26 : Spectral signatures measured in the turbulent flow past a cylinder at Reynolds number  $4.7 \cdot 10^4$ : (a) at the center in the wake ; (b) in the shear layer past the cylinder from (Boudet et al., 2016).

### 1.2.2 Detachments and vortex shedding of the wake flow past an inclined ramp

The complexity of detached flows is particularly observed in the simplified benchmark of the backward facing step (Creusé et al., 2009; Heenan and Morrison, 1998; Spazzini et al., 2001; Varon, 2017) or the  $25^\circ$  inclined ramp (Kourta et al., 2015; Stella et al., 2017a; Thacker, 2010). The following paragraph reviews how the turbulence due to flow detachments

influences the wake topology. The mechanisms highlighted here will bring the main keys to evaluate the role of the flow dynamics in the wake of a realistic car.

Figure I.27 summarizes the turbulent structures emerging in this test case. The upstream boundary layer is characterized by a quantity momentum thickness  $\theta_{bl}$  containing eddies of different wavelengths and frequencies. The boundary layer separation forced by the geometric discontinuity leads to the shear layer development driven by the fluid momentum. The shear stress induces the apparition of Kelvin Helmholtz instabilities, which is unstable waves growing along the separation interface. They are responsible for the shear layer roll-up and turbulent mixing. The amplification of the waves generates vortical structures transported with the flow momentum. The vortices interaction results in a pairing process by rolling around each other, enhancing the turbulent mixing intensity in the shear layer. All these phenomena drive the growth of the shear layer quantity momentum thickness  $\theta_{sl}$ . The latter surrounds the recirculation bubble behind the backward facing step until the reattachment point where the freestream flow overcomes the wake pressure drop. (Kourta et al., 2015) demonstrates empirically the relation between  $\theta_{sl}$  and the recirculation length  $L_r$ . Finally, the vortical structures embedded in the shear layer lead to a vortex shedding downstream the reattachment.

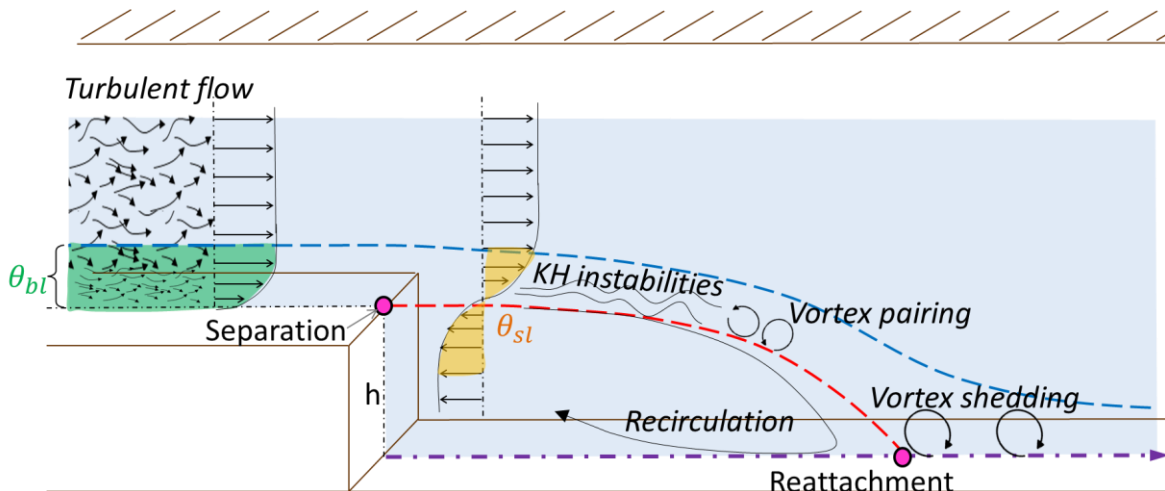


Figure I.27: Sketch of the turbulent structures observed in the flow over a backward facing step: the turbulent boundary layer evolved in a shear layer leading to Kelvin-Helmholtz instabilities. The roll-up of the shear layer generate vortex structures sheds downstream the recirculation area.

This gives a global overview of the inter-correlation existing between the boundary layer momentum, the separation, the shear layer momentum, the Kelvin-Helmholtz instabilities and the wake topology. It is deeply investigated in the analysis of the scaling of the shear layer performed by (Stella et al., 2017b) on the  $25^\circ$  inclined ramp. It proves the dependency of the shear layer characteristic thickness (Figure I.28a) and the dependency of the recirculation length (Figure I.28b) with the upstream boundary layer momentum thickness.

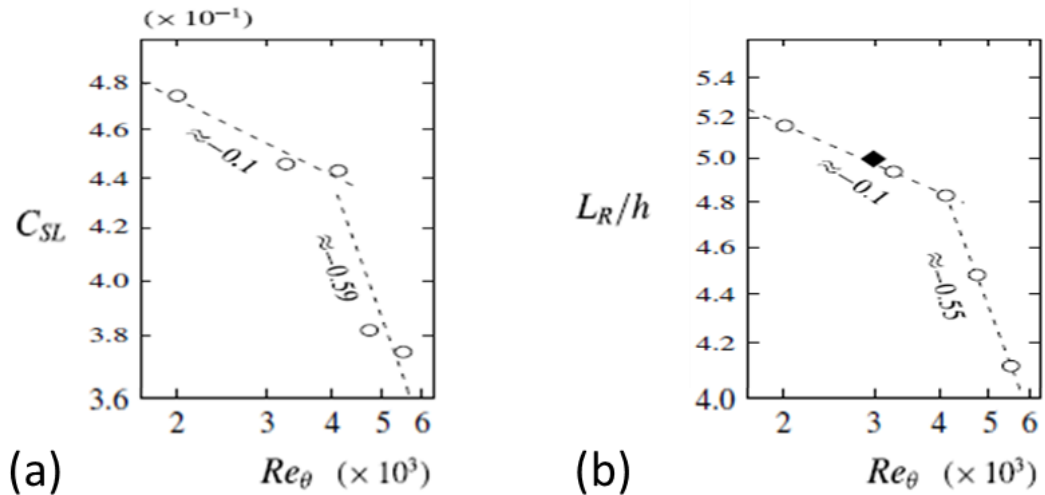


Figure I.28: Influence of the upstream boundary layer quantity momentum on: (a) the shear layer characteristic thickness and (b) the recirculation length (Stella et al., 2017b).

All these observations are used to understand the wake flow behavior on a simplified car even if they are much more difficult to highlight. Indeed, the three-dimensionality brings an additional feature modifying the interaction of the turbulent structures.

### 1.2.3 Detachments and vortex shedding of the wake flow past the Ahmed Body

A classic example of wake stability analysis comes from the Ahmed Body mockup (Figure I.29). It is a well-known benchmark used in external aerodynamic automotive research. As proposed by (Ahmed et al., 1984a), it is used to reproduce characteristic vortices observed around a simplified car. This benchmark extensively explored by (Brunn and Nitsche, 2006; Dobrev and Massouh, 2014; Martinat et al., 2008; Metka, 2013), exhibits the importance of the slant angle on the wake features and the influence on the drag coefficient long before the measurements on realistic car presented in the paragraph 1.1.

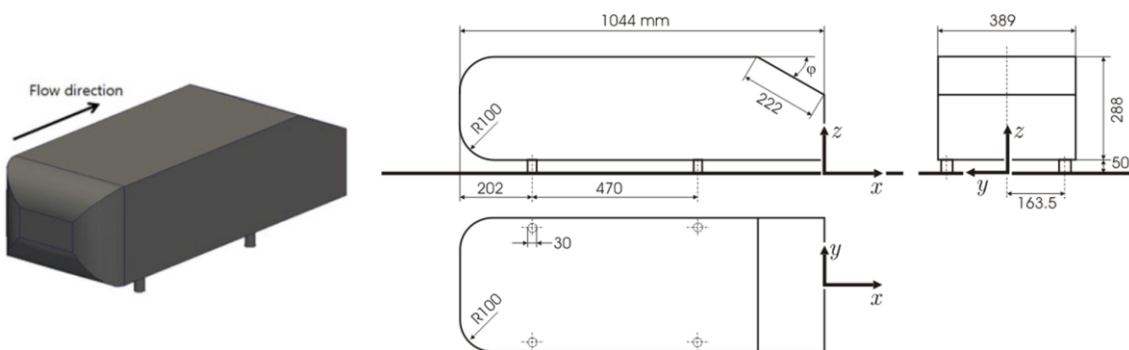


Figure I.29: Geometry of the Ahmed Body according to (Ahmed et al., 1984a).

- Wake topology as a function of the slant angle

Three main vortex types were described in the wake flow of the Ahmed body. The shear layers from the lateral edges of the slant window roll-up into longitudinal vortices  $\omega_C$  (in yellow on Figure I.30). They develop from the top slant corners until the wake, overlapping the recirculating flow. The separation bubble formed behind the vertical base of the mock-up encloses two recirculation regions. The lower vortex  $\omega_B$  (in pink on Figure I.30b) is due to

the roll-up of the shear layer generated at the lower edge of the vertical base and is mainly driven by the structures coming from the ground clearance. The vortex  $\omega_A$  (in blue on Figure I.30b) comes from the roll-up of the shear layer coming from the roof. The vortex  $\omega_A$  mainly depends on the strength of the boundary layer on the slant window, itself governed by the adverse pressure gradient due to the slant break angle.

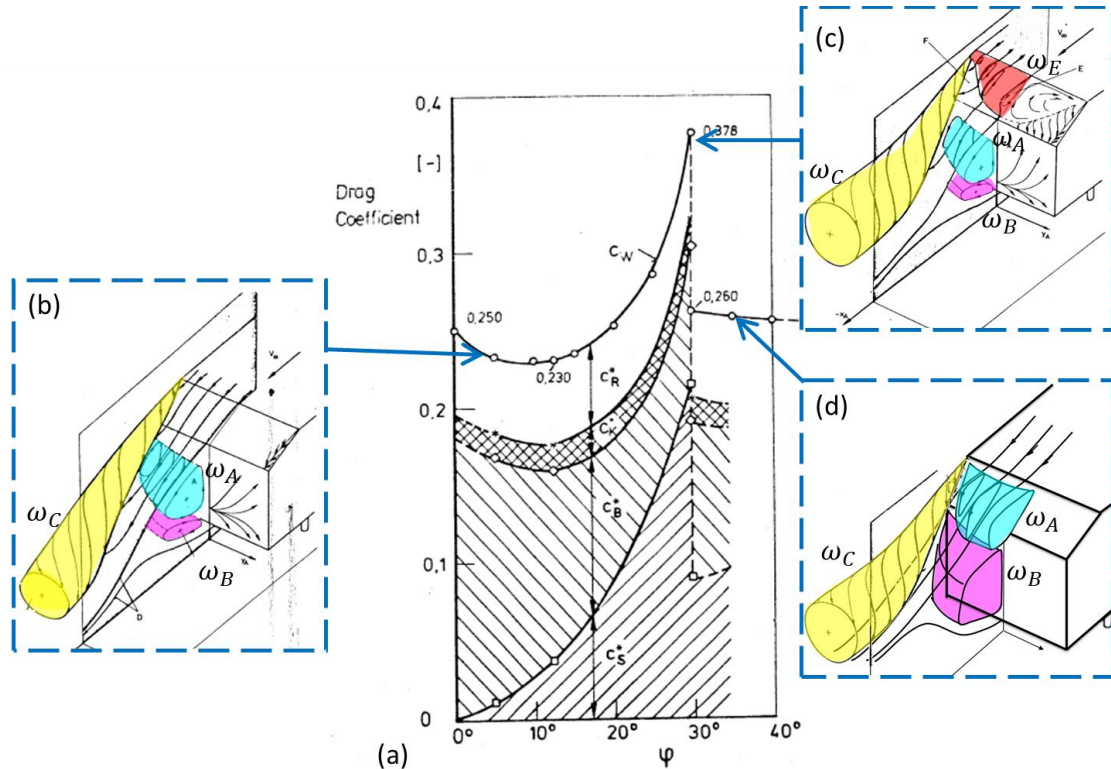


Figure I.30: (a) Variation of the drag coefficient as a function of the slant angle with the contribution of the vertical base  $C_B$  compared to the contribution of the slant area  $C_S$ ; (b) Horseshoe vortex in wake for slant angle below  $10^\circ$  with low drag coefficient; (c) Partially detached flow observed for slant angle between  $10^\circ$  and  $30^\circ$  with high drag coefficient (Ahmed et al., 1984); (d) Fully detached flow for a slant angle beyond  $30^\circ$  leading to a wake topology and a drag coefficient similar to the attached boundary layer configuration.

For a slant angle  $\alpha$  below  $10^\circ$ , the boundary layer remains attached, the aerodynamic loss is only due to the recirculation on the vertical base and the drag coefficient is significantly low (Figure I.30a). For a slant angle  $\alpha$  between  $10^\circ$  and  $30^\circ$ , the boundary layer detaches at the edge between the roof and the slant, generating the vortex  $\omega_E$  (in red on Figure I.30c) until the reattachment point on the slant window. In this configuration, additional aerodynamic loss comes from the slant recirculation and the drag coefficient increases as the angle  $\alpha$  grows. For a slant angle  $\alpha$  beyond  $30^\circ$ , the flow over the slant is fully detached and vortices  $\omega_A$  shifts upstream and merged with  $\omega_E$  to form one unique vortex (in blue on Figure I.30d). The wake flow topology is similar to the attached boundary layer configuration (Figure I.30a) and the aerodynamic loss is only related to the recirculation except that the separation bubble is extended to the slant plus the vertical base.

Shear layers developing on the side edges of the vertical base also feed both vortices  $\omega_A$  and  $\omega_B$  and participate to the three dimensionality of the wake. The balance between all vortices determined the time averaged wake flow topology. For the square back Ahmed Body, it is often described as an O-ring structure (Figure I.31). (Wassen et al., 2010) shown the

sensitivity of this balance to the ground clearance conditions exhibiting 4% drag reduction with moving floor instead of static floor.

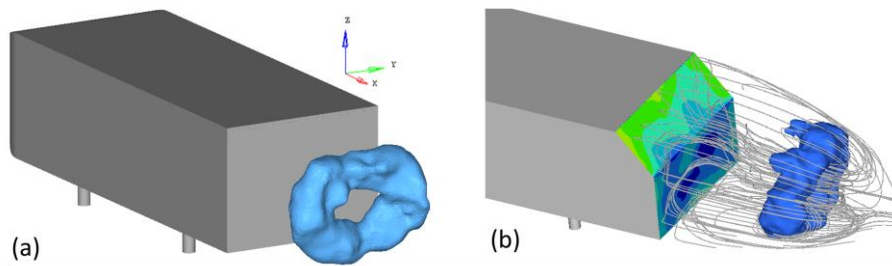


Figure I.31: O-ring structure observed in time averaged pressure iso-value: (a) in the wake of a square back Ahmed Body (Eulalie, 2014a); (b) in the wake of an Ahmed Body with a  $47^\circ$  slant angle.

The benchmark of the Ahmed Body was created with the objective to minimize the complexity of the front in order to generate a wake flow free of disturbances coming from the upstream flow. However, experimental visualization of the separation in the front part of the mockup performed by (Spohn and Gilliéron, 2002) demonstrates the existence of periodical vortex shedding displayed in Figure I.32, which increases the wake unsteadiness and deteriorates aerodynamic features.

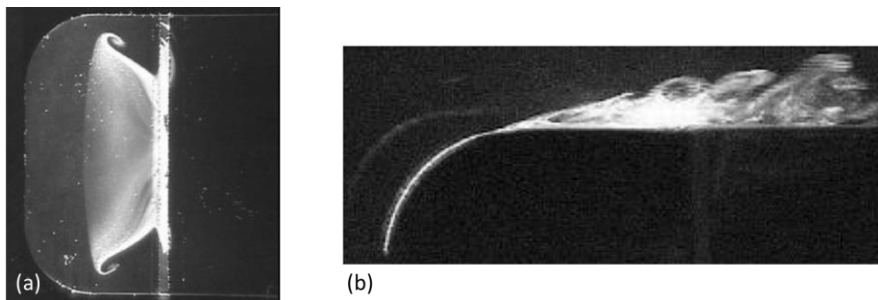


Figure I.32: Flow structure in the separation zone of the front part: (a) Top view; (b) Side view from (Spohn and Gilliéron, 2002).

- Bi-stability of the square back wake flow

(Bonnavion, 2018; Grandemange, 2013; Li, 2017a; Varon et al., 2017a; Volpe et al., 2015) describe the wake dynamics with stochastic approach and highlight the bi-stability behavior behind a square back Ahmed body. A wake dynamic is defined stable if the fluctuations are varying around a unique time averaged topology and the flow observers are statistically described by Gaussian distributions. In the case of bi-stability, the wake dynamics vary around two uncorrelated states and the resulting flow observers outline two disjointed Gaussian distributions. In bi-stable flow, the straightforward time averaged field does not correspond to the most probable flow topology physically observable but it is a visualization of the mathematical superposition of the two most probable states occurring in the wake. This brings out the interest of methods computing statistical average instead of time averaged computation. It is generally done thanks to conditional averaged as shown in Figure I.33a on a square back Ahmed Body. The statistical discrimination reveals that the rear end pressure is a combination of two off-centered states with a low pressure area located on the bottom corners of the mockup.

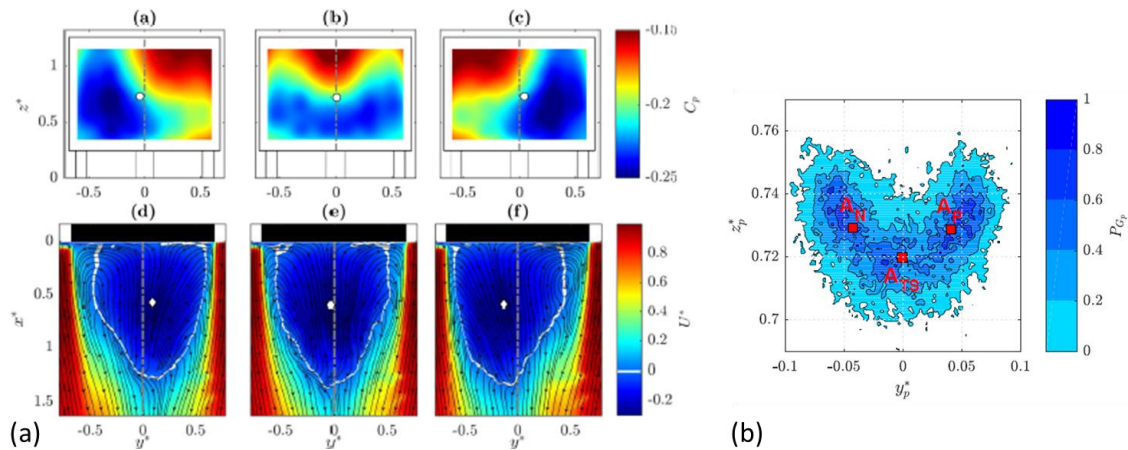


Figure I.33: Identification of the bi-modal component from (Varon et al., 2017b): (a) From left to right, comparison of the left state averaged, total averaged and right state averaged on the rear end pressure and in the wake velocity from PIV measurements; (b) Normalized 2D Probability Function of pressure barycenter measured on the squared back Ahmed Body.

The switch between each state occurs randomly but (Grandemange et al., 2013) exhibits a time scale exceeding a second duration. Thus, more than 1Hz frequency window is required to capture this phenomenon (Figure I.34). In addition, it should be mentioned that no periodical law can modeled this unstable behavior but as proposed by (Varon et al., 2017b), the flow can be approximated by a chaotic dynamic behavior varying around two uncorrelated topology.

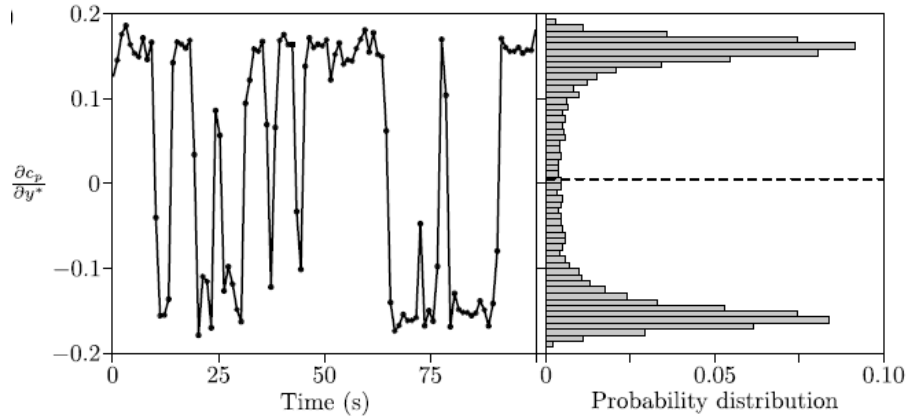


Figure I.34: Time scales of the bi-stability behavior measured on pressure transversal gradient on the square back correlated with the PDF highlighting the characteristics 2 disjointed Gaussian distributions (Grandemange et al., 2013b).

For now on, no real frequency estimates the time delay of the switch between the two states. The current available studies using modal analysis on the fluctuating database do not give either a clear evidence of the spectral information responsible for the bi-stability. An approach using coherent decomposition on the direct flow data instead of the fluctuating data may give more insight on the dynamic modal behavior of the bi-stable flow. This study would be required in the case of square back vehicle such as van vehicles.

## 1.3. Flow control and optimization techniques

The flow control can be performed either in order to define optimum parameter of passive solutions, or in order to continuously improve the efficiency of adaptive solutions or active flow control solutions. Active flow control refers to techniques using an external source of energy in order to modify the wake flow while the passive or adaptive solutions refer to solutions, which do not inject any additional energy in the system.

In this section, after a non-exhaustive description of the mechanism leading to aerodynamic loss reduction in open-loop which use frozen set of parameters, we will present closed loop and optimization techniques, either model-free or model based, in real time or in adaptive.

### 1.3.1 Flow control solutions

Both passive and active flow control solutions can be applied to modify the flow topology. Passive control can be achieved with porous media, deflector, vortex generators and active flow control is achieved with steady blowing, pulsed, synthetic jets, fluidic oscillators and plasma.

#### 1.3.1.1 Passive flow control solutions

The exploration of passive solution shows how external appendices change the flow topology. The solutions presents here are the results of Design of Experiments or shape optimization. Devices such as porous media, boat tailing, vortex generators or spoilers were explored in many studies for automotive applications. The interests of each of these will be discussed here. It worth mentioning other techniques developed for aeronautic applications such as compliant walls (Ehrenstein and Eloy, 2013) or shape memory alloy (Scheller et al., 2016) but we will focus in this section on solutions already tested on automotive benchmarks. The following section deals with open-loop investigation of different types of control solutions.

- Boat-tailing, deflectors and spoilers

The boat tailing appendix was proposed in order to control the bi-stability behavior of the wake behind a square back mockup. This is highlighted in the study of the deflector influence for simplified and industrial models (Bonnavion, 2018). The application of this solution on an Ahmed Body (Figure I. 35a) leads to an optimal design reducing the drag coefficient of 16% with a roof deflector inclined at  $7.5^\circ$  and a bottom deflector inclined at  $5^\circ$ . In the same study, the application of the boat-tailing technique on a full scale Peugeot Partner (Figure I. 35b) reveals a 6% drag reduction.

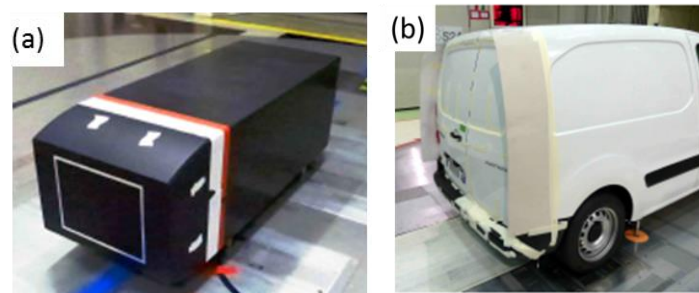


Figure I. 35: (a) Picture of a boat tailing appendices integrated on a reduced scale Ahmed Body, (b) Picture of the lateral deflectors integrated on the full scale Peugeot Partner (Bonnavion, 2018).

The study of the tapered effect of the rear end of a simplified car (Perry et al., 2016) also shows the wake bi-stability damping associated due to a reduction of the coupling between lateral vortices. flaps (Beaudoin and Aider, 2008)

In addition, in the analysis of turbulent 3D wake of road vehicles of (Grandemange, 2013) the drastic influence of the roof spoiler on the wake topology is demonstrated on a full scale Citroën C4 mockup. For this type of rounded rear shape, no roof spoiler leads to a wake flow topology (Figure I.36a and b) characterized by a short recirculation and with two strong counter-rotating vortices. This results in poor aerodynamical performance. The integration of the roof spoiler allows a development of the recirculation area associated to a weakening of the counter-rotating vortices (Figure I.36b and c).

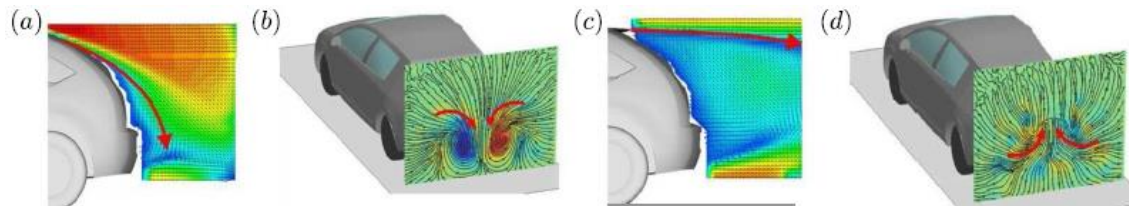


Figure I.36: Wake topologies past a Citroën C4 (a,b) without spoiler and (c, d) with roof spoiler (Grandemange, 2013).

This shape optimization is nowadays integrated on almost all passenger cars but this proves the sensitivity of the wake flow to separation control techniques.

- Porous media

Other techniques are proposed to optimize the wake flow based on the alteration of the boundary layer characteristics around the body panel. Among them, there is the solution of porous media relying on the theory that the weakening of the turbulent energy in the boundary layer through a diffusive region reduces the aerodynamic loss in the wake. It is investigated in (Bruneau et al., 2014, 2010) on a square back Ahmed body with 2D DNS computation at a Reynolds number of 8500. Two controlled configurations were tested: one with a porous slice on the roof of the mockup (Figure I.37a) and another one with an additional porous layer on the bottom (Figure I.37b).

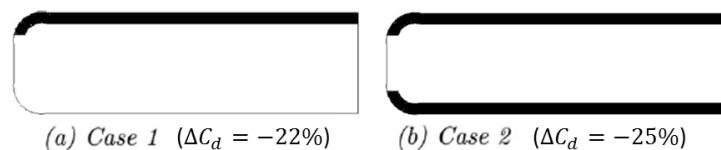


Figure I.37: Two configurations of porous media control integrated on a square back Ahmed Body from (Bruneau et al., 2010b).

These studies confirm the benefit of this type of strategies displaying 25% drag reduction in the configuration b. So far, the porous media technique was mainly tested for mirror aerodynamical optimization (Mimeau et al., 2017). These results also underline the importance of the turbulent intensity of the boundary layer around the body panels in the wake aerodynamic loss.

- Vortex generators

The vortex generators are another technique used to modify the boundary layer. They are based on the forcing of the flow separation at a predefined position. Several studies of vortex generators over a flat plate describe the mechanism involved in this control solution. (Brunet

et al., 2006) exhibits the generation of longitudinal transient vortices adding momentum in the boundary layer close to the wall. Time averaged PIV measurements achieved by (Duriez, 2009; Duriez et al., 2008) bring out the alteration of the boundary layer profile close to the wall. It can be assimilated to a “comb effect” weakening the boundary layer stress. This control solution was also tested on a modified Ahmed Body (Figure I.38a) with a rounded rear (Aider et al., 2010). The detachment is forced and the separation line is shifted upstream (black solid line in Figure I.38b). The controlled wake recirculation is larger than in the baseline case and the low pressure region acting on the rear end surface is significantly reduced (Figure I.38c).

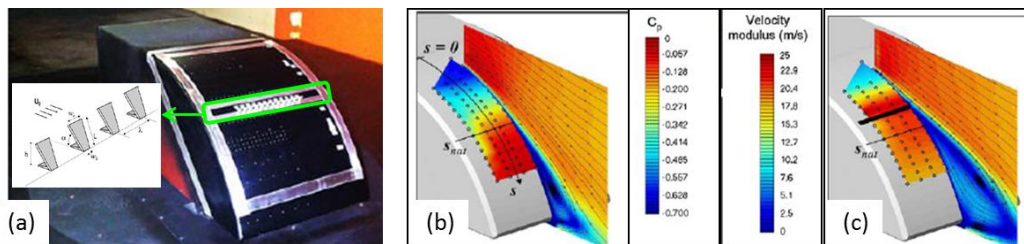


Figure I.38: Vortex generator used on a round rear end Ahmed Body: (a) Picture of the device mounted on the mockup, (b) Baseline flow with a short recirculation bubble close to the rear end; (c) Controlled flow with a larger recirculation bubble and vortex center shifted away from the rear end.

The efficiency of the vortex generators was also proven on a full scale C4 car (Figure I.39a) by (Aider et al., 2014). As show in Figure I.39b, the flow past a rounded rear shape without spoiler remains attached on the rear window and the recirculation area affecting the rear end is drastically short. The wake flow with the vortex generators (Figure I.39c) is fully detached similarly to the wake topology observed on hatchback vehicles. The recirculation area becomes larger, which yields to 14% drag reduction.

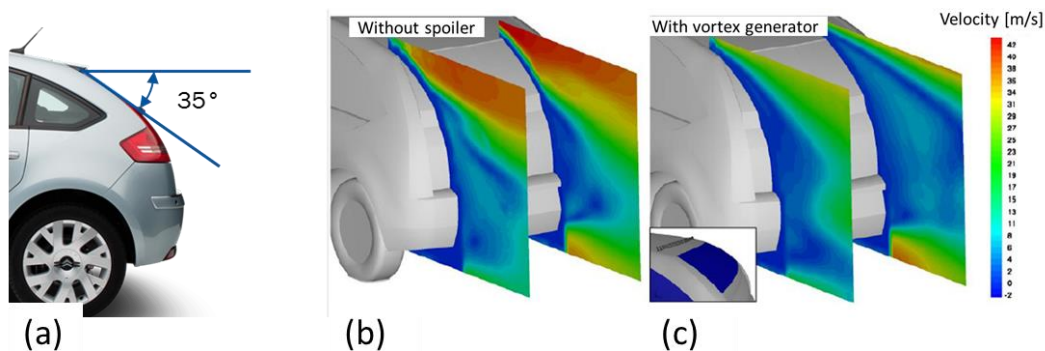


Figure I.39: (a) Picture of a full scale PSA C4 characterized with a  $35^\circ$  rear window; (b) PIV measurements of the baseline flow; (c) PIV measurements of the controlled flow with vortex generator from (Aider et al., 2014).

### 1.3.1.2 Active flow control solutions

- Plasma actuators

Dielectric Barrier Discharge (DBD) plasma actuators is another control device consisting to create a ionized gas call plasma, tending to feed the local quantity momentum of the passing flow used by (Boucinha et al., 2010; Khalighi et al., 2016). Recently, (Shadmani et al., 2018) shown 7% drag reduction on a  $25^\circ$  slant angle Ahmed Body. The actuation maintains the flow over the rear window attached and reduced the recirculation bubble (Figure I.40).



Figure I.40: Pattern of the flow passing through the 25° Ahmed Body behind the model at 10m/s: (a) Baseline wake flow; (b) Steady plasma actuation leading to a drag reduction of 7.3%; (c) Unsteady plasma actuation leading to a drag reduction of 4.88% (Shadmani et al., 2018).

The integration of steady blowing plasma actuators on the A-pillar of a front truck cabin (Figure I.41) shows the feasibility of this solution on a realistic mockup (Vernet et al., 2018) and a potential of 20% gain is measured with lateral blowing wind condition.



Figure I.41: (a) Picture of the reduced scale truck mockup with the unactive DBD actuators, (b) Focus on the A-pillar with the active DBD actuators.

- Steady blowing jets

(Wassen et al., 2010) investigates numerically the efficiency of steady blowing jets with discontinuous slots on a square back Ahmed Body. Thanks to LES simulation, a comparative study of uncontrolled and controlled flow yields 11 % drags reduction. 3% drag reduction was also observed with numerical simulation of square back Ahmed body in (McNally et al., 2015) with steady blowing micro-jets. The interaction between the jet momentum and the shear layer was highlighted (Figure I.42).

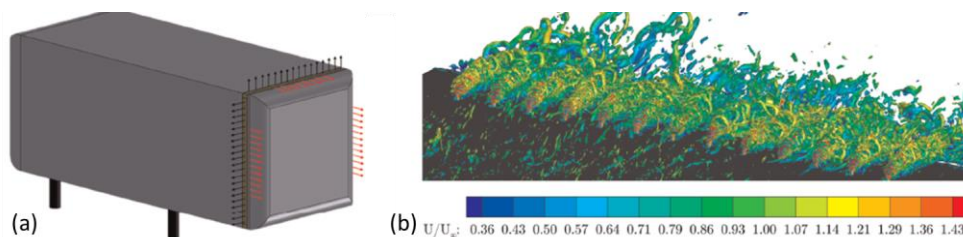


Figure I.42: (a) 3D view of the blowing jets integrated on the square back Ahmed body; (b) Interaction of micro-jet quantity momentum with the shear layer observed with iso-Qcriterion.

Experimentally, steady micro-jets were tested by (Aubrun et al., 2011) at the roof-slant edge of a 25° Ahmed Body. 9 to 14/% drag reduction were measured at different Reynolds number. PIV measurements in the transverse vertical plane  $Y_0$  show the topology change. The active flow control induced a growth of the recirculation bubble acting on the rear end and the vortices centers were shifted away from the rear base (Figure I.43).

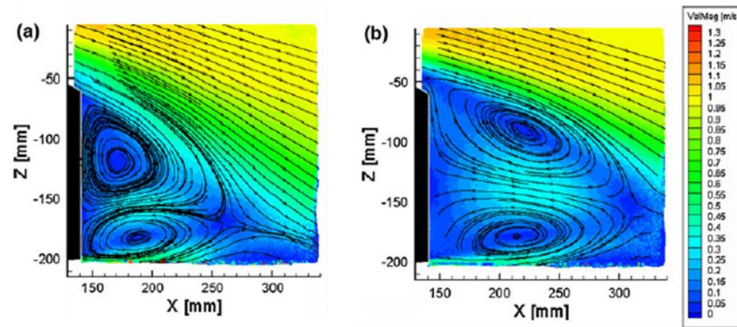


Figure I.43: PIV measurements of the (a) baseline and (b) controlled flow behind a 25° Ahmed Body in (Aubrun et al., 2011).

- Fluidic oscillator

Other researches such as (Arwatz et al., 2008; von Gosen et al., 2015), propose to take benefit of the fluid flow instability in a mixing chamber to generate a sweeping jet (Figure I.44).

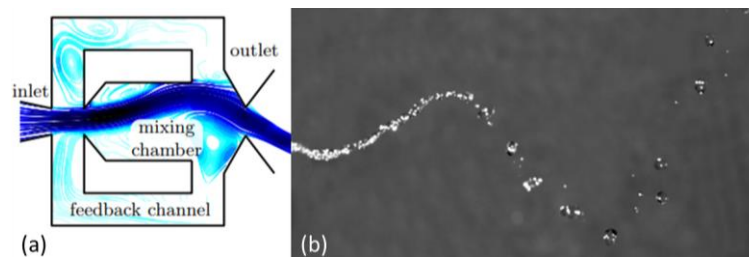


Figure I.44: The flow in a fluidic oscillator: (a) with air; (b) with water (von Gosen et al., 2015).

7.5% drag reduction on the 25° Ahmed Body were measured with fluidic oscillators at the roof-slant edge by (Metka and Gregory, 2015). This actuator yields 5% power saving ensuring the viability of the system. In this study, the effect of the fluidic oscillator actuators is described as a sweeping mechanism mixed with the outer boundary layer. This enhances the convection above the slant window and the controlled flow remains fully attached (Figure I. 45).

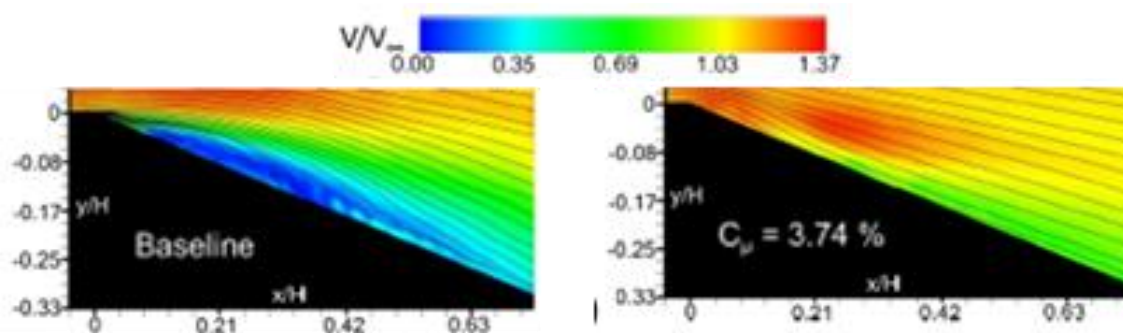


Figure I. 45: Comparison of baseline and controlled flow measured in the PIV transverse vertical cut-plane Y0 by (Metka and Gregory, 2015).

- Synthetic jets

Synthetic jet is an active flow control solution based on a sinusoidal variation of the quantity momentum with an alternate blowing/suction phase. A description of the vortices injected by the synthetic jets is performed by (Leclerc, 2008) on a  $25^\circ$  slant angle Ahmed Body. PIV measurements highlighted counter-rotating vortices (Figure I.46) spreading into the fluid flow. 8% drag reduction is reached with this control.

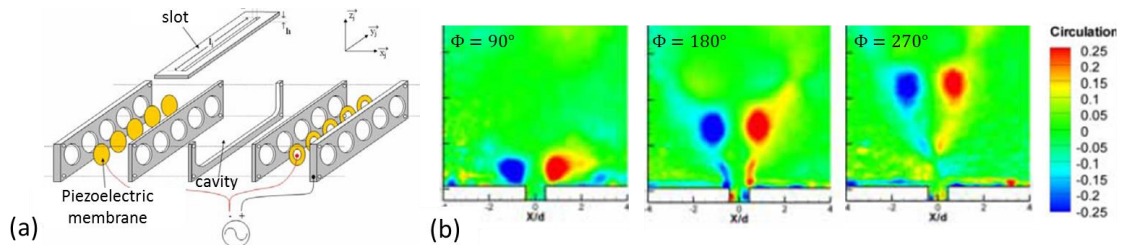


Figure I.46: (a) Synthetic jet system; (b) PIV snapshots close to the synthetic jets at the maximum blowing phase ( $\Phi = 90^\circ$ ), the zeros blowing phase ( $\Phi = 0^\circ$ ) and at the maximum suction phase ( $\Phi = 270^\circ$ ) measured by (Leclerc, 2008b).

Similar behavior is described by (Eulalie, 2014) on a square back Ahmed body. In this case, the sinusoidal pulse combined with discontinuous slots generates 3D torus structures transported into the wake flow (Figure I.47c). These small structures tend to prevent the development of the shear layer into large structures responsible for the aerodynamic loss as shown in the comparison of the baseline iso-Qcriterion snapshots versus the controlled snapshots (Figure I.47a and b).

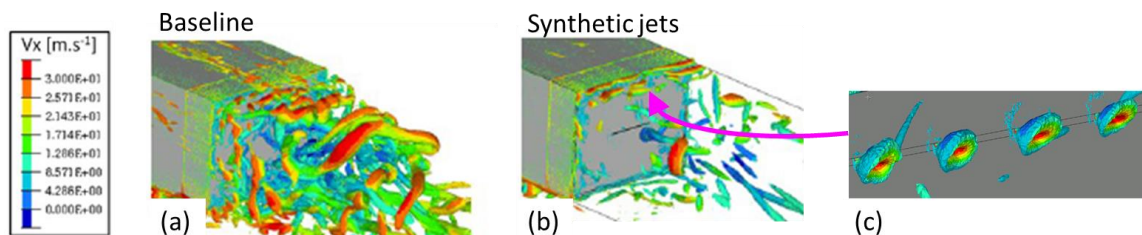


Figure I.47: iso-contour of Qcriterion for (a) baseline flow; (b) Controlled flow; (c) Vortex rings blown on the top edge of the square back Ahmed Body (Eulalie, 2014b).

This technique was also used to control the boundary layer detachment on the A-pillar of a full-scale front truck cabin (Figure I.48a) by (Minelli et al., 2018). The experimental PIV results evidence the control efficiency to damp the transient turbulent structures (Figure I.48b and c). The time averaged field displays a partially detached lateral flow with the control configuration contrary to the fully detached lateral flow in the baseline configuration. The recirculation area developing on the rear end is significantly reduced.

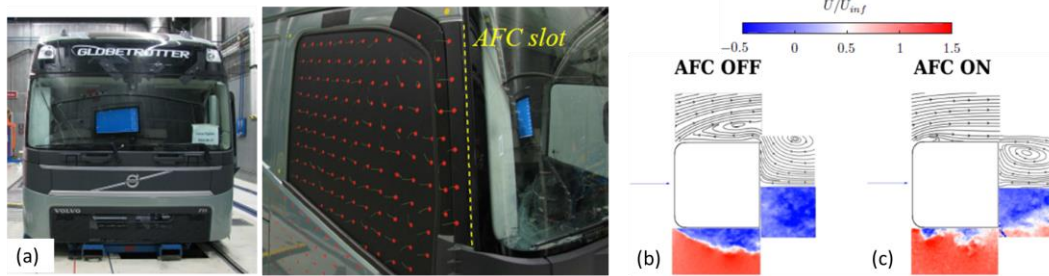


Figure I.48: (a) Pictures of Volvo front Truck cabin; Time averaged streamlines and transient snapshot of velocity field of PIV measurements: (b) Baseline, (c) Synthetic control at the shear layer frequency (Minelli et al., 2018).

(Minelli et al., 2018) also performed a numerical investigation of the reduced scale front truck cabin. 3D Partially Average Navier-Stokes simulations (PANS) were in accordance with the experimental observations. For the baseline flow, 2D structures emerging from the boundary layer detachment expands into large scale structures (Figure I.49a). The resulting turbulent energy prevents the reattachment of the boundary layer. For the controlled configuration, the blown quantity momentum forces the decay of the 2D structures, allowing the reattachment of the boundary layer (Figure I.49b).

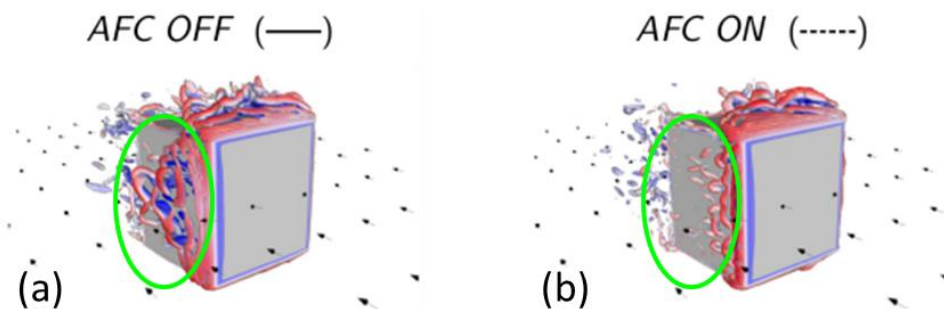


Figure I.49: Comparison of iso-contour of second invariant of the velocity for : (a) Baseline flow around a the Volvo Truck cabin; (b) with synthetic jets on the A-pillar of the Front cabin (Minelli et al., 2018).

- Pulsed jets

Pulsed jets are efficient actuators to control the wake flow shedding. Periodical forcing was explored in the work of (Barros et al., 2016) with continuous slot along the top edge of the square back Ahmed Body. The flow appears to be extremely sensitive to the frequency setup. Actuation around the natural flow frequency tends to increase the aerodynamic loss while high frequency actuation ( $St=12$ ) promotes the pairing, merging and convection of the blown structures. The enhancement of the shear layer momentum increases the recirculation length leading to 10% drag reduction.

Discontinuous pulsed jets with different flow rates and frequencies were tested on the  $35^\circ$  Ahmed Body by (Bideaux et al., 2011; Gilliéron and Kourta, 2013). A maximum drag reduction of 20% was obtained in the configuration of low flow rate and high frequency of 500Hz (Figure I.50).

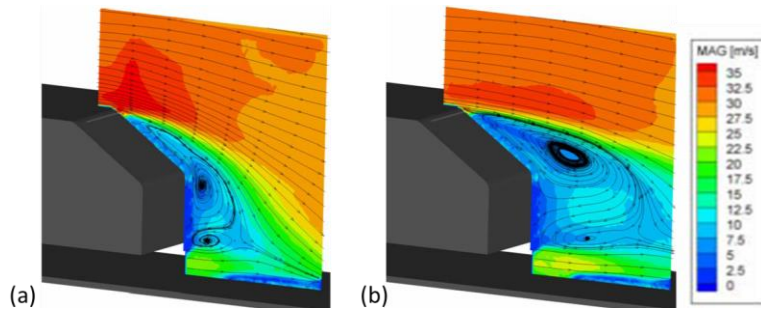


Figure I.50: Comparison of the (a) baseline and (b) controlled flow at 500Hz behind a 35° Ahmed Body from (Bideaux et al., 2011).

Influence of discontinuous pulsed jets on a full scale C6 mockup (Aider et al., 2014) was demonstrated at high frequency ( $St=2.91$ ). An increase of the pressure coefficients are measured (Figure I.51). Even if the drag reduction was not consistent, 9% reduction of the lift component proves the aerodynamic impact of this control solution.

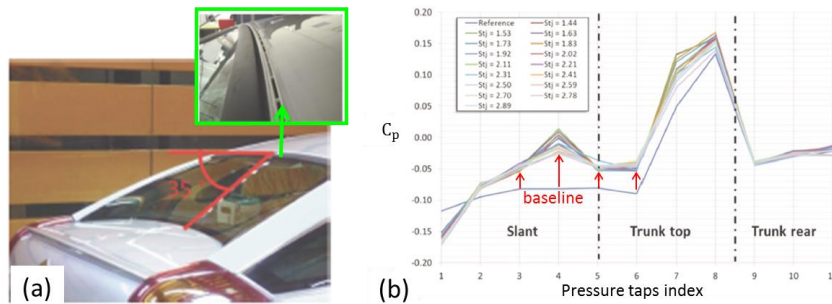


Figure I.51: (a) Pulsed jet actuators integrated on a full scale C6 car; (b) Pressure coefficient profiles measured over the rear end (Aider et al., 2014).

- Discussion

In this section, a large variety of control solutions was explored. The main conclusion of the examination of the control solutions is the importance of the actuation frequency for the modification of the wake stability. Two operating modes are observed at low and high frequency. It is highlighted thanks to the flow visualizations of the controlled mixing layer performed by (Parezanovic et al., 2014). If the low frequency jet actuation tends to promote the generation of large scale structures (Figure I.52b) compared to the unactuated flow (Figure I.52a), the high frequency periodic jet tends to smooth these turbulent structures and prevent the generation of wake vortex shedding (Figure I.52c).

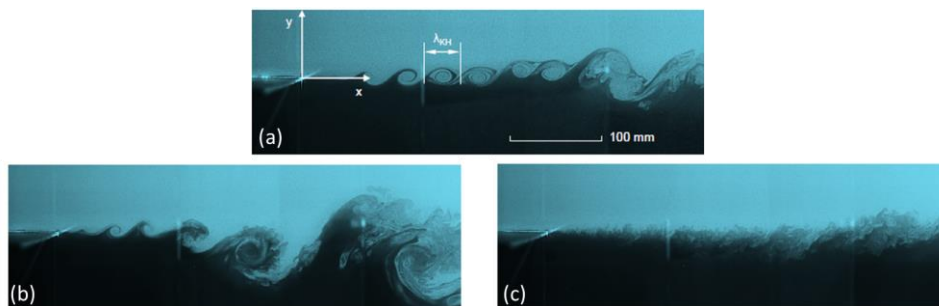


Figure I.52: Smoke laser visualization of the mixing layer after a splitter plate: (a) Baseline flow; (b) 10Hz low frequency control configuration; (c) 400Hz high frequency control configuration from (Parezanovic et al., 2014).

Research studies tend to promote the efficiency of the control of the shear layer for automotive applications. It is interesting to notice how several high frequency control solutions such as, synthetic, pulsed blowing or oscillating jets, tends toward similar effects on the shear layer. However, some solutions seem more suitable for the automotive benchmark. In this work, the pulsed jet actuators are selected because of its demonstrated capabilities on full-scale realistic car.

More generally, the interest of active flow control relies on the fact that it is a useful tool to improve our knowledge of the flow sensitivity to the boundary conditions. On one hand, this sensitivity can be done by the mean of quantity momentum injection (with jet). On another hand, similar effects can be achieved using passive solutions once the knowledge of the sources of aerodynamic loss is assimilated. At this stage, mathematical algorithms are of major interest to determine the optimal setup of the active flow control solution.

### 1.3.2 Closed-loop and automatic control/optimization methods

Multiple solutions exist for aerodynamic optimization for automotive applications. On a first hand, closed-loop flow control strategies based on the coupling of sensors/actuators are implemented to optimize active control solutions. It is particularly suitable for experimental applications, as it often requires a long period of acquisition. These strategies are even more appealing since they can be embedded in production vehicles. On the other hand, optimization algorithms based on sensitivity computations are particularly interesting for the definition of an optimal passive solution to reduce the aerodynamic loss during the early design stage.

#### 1.3.2.1 Strategies for active flow control

For active flow control solutions, optimization strategy would be focus on closed loop control between sensors and actuators. Figure I. 53 illustrates the block diagram with automation system terminology defining the feedback coupling between the sensors (denotes by the measurement signal  $y_m$ ) and the actuators (denotes by the control signal  $u$ ) for the control of a system (denotes by “plant”).

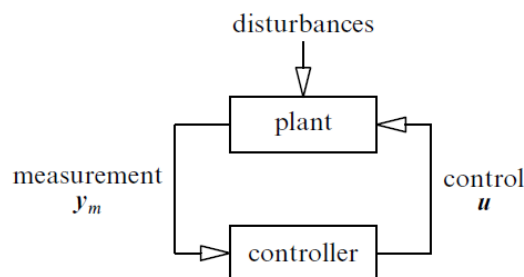


Figure I. 53: Block diagram of a closed-loop control system using automation terminology (Bewley and Liu, 1998).

The optimal control algorithms can be achieved with closed loop control with reactive or real time algorithms. Reactive algorithms are based on time averaged cost function evaluation and can be subdivided in two main techniques: extremum seeking and genetic algorithms using time averaged cost function.

Real time control algorithms based on transient cost-function evaluation, are also subdivided in two categories. Model based approaches gathered the methods requiring a preliminary knowledge of the sensors and actuators behavior. They are presumably more difficult to dimension but they are interesting as they efficiently adapt to physical flow dynamic. Among these techniques, there are for automotive applications, Linear Quadratic Regulation

(Bergmann, 2004a), time resolved sensitivities or Reduced Order Model (Barbagallo et al., 2009; Bergmann and Cordier, 2008; Proctor et al., 2014a). Model-free real time approaches are self-updating algorithms fitting the actuators/sensors behavior without any preliminary assumptions on the flow dynamic. Among them, there are opposition control ((Bruneau et al., 2010; Chovet, 2018; Varon, 2017)), and Machine Learning Control (Li, 2017a; Li et al., 2017b).

- Feedback, opposition or tracking techniques

These techniques consist in the definition of a dynamically updating actuation controller based on the flow state identification using flow sensors measurements. The most straightforward law is the opposition control linking the actuation parameters to the sensors signals with an analytic functional. The efficiency of this control to reduce the rear end pressure of a square back Ahmed Body using blowing jet (Bruneau et al., 2010) was validated at low Reynolds number with 31% drag reduction. However, it is difficult to implement for higher Reynolds number flow since the turbulence unsteadiness and chaotic behavior complicate the identification of the flow state based on few local sensors.

Extremum seeking or slope seeking algorithms are more suitable to identify the state of a complex dynamic system. They consist in a dynamic feedback controller coupled with a model identification of the steady state flow (Figure I.54). The integration of the slope seeking algorithm to control a mixing layer (Parezanovic et al., 2014) or the shear layers of the D-shaped bluff body (Pastoor et al., 2008), shows how the mapping of the system response to actuation periodic forcing converged toward an optimal solution. A gain up to 40% of rear end pressure has achieved on the D-shape mockup. This technique may result in a local minimization but a wide range of actuation parameters has to be tested to ensure the convergence toward a global minimum.

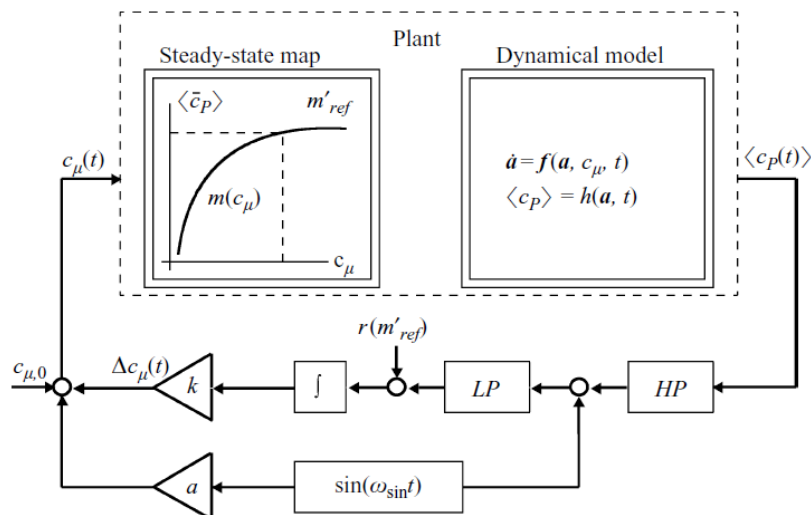


Figure I.54: Block diagram of the slope seeking algorithm using high-pass and low-pass filters for the identification of the dynamic model (Pastoor et al., 2008). The arrow on the left indicates the feedback between the sensor  $\langle C_p \rangle$  toward the controller blocks and the arrow on the right indicates the input control signal  $C_\mu$  used to the physical system.

There are also several solutions based on the tracking of vortex dynamics in the wake flow. Observers theory and Kalman filters algorithms were applied for the phase control of the vortex shedding (Pastoor et al., 2008; Tadmor, 2004). This type of control algorithm is particularly appropriate for the synchronization of the actuator on a unique characteristic frequency measured in the wake flow. However, a long convergence step is required to

stabilize the controller on the wake motion. Similarly, the implementation of dynamic observers to control the chaotic bi-stable behavior of the wake flow behind a square back Ahmed body (Varon, 2017) was tested using time resolved PIV measurements for a feedback on the transient wake state. The algorithm is presented in Figure I.55a. The observer is defined as the wake recirculation velocity barycenter. Three rows of discontinuous slots were integrated on the roof edge. The flow rate magnitude of the 3 pulsed blowing signals at  $St=0.2$  were spatially modulated as a function of the wake barycenter coordinate. The objective was to activate the actuation on the side of the pressure loss. Figure I.55b shows the comparison of the statistical analysis of the baseline rear end pressure compared to the control configuration. The pressure barycenter impacting the rear end is more widely distributed over the rear surface in the controlled flow. In addition, the controlled transient wake also exhibits a periodic oscillation dynamics contrary to the chaotic span wise motion observed in the baseline flow.

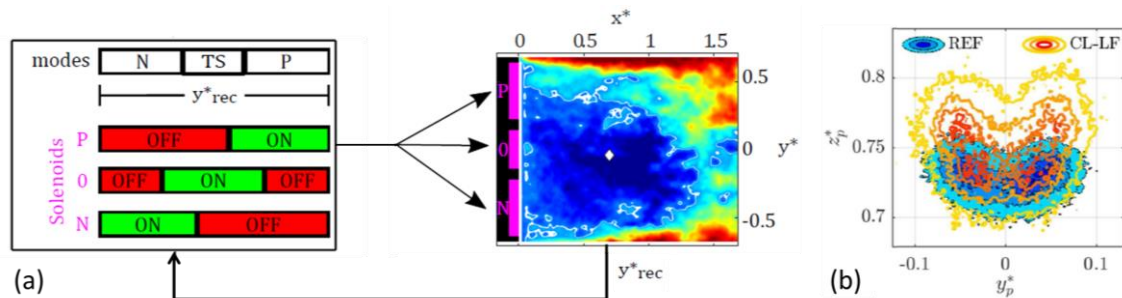


Figure I.55: (a) Sketch of the opposition closed-loop control law based on the detection of the horizontal position of the recirculation barycenter (white diamond) integrated from the transient wake PIV measurement; (b) 2D Power Density Function of the rear end pressure barycenter: the blue distribution corresponds to the baseline mapping, the yellow contour corresponds to the closed-loop control of the pulsed jet magnitude ( $St=0.2$ ) (Varon, 2017).

The vortex shedding is efficiently controlled but this technique requires a wake flow observer, which may be hard to obtain for a road vehicle.

Sliding mode control (Chovet, 2018) is a closed loop strategy for the phase and frequency optimization. It was tested on a square back Ahmed Body leading a pulsed Coanda jet located on the top of the mockup.

- Machine learning techniques

Machine learning is the mathematical domain derived from the computer logical system science. It gathers algorithms used to boost the performances of a system based on a progressive study of the benchmark capabilities. The most used machine learning models are the neural network, Bayesian network or support vector machine but in automotive applications, the genetic algorithm is the most recurrent solution. The control of the wake flow behind a square back Ahmed Body, based on the Learning Genetic Programming Control (Li, 2017b; Li et al., 2017a) was tested using rear end pressure cost function and pulsed blowing Coanda jet actuators. Figure I.56a illustrates the LGPC algorithm with a dual closed-loop system. A real time feedback is used for the dynamic update of the actuators parameters depending on the transient sensors measurements. Simultaneously, a phase averaged learning loop is integrated to design the optimal control law (denoted by K) between actuators/sensors. Figure I.56b summarizes learning process allowing the design of an optimal control law. The result of this flow control strategy leads to 33% base pressure recovery and 22% drag reduction.

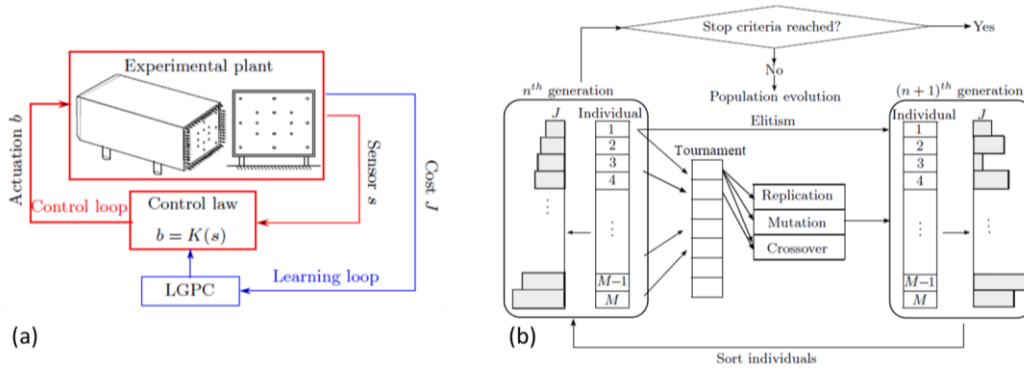


Figure I.56: Linear Genetic Programming Control (LGPC) algorithm: (a) closed loop control with a real time feedback combined with a phase averaged learning loop. (b) Genetic algorithm learning process (Li et al., 2017a).

The genetic programming control is a powerful optimization tool for the identification of the best operating point contained in a large Design of Experiment, in an unsupervised manner.

### 1.3.2.2 Shape optimization with sensitivities

For shape optimization, the research of an optimal point in a large Design of Experiments (DOE) is challenging in the case of highly turbulent detached flow. Gradient based algorithms with sensitivities are computed in order to converge toward an efficient operating point. This is performed thanks to adjoint method (El Shrif, 2008; Karpouzas et al., 2016, 2016; Kavvadias et al., n.d.; Zaya, 2013) or discrete differentiation.

In this approach, the optimization problem consists in the definition of an optimal boundary condition minimizing the cost function computed with the drag force or the pressure loss as formulated. The objective is to find the state variable  $(\vec{u}, p)$  and the control parameter  $A$  minimizing the cost function  $J(p)$  constraint to the state-space equation  $F(\vec{u}, p, A)$ . The Lagrange Multiplier is a suitable method to reduce the optimization problem with constraint into an optimization problem without constraint only based on the Lagrange functional. The idea is to associate to each constraint equation, an adjoint variable of same dimension. The equation system is reduced to a unique, one component, equation gathering the contribution of the cost function plus the state-space equations

$$\mathcal{L}(\vec{u}, p, A, \vec{u}^*, p^*, \xi^*) = J(p) - \langle (\vec{u}^*, p^*, \vec{\xi}_j^*, \vec{\xi}_c^*, \vec{\xi}_{in}^*, \vec{\xi}_w^*, \xi_{out}^*); F(\vec{u}, p, A) \rangle \quad \text{Eq.13}$$

Where:

$p$  is the pressure

$\Gamma_B$  is the surface where the cost function is integrated.

$J = \int_{\Gamma_B} \frac{p^2}{2} d\Gamma$  is the cost function

The optimal set of parameters  $(\vec{u}, p, A, \vec{u}^*, p^*, \xi^*)$  is obtained by computation of the Frechet derivative of  $\mathcal{L}$ . This strategy can be performed thanks to numerical simulations with steady state cost function to help freezing the optimal design of realistic cars on specific range of Reynolds number. This numerical optimization method could be an alternative to move backward the detachments around the car responsible for the aerodynamic loss propagating in the wake. Figure I.57 shows the sensitivity map computed on the RANS numerical solution compared to the sensitivity computed with the time averaged results of a DES computation.

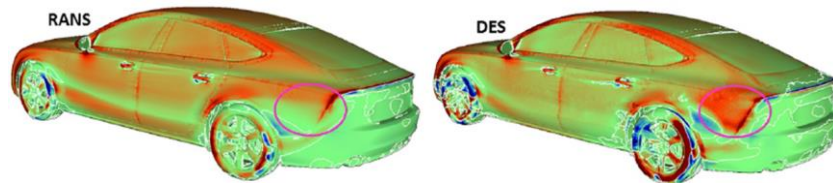


Figure I.57: Comparison of RANS and DES sensitivities to compute the optimal morphing of lateral tapering of the rear end on the Audi A7.

For transient state-space equations, the solution of the optimization problem has to satisfy the zero variational condition at any time, increasing drastically the complexity of the problem. An algorithm with backward time integration is proposed in (Bergmann, 2004b). The requirements for the resolution of this optimization on highly turbulent and unsteady flow appear to be unreachable knowing that there is an additional 4 component adjoint equations system. Reduced Order Model provides an alternative to the Navier-stokes equations allowing an easier way to compute the flow sensitivity (Bergmann and Cordier, 2008) but this requires a preliminary model construction.

It should be mentioned that adjoint solver can also be extended for active flow control optimization. Figure I.58 shows the sensitivity map used to evaluate the optimal jet actuation location leading to the best drag reduction.

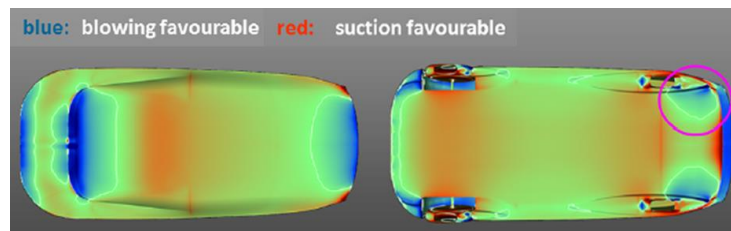


Figure I.58: Drag force sensitivities to active flow control blowing symmetrically in the region of the pink circle.

- Discussion

In this section, we reviewed a preselection of existing closed loop control and optimization techniques which show interesting potential to reduce aerodynamic loss in the field of ground transportation. These techniques can be classified according to several criteria (Figure I.59) such as the modeling effort, the time scale definition and the domain of application (CFD or experiment). Model-free solutions seem attractive for highly turbulent flows since they update automatically to any environment variation and required less mathematical assumptions on the physical flow behavior. They seem particularly suitable for experimental applications because of the long convergence time generally required. The model-based methods allow the reduction of this convergence duration using predictive law to describe the flow behavior but they are particularly difficult to implement on highly turbulent flow around complex geometries. We can conclude on the benefit of learning methods, such as genetic algorithm, allowing the improvement of the flow description while the algorithm run.

One can also question the choice of real-time algorithms compared to adaptive ones. In the case of real-time algorithm, high frequency update of the control parameters depending on instantaneous measurements seems to be promising since the system is continuously constraint to remain in its optimized topology (such as tracking using dynamic observers). It is often considered as a pertinent choice for energy saving considerations with active flow control. However, these schemes also bring difficulties dealing with consistency or stability

considerations. A brief exploration of real-time control is presented and discussed in the following work in section 2.1.3.

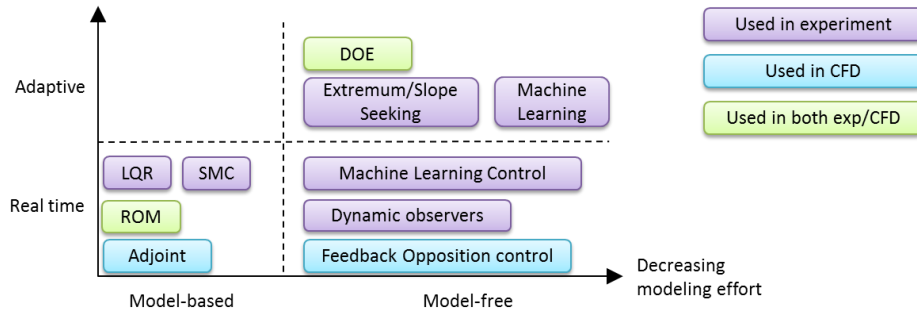


Figure I.59: Classification optimization methods as a function of model requirements and of the time scale consideration. The purple, blue and green colored boxes refer respectively to method used in experiment, CFD or both.

Finally, model-free adaptive algorithms appear to be turnkey solutions deployable for highly turbulent flows for such a complex benchmark. This explains the selection of genetic algorithm applied for experimental optimization of the aerodynamics of the generic SUV.

## 1.4. Modal decompositions

According to the previous sections of this review, different reasons lead to the development of a dynamic model. It may help to identify periodic phenomena underlying in statistical flow description and also to construct a Reduced Order Model. This model should enable our understanding of the energy transfer. In addition, this model should allow the optimization computation based on the experimental database. It must result in an identification of periodicity and coherence information in the flow. In this perspective, the Dynamic Modal Decomposition with Control (DMDc) is a good candidate for the development of a dynamic model.

Indeed, this algorithm quantifies the energy transfer between actuation and sensors. It requires a preliminary orthogonal Singular Value Decomposition (SVD) for spatial coherent structures identification. This decomposition enable to evaluate the energy per mode associated to the flow dynamic.

### 1.4.1 Orthogonal Decompositions

Introduced for the first time in (Lumley, 1981, 1967), Proper Orthogonal Decomposition is a method used to identify correlated coherent structures in turbulent flow. Different approaches are available depending on the initial database characteristics. The algorithm is extensively described in (Cordier and Bergmann, 2008; Tissot, 2018). It relies on the construction of a transient database  $[P_1 \dots P_m]$  constituted of  $m$  snapshots with  $n$  measurement points (Figure I.60). The analyzed database  $\Psi$  is a concatenation of fluctuating part defined in (Eq.14).

$$\Psi = [P'_1 \dots P'_m] \tag{Eq.14}$$

Where :

$$P'_i(\vec{x}) = P_i(\vec{x}) - \bar{P}(\vec{x}) \text{ is the fluctuating part of } i^{th} \text{ snapshot}$$

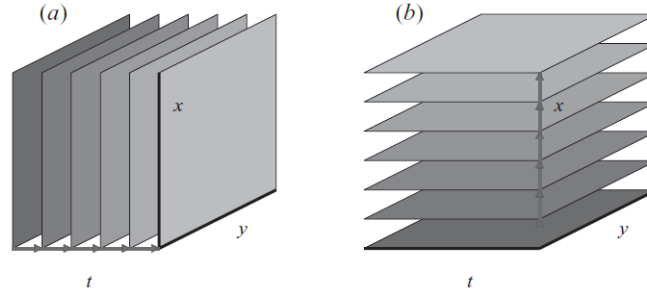


Figure I.60: Sketch of the snapshot sequence for a (a) temporal (b) spatial modal analysis (Schmid, 2012).

There are two methods leading to the orthogonal decomposition of the flow. The classical POD method is based on eigenvalues and eigenvectors decomposition of the spatial correlation matrices computed as shown in Eq.15a.

$$R^x = \Psi\Psi^* \quad (a) \qquad R^t = \Psi^*\Psi \quad (b) \qquad \text{Eq.15}$$

Where

$\Psi = [P'_1 \dots P'_m]$  the database containing the fluctuating data.

The modes  $\Phi$  are obtained by projection of the eigenvectors on the initial database  $\Psi$ . As the POD modes form an orthogonal base of the database, the temporal contribution  $\zeta_k(t)$  of each mode  $\Phi_k$  can be easily evaluated by projection on the database. This approach is suitable for database with higher temporal information than spatial information so that the correlation matrix  $R^x$  of size  $n \times n$  is not too large for limited computers resources.

CFD applications do not reach this criterion because there is much more spatial information due to mesh discretization than temporal information. The suitable approach for CFD database is the snapshots methods, introduced by (Sirovich, 1987). It consists in the Eigen decomposition of temporal correlation matrix  $R^t$  defined in Eq.15b.

In classical POD, the  $i^{th}$  column of  $R^x$  gives an estimation of the dependence of coherent structures measured in points  $\vec{x}_i$  with all other turbulent coherent structures of the fluid flow. Thus it is a spatial statistical analysis. In the snapshots POD, the  $i^{th}$  column of  $R^t$  gives the dependence of all coherent structures observed in the snapshot of the  $i^{th}$  iteration with coherent structures observed in all other snapshots as displayed in Figure I.60. The modes are obtained by projection on the database  $\Psi$  and associated transient evolution of modes  $k$  is computed.

Proper Orthogonal Decomposition is particularly relevant to highlight coherent structures in turbulent flows. It has the advantage to isolate in few modes main contributions in turbulent flows and it is a pure statistic tools without any physical assumption. The reconstructed field can be reassemble as Eq.16

$$\Psi^{rec} = T\Phi = \sum_{k=1}^m a_k(t)\Phi_k \qquad \text{Eq.16}$$

- Applications and interests

Several studies use POD analysis to highlight the coherence existing in the wake and the flow modification induced by the control.

In the test case of the square back Ahmed Body, the POD is used to highlight the bi-stability sensitivity to the taper shape optimization (Perry et al., 2016). (Varon et al., 2017a) also investigates the influence of two closed-loop control strategies on the first POD modes of the rear end pressure compared to the baseline decomposition. Figure I.61 shows the three dominant orthogonal modes obtained in the case of the baseline flow, low frequency closed loop control (denotes by CL-CONT) and high frequency closed loop control (denotes by CL-HF). The baseline modes are characterized by the vertical symmetry correlated to horizontal wake flow fluctuations. This analysis reveals how periodic actuation changes the 2<sup>nd</sup> and 3<sup>rd</sup> POD modes. Indeed, low frequency closed-loop control promotes vertical rear end pressure fluctuations while the high frequency control tends to reinforce the horizontal fluctuations. This method is powerful to extract the coherence of the flow and more precisely to identify the main fluctuations direction defining the wake stability. It is used as a Reduced Order Model for gradient based optimization (Bergmann and Cordier, 2008) or as a wave length identification method for the closed loop control of a mixing layer (Parezanovic et al., 2014).

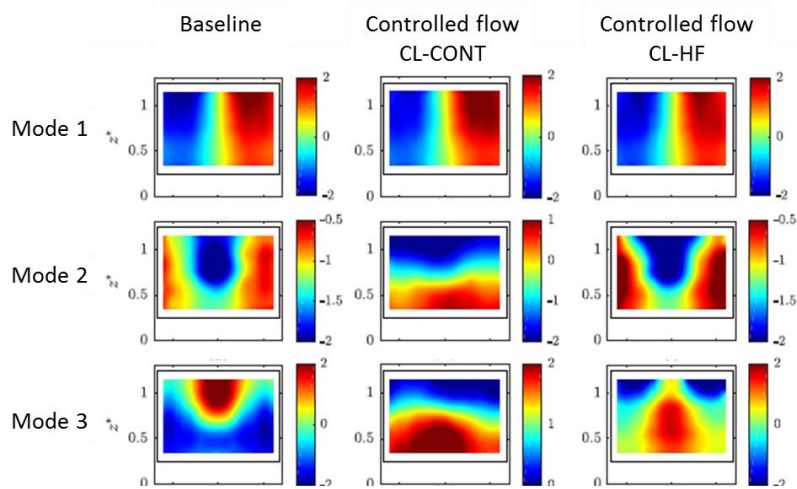


Figure I.61: POD results of pressure measurements on square back Ahmed Body and comparison of the baseline decomposition with the closed loop continuous blowing and with the closed-loop high frequency pulsed jet from (Varon et al., 2017a).

However, with the POD approach, the transient evolution of the modal behavior remains chaotic, which limit the spectral analysis of the flow coherence. Some methods propose to improve the transient flow decomposition based on phase averaging of the temporal projection of the POD (Oberleithner et al., 2011; Sieber et al., 2016). Despite this, POD cannot be use for the real time tracking of isolated periodic vortex shedding since there is no phase discrimination of the flow feature.

## 1.4.2 Dynamic Modal Decomposition

- DMD based on correlation matrix

The Dynamic Modal Decomposition consists in the decomposition of phase synchronized structure in the flow. It has the advantages to associate a unique frequency to each mode plus a growth rate value related to the mode energy behavior. With this approach, exact periodic structures are isolated in modes with growth rate value close to zero, decaying flow features are captured in modes with negative growth rate value and energy producing structures are catch in positive growth rate modes.

The algorithm is based on the assumption of the existence of a linear decomposition of the snapshots. These linear features are estimated thanks to the temporal correlation matrix  $R^t$  of

size  $m \times m$ . For a better understanding, the notation  $R$  will stand for  $R^t$  in the following section. As shown in (Frederich and Luchtenburg, 2018), the flow linearity can be obtained from the linear decomposition of the last column of  $R$  with respect to the  $m - 1$  first column of  $R$ . Then, the companion matrix is constructed. It should be mentioned that the companion matrix verifies Eq.17 and contains the information of delay between snapshots correlation. In addition, the  $m - 1 \times m - 1$  matrix  $C$  is square but not definite positive.

$$R_2^m = R_1^{m-1}C \quad \text{Eq.17}$$

Where

$R_2^m$  is the matrix of the last m-1 columns of  $R$ .

$R_1^{m-1}$  is the matrix of the last m-1 columns of  $R$ .

$C$  is the companion matrix constructed with the linear coefficient  $c_i$  of the last column of  $R$  as a function of the m-1 first column of  $R$ .

But the complex eigenvalues  $\mu$  and complex eigenvectors  $Y$  can be easily obtained as it is a sparse matrix

If this algorithm gives a direct technique to obtain frequency identification, there is also an important sensitivity due to the choice of the last snapshot. Indeed, it enables the propagation of uncertainty and generates noise in modal energy distribution. Consequently, the selection of relevant modes for low order model is problematic.

- DMD based on SVD

The SVD based DMD proposed by (Schmid, 2012) is an enhancement of the original DMD algorithm allowing to estimate the phase shift Eq.18 between each snapshot using a projection in an orthogonal base. This solves the problem of the uncertainties propagation mentioned in the classical algorithm.

$$\Psi_1 = A\Psi_0 \quad \text{Eq.18}$$

Where

$\Psi_0$  is the first bloc of snapshots

$\Psi_1$  is the delayed bloc of snapshots.

$A$  is the phase shift between each snapshots.

The complete algorithm is summarized in Figure I. 62. The preliminary Singular Value Decomposition of  $\Psi_0$  allows an inversion of the matrix  $\Psi_0$  for the evaluation of the phase shift matrix  $A$ . It should be mentioned that the matrix  $U$  obtained with the SVD of  $\Psi_0$  corresponds to the spatial orthogonal base obtained in classical POD (Cordier, 2008). In practice, the Eigen computation is performed on  $\tilde{A}$ , the reduced projection of the matrix  $A$  into the POD matrix  $U$ . The eigenvectors are then projected on the POD for the spatial visualization of the DMD mode  $\Phi$ . The complex eigenvalues contained the periodicity information associated to each mode.

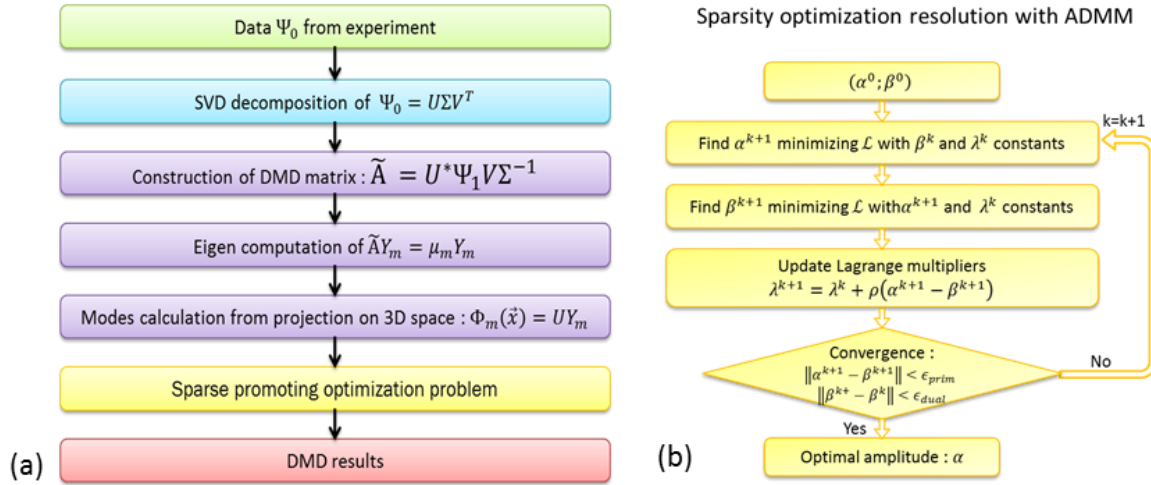


Figure I. 62: Sparsity promoting DMD algorithm from (Jovanović et al., 2014b) source code.

The modal magnitude is evaluated thanks to the resolution of a sparsity optimization problem based on the residual of the reconstructed field (Jovanovic et al., 2010; Jovanović et al., 2014a). The augmented Lagrangian formulation  $\mathcal{L}$  coupling the reconstructed residual with the sparsity constraint (Eq.19) is solved with the Alternating Direction Method of Multiplier (ADMM).

$$\mathcal{L}(\alpha, \beta, \lambda) = \underbrace{J(\alpha)}_{\text{Residual minimization}} + \underbrace{\gamma g(\beta)}_{\text{Sparsity promoting constraint : } g(\beta) = |\beta|} + \underbrace{0.5 \times (\lambda^*(\alpha - \beta) + (\alpha - \beta)^* \lambda + \rho \|\alpha - \beta\|_2^2)}_{\text{Coupling of residual optimization with sparsity promoting problem : } \alpha - \beta = 0} \quad \text{Eq.19}$$

Where

$\alpha$  is the vector of modal magnitude.

$\beta$  is the dual vector used for the application of the sparsity constraint.

$\gamma$  : Weight of the sparsity promoting constraint

$\lambda$  : Vector of Lagrange multipliers

$\rho$  : Quadratic penalty coefficient (for convex problem)

- High Order DMD for experimental applications

The domain dimension in numerical simulation is associated to a large number of probes with small number of snapshots. In experiments, the spatial discretization can be lower than the temporal discretization. A direct application of the SVD based DMD algorithm on experimental database leads to a phase shift matrix constraint by the low number of sensors as shown in Figure I.63a. The resulting DMD modes extracted is restricted by the size of  $A$ , there not enough spectral information to decompose the flow. High Order Dynamic Modal Decomposition proposed by (Le Clainche and Vega, 2017) is an update of the SVD based DMD allowing to increase the order of the phase shift matrix  $A$  for experimental applications. The idea is to extend fictively the database dimension with sliding time windows slice contained in the original database. The matrix length is increased by concatenation along the spatial direction as illustrated on Figure I.63b.

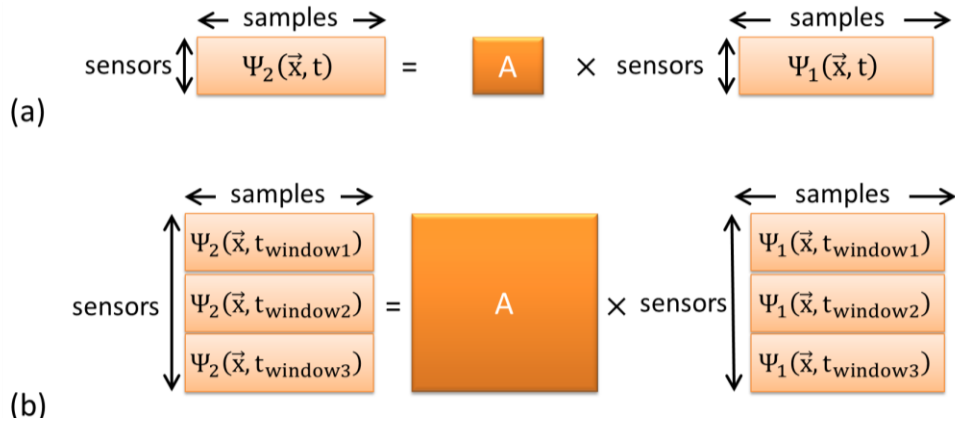


Figure I.63: Illustration of the rank of the phase shift matrix  $A$  in experiments with (a) DMD, (b) High Order DMD.

The parameter  $d$  defined the number of stacked slices used to increase the rank of the database. The consistency of the resulting DMD base when  $d$  is gradually increased, gives the optimal parameter to capture the overall spectral information. The investigation of (Le Clainche and Vega, 2017) shows that depending on the application, the optimal value of  $d$  is between 1 and  $m/3$  (with  $m$  the number of snapshots). It can also be set in order to obtain an extended database close to a square matrix. Even if it is not the optimal parameter, this choice ensures the computation of a maximum range of spectral information.

On this basis, the DMD algorithm is applied replacing the original database  $\Psi$  by the extended database. After the projection of the eigenvectors on the POD base, the DMD modes are obtained using the last  $n$  rows of the extended modes (with  $n$  the number of sensors). This technic shows interesting prospects for experimental applications such as local pressure sensors.

- Applications and interests

The classical DMD is used to identify low frequency periodic behavior on the pressure sensors of the experimental analysis of a full scale BMW mockup (Eulalie et al., 2018b). Pressure fluctuations located on the bottom of the tailgate were correlated to the normalized spectral characteristics at  $St = 0.0036$ ,  $St = 0.006$  and  $St = 0.013$  (Figure I.64). This leads to the extrapolation of a swirling motion of the rear pressure loss. It would have been interesting to enhance these observations with the SVD based and sparsity promoting optimization.

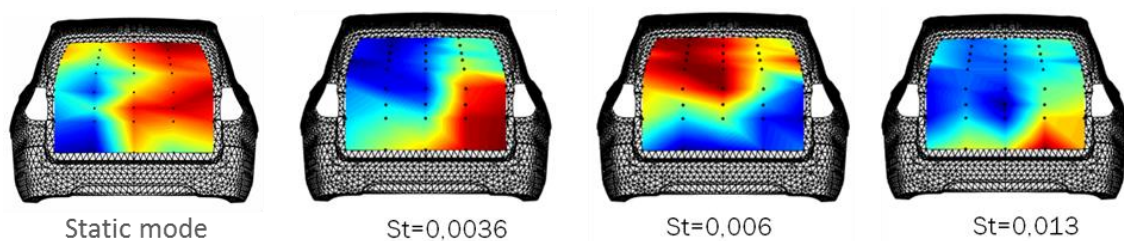


Figure I.64: Results of classical DMD obtained on transient rear end pressure on a full scale BMW X5 mockup (Eulalie et al., 2018).

The SPDMD was applied to characterize the detached flow behind bluff bodies (Parkin et al., 2014; Tu, 2013) and for jets flow analysis (Jovanovic et al., 2010; Jovanović et al., 2014a; Schmid, 2011). Figure I.65 shows the results of the DMD analysis performed on the wake of

a bluff body (Tu et al., 2014). The result successfully exhibits the change of flow topology depending on the actuation frequency.

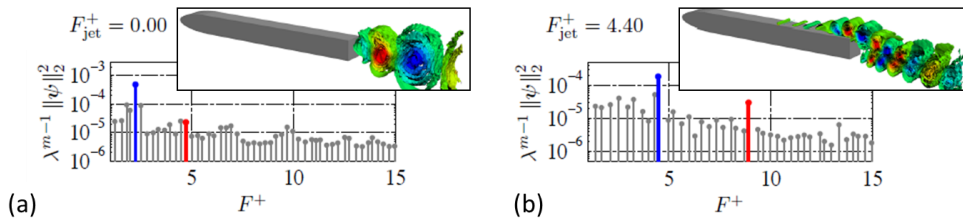


Figure I.65: DMD results obtained on a controlled blunt body wake: (a) DMD spectra on continuous blowing jet with main mode iso-contour; (b) DMD spectra of obtained on best actuation frequency from (Tu, 2013; Tu et al., 2014).

To go further in the evaluation of the actuation efficiency, (Proctor et al., 2014b) proposed the Dynamic Modal Decomposition with control consisting in a concatenation of synchronized sensors and actuators signals. In this extension of the DMD, the snapshots are constructed based on the original database  $X$ , the delayed database  $X'$  and the actuation signals  $Y$  as shown in Figure I.66. This technique is an efficient way to estimate the transfer function between actuators and sensors per modal component.

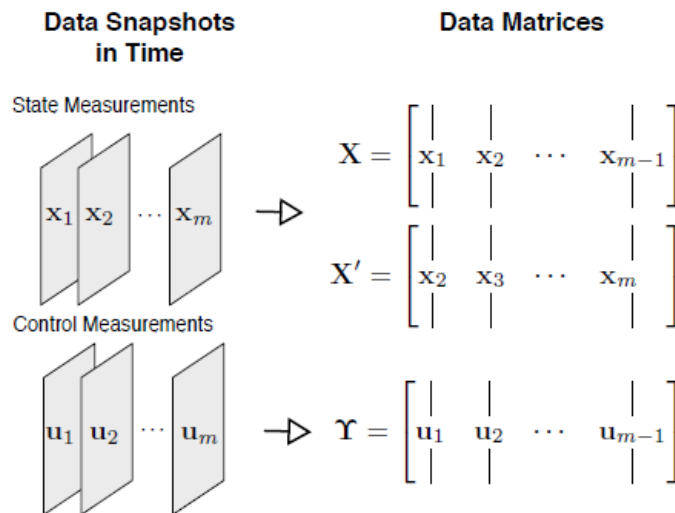


Figure I.66: scheme of periodic decomposition obtained with the DMD with control.

- Discussion

This review provides a comparison of interests and limitations of orthogonal and dynamic decompositions to capture the flow complexity measured in experiments or obtained in CFD. They both give an important description of flow features based on correlation discrimination in POD and spectral isolation in DMD. Even if some methods, such as SPOD, attempt to combine the benefit of the POD and DMD, the result does not allow a proper tracking of the dynamic vortex shedding.

We can conclude on the interest of the SVD-based DMD to apprehend the fluid flow mechanic. The additional application of the sparsity optimization gives an efficient way to reduce the size of the problem. The High Order DMD also provides a practical solution for low space resolution databases. It also gives good prospect to evaluate the flow sensitivity to actuation as it was already demonstrated with active flow control using DMDC algorithm.

To our knowledge, the application of the orthogonal decomposition embedded in the SVD algorithm has never been used to correlate the periodic dynamic features extracted thanks to DMD. In this work, we will try to go deeper in this matter starting from sparsity promoting, SVD based and High Order DMD algorithms.

The modal analysis performed on experimental results gives a realistic description of the flow features limited to the measurement windows. On the opposite, numerical simulations provide an exhaustive description of the 3D state flow behavior computed with approximation techniques. A good knowledge of the numerical methods is required to set up an accurate simulation of the flow around the POSUV.

## 1.5. Numerical methods

Numerical simulations provide more detailed flow description for the flow control and the aerodynamic optimization. This explains the interest of the resolution of the Navier-Stokes equations (Eq.20) for the simulation of the three dimensions transient flow features around the car.

$$\begin{cases} \rho \frac{\partial \vec{u}}{\partial t} + \rho \vec{u} \cdot \nabla \vec{u} = -\nabla p + \vec{\nabla} \cdot \tau + \rho \vec{F} \\ \nabla \cdot \vec{u} = 0 \end{cases} \quad \text{Eq.20}$$

where

$\vec{u}$  the velocity vector [m/s]

$p$  the pressure [Pa]

$\rho$  the fluid density with  $\rho_{air} = 1.225$  [kg/m<sup>3</sup>]

$\mu$  the dynamic viscosity with  $\mu_{air} = 1.8e^{-5}$  [Pa.s]

$\tau = \mu(\nabla \vec{u} + (\nabla \vec{u})^T) = \mu \nabla^2 \vec{u}$  the shear stress tensor

$\vec{F}$  external forces

These types of simulations are known to be expensive. The implementation of turbulent model provides convenient solutions for a partial resolution of the turbulent scales in the 3D unsteady flow. After a brief description of the existing numerical approaches, this section details the Large Eddy Simulation (LES) approach used in this work. The selected Dynamic Smagorinsky subgrid scale model will also be discussed. Finally, the interests and constraints of the Finite Element Method (FEM) which is the selected numerical approximation technique used in this work will be investigated.

### 1.5.1 Numerical approaches

Computational Fluid Dynamics (CFD) embraces three main approaches to simulate turbulent flows. The most straightforward one is the Direct Numerical Simulation (DNS) consisting in the resolution of the discretized Navier-Stokes equations. As it was stated in the theory of (Kolmogorov, 1991), high Reynolds number flows involve a large range of turbulence scales so that the spatial and temporal discretization have to be precise enough to capture smallest structures. Hence, this solution appears to be, in most cases, expensive or unrealistic with limited CPU restriction. Figure I.67 shows the resolved spectral range depending on the numerical approaches, RANS, Hybrid, LES or DNS.

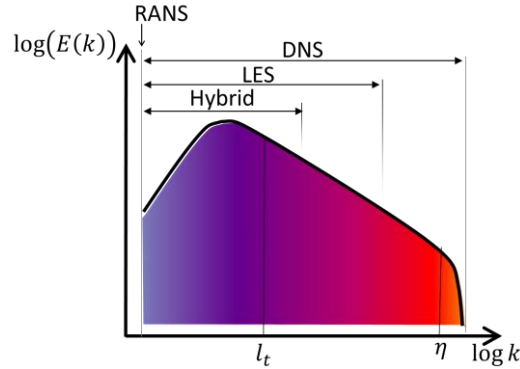


Figure I.67: Sketch of the resolved turbulent energy as a function of the length scale depending on the numerical approaches.

Computational cost is typically reduced in CFD by solving only the averaged quantities constraint to the Reynolds Average Navier-Stokes equations (RANS). In this approach, the governing equations are obtained introducing the state variables Reynolds decomposition (Eq.21) into the Navier-Stokes equations (Eq.20).

$$\begin{aligned} u_i &= \bar{u}_i + u_i' \\ p &= \bar{p} + p' \end{aligned} \quad \text{Eq.21}$$

where

$u_i, p$  are the transient velocity and pressure variables  
 $\bar{u}_i, \bar{p}$  are respectively the time averaged velocity and pressure variables  
 $u_i', p'$  are the fluctuating part of velocity and pressure variables

From the RANS equations emerged the Reynolds stress tensor  $\tau^R$  wrapping the contribution of the fluctuating turbulent velocity. The closure problem consists in the evaluation of this unknown tensor as function of Reynolds averaged quantities. Analogously to the dissipation generated by molecular viscosity, It is postulated in (Boussinesq, 1877) that the dissipation induced by turbulent eddies momentum is proportional to an eddy viscosity.

It was the privileged approach used in the past for industrial applications but hybrid methods tend to replace RANS for a better resolution of detached flows.

Large Eddy Simulation (LES) approach appears to be a better solution because smallest structures are managed by a subgrid-scale model. The remaining scales are computed solving Navier-Stokes equations in the same way as DNS. Consequently, the mesh does not have to be as fine as the DNS one.

Hybrid approaches are developed in order to optimize the simulation cost such as Detached Eddy Simulation (DES), derived methods (Delay DES, Attached DES, Improved DES), or Partially Average Navier-Stokes method. A whole range of possibilities are proposed around hybrid methods as discussed in (Delassaux et al., 2018; Krajnovic et al., 2012; Krajnović et al., 2016; Martinat et al., 2008; Serre et al., 2013). However, the cost reduction with the hybrid approach is obtained thanks to the modeling assumption enforced within the boundary layer. Thus, they show limitations for applications, which required a high level of information in the nearfield fluctuations.

Considering the importance of the turbulent features in the mockup boundary layers and the frequency range needed for the aerodynamic optimization, the LES approach appears to be suitable for the numerical simulation of the reduced scale SUV. This is the tradeoff chosen considering CPUs, time limitations and the required accuracy level. It is the solution used for

the numerical simulation of the flow past the Ahmed using LES (Hinterberger et al., 2004; Howard and Pourquie, 2002; Krajnovic and Davidson, 2004). Even if this solution will have to be reconsidered for full-scale simulation where the trends go toward hybrids, we will now focus on the LES method.

### 1.5.2 Large Eddy Simulation

The Large Eddy Simulation approach is based on the resolution of the filtered Navier-Stokes equations.

$$\begin{aligned} u_i &= \tilde{u}_i + u'_i \\ p &= \tilde{p} + p' \end{aligned} \quad \text{Eq.22}$$

Where;

- $u_i, p$  are the transient velocity and pressure variables
- $\tilde{u}_i = \iiint G(\vec{x}, \vec{x}') u_i(\vec{x}', t) d\vec{x}'$  is the filtered velocity and pressure variables
- $u'_i, p'$  are the sub filtered velocity and pressure variables
- $G(\vec{x}, \vec{x}')$  is the test filter dimensioning the resolved cut-off frequency.

There are different methods used to model the non-resolved turbulence due to the grid cutoff frequency. One can mentioned the viscosity models based on molecular dissipation analogy such as the Wale model (Nicoud and Ducros, 1999), Lilly model (Lilly, 1967), wave number dependent eddy viscosity (Chollet and Lesieur, 1981), spectral vanishing viscosity technique (Minguez et al., 2008) or the structure function (Lesieur and Metais, 1996). Otherwise, there is similarity model (Bardina et al., 1980), deconvolution model (Adams and Stolz, 2001), regularized deconvolution models (Sagaut, 2006). In the following, we will focus in the Smagorinsky type models.

The constant Smagorinsky subgrid scale model defined the subgrid stress tensor as a function of the resolved strain rate tensor and the mesh cutoff frequency, as shown in Eq.23.

$$\tau'_{ij} = -2\mu_s \widetilde{S}_{ij} \quad \text{Eq.23}$$

where

$$\mu_s = \rho(C_s \Delta)^2 \sqrt{2\widetilde{S}_{ij}\widetilde{S}_{ij}} \text{ is the subgrid turbulent viscosity}$$

In this model, the dissipation induced by the unresolved contribution is related to the mesh cutoff frequency with a constant factor  $C_s$  estimated empirically between 0.17 and 0.21. The dynamic Smagorinsky subgrid scale model, proposed by (Massimo Germano et al., 1991) and (Ghosal et al., 1995), is an adaptation of the previous approach with an additional estimation of the local and transient turbulent energy, as shown in Figure I.68.

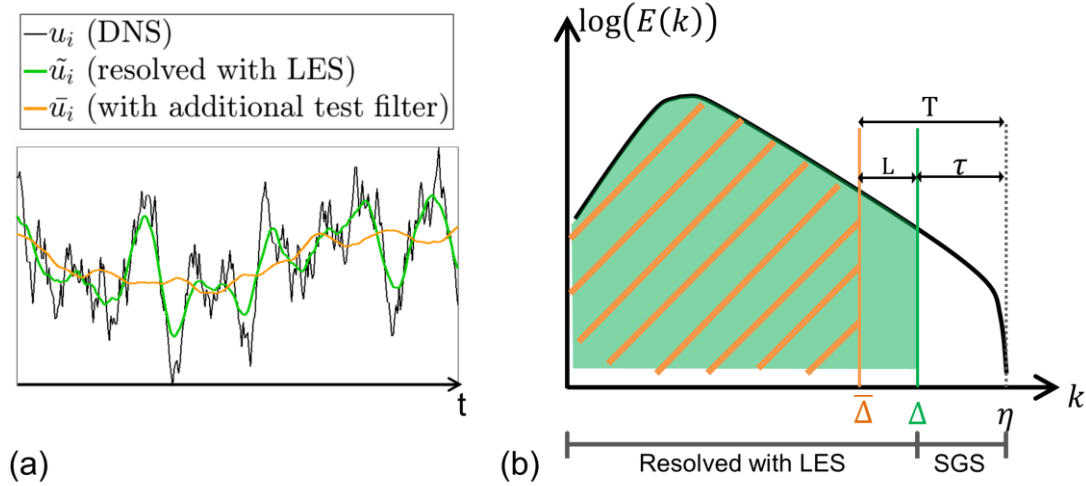


Figure I.68: (a) Illustration of filtered velocities used in LES; (b) Scheme of the turbulent energy distribution with the subgrid stress tensors contribution used to model the filtered dissipated energy according to the dynamic Smagorinsky subgrid scale model.

This model is based on the theory that the difference between the modeled turbulent stress tensor  $\tau$  below the mesh cutoff frequency  $\Delta$  and the modeled turbulent stress tensor  $T$  that would be calculated with a test filter  $\bar{\Delta}$  is equal to the resolved stress tensors  $L$  of turbulent contribution in the scale length range of  $\Delta$  and  $\bar{\Delta}$ . This leads to the Germano identity of Eq.24:

$$\begin{aligned}
 T_{ij} &= \tau_{ij} + L_{ij} \\
 \overline{\tilde{u}_i \tilde{u}_j} - \tilde{u}_i \tilde{u}_j &= \overline{\tilde{u}_i \tilde{u}_j} - \tilde{u}_i \tilde{u}_j + \overline{\tilde{u}_i \tilde{u}_j} - \tilde{u}_i \tilde{u}_j \\
 -2(C_s \bar{\Delta})^2 |\bar{\tilde{S}}| \bar{\tilde{S}}_{ij} &= -2(C_s \Delta)^2 |\tilde{S}| \tilde{S}_{ij} + L_{ij}
 \end{aligned}
 \tag{Eq.24}$$

The dynamic  $C_s$  factor can be deduced by substituting the Smagorinsky model of Eq.23 into  $T_{ij}$  and  $\tau_{ij}$  in Eq.24 leading to the final equation of the dynamic constant expressed as a function of the local resolved turbulent stress tensor and two scales filtered subgrid turbulent stress tensors in Eq.25.

$$C_s^2 = L_{ij} / M_{ij}
 \tag{Eq.25}$$

Where

$$\begin{aligned}
 L_{ij} &\text{ the resolved stress tensor between } \Delta \text{ and } \bar{\Delta} \\
 M_{ij} &= 2\Delta^2 \left( |\bar{\tilde{S}}| \bar{\tilde{S}}_{ij} - \alpha^2 |\tilde{S}| \tilde{S}_{ij} \right) \\
 \alpha &= \bar{\Delta} / \Delta.
 \end{aligned}$$

A comparison of the constant and dynamic Smagorinsky models will be performed in the section 3.2.1.

- Wall models

The wall profile is enforced depending in the normalized wall distance  $y^+$  of the first mesh point to the bounding surface. The linear profile is applied in the viscous layer when  $y^+$  is below 5 (Eq.26a). The logarithmic law is applied in the outer region when  $y^+$  is above 30 and below 500 (Eq.26b). The definition of the first layer in the buffer layer at  $y^+$  between 5 and

30 is generally avoided since the boundary layer in this region is not analytically defined. The turbulence modeling is then estimated using the eddy viscosity formulation (Eq.26c).

$$U^+ = y^+ \quad \text{if } y^+ < 5 \quad (\text{a})$$

$$U^+ = \frac{1}{\kappa} \log(y^+) + B \quad \text{if } 30 < y^+ < 500 \quad (\text{b}) \quad \text{Eq.26}$$

$$\mu_t = \rho \kappa y u_\tau \quad (\text{c})$$

Where:

$y^+ = y u_\tau / \nu$  is the normalized wall distance

$U^+ = \bar{u} / u_\tau$  is the normalized tangential velocity over the wall.

$u_\tau = \sqrt{\tau_w / \rho}$  is the skin friction velocity.

$\kappa = 0.4$ ,  $B = 5.5$

If we want to capture accurately the boundary layer quantity momentum, the first mesh cell has to be placed in the viscous layer. This is a strong constraint in the mesh quality leading to a really thin element size close to the wall. However, it is a primal condition for an accurate simulation of separated flow.

### 1.5.3 Numerical approximation techniques

Several methods exist to approach the numerical solutions of the equations stated in previous paragraph.

Finite Difference Method consists in the evaluation of the derivative terms in the governing equations with truncated Taylor approximation. This gives an efficient, easy to implement and low cost technique in order to solve the governing equations but it requires a structured grid point discretization of the computational fluid domain that is difficult to achieve for complex geometry. Some techniques as penalty method or immersed boundary method allow more flexibility on the domain discretization but the boundary layer refinement constraint is still too expensive.

With Finite Volume Method, the fluid domain is discretized in small volumes and the numerical solution is approximated by applying conservation law on state variables (mass, momentum, energy) in each volume. This technique has the advantage to work efficiently with unstructured mesh suitable with complex geometry but can lead to numeric diffusivity in case of mesh quality lack in strong gradient region. This approximation technique is still widely used in industry and supports a lot of turbulent subgrid scale models.

The Finite Element Method was historically implemented for solid structure simulations. It consists in the approximation of the numerical solution by solving a minimization problem on the variational formulation of the governing equations. It was applied on fluid application thanks to the work of (Shakib, 1991) ensuring robustness quality with the integration of combined with a permissibility on the mesh complexity thanks to a new formulation of the residual operator.

However, we cannot bypass the potential of Lattice Boltzmann Method (LBM) based on stochastic assumptions on gas kinetic equations for automotive applications. This is demonstrated for instance in the comparison of the LBM simulation with experiments on a full scale realistic car by (Eulalie et al., 2018a). This approximation technique yields to efficient simulations because of high parallelization of the distribution functions even if a LES turbulence model is still required for the estimation of the subgrid scale energy. For this reason, this numerical technique is now highly used for flow dynamical computation at full scale.

We can also mention spectral methods and particularly the spectral element method proposed by (Karniadakis and Sherwin, 1999) which solves directly the spectral decomposition of the flow. Algorithm based on High Order LES with spectral vanishing viscosity subgrid scale model is also proposed by (Minguez et al., 2008). This spectral approximation technique remains difficult to use for three-dimensional flows due to the CPU time performances.

In the case of the reduced scale model developed here, we retained the solution FEM techniques. This choice is mainly explained by the confidence developed with the previous numerical studies on simplified car mockup (Eulalie, 2014). In the following, we will explore the mathematical assumptions behind this method and we will focus on the critical points that must be take care of in order to ensure the simulation accuracy. The Navier-Stokes equation in its conservation form is Eq.27.

$$\mathcal{L}(U) = \frac{\partial U}{\partial t} + \frac{\partial F_i}{\partial x_i} - \frac{\partial F_i^d}{\partial x_i} - \mathcal{F} = 0 \quad \text{Eq.27}$$

Where:

Conservative variables:	Euler flux:	Diffusive flux:	Source vector:
$U = \rho \begin{pmatrix} 1 \\ u_1 \\ u_2 \\ u_3 \end{pmatrix}$	$F_i = \rho u_i \begin{pmatrix} 1 \\ u_1 \\ u_2 \\ u_3 \end{pmatrix} + p \begin{pmatrix} 0 \\ \delta_{1i} \\ \delta_{2i} \\ \delta_{3i} \end{pmatrix}$	$F_i^d = \begin{pmatrix} 1 \\ \tau_{1i} \\ \tau_{2i} \\ \tau_{3i} \end{pmatrix}$	$\mathcal{F} = \rho \begin{pmatrix} 0 \\ b_1 \\ b_2 \\ b_3 \end{pmatrix}$

The space time computational domain is subdivided into  $n_{el}$  finite elements, and in  $n_t$  time intervals (Eq.28). Each finite element defined in this space-time domain is associated to a trial function  $V^h$  and a weighted function  $W^h$  approximated by a  $k^{\text{th}}$ -order polynomial  $\mathcal{P}_k$ . These functions are  $C^0$  continuous within each element and discontinuous in  $Q_n$ .

$$Q_n = \Omega_n^e \times I_n \quad | \quad P_n = \Gamma \times I_n \quad \text{Eq.28}$$

$$u. \approx v. = \sum_i N_i \varphi_i(x)$$

Where:

$Q_n$  is the discretized time space domain.

$P_n$  is the time-space boundary.

$u.$  are the state variables.

$v. \in V_h = \{\mathcal{P}_k(Q_n)^3\}$  is the trial function approaching  $u.$

$N_i$  is the prescribed shape function.

$\varphi_i$  the unknown value of the state variable at the nodal points of the element.

Replacing the trial function into Eq.27, and considering the induced error  $\epsilon$ , the residual function in its strong form can be expressed as  $\mathcal{L}(v) = \epsilon$ . This residual minimization problem is managed thanks to a Galerkin Least Square method: It is a Galerkin weighted residual function (first term in Eq.29) combined with a least square operator  $\mathcal{L}$  (second term in Eq.29). The least square operator applied to  $\mathcal{L}$  is constructed by taking the inner product of the residual function with itself pondered by the stabilization matrix  $\tau$ .

$$\int_{\Omega} \mathcal{L}(v) w_i d\Omega + \sum_{e=1}^{n_{el}} \int_{Q_n} \mathcal{L}(w_i) \cdot \tau[\mathcal{L}(v)] dQ = 0 \quad \text{Eq.29}$$

Where:

$v$  is the trial function.

$w_i \in W_h = \{\mathcal{P}_k(Q_n)^3\}$  is the prescribed weighted function.

$\tau = f(Pe)$  is the symmetric positive-semidefinite least-squares matrix.  
 $Pe = \|u\|h/\nu$  is the element Peclet number ( $h$  is the element edge length).

If the Galerkin term ensures the accuracy of the approximation, the regularization operator prevents the oscillatory behavior frequently observed with Galerkin formulation in the vicinity of discontinuities. This guarantees the robustness of FEM applied to highly turbulent flows. However, a special care has to be taken in the regions of high regularizations since it can result in a numerical error.

- Discussion

The elements explored here confirm the relevance of Large Eddy Simulation with Finite Element Method to compute the flow around the generic SUV. Even if other options could have been selected, this choice is also explained by the background acquired on the numerical solver which has validated on the Ahmed Body simulations (Eulalie, 2014). These review of the mathematical definitions behind the solver, allows being aware of the sensitive points that have to be take care of.

## 1.6. Partial conclusions

The flow surrounding the car in high-speed driving conditions reveals the importance of turbulence in the aerodynamic loss. This turbulent behavior was shown to be complex with strong interactions between turbulent boundary layers, separations, shear layers and detached flow shedding vortices. The exploration of control solutions brings non negligible prospects to enhance the wake pressure loss responsible for the aerodynamic loss. We mentioned the interest of active flow control to understand the wake flow sensitivity to control system even if the potential extrapolation to adaptive optimization were identified for integration in production. This was particularly demonstrated for the control of the shear layers, which seems to be an efficient strategy for automotive applications. This leads to the choice of the pulsed blowing jet actuation for this work. The question of the selection of the optimal control parameters such as the jet flowrate and the periodic forcing frequency was raised. The exploration of closed-loop control strategies underlined the potential of machine learning using genetic algorithm for experimental applications. To go further in the understanding of the physics of flow control, modal analysis methods were introduced. The benefit of SPDMD using preliminary SVD was suggested. Finally, the numerical methods used to simulate the wake flow behind a reduced scale model were explored. A focus on the strengths and weaknesses of LES with FEM approximation techniques provided the background to implement the numerical simulation of the reduced scale generic SUV. All these points lay the foundations of the following work, which aims to identify the flow features responsible for the aerodynamic loss on the POSUV mockup and to minimize their influence.

Chapitre 2:  
Experimental investigation and control on a  
reduced scale generic SUV

The objective of this study is to explore the aerodynamic features of a generic Sport Utility Vehicle for an optimization of the wake flow loss. It will be based on a reduced scale mockup reproducing the flow around a realistic car. This will provide a benchmark for the investigation in experiments as well as in numerical simulation with the available tools.

This chapter details the experimental results obtained on the POSUV mockup in TU-Berlin reduced scale wind tunnel. The experimental conditions in agreement with the full-scale observations will be defined ensuring a correct baseline flow. The implementation of a reactive control with machine learning using genetic algorithm was achieved in order to extract an efficient operating point for the minimization of the aerodynamic loss thanks to micro-jets active flow control. The results will be deeply analyzed thanks to a cross-modal method in order to bring out the actuation mechanism.

## 2.1 Experimental setup of the POSUV

### 2.1.1 Wind tunnel characteristics and POSUV mockup

The POSUV mockup was designed at Plastic Omnium, in order to match the characteristic features of Sport Utility Vehicles with a specific rear end window angle of  $47^\circ$  (Figure II.1a). A scale of 1/6 compared to a real car was applied leading to a reference height of 200mm used for the normalization of the Reynolds number and force coefficients. An averaged ground clearance of 50mm was set associated with a  $3^\circ$  pitch angle. This configuration was selected thanks to preliminary experiments in order to begin this active flow control campaign, with a passive optimized design. The corresponding frontal area is about  $0.06\text{m}^2$  as shown in Figure II.1b.

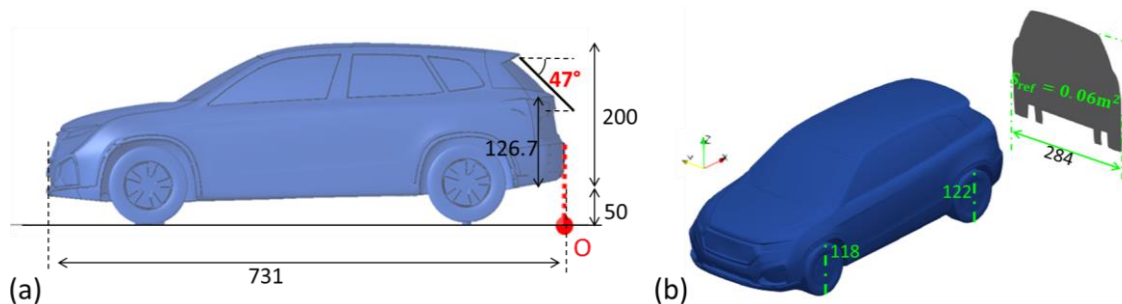


Figure II.1: Geometric features of the reduced scale generic SUV in millimeter: (a) Side view; (b) 3D view with a projected frontal area visualization.

The experiments were realized in the TU-Berlin wind tunnel (Figure II.2a). The dimensions of the tunnel are sketched in the figure below (Figure II.2b). The main section measures 2m width over 1.4m height and 10m in the stream wise direction. The blockage ratio induced by the model in the main section is evaluated at 2%. Effect of this blockage on the wall pressure, the  $C_d$  values and the velocity fields were evaluated thanks to previous measurements performed on the Drivaer model with equivalent dimensions (Wieser et al., 2014) in the same wind tunnel (Figure II.2b). The reference velocity measured at the Pitot tube remains constant in the far field around 30m/s. As the wind tunnel is not regulated, the internal temperature is measured in order to correct the density deviation. Following numerical simulation will also validate the velocity acceleration due to this blockage.

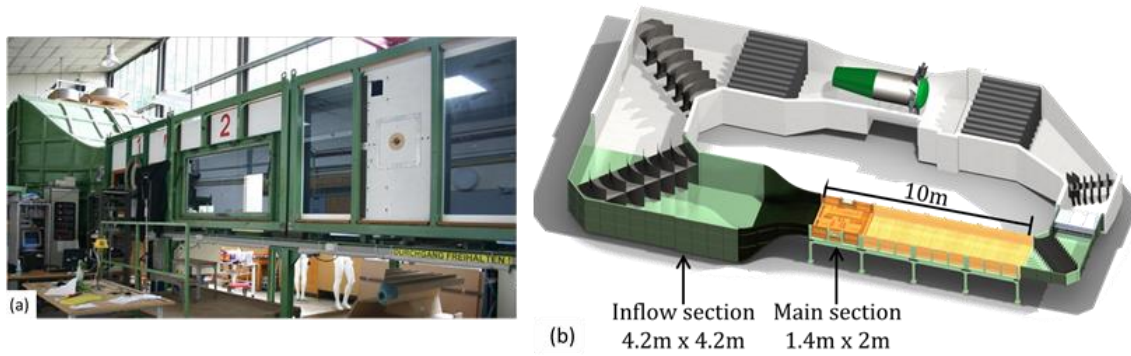


Figure II.2: (a) Picture of TU-Berlin wind tunnel; (b) Sketch of the wind tunnel dimensions.

The external flow conditions were defined with a Pitot reference point located at 63cm in front of the mockup nose and 1.084m from the floor (Figure II.3a and b). The wind tunnel flow rate was setup in order to have a reference velocity of 30m/s at the Pitot. This leads to a Reynolds number of 400 000 based on the mockup height. The static pressure is computed by applying an offset of the atmospheric pressure also measured at the Pitot tube. Turbulence intensity in the measurement section of the wind tunnel is below 0.5%.

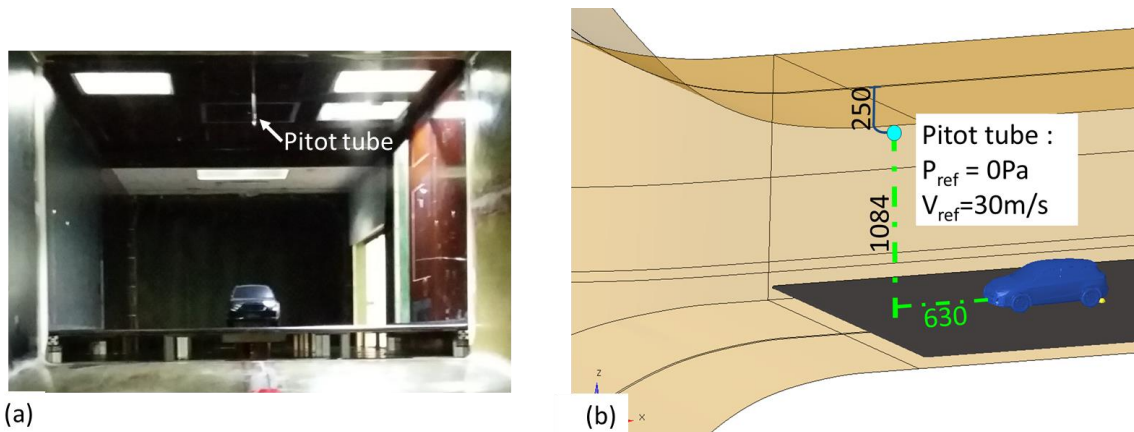


Figure II.3: (a) Picture of the POSUV mockup placed in the main section with the Pitot tube probe; (b) Sketch of the main section of the wind tunnel with a highlight on the Pitot tube located at 63cm from the nose of the mockup and 1.08m from the floor.

The campaign was achieved without moving floor condition and without rotating wheels. Therefore, the underbody flow is not completely similar to real driving condition but an evaluation of this discrepancy will be more widely discussed later on.

### 2.1.2 Pressure sensors, PIV and actuators setup

The flow description is realized with time resolved sensors, synchronized at high sampling frequency in order to capture spectral and cross-correlations information. The acquisition system used to characterize the pressure variations is constituted of 48 local pressure, distributed on the rear end tailgate (Figure II.4a) and sampled at 1600Hz during 1 minute (0.0167Hz frequency window). Additional wake measurements were achieved on the baseline flow with a synchronized two-dimensional high speed PIV.

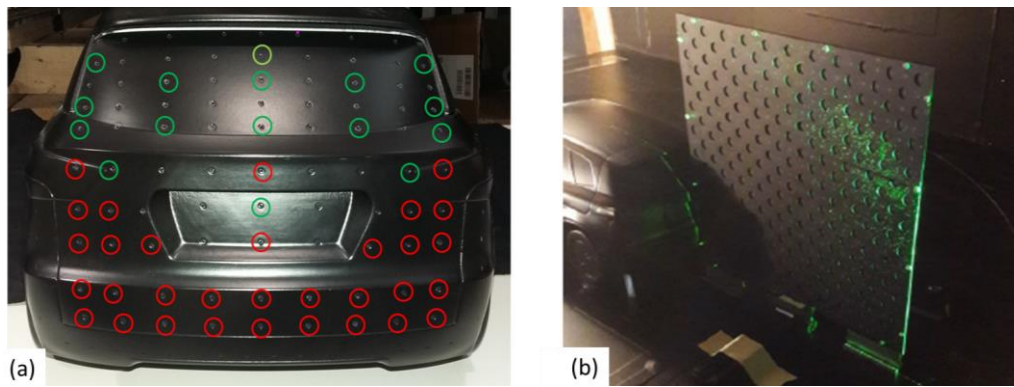


Figure II.4: (a) Picture of experimental 48 pressure sensors distributed on the rear tailgate; (b) Time resolved 2D PIV acquisitions.

A steady-state external balance system was also used to measure the forces and torques applying on the mockup.

The actuators selection was based on 2 different preliminary studies. Integration efficiency of the pulsed blowing micro-jets control were validated on previous experiments performed on a square back Ahmed body and on two different vehicle prototypes (see chapter 1). A detailed flow characterization of this pulsed jets behind a SUV vehicle prototype is presented in the work of (Eulalie et al., 2018a). However, efficiency on the wake losses of these actuators integrated on the roof spoiler were not clearly evidence as the shear layer separation was already controlled by the sharp edge design. The other preliminary study performed on the Ahmed Body with a  $47^\circ$  slant angle (Edwige et al., 2018), reveals interesting prospects of the micro-pulsed jet placed on the lateral and bottom rear end in order to control the strong vortices impacting the rear end vertical base. This is the selected solution integrated on the POSUV mockup (Figure II.5a).

Micro-jets of  $2.5 \times 0.5$  mm were evenly distributed along the edges of the rear bumper. The jets arrays are organized in 4 independent actuators placed on each lateral side and on lower edge (Figure II.5).

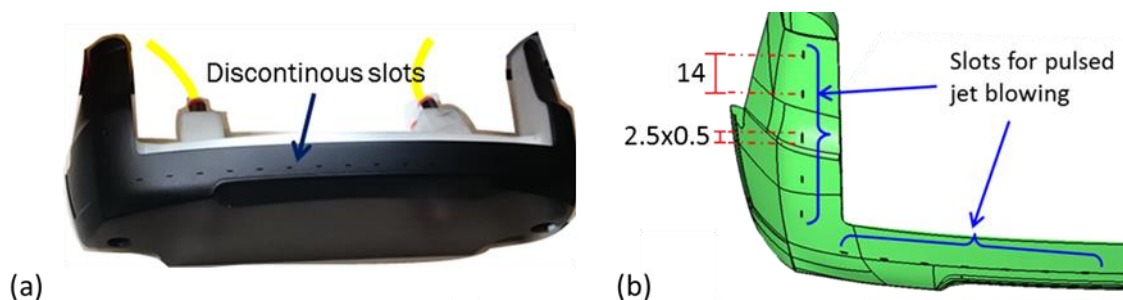


Figure II.5: (a) Pictures of the rear end module with the discontinuous slots; (b) Sketch of the geometry of the slots in millimeter.

The jet actuation consists in a pulsed blowing signal characterized by a frequency  $f_i$ , a magnitude  $A_i$  and a phase  $\phi_i$ . Figure II.6b displays the command-acquisition system implemented during the experimental campaign. Two pneumatic circuits were setup providing the air flowrates separately for the lateral jet and the bottom jet groups (black and orange connection of Figure II.6b). Both circuits are symmetric according to the middle vertical plane of the mockup, which means that the same flow rate passes through the right and the left sides. According to Figure II.6b, this symmetrical constraint on the flow rate distribution

leads to the following conditions:  $V_{j3}$  and  $V_{j1}$  on the lateral edges and  $V_{j2}$  and  $V_{j4}$  on the lower edge.

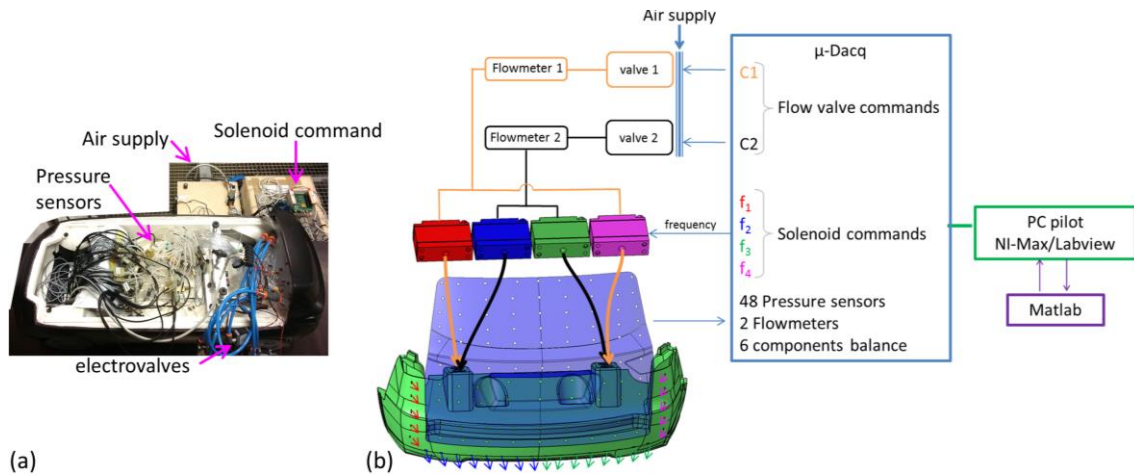


Figure II.6: (a) Picture of actuators and sensors system; (b) Diagram of command-acquisition system.

Both flow circuits were again subdivided in order to pass through 2 solenoids more. This setup enables to control 4 independent actuation frequencies: 2 on the lateral sides and 2 on the bottom edge. Therefore as presented on figure 75b, a total of 6 actuation parameters defined the design of experiment.

The flow valve commands are defined as an opening percent. The resulting averaged flow rate value is deduced by a preliminary calibration thanks to the flowmeters. The characterization of the flow circuits as a function of the solenoid frequency and the valve opening is presented in (Figure II.7). The flow circuits are globally equilibrated. A maximum averaged flow rate value of 78L/min is measured for an actuation frequency between 50 and 150 Hz in the bottom circuit and at 50Hz in the lateral circuit. The measurements of the flowrate losses in the circuits give 18% reduction above 200 Hz. These abaqus will be used later in order to compare the flow rate magnitude of the optimal actuation solution.

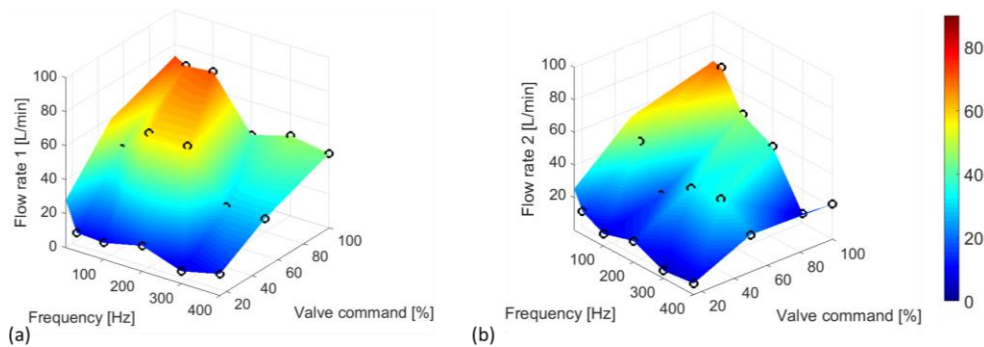


Figure II.7: Surface distribution of flowmeter measurements in each pneumatic circuit: (a) Bottom circuit, (b) Lateral circuit.

Finally, all sensors and actuators were connected to an acquisition card piloted driven by a Labview program preliminary implemented during the work of a previous PhD thesis (Varon et al., 2017c) and enhanced thanks to TU-Berlin development competencies. A bi-directional communication system was implemented between the Labview program and the optimization tool in Matlab. This allows the automated process between the sensors data and the reactive control parameters.

### 2.1.3 Reactive flow control by machine learning with a genetic evolution process

The research of an optimal operating point in order to increase the tailgate wall pressure and therefore to reduce the drag, is particularly challenging considering the size of the Design of Experiments (DOE). The spectral domain explored in a discretized logarithmic scale in the range of 0Hz (steady blowing) to 500Hz (according to the equipment feasibility) leads to 100 frequency possibilities per solenoid. If we suppose a flow magnitude resolution of 5% in the range of 1% to 100%, this leads to 20 possibilities per flow valve. The resulting number of combinations in the DOE reaches  $100^4 \times 20^2 = 4.10^{10}$  candidates. This is therefore essential to choose an efficient optimization strategy to identify a good operating point.

Several options were considered. A machine learning technique based on a DMDc algorithm was tested (Figure II.8). The objective was to adjust dynamically the actuator command law to the pressure sensors behavior. However, some difficulties were encountered to converge toward a set of stable frequencies for the 4 valves. The calibration of the high frequency feedback loop was issuing robustness restriction in order to maintain the system in the range of the bounding domain conformed to the equipment limitation.

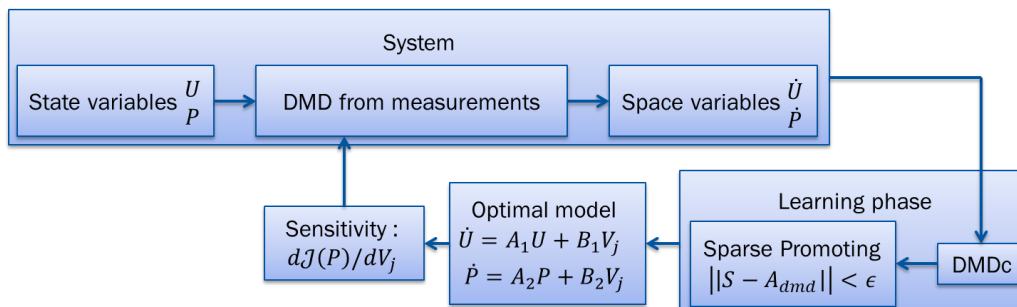


Figure II.8: System diagram of potential application of the DMDc for closed loop control.

The reactive control strategy appears to be more appropriate for the identification of an optimal control solution. The optimization procedure used in this work is a modification of the Machine Learning Control (MLC) algorithm developed by (Gautier et al., 2015) in Matlab. It is a model-free optimization tool suitable for the identification of the best operating point in a multi-parameters Design of Experiments (DOE). Contrary to a straightforward DOE exploration, the choice of the control parameters is determined by the previous measurements. Simultaneously, the injection of random input through mutation process, ensure a global exploration of the DOE for the research of an optimal solution. The initial input only requires the domain range of the control parameters. The exploration domain is then naturally bounded through generation evolution by the initial user settings. This prevents any risk of divergence. Except for the initial input, this method does not require any physical assumption and can be apply to any system. However, the model-free approaches are known to outcome non-trivial solutions which are often difficult to explain afterward. The result of the machine learning solution obtained in this campaign will be deeply analyzed thought cross-analysis investigations in sections 2.2.2 and 2.3.3.

The jet actuations signals  $V_j$  are defined as pulsed blowing jets based on the machine learning magnitude  $A_k$  and frequency parameters  $f_k$  according to the function in Eq.30. This restriction comes from the characteristics of the available experimental solenoids.

$$V_{jk} = A_k \cdot H(f_k) \tag{Eq.30}$$

Where:

H is the Heaviside function defining the pulsed blowing signal associated to the frequency  $f_k$  and the flow magnitude  $A_k$ .

First, the objective is defined in order to maximize the mean pressure on the tailgate during a measurement window of one minute of acquisition. The optimization problem is formulated as:

Find the best combination of actuation parameters for the minimization of the cost function  $\mathcal{J} = -1 \times \overline{C_p}$  from Eq.31.

$$\overline{C_p} = \frac{1}{T} \int_{t=0}^T C_p(t) dt \tag{Eq.31}$$

Figure II.9 summarizes the Machine Learning algorithm used to determine the best actuation operating point in order to minimize the tailgate pressure loss. The workflow of the research algorithm consists in the evaluation of the cost function  $\mathcal{J}$  for multiple sets of actuation parameters. The evolutionary process based on the genetic algorithm selects the best sets and proposes new sets by evolution of the actuation solutions bringing the most potential. The new selection is then evaluated during the next generation.

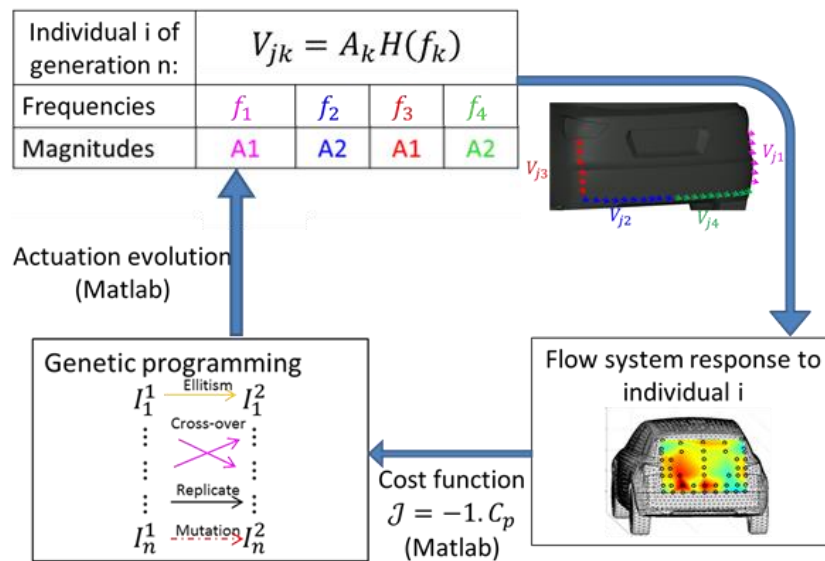


Figure II.9: Reactive flow control algorithm used for the research of an efficient operating point for the reduction of the rear end pressure.

During the genetic evolution process, the control parameters are assimilated to characters defining an individual and a population is defined as a group of individuals. The genetic algorithm proceeds in three steps as shown in Figure II.10. Each individual in the population is tested during the first evaluation step yielding a cost function table. This is followed by a tournament step performed to sort the population. Then, the evolution processes are based on the transmission of best characters through elitism mechanism, replication to ensure the superiority of certain characters, cross-over in order to check if a combination of 2 individuals can yield better gain and mutation to inject new random characters in the population. The modified population gives the following generation to evaluate.

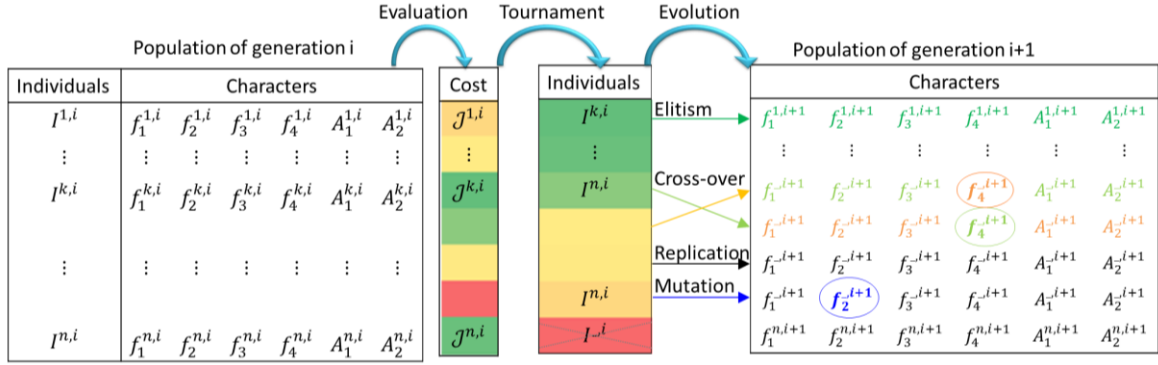


Figure II.10: Evolution process implemented in the genetic program.

In this work, the genetic algorithm is operated on a population of 51 individuals per generation, evolved at 19% by mutation, 69% by cross-over, 10% by replication and 2% by elitism. A total of 16 generations, corresponding to 816 acquisitions, was tested in order to converge towards the optimal solution.

## 2.2 Comparison of the time averaged flow topology

First, a global description of the baseline flow is achieved in order to ensure the physical reproduction of the flow developing around a realistic car mockup despite the static wheels and floor. Once we validated the representativeness of the flow behavior around the POSUV, we will present the results of the best active flow control solution on the time averaged rear end pressure topology.

### 2.2.1 Topology of the time averaged baseline flow

According to paragraph 2.1.2, the pressure averaged and RMS are computed on 96000 snapshots sampled during 1 min. The baseline flow is characterized by a low pressure area localized on the rear bumper and the lower part of the tailgate while there is higher pressure level on the rear window (Figure II.11a). This pressure distribution is in accordance with averaged pressure fields measured behind realistic SUV vehicles, presented in the literature survey in paragraph 1.1.

A mean value of  $\overline{C_p} = -0.23$  was measured on the rear end with a total drag force of  $C_d = 0.36$ , which is higher than the value of 0.32 generally obtained on SUV cars. The ratio between the rear pressure loss and the total aerodynamic force reaches 64% instead of 40% for realistic cars. The high value of drag coefficient can be correlated to the over contribution of the rear end pressure loss.

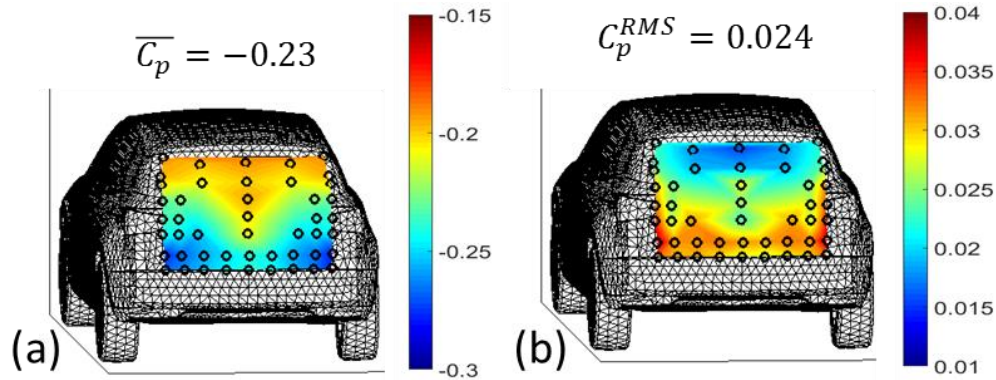


Figure II.11: Time averaged rear end pressure coefficient distribution corresponding to a mean value of  $\overline{C_p} = -0.23$ .

However, the tunnel effect and the no-moving floor are known to affect the strength of the rear end vortices. Usually, the moving road condition induces a ripple effect on the boundary layer of the floor. Without this condition, there is presumably higher blockage in the underbody flow affecting the detachment on the rear bumper corners. Despite this discrepancy, the time averaged rear end distribution is representative of the realistic flow.

To go further, the baseline wake flow was characterized thanks to high speed 2D PIV measurements performed by TU-Berlin team on the vertical transverse cut-plane Y0 and the horizontal transverse cut-plane at 140mm from the floor. The image processing from the PIV measurements exhibits noises due to laser reflection in the close vicinity of the mockup. The final cut-planes were restricted at a distance of 10mm from the rear bumper. The time averaged field, in Figure II.12, displays the recirculation zone responsible of the pressure loss in the wake. The Y0 cut-plane reveals a backflow generated from the detachment of the bottom rear bumper (Figure II.12a). There is no clear evidence of backflow from the roof spoiler separation. The wake topology in the horizontal cut-plane (Figure II.12b) is symmetrical and two main vortices emerged from the lateral rear bumper separation. The backflow pointing toward the tailgate explains the pressure drop on the rear end pressure.

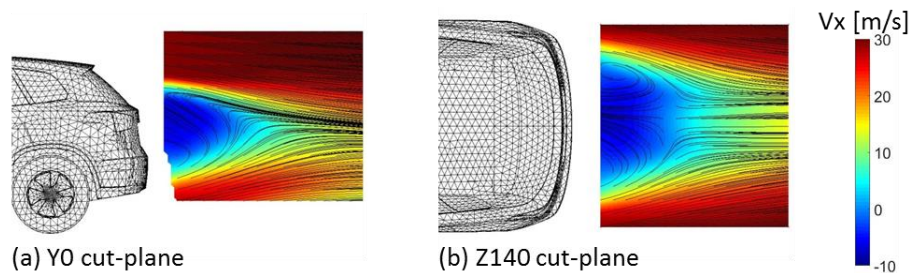


Figure II.12: Time averaged PIV measurements of the stream wise velocity in: (a) Y0 cut-plane; (b) Z140 cut-plane.

The velocity fluctuations measured in the wake show a high contribution of the shear layer mixing effect from the bottom rear bumper separation but even more from the roof spoiler separation (Figure II.13a). However, the turbulence induced in the bottom shear layer has more effect on the rear bumper pressure fluctuations reaching a RMS magnitude of 0.024 on the rear bumper as shown in (Figure II.11b). In addition, pressure fluctuations measured on the lateral sides of the rear bumper can also be related to the velocity fluctuations induced in the Z140 cut-plane (Figure II.13b).

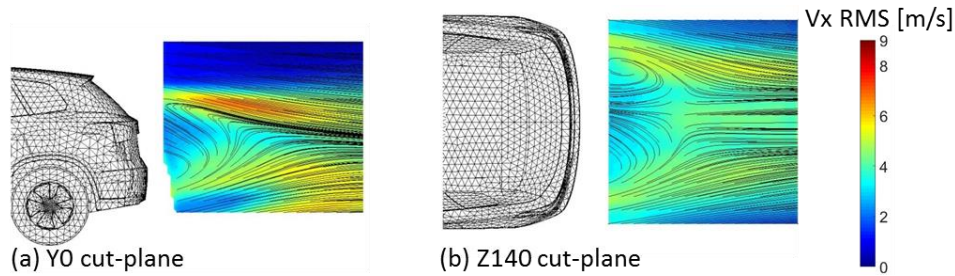


Figure II.13: RMS of PIV measurements of the stream wise velocity in: (a) Y0 cut-plane; (b) Z140 cut-plane.

Even, if the maximum of velocity fluctuations are situated on the roof shear layer, the top shear layer fluctuations do not significantly affect the pressure distribution on the tailgate. The pressure fluctuations on the rear bumper prove the important effect of the bottom and lateral shear layers on the pressure loss. The vicinity of the vortices on the bottom part of the rear bumper confirms the choice of the active flow control placed on the rear bumper corners.

### 2.2.2 Time averaged results of the active flow control

Description of the baseline flow explains the selected blowing jet geometry presented in a previous paragraph. The reactive flow control optimum  $C_d$  result based on genetic algorithm leads to the active flow control parameters displays in Figure II.14. The algorithm promoted high frequency parameters especially on the underbody slots. In addition, the jet flow magnitude was set at 15% valve opening on the sides instead of 50% on the bottom. This means that the control system does not require as much momentum for the control of the lateral detachment then for the underbody flow. Depending on the pressure loss in the bumper ducts, abaqus of Figure II.7 suggests that the flowrate in the lateral jets reaches 15L/min while the flowrate on the bottom jets is estimated at 30L/min.

We can also notice that without any constraint imposed on the AFC parameters, the algorithm did not converge toward a symmetrical control configuration despite the symmetrical time averaged baseline flow. The setup imposed a symmetric flowrate but frequencies do not follow the symmetry condition. We can question the sensitivity of the system to the unsymmetrical actuation. To argue on this point, we have to investigate on how the introduction of a bias in the lateral shear layers contributes to the modification of the wake balance.

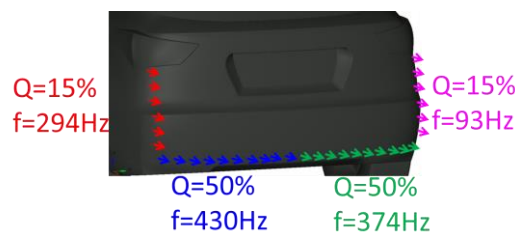


Figure II.14: Best operating point identified with the machine-learning algorithm.

The time averaged rear end distribution remains approximately symmetrical as shown in Figure II.15a. The active flow control leads to a mean pressure coefficient of -0.19 corresponding to a gain of 20% compared to the baseline pressure loss.

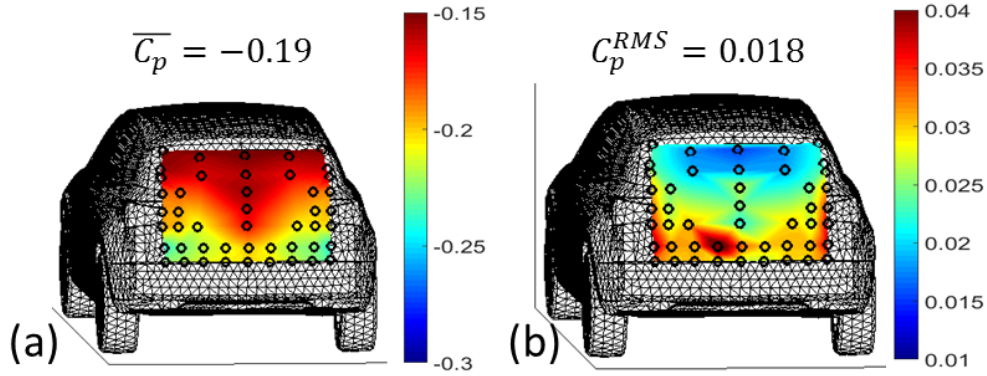


Figure II.15: (a) Time averaged pressure coefficient and (b) RMS of the pressure coefficient of the controlled flow.

A deviation of 0.018 on the RMS of the pressure coefficient (Figure II.15b) is measured around the averaged  $C_p$  instead of 0.024 in the baseline flow.

To go deeper in the understanding of the influence of the active flow control on the tailgate pressure behavior, Dynamic Modal Decomposition is achieved.

## 2.3 Modal cross-analysis

The previous paragraph shows the global characteristics of the wake flow behind the SUV in the baseline and the controlled cases. The analysis of the temporal flow behavior requires more sophisticated mathematical tools. This work is particularly pertinent to understand the non-trivial result of the machine learning.

In this paragraph, we will begin with a presentation of the Sparsity Promoting Dynamic Modal Decomposition applied on the experimental results. A first modal analysis will be performed on the baseline flow in order to capture the reference flow dynamics. Then, an extension of the modal decomposition will be proposed to enhance the identification of singularities and changes between the modal decompositions of the baseline and controlled flow.

### 2.3.1 Hypothesis and method

The modal analysis proposed in this work is based on multiple assumptions.

Synchronized variables measuring different physical quantities (for instance velocity and pressure) may have shared deterministic information, which can be brought out by a cross-correlation analysis. For instance, acoustic studies often use pressure-displacement correlations to extrapolate noise sources.

$$(f * g)(\tau) = \int_{-\infty}^{\infty} f^*(t) \cdot g(t + \tau) dt \quad \text{Eq.32}$$

Where :

- $f$  and  $g$  are 2 continuous functions.
- $f^*$  is the complex conjugate of  $f$

If 2 non-synchronized databases, obtained by different techniques (whether by different sensors equipment or by different computation solvers), contains a shared information, it can be extracted by statistic correlation analysis. This assumption allows the concatenation of the PIV database from the horizontal cut-plane Z140 and the vertical cut-plane Y0 plus the rear end pressure.

The Dynamic Modal Decomposition provides an interpretation of the flow behavior emphasizing the periodicity existing in the data dynamic. It is based on the discrimination of the phased synchronized information contained in a database. If two non-synchronized databases contained shared spectral information, the in-phase signals discrimination extracts the shared periodic features, assuming that all sensors and probes have the same acquisition sampling frequency. This means that the application of the DMD on the concatenation of experiments and numerical databases should exhibit the synchronized periodic mechanisms in both experiments and CFD results. The DMD matrix  $A$  contains the phase shift information of the flow and can be formulated as shown in Figure II.16. It corresponds to the linear decomposition of each snapshot in the shifted database  $\Psi_2$  as a function of the previous snapshot in the original database  $\Psi_1$ . Giving the size of the problem, the computation of  $A$  by inversion of  $\Psi_1$  is not a conceivable option.

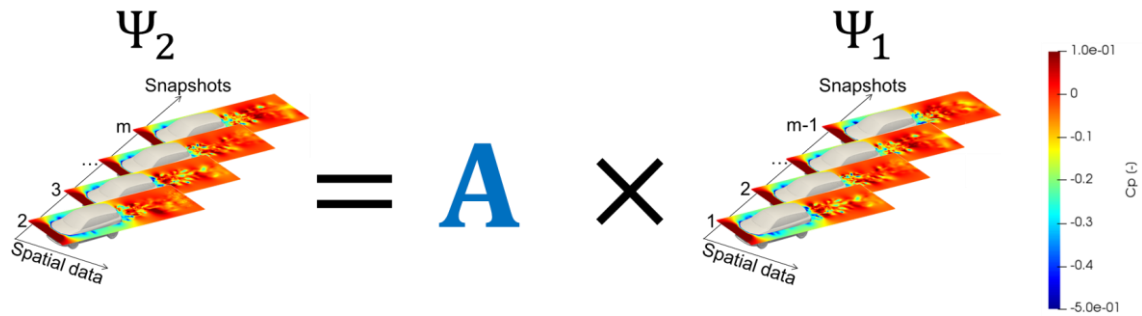


Figure II.16: Linear decomposition formulation used for DMD analysis; the matrix  $A$  corresponds to the phase shift matrix measured between each snapshot.

However, a projection of the matrix  $A$  can be obtained thanks to a preliminary Singular Value Decomposition (SVD) decomposition of  $\Psi_1$  (Eq.34). The SVD is a factorization process, which can be applied on any matrix type. For a database  $\Psi_1$  defined as time-space fluctuations, the SVD factorization can be formulated as in Eq.33. Statistically, column vectors of  $U$  can be understood as the spatial distribution of main varying mechanism extract in the database. The associated singular values decomposition corresponds to the representativeness of the mechanism in the initial sample and the matrix  $V$  can be associated to the occurrence signal of the mechanism during the acquisition.

$$\Psi_1 = U\Sigma V^* \quad \text{Eq.33}$$

Where

$U$  the unit matrix containing the left eigenvectors of  $\Psi$

$$(U^*U = I_n)$$

$V^*$  the adjoint of  $V$ , a unit matrix containing the right eigenvectors of  $\Psi$

$$(V^*V = I_n)$$

$\Sigma = \text{diag}(\sigma_1, \sigma_2, \dots, \sigma_r)$  the diagonal matrix containing the singular values of  $\Psi$ , with  $r = \text{rank}(\Psi)$

There is a straightforward relation between SVD and Proper Orthogonal Decompositions (POD) since the matrix  $U$  corresponds to the spatial POD modes, the matrix  $V$  corresponds to the snapshots POD eigenvectors and the singular values are equal to the square roots of the POD eigenvalues. This gives a powerful tool to extract the statistically correlated information in the database (Figure II.17). In the following section, the matrix  $U$  will denote the POD matrix.

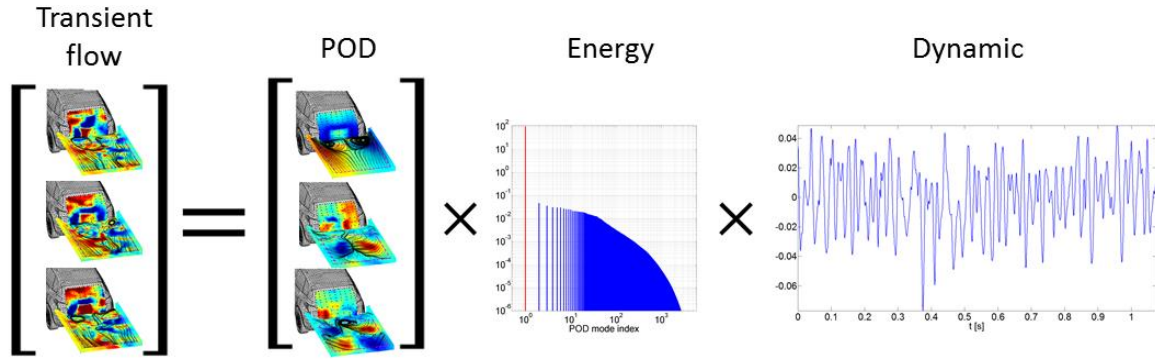


Figure II.17: Scheme of the SVD of a database decomposed into POD modes associated to an energy level and a dynamic signal.

The computation of the matrix  $A$  can be obtained by replacing  $\Psi_1$  with its SVD formulation.

$$A = \Psi_2 \Psi_1^{-1} = \Psi_2 V \Sigma^{-1} U^* \quad \text{Eq.34}$$

Where :

$$\Psi_1 = U \Sigma V^* \text{ and } \Psi_1^{-1} = V \Sigma^{-1} U^*$$

This leads to a  $n \times n$  dense matrix, which is almost impossible to decompose in eigenvectors. A low order ( $m - 1 \times m - 1$ ) matrix  $\tilde{A}$ , is obtained by projection in the POD orthogonal basis (Eq.35).  $\tilde{A}$  is called the DMD matrix and have similar eigenvalues than  $A$ .

$$\tilde{A} = U^* A U = U^* \Psi_2 V \Sigma^{-1} \quad \text{Eq.35}$$

Where :

$\tilde{A}$  is the DMD matrix projected in the POD base.

The phase decomposition is computed with the  $m - 1$  eigenvalues  $\mu_k$  and eigenvectors  $Y_k$  of matrix  $\tilde{A}$  (Eq.36). Since  $\tilde{A}$  is not definite positive, these eigenvalues and eigenvectors are complex.

$$\tilde{A} Y = Y D_\mu \quad \text{Eq.36}$$

Where :

$D_\mu$  is the diagonal matrix of complex eigenvalues  $\mu_k$  of  $\tilde{A}$

$Y$  are the complex eigenvectors of  $\tilde{A}$ .

The associated DMD spatial modes  $\Phi$  are obtained by projection of the eigenvectors on the POD matrix  $U$  (Eq.37).

$$\Phi = U Y \quad \text{Eq.37}$$

The phase shift matrix  $A$  can be reduced to a simple expression depending on the dmd mode  $\Phi$  and the eigenvalues as demonstrated in Eq.38.

$$A = U\tilde{A}U^* \Leftrightarrow A = \Phi D_\mu \Phi^{-1} \quad \text{Eq.38}$$

Based on the linear formulation of  $\Psi_2 = A\Psi_1$ ,  $A$  appears to be the ratio in the geometric series of the snapshot  $P_k$  as shown in Eq.39.

$$\begin{aligned} \forall k \in [2; m], \quad P_k &= AP_{k-1} = A^{k-1}P_1 \\ P_k &= \Phi D_\mu^{k-1} \Phi^{-1} P_1 \end{aligned} \quad \text{Eq.39}$$

An analytic formulation can be found by recurrence, iterating until the initial snapshot, based on the eigenvalues  $D_\mu$ , the DMD modes  $\Phi$  and a constant magnitude vector  $D_\alpha$  (Eq.40).

$$P_k = \Phi D_\mu^{k-1} D_\alpha \quad \text{Eq.40}$$

Where :

$D_\alpha$  is a diagonal matrix of complex coefficients

The complex part of the eigenvalues  $\mu_j$  gives the periodic pulsation per mode while the real part gives the temporal damping or growing of the mode.

$$\mu_j = e^{(\sigma_j + i2\pi f_j) \delta t} \quad \text{Eq.41}$$

Where :

$f_j = \frac{\Im(\ln(\mu_j))}{2\pi \cdot \delta t}$  is the frequency associated to the eigenvalue  $\mu_j$   
 $\sigma_j = \frac{\Re(\ln(\mu_j))}{\delta t}$  is the growth or decay rate associated to the eigenvalue  $\mu_j$   
 $\delta t$  is the time step between the snapshots

Taking the real part of Eq.40, any snapshots of the database can be expressed as Eq.42 and illustrated in Figure II.18.

$$P_k = \sum_{j=1}^{m-1} e^{k \cdot \sigma_j \cdot \delta t} \cdot [\cos(2\pi f_j \cdot k \cdot \delta t) \times \Re(\alpha_j \Phi_j) - \sin(2\pi f_j \cdot k \cdot \delta t) \times \Im(\alpha_j \Phi_j)] \quad \text{Eq.42}$$

Where :

$f_i = \frac{\Im(\ln(\mu_i))}{2\pi \cdot \delta t}$  is the frequency associated to the eigenvalue  $\mu_i$   
 $\sigma_i = \frac{\Re(\ln(\mu_i))}{\delta t}$  is the growth or decay rate associated to the eigenvalue  $\mu_i$   
 $\alpha_i$  the magnitude associated to the mode  $\Phi_i$   
 $\delta t$  is the time step between the snapshots

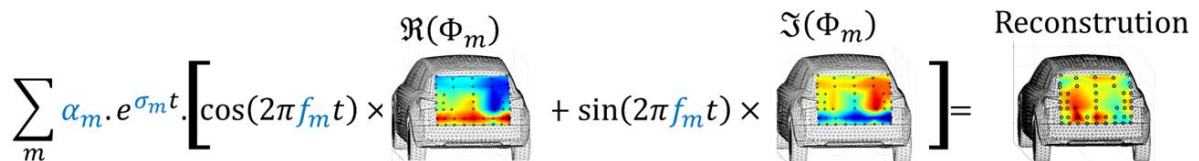
$$\sum_m \alpha_m \cdot e^{\sigma_m t} \cdot \left[ \cos(2\pi f_m t) \times \Re(\Phi_m) + \sin(2\pi f_m t) \times \Im(\Phi_m) \right] = \text{Reconstruction}$$


Figure II.18: Interpretation of the database reconstruction based on the DMD decomposition.

DMD is a powerful tool to perform spectral decomposition related to a 3D map of where the identified frequencies are significant. In addition, the complex modes  $\Phi$  give the information of phase delay between the different sample nodes in the fluid flow.

At this stage, the magnitudes are still unknown. They are obtained by resolving the minimization problem on the residual between the initial database and the reconstructed database (Eq.43).

$$\epsilon = \|\Psi_1 - \Phi D_\alpha V_{and}\| \quad \text{Eq.43}$$

Where :

$\epsilon$  is the residual between the initial and the reconstructed.

$r$  is the rank of the SVD decomposition.

$V_{and}$  is the Vandermonde matrix obtained by stacking the column vectors  $\mu^{k-1}$ :

$$V_{and} = \begin{bmatrix} 1 & \mu_1 & \cdots & \mu_1^{m-1} \\ 1 & \mu_2 & \cdots & \mu_2^{m-1} \\ \vdots & \vdots & \ddots & \vdots \\ 1 & \mu_r & \cdots & \mu_r^{m-1} \end{bmatrix}$$

Introducing the SVD decomposition into Eq.43, and the mode definition of Eq.37, the residual can be expressed as Eq.44.

$$\epsilon = \|U\Sigma V^* - UYD_\alpha V_{and}\| \quad \text{Eq.44}$$

By factorization of  $U$ , the magnitude vector  $D_\alpha$ , solution of the minimization problem Eq.43, is also the solution of the minimization of  $\tilde{\epsilon}$  defined as Eq.45.

$$\tilde{\epsilon} = \|\Sigma V^* - YD_\alpha V_{and}\| \quad \text{Eq.45}$$

(Jovanović et al., 2014b) demonstrated that the magnitudes vector of Eq.46 is the optimal solution of this minimization problem.

$$\alpha = ((Y^* Y) \circ (\overline{V_{and} V_{and}^*})^{-1} \overline{\text{diag}(V_{and} V \Sigma^* Y)}) \quad \text{Eq.46}$$

- Sparsity optimization problem

The Sparse Promoting DMD goes further and suggests resolving this minimization problem with an additional constraint on the number of non-zeros contribution. To do so, as shown in (Jovanović et al., 2014a), this minimization problem is equivalent to the unconstrained problem of minimization of the Lagrange functional:

$$\mathcal{L} = J(a) + \gamma \sum_{m=1}^{N-1} |a_m| \quad \text{Eq.47}$$

Where :

$J(\alpha)$  is the cost function associated with the reconstruction residual.

$\gamma$  is the Lagrange multiplier vector.

The cost function can be expressed as:

$$J(a) = a^* \tilde{P} a - q^* a - a^* q + s \quad \text{Eq.48}$$

Where :

$$\tilde{P} = (Y^* Y) \circ (\overline{V_{and} V_{and}^*})$$

$$q = \overline{\text{diag}(V_{and} V \Sigma^* Y)}$$

$$s = \text{trace}(\Sigma^* \Sigma)$$

$V_{and}$  the Vandermonde matrix constructed with the eigenvalues

$$V_{and} = \begin{bmatrix} 1 & \mu_1 & \cdots & \mu_1^{N-1} \\ 1 & \mu_2 & \cdots & \mu_2^{N-1} \\ \vdots & \vdots & \ddots & \vdots \\ 1 & \mu_r & \cdots & \mu_r^{N-1} \end{bmatrix}$$

This optimization problem is resolved with a dual ascend method iterative algorithm provided in ([www.umn.edu/~mihailo/software/dmdsp/](http://www.umn.edu/~mihailo/software/dmdsp/)).

### 2.3.2 Pressure-velocity cross-analysis of the baseline flow

The objective is to understand the flow behavior responsible for the pressure loss on the rear tailgate for the baseline flow. The correlation with the wake velocity dynamic behavior is then obtained with a cross analysis between PIV measurements synchronized at 2000Hz with the rear end pressure probes. This gives a dynamic model of the wake flow.

- DMD of the rear pressure baseline flow

First, a DMD analysis is applied on the rear end only. The Sparsity Optimization algorithm converged toward a minimal error with a Lagrangian multiplier at  $\gamma = 7$  corresponding to a 512 non-zero modes required to characterize the pressure dynamic (Figure II.19).

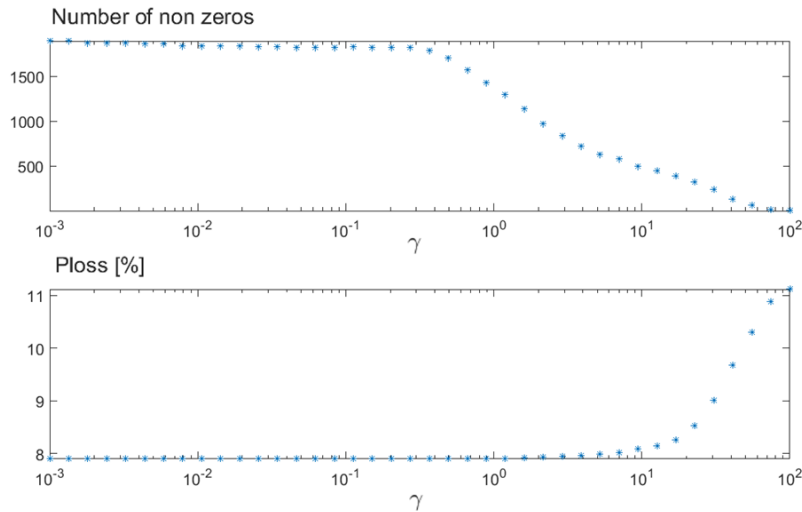


Figure II.19: Sparsity optimization convergence.

The modal magnitude contributions are normalized thanks to an overall modal energy estimation  $\alpha_{tot}$  gathering the steady state contributions  $\alpha_{steady}$  plus the contribution brought by the fluctuating part. It is an analogy to the evaluation of total kinetic energy as a summation of the energy from the time averaged quantity and the energy due to the fluctuations due to the turbulence.

$$\alpha_{tot} = \alpha_{static} + \alpha_{rms} \quad \text{Eq.49}$$

Where:

$\alpha_{static} = \sum_m [|\alpha_m| \cdot (if f_m = 0)]$  is the contribution of the static mode.

$\alpha_{rms} = \sum_m [\sqrt{\alpha_m \alpha_m^*} \cdot (if f_m \neq 0)]$  is the contribution of the oscillating

modes.

This formulation gives a direct estimation of the modal intensity  $\alpha/\alpha_{tot}$  per mode. The results of the DMD on the baseline rear end pressure highlight the ratio between the static mode compared to the overall modal energy. Indeed 95% of the total DMD magnitude is embedded in this static component, displayed on the yellow box of Figure II.20. The pressure fluctuations responsible for the oscillation around the static mode are distributed between several frequencies mainly below 10Hz. Important DMD modes at 1.8Hz and 9.3Hz appear to be symmetrical homogeneous pressure fluctuations on the rear tailgate while 4.3Hz and 8.2Hz are antisymmetric components associated to vertical oscillations. High frequency modes at 81Hz, 90Hz influence the rear end pressure especially on the sides of the tailgate. This is presumably the spectral signature induced by the shear layer turbulence from the separation on the sides of the rear bumper.

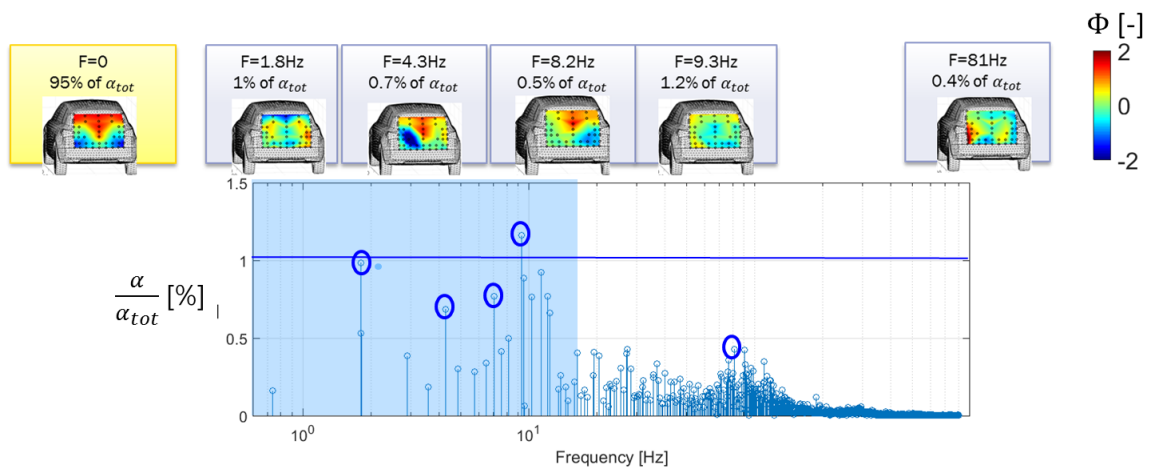


Figure II.20: Energy distribution as a function of the frequency obtained on the Dynamic Modal Decomposition of the rear end pressure sensors distributed on the tailgate on the database of the uncontrolled flow sampled at 2000Hz during one minute of acquisition. Main DMD components are highlighted and the associated DMD modes are plotted. (See Appendix 1 for a larger view).

This result gives a pertinent description of the rear end pressure spectral characteristics. A deeper investigation is required to understand the relation between the low and high frequency modes. We also need to explain the amount of energy bring in the static mode.

- From coherent wake velocity fluctuations to tailgate periodic behavior

According to the assumptions discussed in section 2.3.1, a cross modal analysis based on the PIV measurements plus the rear end pressure gives the correlated periodical modes between the wake and the rear end pressure fluctuation. The resulting modal distribution is significantly different compared to the rear end pressure alone. In the horizontal cut-plane at Z140 (Figure II.21), the modal energy is governed by low frequency fluctuations at 0.8Hz, 2.5 and 7Hz. Between 10Hz and 100Hz, the modal fluctuations are more widely distributed between the DMD modes except for the peak at 17Hz.

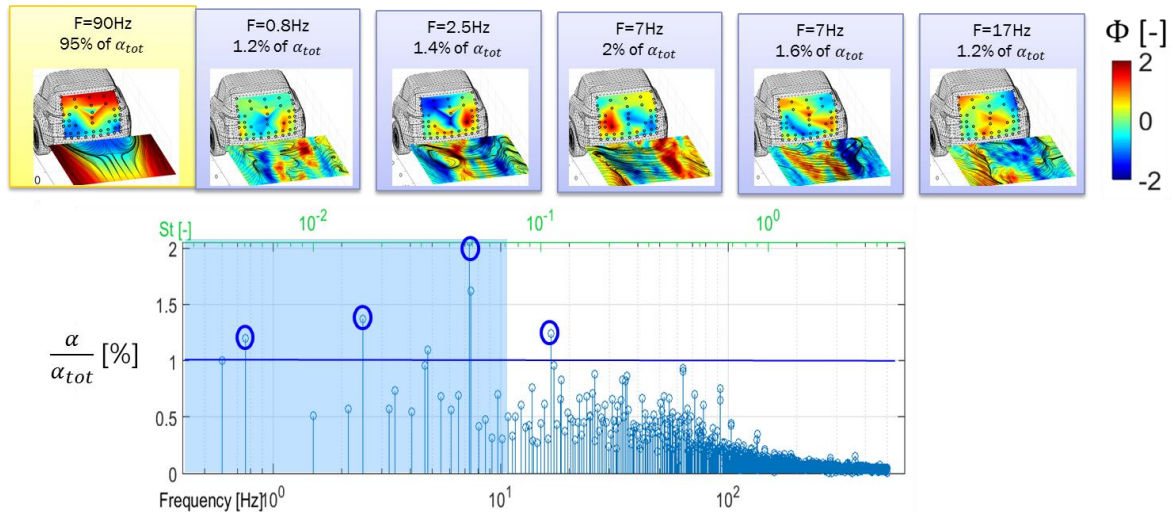


Figure II.21: Projection of the cross modal decomposition as a function of the frequency on the horizontal Z140 cut-plane synchronized with the rear end pressure. (See Appendix 2 for a larger view).

The motion due to the low frequency modes is analyzed thanks to the field reconstruction with the DMD frequencies below 10Hz. The rear end pressure dynamics evidence a swirling motion affecting the position and the intensity of the low pressure area on the tailgate (Figure II.22). This is associated to a horizontal flapping motion of the wake recirculation especially visible thanks to the backflow centerline direction (pink arrows on Z140 cut-planes of Figure II.22). The straight wake orientation generates a high pressure on the rear window and on the cavity of the license plate. The swirling motion tends to push the low pressure area alternatively on each side of the tailgate and slightly affect the rear window. The oscillation magnitude of this motion is not perfectly balanced around the centered position since the motion on the right goes higher than on the left side. This could mean that the flow is sensitive to side effects explaining that the wake motion was more constrained on the passenger side during the experimental measurements.

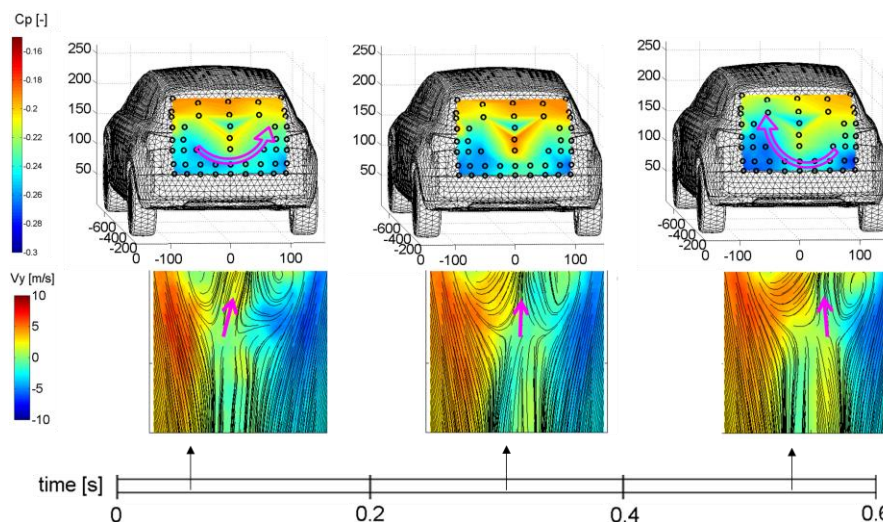


Figure II.22: Reconstruction of the cross-DMD pressure coefficient correlated to the wake velocity based on the DMD modes below 10Hz.

The DMD results with the vertical Y0 cut-plane give additional information on the wake behavior (Figure II.23). In this cut-plane, the low frequency modes are less dominant and the

vertical wake motion is driven by 38Hz and 50Hz modes even if low frequency modes at 2Hz and 9Hz are still visible.

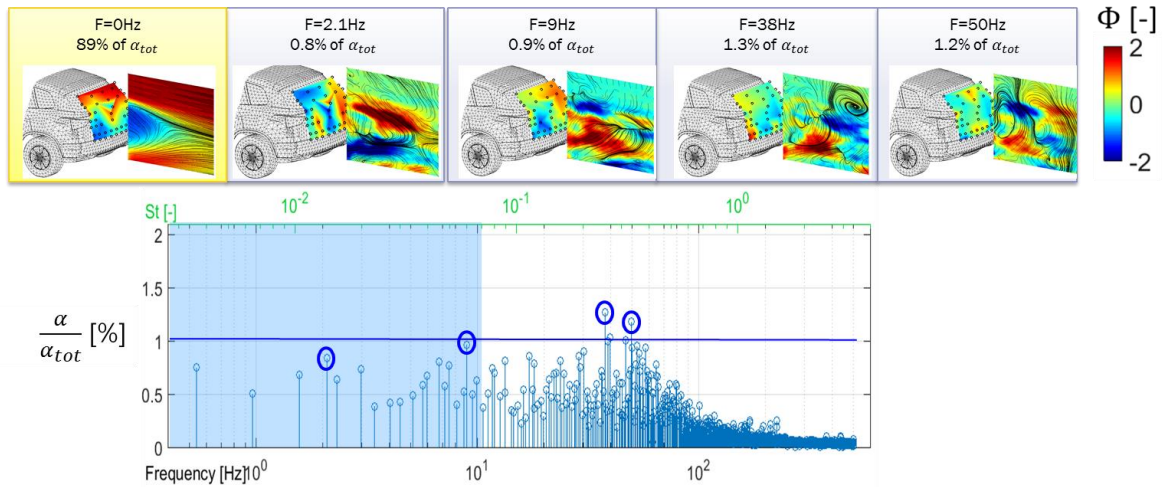


Figure II.23: Projection of the cross modal decomposition on the vertical Y0 cut-plane. (See Appendix 3 for a larger view).

Thanks to the field reconstruction, the low frequency components observed on the rear end pressure are correlated to the vertical sweeping motion of the backflow coming from the underbody (Figure II.24).

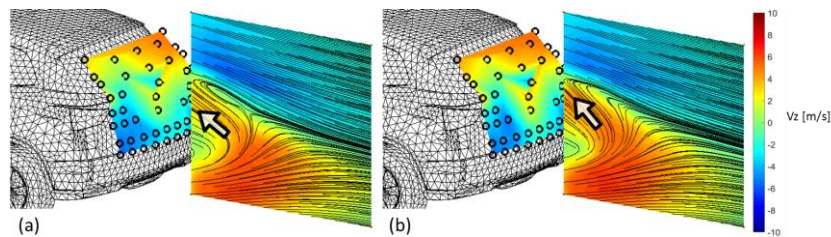


Figure II.24: Periodic vertical motion observed on the reconstruction of the 2Hz DMD mode.

- Discussion

We can already conclude on the impact of the low frequency motion applied on the rear end pressure. However, the wake analysis reveals the existence of much complex flow dynamics with the frequency of 17Hz contained in the velocity fluctuations of the Z140 cut-plane and until 50Hz in the Y0 cut-plane. This demonstrates the complexity of the wake despite the finite number of periodic components required to characterize the flow dynamic. This shows the interaction between the tailgate pressure dynamics and the wake turbulent behavior. The following analysis based on the controlled flow allows the identification of the energy transfer process applied on the tailgate pressure loss.

### 2.3.3 AFC and baseline pressure cross-analysis

The previous section highlights the dynamics of the rear end pressure and the interaction with the wake motion. Based on the previous understanding, we can now emphasize how the actuation changes the pressure dynamics and how injected momentum in specific frequency range is an efficient solution to reduce pressure loss.

In this section, the pressure dynamics of the rear end baseline flow will be investigated. The DMD results applied on the controlled flow will be used to demonstrate the change of energy distribution between the low and the high frequency. Finally, the cross modal analysis will highlight the singularities emerging with the control and the contribution damped based on a common spectral base.

- DMD of the controlled rear end pressure

The rear end pressure DMD of the controlled flow is displayed in Figure II.25. First, in the case of the controlled flow, the static mode contributes to 94% of the total energy. The spectral distribution reveals that the low frequency modes below 10Hz, that were dominant in the baseline flow decreased below 1% of the modal energy breakdown. The actuation frequencies emerged on the pressure DMD spectra at 293Hz, 374Hz and 430Hz but most importantly at 93Hz. The associated spatial DMD modes reveal which pressure probes carries the actuation frequencies. The high frequency of the bottom jet at 374Hz and 430Hz is directly measurable on the probes of the rear bumper and most importantly at the center of the tailgate (green and blue boxes on Figure II.25). The pulsed jets from the lateral slots have a wider impact on the rear end pressure sensors. The pulsed jet on the right side at 293Hz (red box on Figure II.25) is visible on the probe at the bottom right but also on the probe of the centerline. The pulsation of the jet on the left slots at 93Hz (pink box on Figure II.25) is also synchronized with the pressure modal fluctuations acting on both sides of the rear bumper.

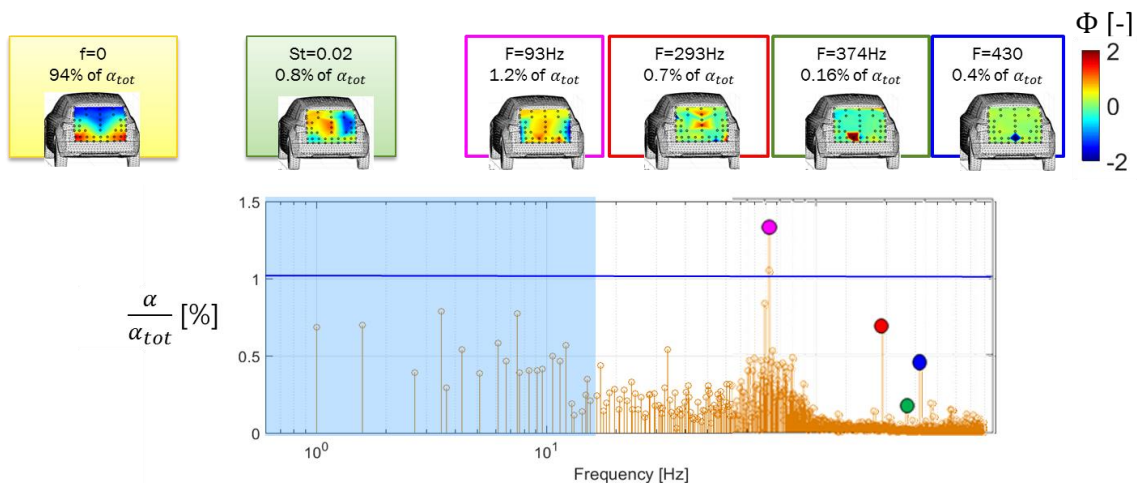


Figure II.25: DMD spectra of the rear end pressure for the controlled flow. (See Appendix 4 for a larger view).

The DMD analysis shows a damping of 19% of the static mode in the controlled flow compared to the baseline database. This is in accordance with the gain measured on the time averaged cost function but we still have to understand the energy transfer occurring between frequencies explaining influence of the actuation on the static mode. The method developed in the following section provides answers to this question.

- Cross DMD with and without control on the pressure

The change in energy transfer occurring between the baseline and controlled flow can be estimated thanks to correlate quantities between periodic components. First, the modal decomposition applied to the concatenation of the baseline and controlled data gives a common spectral base between the two acquisitions. It should be mentioned that even if the two databases were measured separately, the cross-analysis is valid since there is a common sampling frequency between each snapshots and the phase delay is maintained constant.

A block decomposition of the resulting DMD modes highlights shared spectral components or singularities belonging to only one component. Since the matrix  $\Phi$  is a unit matrix, the evaluation of the magnitudes of each vector in the block matrices  $\Phi_{ref}$  and  $\Phi_{afc}$  gives an estimation of the energy distribution between the baseline flow and the controlled per DMD mode as shown in Eq.50.

$$\Phi = \begin{bmatrix} \Phi_{ref} \\ \Phi_{afc} \end{bmatrix} = \begin{bmatrix} E_{ref}^{dmd} & 0 \\ 0 & E_{afc}^{dmd} \end{bmatrix} \times \begin{bmatrix} \Phi_{ref}^1 \\ \Phi_{afc}^1 \end{bmatrix} \quad \text{Eq.50}$$

Where:

$\Phi$  is the DMD modes matrix.

$\Phi_{ref}$  and  $\Phi_{afc}$  are respectively the baseline/controlled block matrices.

$\Phi_{ref}^1$  and  $\Phi_{afc}^1$  are the normalized baseline/controlled modes.

$E_{ref}^{dmd}$  and  $E_{afc}^{dmd}$  are  $m \times m$  diagonal matrices containing the energy contribution of respectively baseline/afc database in DMD modes.

The contribution of baseline and AFC is obtained using the energy evaluation from the block matrix. The ratio between numerical and experimental contributions in cross-DMD analysis is obtained as shown in Eq.51.

$$\alpha_{ref} = E_{ref}^{dmd} \times \alpha \quad \alpha_{afc} = E_{afc}^{dmd} \times \alpha \quad r_{afc} = \frac{\|E_{afc}^{dmd}\|}{\|E_{ref}^{dmd}\|} \quad \text{Eq.51}$$

Where:

$\alpha$  is the magnitude from the cross DMD

$\alpha_{ref}$  and  $\alpha_{afc}$  are respectively the magnitudes of the baseline/afc mode.

$r_{afc}$  is the ratio of afc/baseline contribution in each DMD mode.

The energy per case is plotted in Figure II.26 and Figure II.27. Here, the cross-DMD exhibits the emergence of modal oscillation at the actuation frequencies. In addition, the low frequency components driving the baseline pressure dynamics show the damping at 0.9Hz, 8Hz and 11Hz. This demonstrates how the actuation efficiently changed the energy distribution per spectral component.

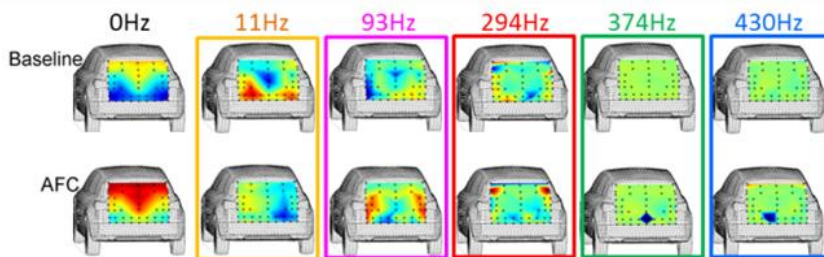


Figure II.26: Synchronized periodic components emerging from the cross-DMD analysis.

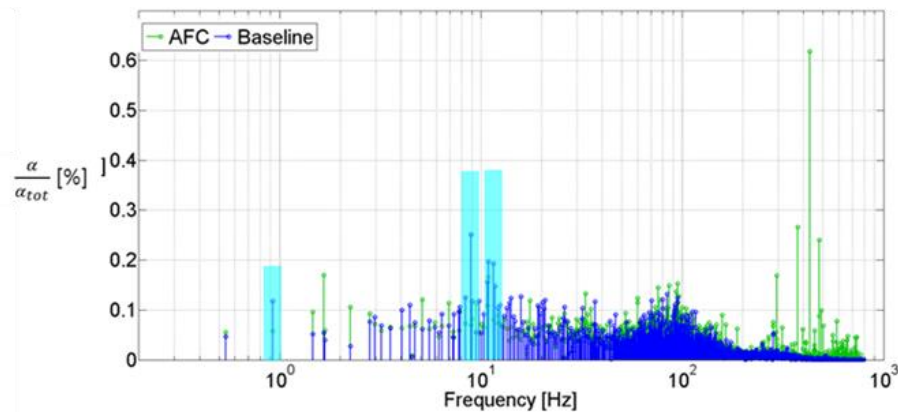


Figure II.27: Result of cross DMD between baseline and controlled rear end pressure database. The components highlighted in blue in the background correspond to the frequencies, which were vanished with control.

This method has the benefit to identify which spectral components are responsible for the increase or the damping of baseline periodic features compared to the control flow. We want to go further to demonstrate the energy transfer occurring with the actuation and responsible for the change of the static mode contribution.

- Relation between frequency and turbulent coherence

As we performed a preliminary SVD decomposition, the matrix  $U$  provides an orthogonal decomposition of the flow dynamics and the square of the singular values give an evaluation of the POD energy. Thus, the coherent behavior embedded in the two databases is also extracted. In addition, as the SVD is directly performed on the transient data instead of the fluctuating data (obtained by suppression of the time averaged field), the first orthogonal mode gives the time averaged distribution because it is statistically the most representative state of the flow (Figure II.28).

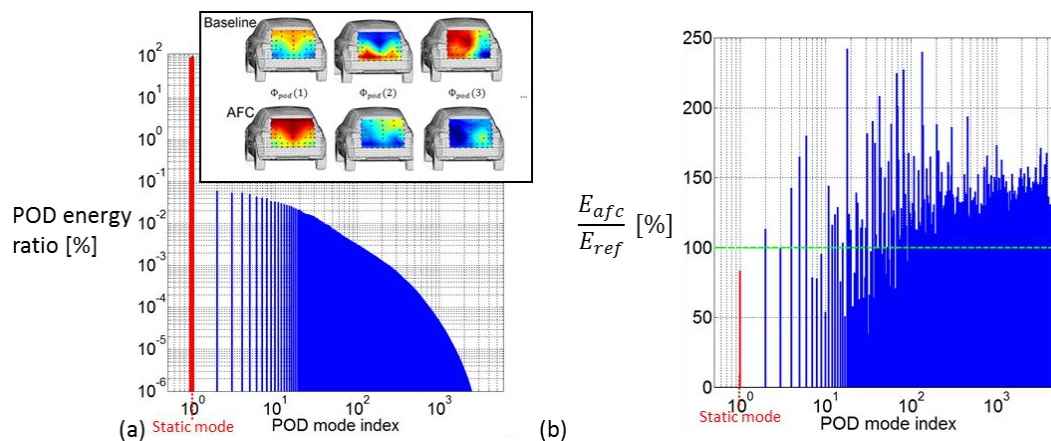


Figure II.28: (a) Correlated POD energy distribution obtained on the concatenated baseline and controlled rear end pressure; (b) ratio of the controlled flow energy compared to the baseline modal energy

In this cross-analysis, each mode gives the correlated information between controlled and baseline flow. The AFC ratio per POD mode (Figure II.28b) is extracted in a same way as for the concatenate cross-DMD analysis. Indeed, peaks above 100% means that the correlated modes are stronger in the controlled flow compared to the baseline, while those below 100% correspond to modal components that were damped with the control. We can see how the energy brought by the correlated modes is reduced for the static component but increased for the first energetic POD modes index 2, 4, 5 and 6 (Figure II.28b). This provides an exact estimation of the flow modification, not even on the time averaged and RMS comparison but on the coherent behavior existing in both databases.

In addition, the decomposition of the flow fluctuations based on periodicity criterion for DMD and coherence for POD gives two descriptions for the same database. These two descriptions are both pertinent but do not give the same information. That is why we propose to compute the transfer matrix between these two basis in order to give a combination of the periodic behavior with the coherent structures of the flow. This is done by projection of the DMD base into the POD base as shown in Eq.52.

$$\begin{aligned} U &= \Phi W & U_j &= \sum_{i=1}^{m-1} w_{ij} \Phi_i \\ W^{baseline} &= \text{diag}(\alpha_{ref}) W & W^{afc} &= \text{diag}(\alpha_{afc}) W \end{aligned} \quad \text{Eq.52}$$

Where :

$W = Y^{-1}$  is the weight matrix balancing DMD modes contribution in POD decomposition

$w_{ij}$  are the weight of each DMD mode  $i$  in the POD mode  $U_j$ .

Thanks to that method, we can extract the correlated periodic allowing the characterization of the pressure dynamic. Contrary to the POD temporal evolution, which cannot be model by an analytic formulation, the correlated periodic mechanism, associated to each POD mode, is a combination of several frequencies weighted by a correlation factor  $W_k$  as shown in Figure II.29.

$$\begin{aligned} \sum_m W_k^{baseline}(m) \alpha_m \cdot e^{\sigma_m t} & \left[ \cos(2\pi f_m t) \times \begin{array}{c} \Re(\Phi_m) \\ \text{Car} \end{array} + \sin(2\pi f_m t) \times \begin{array}{c} \Im(\Phi_m) \\ \text{Car} \end{array} \right] = \begin{array}{c} C_p^{baseline} \\ \text{pod}(k) \\ \text{Car} \end{array} \\ \sum_m W_k^{afc}(m) \alpha_m \cdot e^{\sigma_m t} & \left[ \cos(2\pi f_m t) \times \begin{array}{c} \Re(\Phi_m) \\ \text{Car} \end{array} + \sin(2\pi f_m t) \times \begin{array}{c} \Im(\Phi_m) \\ \text{Car} \end{array} \right] = \begin{array}{c} C_p^{afc} \\ \text{pod}(k) \\ \text{Car} \end{array} \end{aligned}$$

Figure II.29: Correlated periodic mechanisms model associated to each POD mode and based on the transfer matrix coefficient.

This approach applied to the concatenate controlled and baseline rear end pressure leads to the transfer matrix  $W$  displayed in Figure II.30 with a logarithmic color scale. This gives a complete visualization of the energy transfer occurring in the wake flow. Indeed, we can see that a significant amount of energy measured in the first 10 POD modes is brought by the low frequency DMD components below 50Hz while the higher frequencies behave as dissipative mechanisms. Moreover, the transfer matrix also gives a criterion on the physics of the modal components since the region where no coherence is measured can be related to residual noise.

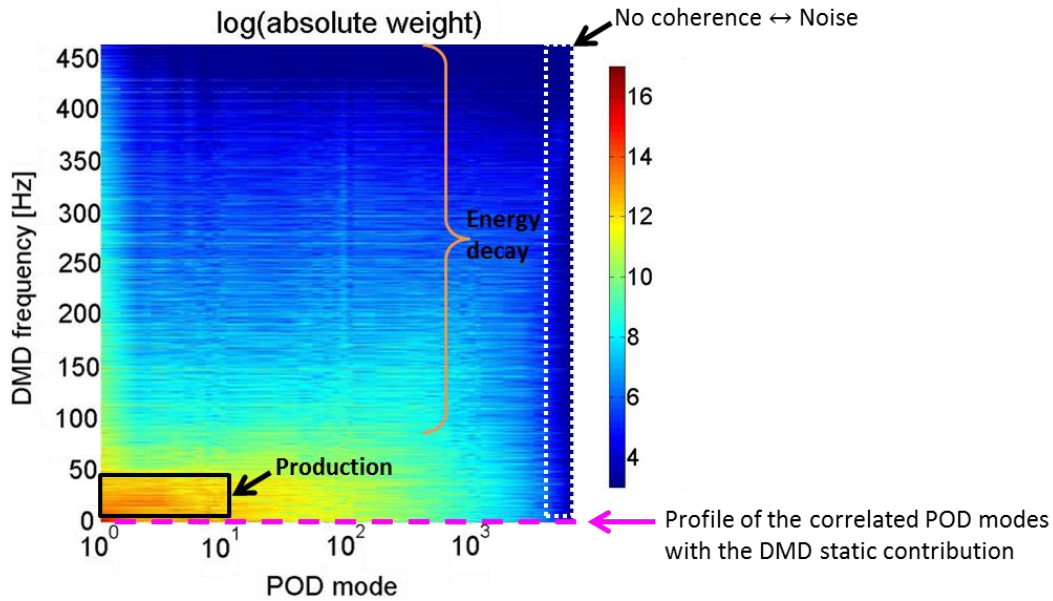


Figure II.30: Logarithm of the weight matrix  $W$  highlighting the energy production and decay as a function of the POD index and of the DMD frequency.

The great advantage of the POD/DMD transfer matrix is that we can determine the influence of the fluctuating coherent modes with the 0Hz DMD static mode. The goal is to propose a definition of the turbulent mechanisms responsible for the aerodynamic loss thanks to a modal formulation taking into account the multi-frequency energy transfer.

- Modal cascade driving the wake motion involved in the static mode

Figure II.31 and Figure II.32 present the research procedure developed to analyze the modal energy transfer process. The benefit of this methodology is also to apprehend the flow coherence emerging in the control flow and responsible for the aerodynamic loss reduction. The projection of the DMD 0Hz static mode on the POD base results in the identification of correlated mechanisms associated with the POD modes  $\Phi_{pod}(2)$ ,  $\Phi_{pod}(4)$  and  $\Phi_{pod}(8)$ . These are the fluctuating contributions affecting the time averaged flow topology. The ratio of the controlled flow, displays in Figure II.31a, demonstrates that these components were amplified thanks to the actuation. The correlated POD modes are displayed in Figure II.32a.  $\Phi_{pod}(2)$  appears to be a vertical motion of the pressure fluctuations distributed between the slant and the bottom tailgate. The projection of the spectral components driving  $\Phi_{pod}(2)$  in Figure II.32b, highlights low frequency oscillations at 1.8Hz and 9.3Hz. The spatial mode  $\Phi_{pod}(4)$  exhibits pressure fluctuations located on the bottom of the rear end tailgate in opposition to the pressure fluctuation on the sensors on license plate at the center of the pressure map.  $\Phi_{pod}(4)$  is a combination of low frequency oscillating motions at 4.3Hz and 8.2Hz. In addition,  $\Phi_{pod}(8)$  is the first mode coupling high frequency fluctuation above 80Hz localized on the lateral edges of the rear bumper and the low frequency 9.3Hz.

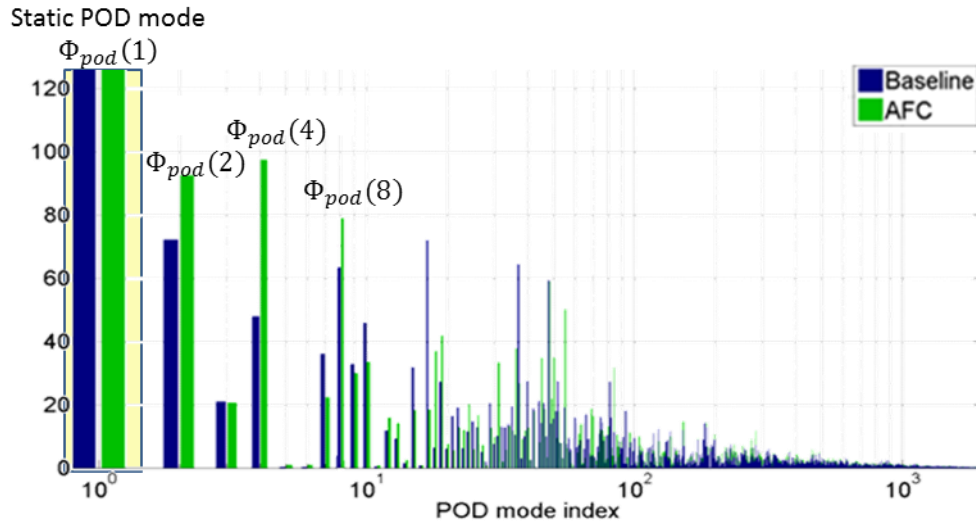


Figure II.31: Correlations with the 0Hz static DMD mode showing the influence of the 2nd, the 4th, and the 8th POD modes.

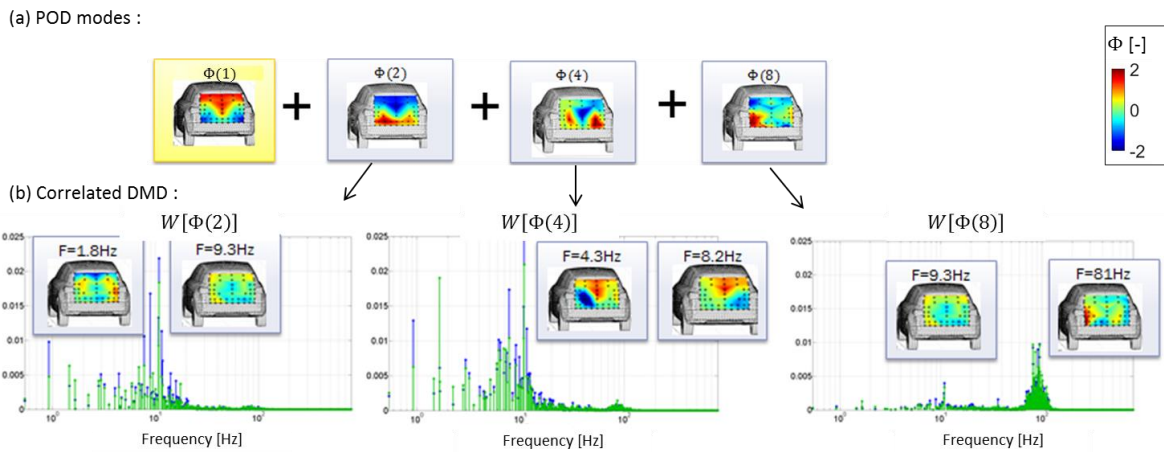


Figure II.32: (a) Spatial distribution of the POD modes affecting the 0Hz static DMD component; (b) Correlated spectra obtained with the row vectors of the transfer matrix. In green, the controlled flow contributions and in blue the baseline contributions. (See Appendix 5 for a larger view).

The flow description, performed here, underlines the complexity of the spectral information existing on the rear tailgate. The transfer function between POD and DMD gives however an appropriate way to interpret the interactions between the spectral signatures existing in the flow. This leads us to the idea that the low frequency behavior responsible for the static pressure loss on the rear end is strongly correlated to high frequency features through a chain reaction. The fact that the correlated modes  $\Phi_{pod}(2)$ ,  $\Phi_{pod}(4)$  and  $\Phi_{pod}(8)$  are reinforced by the control, proves that the associated coherent mechanisms were enhanced by the pulsed blowing jet. Since it was demonstrated that the energy distribution has been reallocated in the control flow, we can assume that the jet high frequency quantity momentum changed the cascade transfer process. Consequently, we can conclude that the high frequency actuation participates to the damping of the low frequency motion on the tailgate.

## 2.4 Partial conclusions

The experimental exploration of the aerodynamic features of the generic reduced scale POSUV model was successfully performed. The experimental campaign provided a full description of the flow features around the POSUV required for the validation of the numerical simulation in the following chapter. This is also particularly valuable since high frequency time resolved acquisitions give the synchronized dynamical behavior between the wake flow and the tailgate pressure loss. The first Dynamic Modal Decomposition on the synchronized multi-variate pressure-velocity database showed the influence of the low frequency motion on the tailgate dynamics while the wake velocity has much more complex spectral information dealing with 17Hz pulsation in the Z140 cut-plane and high frequency signals until 60Hz in the Y0 cut-plane.

An optimal flow control strategy was deployed using machine learning with genetic algorithm leading to the identification of the optimal set of parameters. A pressure increase of 19% was obtained. As the optimal parameters were not trivial, a cross modal analysis of the baseline and controlled pressure databases was realized. This showed a reduction of 19% of the static component between the baseline and the controlled configurations. The result also outcomes the change of energy distribution between high and low frequencies on the rear tailgate. Finally, the correlation analysis exhibited an enhancement of the energy transfer by the flow control occurring on the most significant fluctuating POD modes affecting the static component. This is interpreted as a cascade effect occurring in the wake flow and stabilizing the low frequency behavior and responsible for the pressure loss. The methodology proposed here gives an innovative way to describe the modal relation between periodicity and turbulent coherence in the flow. This is a brand-new way to evaluate the flow sensitivity to the actuation.

Concerning the optimization phase, the fact that the machine-learning algorithm did not converged toward a symmetrical actuation solution on the frequency parameters, raises some interrogations. Indeed, it has been decided to leave the frequency optimization process free of any symmetry constraint between the left and the right side. It should be mentioned that the evaluation of 816 individuals comforts us on the exploration of a large range of the design space. In addition, we questioned the benefit of synchronization of the fluctuations coming from the shear layers and the impact on the wake stabilization.

There are still some questions on the flow behavior due to the restricted information measured in experiment. The numerical studies will go further on the understanding of the aerodynamic loss. The application of this methodology on the numerical results will help the identification of the transfer mechanism between the wake velocity and the tailgate pressure.

Chapitre 3:  
Numerical investigations and wake flow  
control on different test cases

The experiments give the foundations of the pressure-velocity flow features in the wake of the POSUV and how they are related to the modal fluctuations. We will now reproduce the experimental results by numerical simulation with an appropriate LES, Finite Element solver. This choice was justified in the literature survey in chapter 1.5. The aim is to go further in the understanding of the correlations between the wake, the shear layers and the tailgate pressure losses thanks to a more detailed flow discretization than what is permit with PIV and pressure sensors.

The numerical simulation of highly turbulent 3D flows is very challenging because of the level of accuracy required to get a solution in accordance with the reality considering the CPUs limitations. This chapter details the numerical study achieved during the PhD work. Two preliminary studies are developed to reach the objective of the numerical simulation of the POSUV in TU-Berlin wind tunnel.

First, the benchmark of the 25° ramp flow has multiple interests. It is a simplified test case reproducing the main features of highly turbulent detached flows. This will give the guidelines for an accurate simulation of the generic SUV. The second objective of the ramp flow analysis is to describe the mechanisms involved in the pressure loss and the interaction with the boundary layer and the shear layer. Then, a close look on the physics of the active flow control provides some insights for the analysis of the POSUV actuation results.

The second benchmark is the Ahmed body with 47° slant angle. This mockup is used to apprehend the relation between wake pressure losses and shear layers. This is also an opportunity to explore some closed-loop control strategy in numerical simulations.

At last, the numerical simulation of the reduced scale POSUV is detailed. Time averaged comparison and cross modal analysis with experiments validate the flow behavior. Three-dimensional results are then extensively analyzed to identify the phenomena responsible for the aerodynamic loss in accordance with what was observed in experiments. The simulation of the control flow on the POSUV will finally help to apprehend how the control solution leads to a wake flow modification.

### 3.1. Numerical simulations with Large Eddy Simulation

The solver used for the numerical simulation of the flow past the POSUV is AcuSolve, from the ALTAIR distribution software. It is a finite element method using Galerkin Least Square (GLS) method. The algorithm was fully described in (Shakib, 1991). The following details the mathematical model used in LES simulations.

The transient state variables  $u_i$ ,  $p$  can be decomposed into a resolved contribution and a fluctuating part as shown in Eq.53.

$$\begin{aligned} u_i &= \tilde{u}_i + u_i' \\ p &= \tilde{p} + p' \end{aligned} \tag{Eq.53}$$

where

$u_i, p$  are the transient velocity and pressure variables

$\tilde{u}_i = \iiint G(\vec{x}, \vec{x}') u_i(\vec{x}', t) d\vec{x}'$  is the filtered velocity and pressure variables

$u_i', p'$  are the sub filtered velocity and pressure variables

A top-hat filtered associated to the mesh cutoff frequency  $\Delta$  is expressed as in Eq.54. The choice of  $\Delta$  depends on the subgrid scale model. (Pope, 2001a) shows that a spatial cutoff

frequency around  $60\eta$ ,  $\eta$  the Kolmogorov scale, is a suitable criteria to model appropriately the unresolved dissipative scales with LES approach.

$$G(\vec{x}, \vec{x}') = \begin{cases} 1/\Delta & \forall |\vec{x} - \vec{x}'| \leq 0.5\Delta \\ 0 & \forall |\vec{x} - \vec{x}'| > 0.5\Delta \end{cases} \quad \text{Eq.54}$$

The filtered Navier-Stokes equations are formulated in Filtered Navier-Stokes equations Eq.55.

$$\mathcal{L} : \begin{cases} \rho \frac{\partial \tilde{u}_i}{\partial t} + \rho \frac{\partial \tilde{u}_i \tilde{u}_j}{\partial x_j} = -\frac{\partial \tilde{p}}{\partial x_i} + 2\mu \frac{\partial \tilde{S}_{ij}}{\partial x_j} + \frac{\partial \tau'_{ij}}{\partial x_j} \\ \frac{\partial \tilde{u}_i}{\partial x_i} = 0 \\ \tau'_{ij} = -2\mu_s \tilde{S}_{ij} \end{cases} \quad \text{Eq.55}$$

Where

$\tilde{S}_{ij} = \frac{1}{2} \left( \frac{\partial \tilde{u}_i}{\partial x_j} + \frac{\partial \tilde{u}_j}{\partial x_i} \right)$  is the filtered strain rate tensor

$\tau'_{ij}$  is the subgrid stress tensor

$\mu_s = \rho (C_s \Delta)^2 \sqrt{2\tilde{S}_{ij}\tilde{S}_{ij}}$  is the subgrid turbulent viscosity model

If the coefficient  $C_s$  is constant and set to 0.2 with the Smagorinsky subgrid scale model, the Dynamic subgrid scale model evaluates locally and dynamically the subgrid dissipated energy using the Germano entity presented in the literature review 1.5.1. Hence, the dimensioning of  $C_s$  is based on the ratio of the local resolved stress tensor  $L_{ij}$  captured with the numerical test filter  $\bar{\Delta} = \alpha\Delta$  and the modeled stress tensor evaluated by the Smagorinsky formulation between  $\bar{\Delta}$  and  $\Delta$  (Eq.56). The grid ratio  $\alpha$  is set to a value of 2 in our solver.

$$C_s^2 = L_{ij}/M_{ij} \quad \text{Eq.56}$$

where

$L_{ij}$  the resolved stress tensor of the eddies between  $\Delta$  and  $\bar{\Delta}$

$$M_{ij} = 2\Delta^2 \left( |\tilde{S}| \tilde{S}_{ij} - \alpha^2 |\tilde{S}| \tilde{S}_{ij} \right)$$

$$\alpha = \bar{\Delta}/\Delta$$

The wall model is defined in order to reproduce the turbulent boundary layer profile using a linearity assumption (Eq.57a) in the viscous sublayer ( $y^+ < 5$ ) and logarithmic assumption (Eq.57b) in the outer layer ( $30 < y^+ < 500$ ). In between ( $5 < y^+ < 30$ ), the velocity profile within the buffer layer is defined using a bridge function. The eddy viscosity profile within the turbulent boundary layer is derived using (Eq.57c).

$$U^+ = y^+ \quad \text{if } y^+ < 5 \quad \text{(a)}$$

$$U^+ = \frac{1}{\kappa} \log(y^+) + B \quad \text{if } 30 < y^+ < 500 \quad \text{(b)} \quad \text{Eq.57}$$

$$\mu_t = \rho \kappa y u_\tau \quad \text{(c)}$$

Where :

$y^+ = yu_\tau/\nu$  is the normalized wall distance

$U^+ = \bar{u}/u_\tau$  is the normalized tangential velocity over the wall.

$u_\tau = \sqrt{\tau_w/\rho}$  is the skin friction velocity.

$$\kappa = 0.4, B = 5.5$$

Thanks to the Finite Element approximation technique, the governing equations  $\mathcal{L}$  are solved in their weak form using a Galerkin Least Square (GLS) operator to minimize the residual function (Eq.58).

$$\int_{\Omega} \mathcal{L}(v) w_i d\Omega + \sum_{e=1}^{n_{el}} \int_{Q_n} \mathcal{L}(w_i) \cdot \tau[\mathcal{L}(v)] dQ = 0 \quad \text{Eq.58}$$

Where:

$v$  is the trial function.

$w_i \in W_h = \{\mathcal{P}_k(Q_n)\}^3$  is the prescribed weighted function of the Galerkin term

$\tau$  is the symmetric positive-semidefinite least-squares matrix.

As discussed in the literature survey 1.5.3, the Finite Element Methods using GLS imply high accuracy level thanks to the Galerkin minimization term while the Least-Square regularization term ensure the robustness of the simulation even with distorted element. Figure III.1 shows the contribution of the regularization term as a function of the convective velocity  $\beta$ . The Least-Square matrix (purple dashed curve on Figure III.1) is defined as a function of the element Peclet number  $Pe$ . This normalized coefficient measures the ratio between the convective and diffusive effects inside an element.  $\beta$  is the convective velocity,  $c$  is the diffusion coefficient and  $h$  is the element size. When the Peclet number is higher than 1, the numerical instabilities generated by the Galerkin term are damped by the Least-Square matrix. The consequences of this approximation technique will be further analyzed in section 3.4.3.

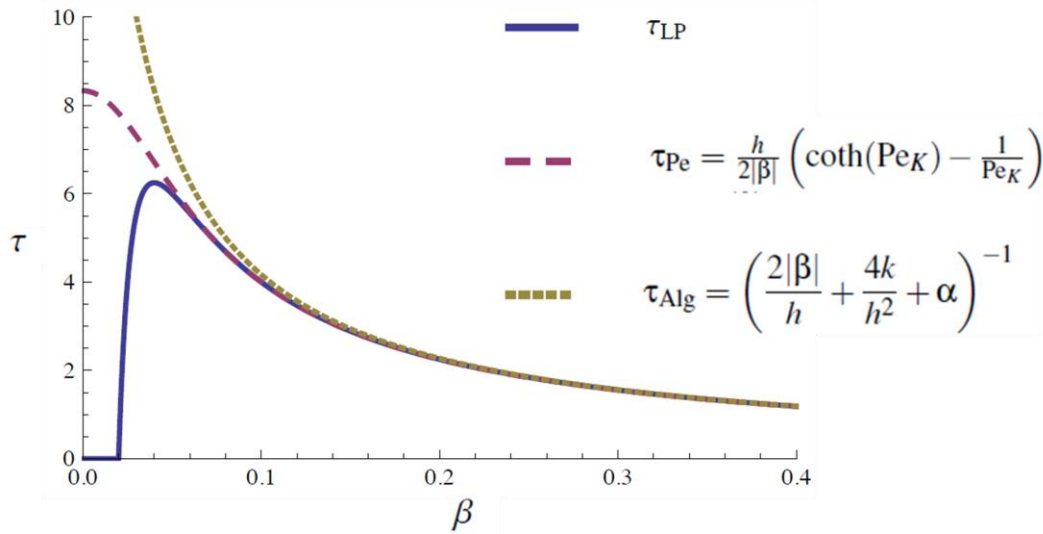


Figure III.1: Dependency of the least square term as a function of the convective velocity  $\beta$  measured for a 1D problem. The curve shows the impact of the regularization term in the low velocity regions ( $\beta < 0.2$ ).

This solver includes a preconditioned iterative linear implementation for the resolution of the coupled pressure-velocity matrix system. The implemented scheme provides a 2<sup>nd</sup> order spatial accuracy on all variables and a semi-discrete generalized alpha algorithm ensures 2<sup>nd</sup> order accuracy for time integration.

## 3.2. First Preliminary study: Detached flow over a 25° inclined ramp

The numerical study of the flow over the 25° inclined ramp is performed on a reduced fluid domain surrounding the ramp wake flow. The upstream flow condition is defined according to experimental measurements. Comparison with some published experimental results (Kourta et al., 2015; Stella et al., 2017a; Thacker, 2010) validates the accurate resolution of the main turbulent flow characteristics. The flow control simulation is used to exhibit the mechanisms of periodic actuation for the control of the shear layer. The impact on the wake flow topology is then demonstrated. The 25° inclined ramp was chosen because we needed straightforward comparisons to experiments and it was only available for this angle. The available numerical results are treated according to the methodology developed in chapter II in order to correlate the actuation forcing to the resultant averaged field. This benchmark is a good example in order to observe how the control of the shear layer fluctuations induces an increase of the wall pressure on the ramp.

### 3.2.1 Numerical setup and convergence according to experimental conditions

The experimental ramp model is presented in Figure III.2. Length is normalized according to the height of the ramp. Inlet velocity is equal to 30 m/s and turbulence intensity to 0,1 % (Stella et al., 2017a). Height of the ramp is  $h = 0,1\text{m}$  leading to a Reynolds number of 170 000. The slant angle of the ramp is at 25°.

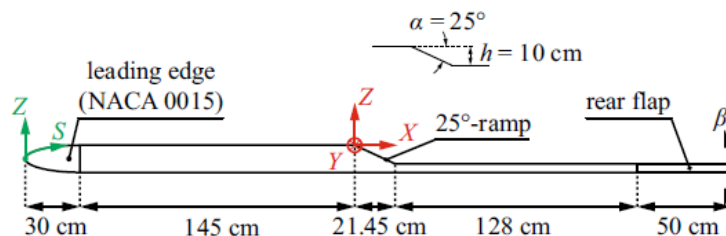


Figure III.2: Scheme of the experiments of the 25° inclined ramp model presented in (Kourta et al., 2015b) .

Inlet boundary conditions are fixed at  $x/h = 15$  upstream the detachment point of the ramp. The wake flow is computed until  $x/h = 18$  and the width is equal to  $x/h = 20$ . Inlet velocity is equal to 30 m/s and turbulence intensity to 0,1 %. (Stella et al., 2017a). Height of the ramp is  $h = 0,1\text{m}$  leading to a Reynolds number of 170 000. The slant angle of the ramp is at 25°.

According to a dimensional analysis, turbulence intensity in the boundary layer is fixed from velocity profile measurements related to DNS simulation performed by Schlatter (Schlatter and Örlü, 2010) as explained by Stella (Stella et al., 2017a).

- Numerical setup description

As these experimental dimensions are quite large, a more compact geometry is chosen for the simulation. Dimension of the numerical model is reduced to  $x/h = 4$  upstream the detachment point, and width is equal to  $x/h = 4$  as presented in Figure III.3.

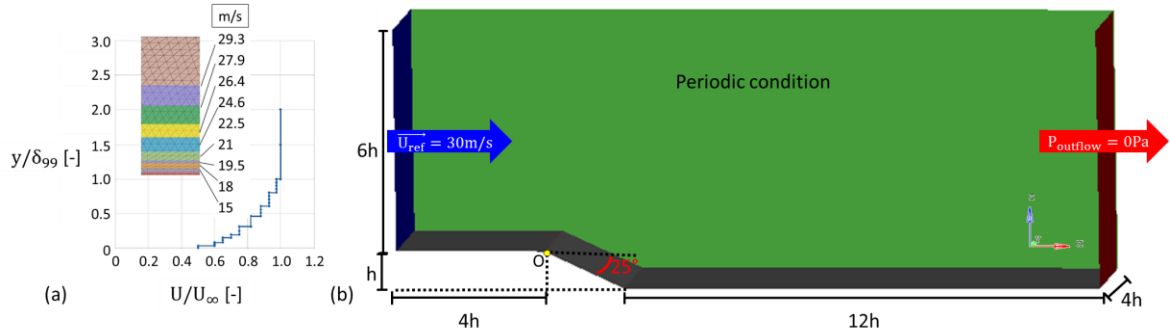


Figure III.3: (a) Boundary layer profile imposed at inlet boundary condition; (b) Scheme of the domain dimensions and boundary condition.

As illustrated in Figure III.4, mesh size of the computation domain is dimensioned in order to reach the LES constraints and Van DRIEST wall function. A logarithmic law will be used for  $Y^+$  comprise between 10 and 500 and the Van Driest dumping function will be used below  $Y^+ = 30$  in the buffer and viscous sublayer in order to impose a zero value at the wall boundary. The boundary layer is discretized with a first layer thickness at 0.2mm with a total thickness of 40mm according to experimental measurements of the boundary layer velocity profile.

Most of the kinetic energy is solved by the filtered LES equations with a mesh cutoff frequency between 1 and 3mm. The closure relation for the turbulent stress tensor is used to compute the eddy viscosity in the core region with the dynamic Smagorinsky turbulence subgrid scale model (Eq. 2). This model proposed by (Massimo Germano et al., 1991) enables to have a more accurate estimation of the dissipative scales correlated to the local level of turbulence. Thus there is a lower dependence on the grid cutoff frequency at  $60 \cdot \eta$  as proposed empirically by (Pope, 2001b) for LES simulation (with  $\eta$  the Kolmogorov scale). According to the numerical domain, these constraints lead to a total number of nodes of 9 million corresponding to 60 million tetrahedral elements. A refinement region is also been defined at 1mm from the detachment edge to discretize inflow synthetic jet conditions. Two other meshes were used to corroborate the numerical results. A coarser one with 6 million of nodes, corresponding to 39 million of elements, showed to weak quality in the resolution of the boundary layer and the shear layer. A thinner mesh with 20 million of nodes, corresponding to 99 million of elements was also tested. However, this is not the final choice selected for the following work. Since the goal of the ramp benchmark was to determine the best trade-off for the numerical setup of the POSUV simulation, a maximum mesh resolution of 1 millimeter imposed in the wake was not a realistic option considering the cluster memory limitation

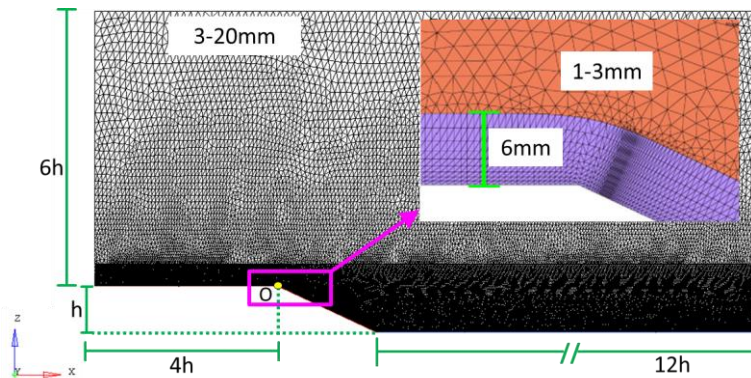


Figure III.4: Domain discretization corresponding to 60 million cells mesh

As mentioned in the introduction, special care needs to be taken on the physical computation time according to the shear layer dynamics. Mean velocity and pressure fields were averaged on a time scale of 1 s at a sampling frequency of 2000Hz. 0.5 seconds of convergence time is require before averaging.

- Incoming boundary layer agreement and discrepancy compared to the experiment

The inlet boundary condition is imposed in order to respect the time averaged turbulent boundary layer profile measured at  $x=-4h$  (Kourta et al., 2015). The second experimental profile at  $-2.5h$  shows that this turbulent boundary layer is still growing according to the value  $Re_x$  Figure III.5.

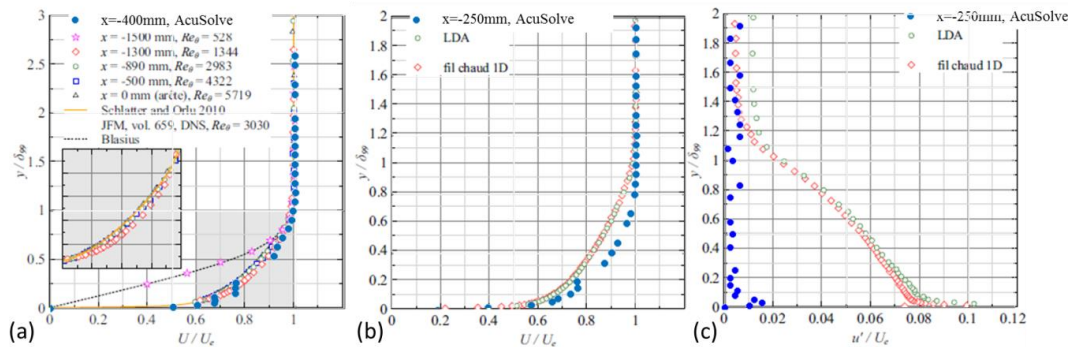


Figure III.5: Boundary layer velocity profile: (a) at  $x=-4h$ , (b) at  $x=-2.5h$  and (c) and turbulence intensity measured by PRISM compared to CFD results

Figure III.6a shows the non-dimensional velocity  $U^+ = \bar{U}/u_\tau$  according to the non-dimensional distance to the wall  $y^+ = y \cdot u_\tau / \nu$ . Computational averaged value is well computed in the logarithmic region with the computed friction velocity (in blue) but is slightly too small with the analytical friction velocity measured by (Stella et al., 2017a) (in green). Friction value was computed in the first cell layer as it should be in the viscous sublayer at  $y^+=5$ . But the first layer based on the analytical friction velocity is at  $y^+$  of 24. Therefore, the first cell layer should be at  $y=0.05$  mm instead of 0.2 mm in order to compute the correct modelled Reynolds tensor value. However the normalized velocity fluctuations  $U'^+ = \sqrt{u'^2}/u_\tau$  displays in Figure III.6b reveals that if the inflow boundary condition allows the reproduction of the time averaged profile, the resolved part of the turbulent intensity is not sufficiently computed.

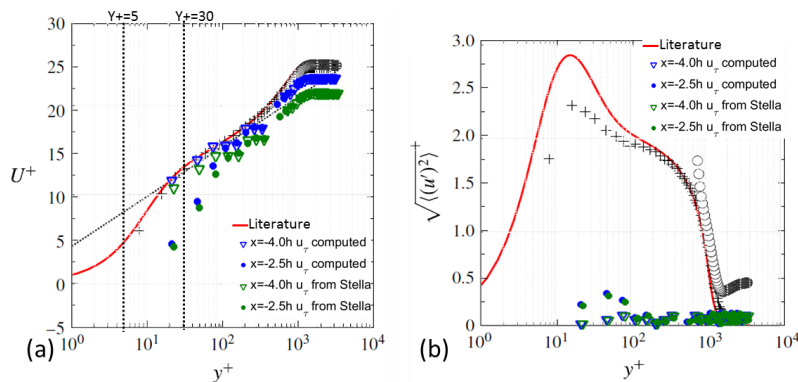


Figure III.6: (a) Normalized averaged velocity profile in the boundary layer as a function of the normalized wall distance; (c) Normalized turbulent intensity profile in the boundary layer.

Despite this discrepancy, the time averaged quantity momentum of the boundary layer is in accordance with experiment. The following investigation is achieved keeping in mind the difference in the upcoming fluctuations.

- Numerical convergence and comparison of subgrid scale model

The selection of the subgrid scale model is determined after a comparison of the numerical simulation with classical Smagorinsky and Dynamic Smagorinsky model. The results of the simulation yield a much more important turbulent intensity with the Dynamic model as shown in Figure III.7a. A monitoring point at the peak of the turbulent intensity measured in experiments is defined to evaluate the dissipation rate occurring in the simulation. The comparison of the Power Spectra Density computed on the velocity signal at this point is presented in Figure III.7b. The Dynamic Smagorinsky model yields a better computation of the turbulent decay process. The magnitude of the low frequency eddies association to the TKE production term is also higher. This is related to the velocity fluctuations distribution observed in the transverse cut-plane and explains why the mixing mechanism is closer to the experimental observations.

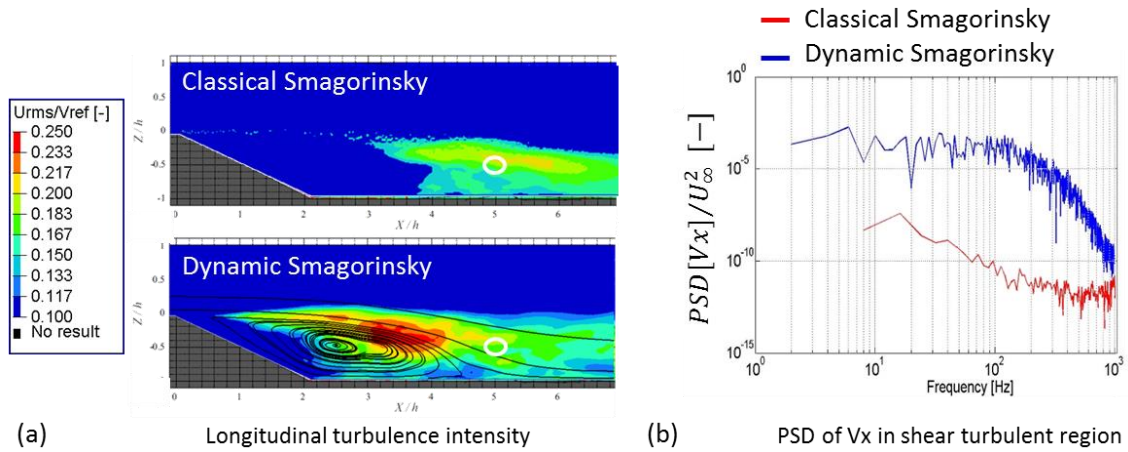


Figure III.7: (a) Comparison of a the resolved turbulent kinetic energy with the constant Smagorinsky subgrid scale model; (b) Comparison of the PSD downstream of the recirculation (white circle on the tke field).

### 3.2.2 Analysis of the baseline wake flow compared to literature

The numerical results were compared to the experimental measurements from (Kourta et al., 2015). In this study, the main features of the ramp flow were described thanks to PIV in the vertical transverse  $Y0$  cut-plane (Figure III.8a) and local pressure sensors distributed in the stream-wise and cross-wise directions (Figure III.8b).

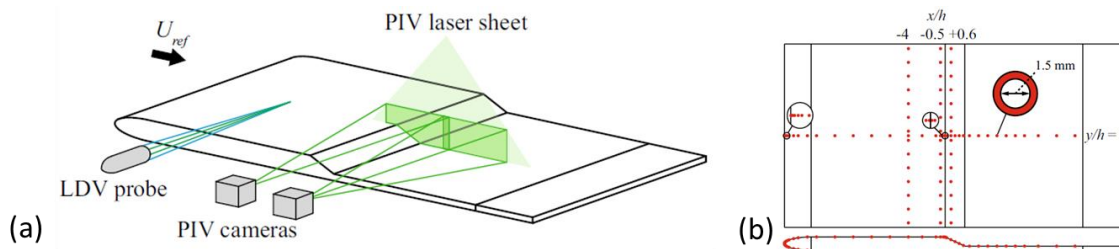


Figure III.8: (a) Scheme of the PIV system capturing the separated flow in the  $Y0$  cut plane; (b) the pressure sensors on the ramp wall used in experiments of (Kourta et al., 2015b).

The time averaged results of the ramp flow obtained with CFD compared to experimental results is illustrated in Figure III.9. The time averaged wake flow topology is globally in agreement with the literature result. The recirculation length is estimated with the iso-contour at zero velocity on the time averaged velocity Y0 cut plane. The characteristic length of  $L_r = 6h$  is obtained in CFD while the experiments exhibit a reattachment around 5.5h.

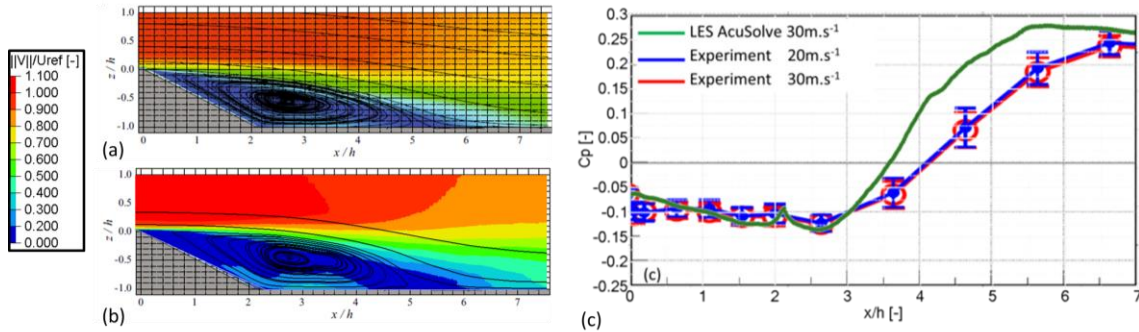


Figure III.9: Time averaged velocity in central cut plane: (a) Experiments (Kourta et al., 2015b); (b) CFD; (c) Profile measured on wall ramp monitoring point and comparison with experiments (Kourta et al., 2015b).

The stream-wise wall pressure coefficient profile reveals a low pressure region until  $2.5h$  for both experiments and CFD. However, the following adverse pressure gradient is stronger in computation than in experiment.

As there is no resolved fluctuation in the boundary layer in the upstream flow (cf. discussion in 3.2.1), it is important to check if the shear layer profiles generated by the separation at the sharp edge of the ramp reproduce the experimental behavior described by (Stella et al., 2017a). The shear layer momentum thickness  $\theta$  is plotted in Figure III.10. In the close vicinity of the edge, there is a lack of shear momentum but it is overcome at  $0.3L_r$ . The breakdown at  $0.5L_r$  is correctly reproduced and the following shear momentum at the reattachment point  $x = L_r$  matches with the experiment.

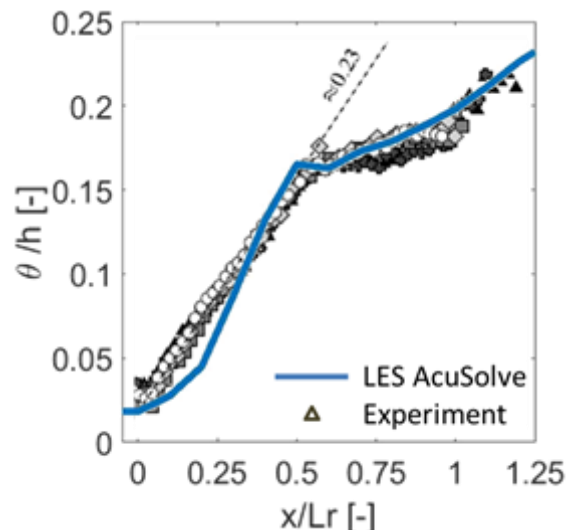


Figure III.10: Shear layer quantity momentum profile along the x axis compared with experiments (Stella et al., 2017b).

The deficit in shear momentum in the close vicinity of the ramp edge can be explained by the turbulence intensity displayed in Figure III.11a. The PIV result exhibits 0.2 turbulent intensity at  $x=0.1h$  while the computed fluctuation from the numerical simulation is below 0.1 turbulent intensity. Downstream, the turbulence peak due to the mixing effect of the shear layer occurs at  $3.5h$  instead of  $5h$  in experiment. The turbulent kinetic energy decay measured at the monitoring point of  $5h$ , compared the spectral distribution in experiments with CFD (Figure III.11b). The energy level at the monitoring point is slightly lower. One can question the turbulent decay at high frequency (above 400Hz) which is stronger than in experiment. In addition, the start of the inertial zone around 60Hz in experiments compared to 120Hz in the numerical simulation, indicates a more significant

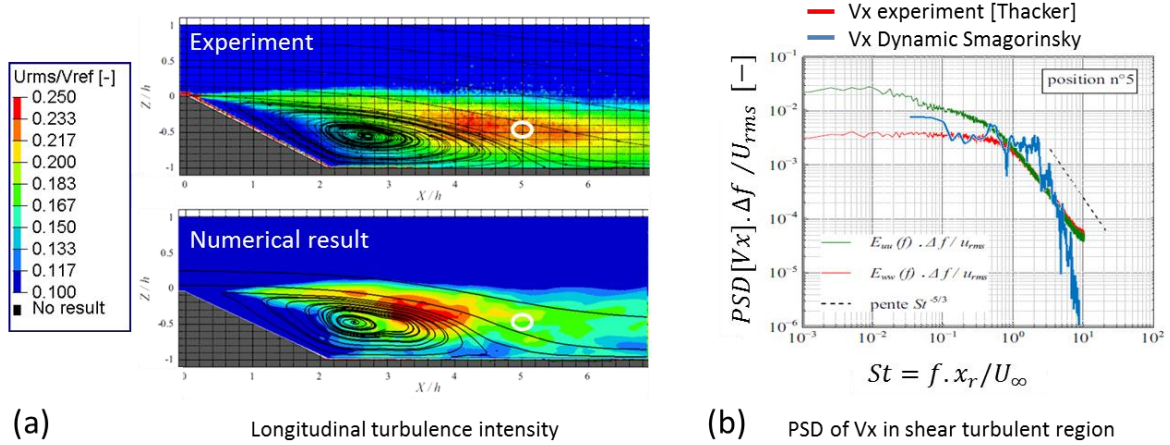


Figure III.11: (a) Comparison of the turbulent intensity between experiments and resolved velocity fluctuations. The white circle indicates the probe location for the spectral analysis; (b) PSD comparison at the reference probe in the wake flow, the blue curve is the numerical results, the red curve is the experimental results.

The difference of energy decay in the PSD analysis can be interpreted with the approximation limitation due to our numerical scheme. We will explore more deeply the impact of the regularization term in the validation of the POSUV simulation in section 3.4.3.

### 3.2.3 Physics of periodic jet actuation

The active flow control strategy was defined based on the design of experiments performed in the study of (Kourta et al., 2015). Here, we will go further in the understanding of the actuation process thanks to the modal analysis. The actuation is operated using synthetic jets injected in a thin slot of 1mm width and placed at 1mm from the ramp edge (Figure III. 12a). The design of experiments measured the influence of the jet momentum coefficient  $C_\mu$  and of the normalized actuation frequency  $F^+$  (Eq.59).

$$C_\mu = \frac{d_{slot} V_{jet}^2}{h U_\infty^2} \quad F^+ = \frac{f \cdot x_r}{U_\infty} \quad St = \frac{f h}{U_\infty} \quad \text{Eq.59}$$

Where :

$d_{slot}$  is the width of the slot [m].

$V_{jet}^2 = \frac{1}{T} \int_0^T V_{jet}(t)^2 dt$  is the time averaged square jet velocity [ $m^2/s^2$ ].

$f$  is the actuation frequency [Hz].

$h$  is the reference height of the ramp [m].

$x_r$  is the recirculation length

$U_\infty$  is the reference far field velocity [m/s].

In this work, we will focus on the response surface (Figure III. 12b) defined on the pressure coefficient value measured at the critical point  $x=2h$  on the ramp wall. The selected solution at  $C_\mu = 0.01$  and  $St = 0.6$  leads to the higher pressure increase of 0.3. The computed time averaged velocity, shown in (Figure III. 12a), gives a significant reduction of the recirculation length at  $L_r = 4h$  compared to the baseline results at  $L_r = 6h$ .

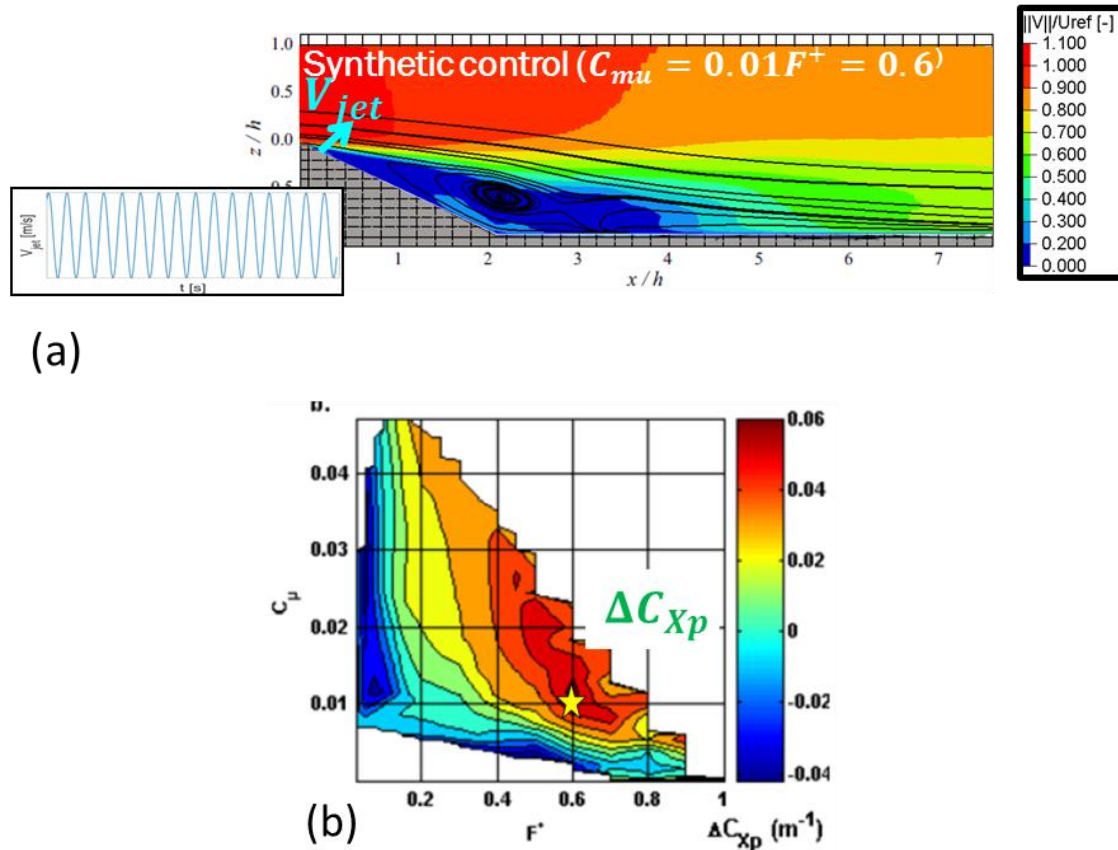


Figure III. 12: (a) Description of the active flow control boundary condition; (b) Design of experiments explored in literature. The star indicated the best operating point based on the pressure coefficient.

The comparison of the time averaged pressure coefficient reveals a drop of pressure at  $x=0h$  in the region of the jet boundary condition (Figure III.13b), also visible on the experimental results (Figure III.13a). It is a suction effect due to the quantity momentum injection. A strong pressure recovery occurs from  $x=0.1h$  until  $3.5h$  contrary to the baseline flow where the adverse pressure gradient starts at  $2.5h$ . The resulting critical pressure coefficient is increased by 0.13, instead of 0.27 in experiment.

There is often debate around the relation between the recirculation length and the resultant pressure drop. In the literature survey, we mentioned a lot of examples showing how the flow control on different bluff bodies, leads to a growth of the recirculation length associated to an increase of the pressure. It can be surprising that, in the case of the ramp flow control, the pressure increase is associated to a 33% reduction of the recirculation length.

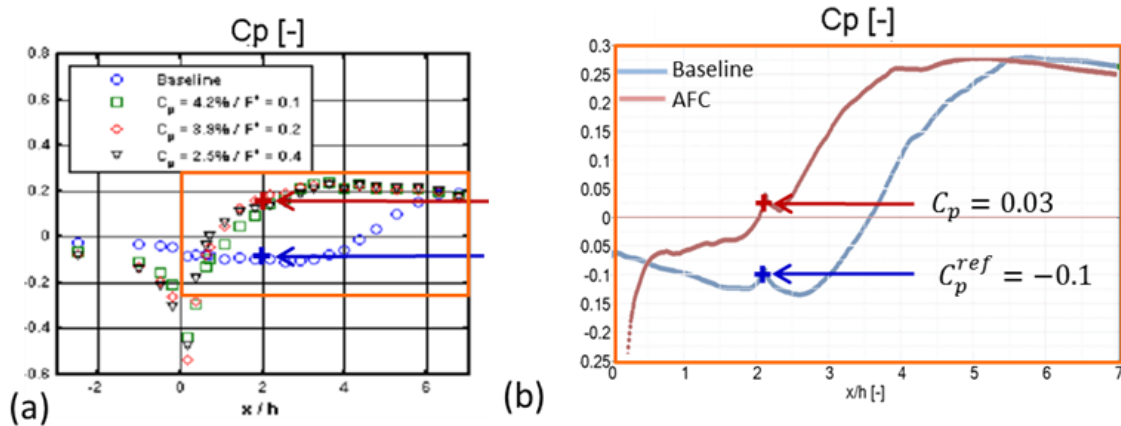


Figure III.13: Comparison of the time averaged pressure coefficient profile along the ramp wall for baseline and AFC: (a) in experiment; (b) in CFD.

This question is more deeply investigate thanks to the comparison of the recirculating flow topology (Figure III.14a and b). In the flow control case, the vortex span is lower but the pressure drop at the vortex center does not go below  $C_p = -0.1$  instead of  $-0.17$  in the baseline flow (Figure III.14c). In addition, the vortex center seems to be closer to the wall with the flow control but thanks to a strong pressure gradient along the ramp normal, the resulting  $C_p$  value acting on the wall is about  $-0.045$  instead of  $-0.15$  for the baseline.

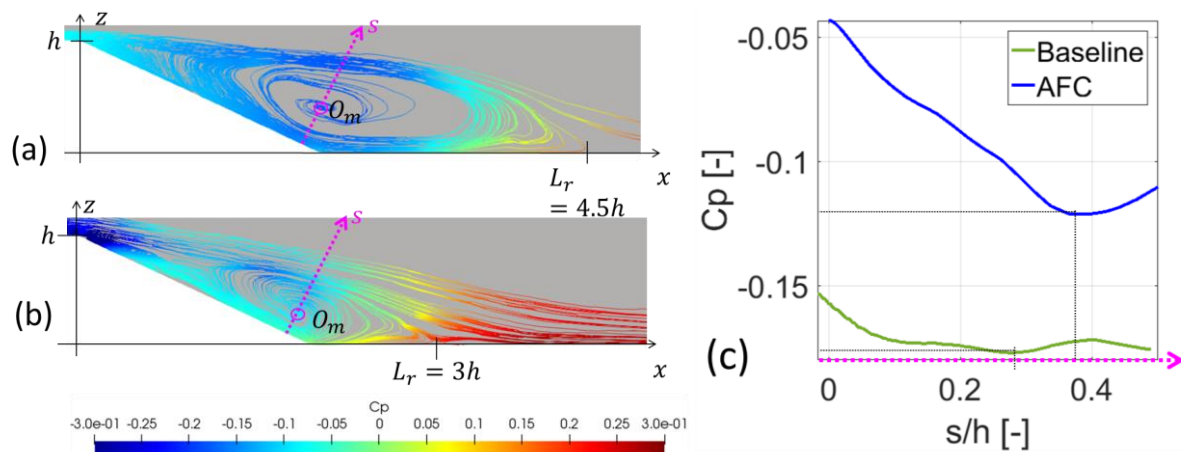


Figure III.14: Time averaged recirculation streamlines colored by pressure coefficient for (a) Baseline flow; (b) AFC flow; (c) Pressure coefficient profiles along the normal axis of the ramp and going through the vortex center  $O_m$ .

These observations underline the importance of the chosen criteria to characterize the wake flow for aerodynamic optimization. The time averaged pressure gradient along the normal to the wall combined with the minimum of pressure give pertinent insight on the aerodynamic loss.

To go further, a description of the transient flow is performed to compare the baseline and the controlled behavior. Figure III.15 displays the transient iso-contour of zero velocity. If the time averaged flow is anisotropic with an invariance along the Y direction, the structures emerging from the separation line on the edge of the ramp in the transient flow evolve into 3D structures in the wake flow. These transverse contributions balanced each other in average leading to the 2D topology wake flow commonly observed behind the ramp. The development

of 3D structures in the recirculation is also associated to a mixing effect with high velocity fluctuation.

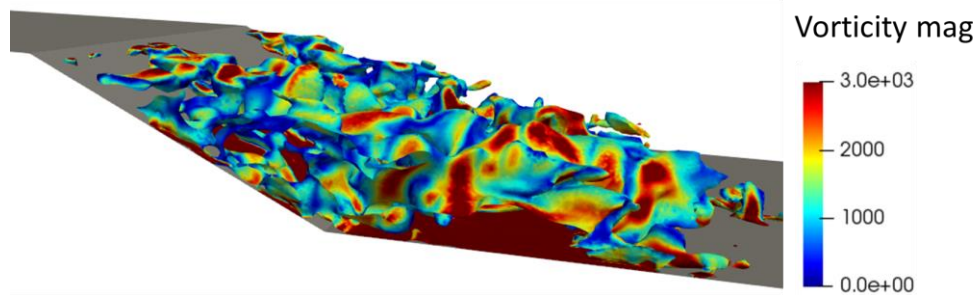


Figure III.15: Transient iso-contour of zero velocity in the baseline flow.

In addition, zero velocity fluctuation at the ramp breakup angle, in the baseline flow (Figure III.16a) suggests that the separation line is maintained on the edge of the ramp. Hence, the flow over the ramp flow is permanently fully detached. The observation of the velocity fluctuations in the controlled flow (Figure III.16b) reveals a strong forcing operating on the separation line. Velocity fluctuations close to the edge are much more important but the energetic turbulent area is smaller than in the baseline flow.

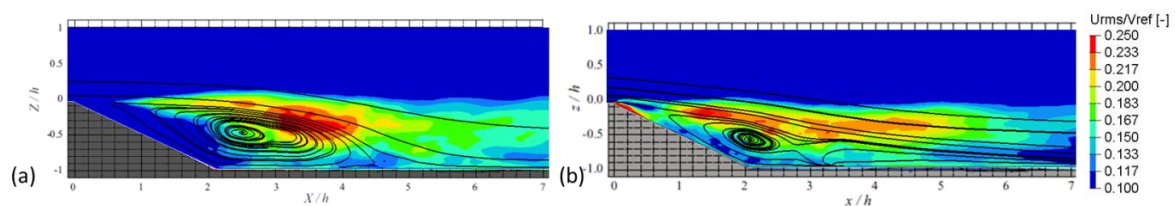


Figure III.16: Comparison of turbulent intensity in the Y0 cut-plane: (a) Baseline flow; (b) Controlled flow.

Transient flow observations reveal a periodic generation of fluid rolls at the jet boundary condition in accordance with the pressure drop observed in Figure III.17. The injected fluid roll is transported downstream thanks to the flow inertia. Between two successive fluid rolls, the flow remains attached and the separation line is periodically shifted along the ramp wall. The trigger of the 3D mixing mechanisms occurs after the burst of the fluid roll due to the turbulent decay process, contrary to the baseline flow where it occurs immediately at the edge of the ramp.

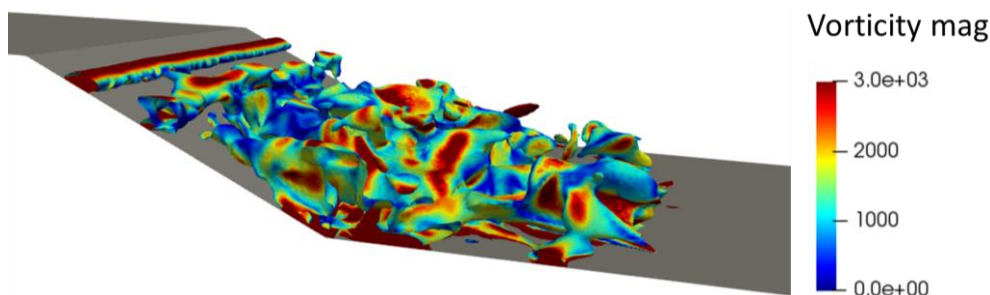


Figure III.17: Visualization of transient iso-contour of zero velocity: (a) baseline; (b) AFC

Thus, the periodic forcing tends to constraint the turbulent energy production after the break-up of the blown vortex leading to a faster pressure recovery. A parallel can be done with the

high frequency control of the shear layer as discussed in the literature review 1.3.1 and particularly with the observations of (Parezanovic et al., 2014).

- Modal analysis of the periodic forcing

The Dynamic Modal Decomposition is applied on 1000 snapshots of the Y0 cut-plane sampled at 2000Hz. Figure III. 18 shows the comparison of the DMD spectra obtained in the baseline and controlled flow. The actuation frequency is significantly increased. Simultaneously, the contribution of the low frequency modes is damped at  $St = 0.01$  and  $St = 0.02$ . The change of frequency distribution enforced by the flow control is similar to what was observed in the DMD of the controlled flow of the POSUV performed in experiment.

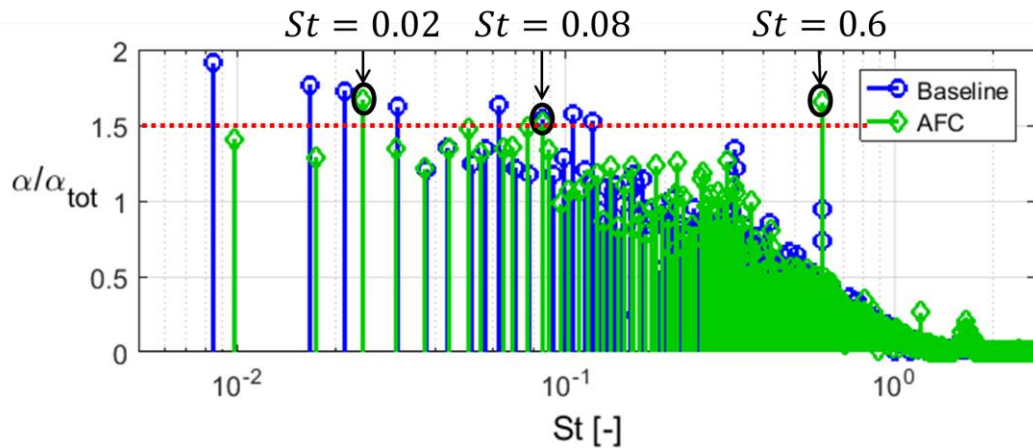


Figure III. 18: Comparison of the DMD spectra obtained with the baseline flow and the controlled flow. The low frequency components are damped with the actuation while a high frequency peak at  $St = 0.6$  emerges. The remaining low frequency peaks identified in the controlled flow are at  $St = 0.02$  and  $St = 0.08$ .

To go further, the comparison of the periodic structures associated to the previous spectral characteristics is presented in Figure III.19. The low frequency periodic pulsations at  $St=0.02$  and  $St=0.08$  are related to the recirculation area. We can see that the actuation managed to change the wake oscillating fluctuations. The mode at  $St=0.02$  seems to be a homogeneous fluctuations of the wake velocity intensity (blue region in Figure III.19a). The actuation expanded the region governed by this pulsation. The periodic motion due to  $St=0.08$  (Figure III.19b) is related to the feedback flow in the recirculation area. The associated recirculation oscillation (red/blue area in Figure III.19b) appears to be more structured in the controlled case. It can be interpreted as a stabilization effect of the recirculating bubble.

The frequency at  $St=0.6$  (Figure III.19c) exhibits in the baseline case, the shear layer fluctuations triggered by the detachment on the edge of the ramp and propagating along the separation line but also in the overall recirculation area. This means that all the wake flow impacted by the turbulent structures induced by the mixing layer. The actuation tends to force the shear layer fluctuations near the separation line but it is quickly dissipated.

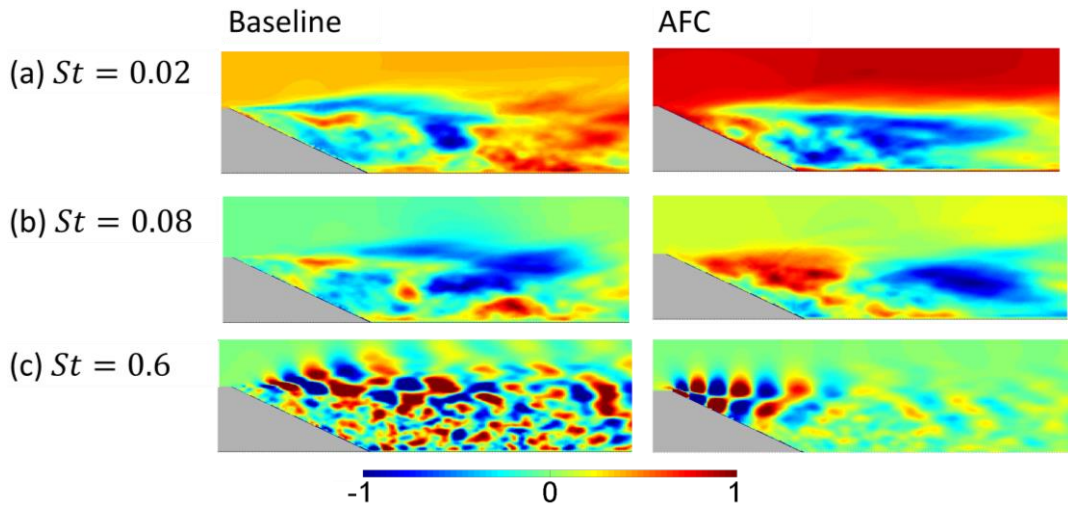


Figure III.19:  $V_x$  DMD modes showing of the frequencies highlighted in the DMD spectra.

The fact that the mixing effect is more localized is consistent with the assumption that the wake recirculation is stabilized by the periodic forcing. The flow coherence analysis is required to understand why the periodic forcing prevents further propagation of shear layer fluctuations and the correlation with the recirculation pulsation. Similarly to the DMD/POD projection performed in 2.3.3, the transfer matrix is computed based on the controlled flow decomposition (Figure III.20). This projection allows the identification of the 4<sup>th</sup> POD mode impacting the static 0Hz DMD component. The projection of the periodic structures embedded in this POD mode is used to describe the actuation process into the static component.

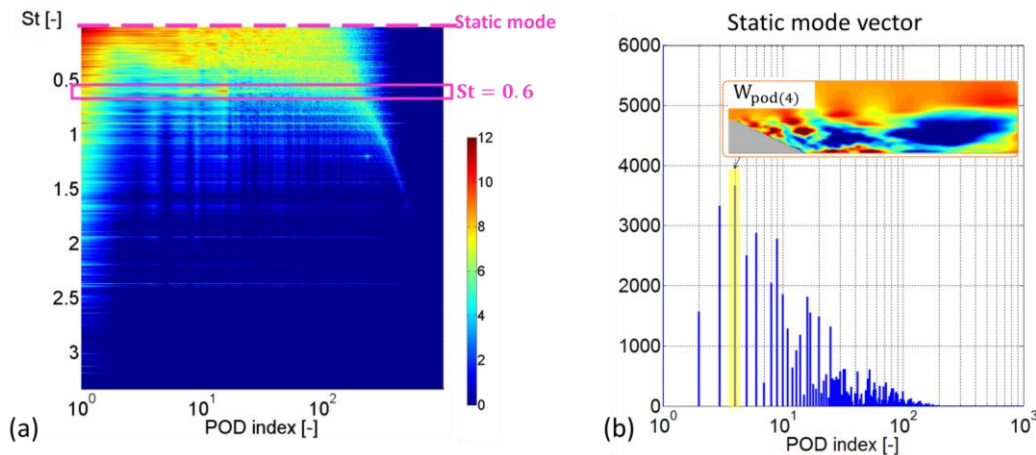


Figure III.20: Weight matrix between DMD base and POD base. The low frequency modes are strong within the POD components below 10.

The spectral projection of the 4<sup>th</sup> POD mode on the DMD base is plotted in Figure III.21. It gives the correlated periodic mechanisms affecting the static mode. We can see the correlations between low frequency  $St = 0.02$ , a periodic feature at  $St = 0.15$  and the actuation mode at  $St = 0.6$ . It is interesting to see how the actuation promote the high frequency fluctuations at  $St = 0.6$ ,  $St = 0.9$ ,  $St = 1$  and  $St = 2.37$ . The energy produced by these high frequency structures is low but they participate to the turbulent dissipation cascade due to the pulsed jet.

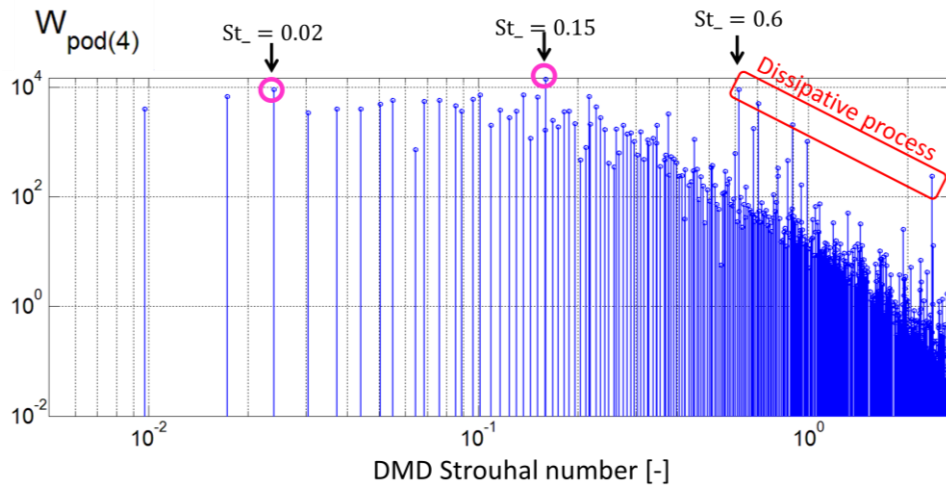


Figure III.21: Spectral projection of the correlated mechanisms associated with POD(4). The dissipation process triggered by the actuation frequency is identified by the logarithmic energy decay between  $St = 0.6$ ,  $St = 0.9$ ,  $St = 1$ ,  $St = 2.37$ .

The visualization of the spatial DMD modes in Figure III.22, describe the correlated periodic flow fluctuations identified with  $W_{pod(4)}$ . The jet quantity momentum induced an increase of the decaying process due to the mixing effect at  $St = 0.9$ ,  $St = 1$  and  $St = 2.37$ . This prevents the spreading of the shear layer turbulent energy in larger scale structures at  $St = 0.15$  and at  $St = 0.02$ .

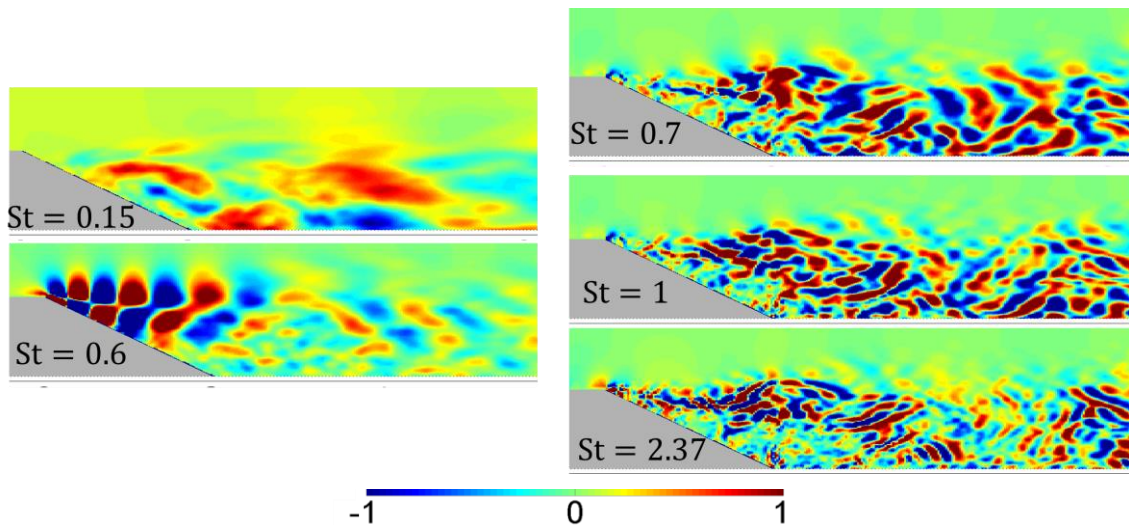


Figure III.22: DMD modes participating to the 4<sup>th</sup> POD mode displaying the actuation dissipation process.

These observations corroborate the assumptions of the wake stabilization achieved by the high frequency periodic jet. It results in a lower energy production coming from the large-scale structures responsible for the wake aerodynamic loss.

### 3.2.4 Partial conclusions and guidelines for detached flow simulation

The numerical simulation of the flow over the 25° inclined ramp demonstrates the capability of the LES approach with Dynamic Smagorinsky subgrid scale model to compute the turbulent detachment. Even if, the turbulent kinetic energy in the upstream boundary layer does not reach the same intensity than in experiment, the time averaged boundary layer was sufficiently simulated in order to produce a similar separation phenomenon. The difference in the upstream flow features induces a lack of turbulence in the close vicinity of the ramp edge after the separation. We should mention that the lack of turbulence in the upstream flow is only a consequence of the boundary condition definition without injection of any synthetic transient velocity fluctuations. This is not a limitation for the simulation of the flow around 3D round geometry inside a wind tunnel, where flow separation governed the turbulent kinetic energy of the boundary layer. In addition, the comparison of the control flow with the best operating point obtained from experiments suggests that the selected numerical approach capture the physics of the flow actuation.

Modal analysis shows that the actuation mechanism can be linked to an energy reduction at the natural frequency, transferred by the higher frequency. One may remark the similitude in the actuation frequency with the flow control optimal forcing at  $St = 0.6$  identified in the study of (Minelli et al., 2018). In the baseline flow, the free turbulent decay leads to high energy production at low frequency associated with strong aerodynamic loss. In the controlled flow, the quantity momentum due to high frequency periodic forcing constraints and accelerates the mixing effect in the shear layer. This prevents the propagation of the shear layer turbulence impacting the wake flow topology.

## 3.3. Second preliminary study: The Ahmed body with 47° slant angle

The benchmark of the Ahmed Body with a 47° slant angle is introduced in order to evaluate the feasibility of the numerical simulation of the flow around a reduced scale model within a wind tunnel.

### PAPER

## WAKE FLOW ANALYSIS AND CONTROL ON A 47° SLANT ANGLE AHMED BODY

### 3.3.1 Introduction

This paper focuses on the numerical investigation of the flow characteristics for a 47° Ahmed Body in order to have a better understanding of wake behavior of SUV type vehicles (Figure III. 23). This modified version of the Ahmed body was proposed in order to reproduce rear proportions that can be observed on commercial cars. The dimensions of the Ahmed body are presented in Figure III. 23 in millimeter. After a numerical validation of this benchmark at Reynolds number of 420 000 corresponding to a velocity of  $V_\infty = 30\text{m/s}$  (based on the body height), time averaged wake features and fluctuations analysis of the uncontrolled flow thanks to dynamic and spectral analysis of forces and torques is performed.

Then, the Sparse Promoting Dynamic Modal Decomposition method is discussed and compared to other modal approaches. This method is relevant in order to emphasize the rear pressure modal behavior related to their energy contributions in pressure, pitch and yaw and the energy transfer quantified in growth rate quantity that occur between modes. Also, based on pitch and yaw wake motion, it permits to explore the correlation with the wake flow modal behavior. This flow analysis and characterization is very useful to design appropriate closed loop flow control strategies.

Then active flow control strategy based on micro-slots is then analyzed. This work also includes a sensitivity analysis on rear Strouhal number and wake flow behavior with the active flow control.

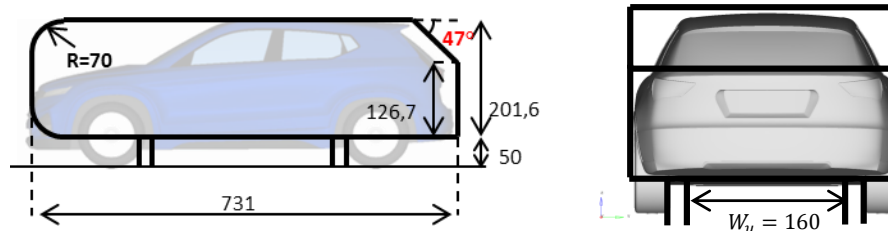


Figure III. 23: Geometry comparison of a generic SUV and the 47° Ahmed Body (in mm)

### 3.3.2 Numerical setup

The geometry, illustrated in Figure III. 23, consists in a 0.7 scale model (compared to the original one of (Ahmed et al., 1984b)) in a  $4m^2$  section wind tunnel. This later is a reproduction of the experimental wind tunnel.

The simulation is achieved with a Large Eddy Simulation approach resolved with the finite element solver. This approach consists in the resolution of the filtered Navier-Stokes equations for incompressible flow. The resolution of these equations requires a closure relation for the turbulent stress tensor. A subgrid scale model is required to estimate the turbulent viscosity. In this work, it is computed with the classical Smagorinsky model. The mesh cutoff frequency was chosen thanks to mesh scale criteria defined by (Pope, 2001b) for LES simulation. Indeed, assuming that 90% of dissipation occurs for scale structures above  $60\eta$ , with  $\eta$  the Kolmogorov scale, the mesh resolution for this simulation has to be at 1mm.

These considerations lead to a mesh discretization constituted of 160 million unstructured tetrahedral elements illustrated in Figure III.24a. It should be noted that the grid convergence study using the same numerical solver, was previously performed for the square back version of the Ahmed Body, which confirms the final mesh choice (Eulalie, 2014).

As shown in Figure III.24b, we measure a turbulent kinetic energy with an energy decay of  $-5/3$  before the LES cutoff filter. For a flow at Reynolds number 420 000, turbulent scales in the production area and inertial area are resolved and dissipative scales are estimated by the subgrid scale model.

Wind tunnel conditions were reproduced so that the same effective blocking cross-section is applied. A pitot probe measuring pressure value at a specific location is used as a reference point to ensure the cross-section integrity. Discrete numerical resolution and experimental data are therefore comparable.

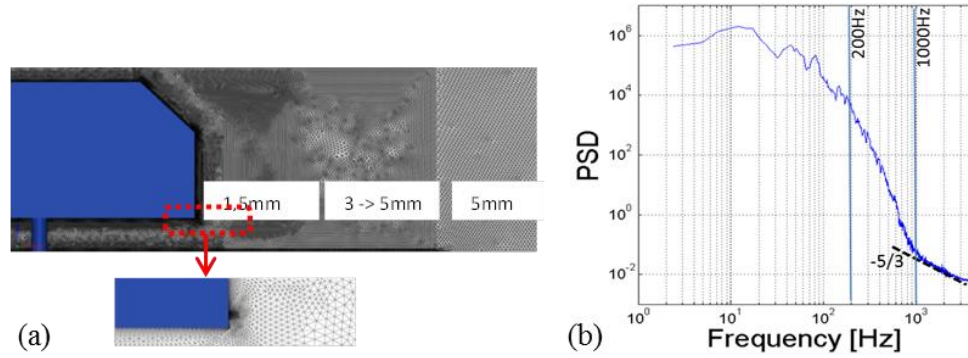


Figure III.24: (a) Ahmed body tetrahedral mesh with active flow control refinement; (b) turbulent kinetic energy PSD in wake flow.

Finally, 0.8 seconds of converged simulation were processed with a sampling frequency of 8000Hz.

### 3.3.3 Baseline flow

- Averaged results

Time averaged forces and pressure coefficients are computed as presented in Eq.60.

$$C_i = \frac{F_i}{0.5\rho V_\infty^2 S_{ref}}; \quad C_p = \frac{P - P_{pitot}}{0.5 \cdot \rho \cdot V_\infty^2} \quad \text{Eq.60}$$

Where:

$i$  corresponds to the  $x, y, z$  directions.

$\rho = 1.225 \text{ kg/m}^3$  is the air density.

$H = 0.2 \text{ m}$  is the reference height.

$V_\infty = 30 \text{ m/s}$  is the reference velocity.

$S_{ref} = 0.06 \text{ m}^2$  is reference section of the Ahmed Body.

A drag coefficient  $C_d$  of 0.272 is measured on this simulation as shown in Figure III.25. It is in good agreement with 3% error compared to the experimental value of 0.28 obtained by (Metka, 2013) at a Reynolds number of  $4 \cdot 10^5$  and 0.31 (Dobrev and Massouh, 2014) at Reynolds number of  $4.7 \cdot 10^5$ . The drag force distribution also indicates that the rear is responsible for 75% of aerodynamic loss.

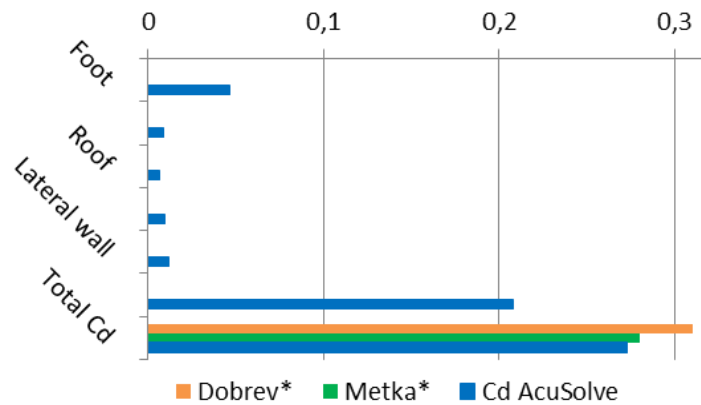


Figure III.25: Computed time averaged drag coefficient per surface and comparison with experimental results of literature marked by \*. Rear end surface contributes to 75% of total drag

The time averaged rear pressure distribution displayed in Figure III.26, reveals the low-pressure area located on the lower part of the rear end with important pressure fluctuations at horizontal middle and lower edges.

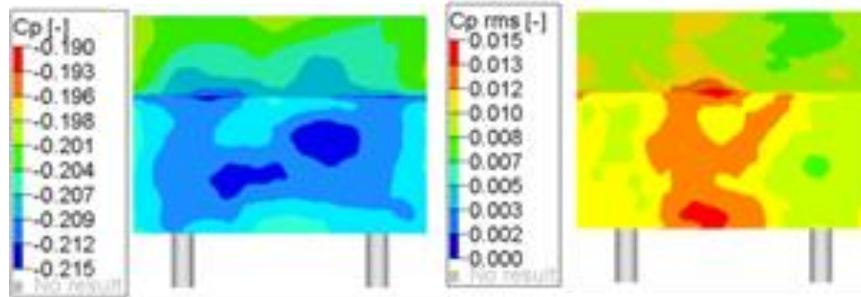


Figure III.26: Time averaged  $C_p$  mean value of -0.21 (75% of total  $C_d$  and its RMS of 0.007;

The Table 1 summarizes forces and their RMS on the overall Ahmed Body. Even if the drag force is the most important averaged contribution, significant fluctuations were measured on lateral and horizontal leading to important torque variations in the transversal directions that are analyzed in the paragraph below.

	average force coefs	associated RMS
$C_x$	<b>0.272</b>	0.007
$C_y$	0.001	<b>0.013</b>
$C_z$	-0.061	<b>0.016</b>

Table 1: Time averaged forces and torques coefficients.

- Torques and body dynamics

Torque coefficients are defined in Eq.61:

$$C_{mi} = \frac{M_i}{0.5\rho V_\infty^2 H S_{ref}} \quad \text{Eq.61}$$

Where:

$i$  corresponds respectively to the x, y and z directions: roll, pitch and yaw torque as illustrated in Figure III.27.

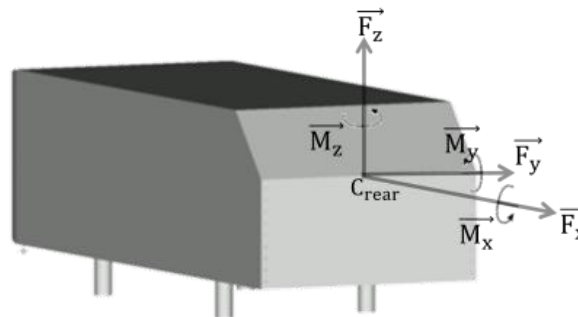


Figure III.27: Axes orientation for forces and torques definition at center of rear.

Torque components were also computed on the rear basis, as shown in Table 2. Only the pitch motion is relevant on this surface in average and in RMS values.

	Average torque coef	RMS
$C_{mx}$ [-]	$8.47 \cdot 10^{-6}$	$2.6 \cdot 10^{-4}$
$C_{my}$ [-]	<b>-0.022</b>	<b>0.0017</b>
$C_{mz}$ [-]	$-4.6 \cdot 10^{-5}$	$5.1 \cdot 10^{-4}$

Table 2: Torques coefficients and RMS at rear center.

- Spectral analysis

Figure III. 28 presents the spectral analysis performed on the overall body forces as a function of this Strouhal number. The Strouhal number  $St_W$  used in this work is based on the width between feet  $W_u$  (Figure III. 23) as we expect a major contribution of structures coming from the underbody flow.

$$St_w = \frac{fW_u}{V_\infty} \tag{Eq.62}$$

Main forces fluctuations are in lateral contributions  $C_y$  at Strouhal number of 1.2 whereas lift force  $C_z$  are at low Strouhal number  $St_W$  of 0.01 and 0.03. When we focus on the rear end and slant window, displayed in Figure III.29a and b, an additional peak in pitch direction  $C_{my}$  appears at Strouhal  $St_W = 0.22$ .

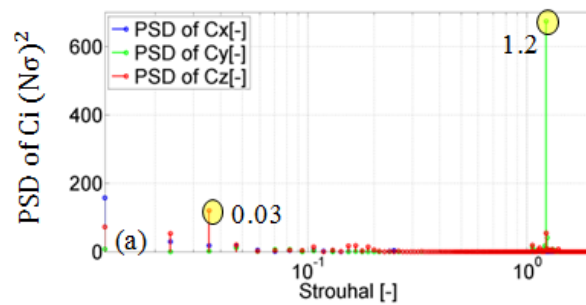


Figure III. 28: PSD forces on Ahmed body as a function of Strouhal  $St_W$

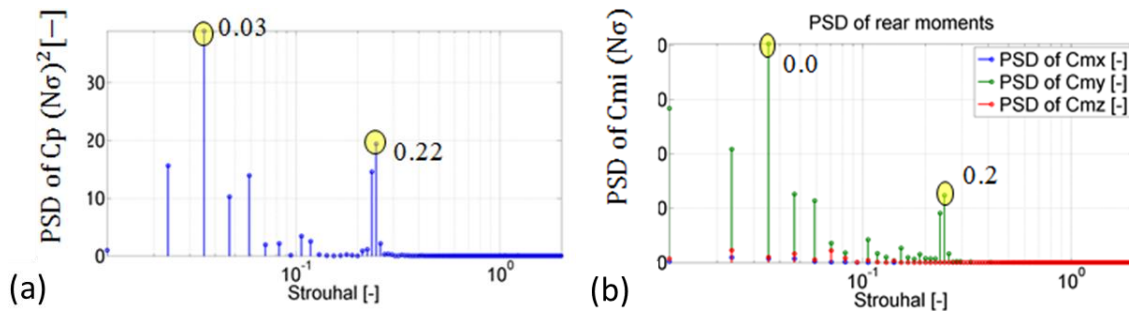


Figure III.29: PSD of rear pressure (a) and torques (b) coefficients at the rear center as a function of Strouhal  $St_W$ .

Figure III. 30 shows the correlation with detachments near lateral and lower edge dynamics as function of the Strouhal number  $St_W$ . The Strouhal number  $St_W = 0.2$  appears in the lower edge horizontal probes so that there is a relation between the lower edge detachment and the pitch torques measured on the rear end. The Strouhal number  $St_W$  of 1.2 corresponds to the foot shedding. The Strouhal number of  $St_w = 0.03$  corresponding to a low frequency of 5.6Hz, measured in vertical probes in regards to the C-pillar vortex.

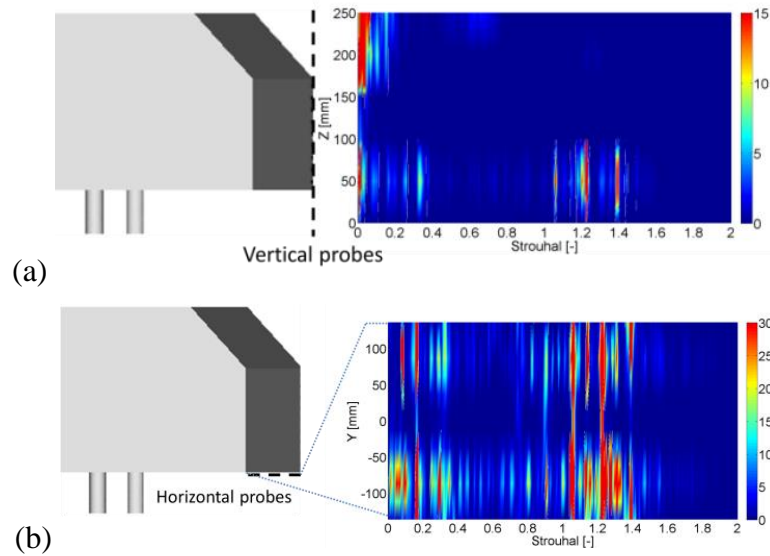


Figure III. 30: PSD of normal velocity in the boundary layer detachment at 3mm to wall, as a function of Strouhal  $St_W$ : (a) On vertical edge; (b) On horizontal edge.

- Wake flow dynamics

As shown in Figure III.31, the pressure minima during the 0.8 seconds of simulation have a probability density function centered at 250mm from rear. This x value is used to compute the virtual torque of the wake flow in pitch  $C_{my}$  and yaw  $C_{mz}$  direction.

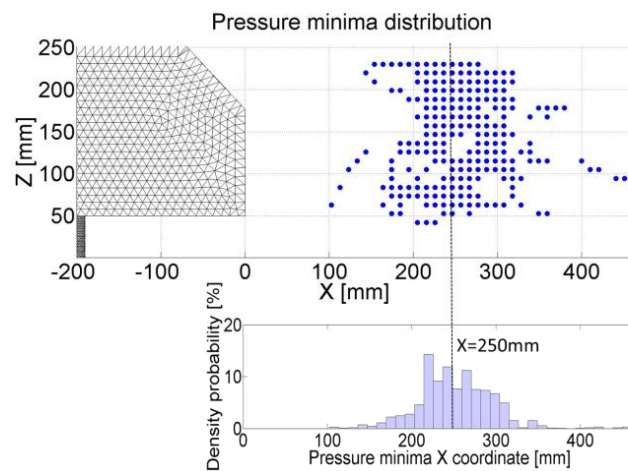


Figure III.31: Pressure minima distribution in wake flow during simulation time.

Thus, the dynamics of the low pressure area can be defined by pressure fluctuation in the transverse cut plane in this position. The time averaged and RMS of the pressure coefficient displayed in Figure III.32, show a circular low-pressure area with energetic RMS peaks localized on the layer corresponding to the strong averaged pressure gradient.

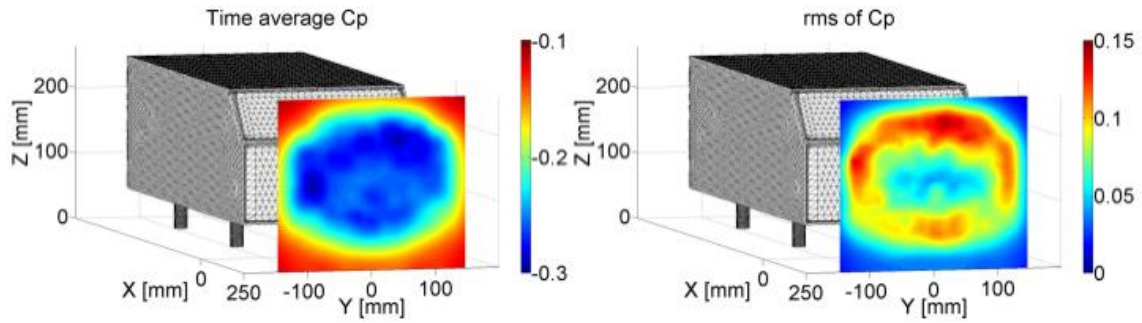


Figure III.32: Time averaged pressure coefficient and RMS transversal cut-plane at 250mm from rear.

Virtual torques  $C_{my}|^{S_x}$  and  $C_{mz}|^{S_x}$  defined in Eq.63a and b, are also estimated in this transversal cut plane in order to quantify the pitch and yaw motion of the wake.

$$\begin{aligned}
 C_{my}|^{S_x} &= \int_{S_x} z \cdot P(y, z) dy dz \quad (a) \\
 C_{mz}|^{S_x} &= \int_{S_x} y \cdot P(y, z) dy dz \quad (b)
 \end{aligned}
 \tag{Eq.63}$$

We observe that there is a similar behavior in this cut plane and on the rear end on averaged and RMS values of pitch and yaw coefficients detailed in Table 3.

	Average torque coef	RMS
$C_{my}$	<b>0.11</b>	<b><math>7.3 \cdot 10^{-2}</math></b>
$C_{mz}$	$1.6 \cdot 10^{-3}$	<b><math>5.8 \cdot 10^{-2}</math></b>

Table 3: Torques coefficients for the uncontrolled flow computed at the of the cut plane.

Indeed, there is a major component on averaged pitch coefficients associated with equivalent order of magnitude on both pitch and yaw fluctuations. This is correlated to a varying wake motion perfectly balanced on yaw direction plus an unbalanced wake motion in pitch direction. This is in agreement with the RMS distribution of pressure in the transverse cut plane displaying symmetry along the Y direction but an unbalanced distribution along the Z direction. Moreover, the positive averaged pitch coefficients mean that the low pressure tends to rotate counter clock-wise in the wake flow (trigonometric direction).

Concerning the spectral characteristics of these virtual torque coefficient shown in Figure III.33, the momentum spectrum obtained in the transversal cut plane, reveals that the maximum components of the wake are measured on the pitch torque in average as shown in table 4, and on fluctuations at Strouhal number of 0.22 based on  $W_u$ .

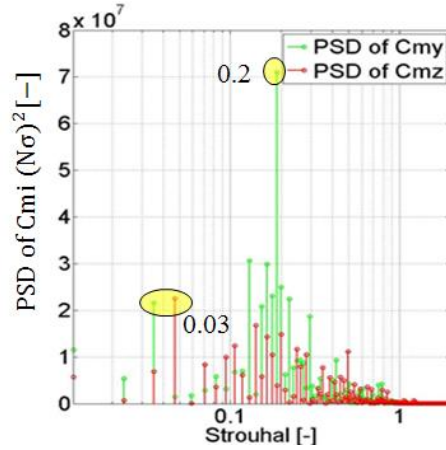


Figure III.33: PSD of virtual torques  $C_{my}|^{S_x}$   $C_{mz}|^{S_x}$  computed in this cut plane as a function of Strouhal  $St_W$ .

Next, the modal analysis will be used to highlight the frequencies and forces directions associated to 3D mechanisms. The next paragraph will detail the modal behavior on the rear end and on the wake flow with a frequency comparison of Dynamic Modes Decomposition and previous PSD results.

### 3.3.4 Modal analysis

- Modal Decomposition: Methods and discussion

The Dynamic Modal Decomposition consists in the decomposition of phase correlated structures in the flow. The SVD based DMD is an algorithm allowing to distribute snapshot uncertainties on the overall database contrary to the classical DMD algorithm based on last snapshot linearization leading to DMD matrix construction. The Sparse Promoting DMD method detailed in (Schmid, 2012) is an enhancement of the SVD based DMD with a resolution of residual minimization between the reconstructed and real snapshot constraint to maximization of the number of modes with zero amplitude.

The solution  $a_m$  gives the mode amplitude, and associated frequency  $f_m$  and growth rate  $\sigma_m$  are defined in Eq.64a leading to reconstructed field in Eq.64b.

$$f_m = \frac{\Im(\ln(\mu_m))}{2\pi\Delta t}; \sigma_m = \frac{\text{Re}(\ln(\mu_m))}{\Delta t} \quad (\text{a})$$

$$P(t_k) = \sum_{m=1}^{N-1} \alpha_m(t_k) \Phi_m(\vec{x}) \quad (\text{b})$$
Eq.64

Where:

$$\alpha_m(t_k) = a_m \cdot \Re(\mu_m^k)$$

is the temporal evolution of each mode.

This optimization problem is solved by dual ascending iterative algorithm detailed in (Jovanović et al., 2014a).

- DMD of pressure in the wake

The Sparse Promoting DMD is achieved on the pressure results in the wake at a sampling frequency of 2000Hz in an averaging window of 2.5Hz. Figure III.34 displays the amplitude and growth rate as a function of the Strouhal number  $St_W$ . The mode amplitude is related to its energy contribution in the overall wake flow dynamic. The growth rate denotes the unsteadiness associated to the corresponding Strouhal number. Indeed, a growth rate setting towards zero, is assimilated to an exact periodic phenomenon while a strictly positive growth

rate is assimilated to growing energy and a strictly negative one is assimilated to decaying energy.

For the uncontrolled flow case, the main contributions are at Strouhal  $St_W$  of 1.167 and 0.126. These modes have significant amplitudes and significant negative growth rates meaning that they correspond to decaying processes. We can also notice that there is a mode at a Strouhal number  $St_W$  of 0.22 with positive amplitude, meaning that it sets to increase the pressure level but with a negative growth rate.

Analysis will now focus on these relevant modes mentioned above even if other modes at Strouhal number  $St_W$  of 0.48, 0.7 and 0.85 seem also to participate to the energy balance.

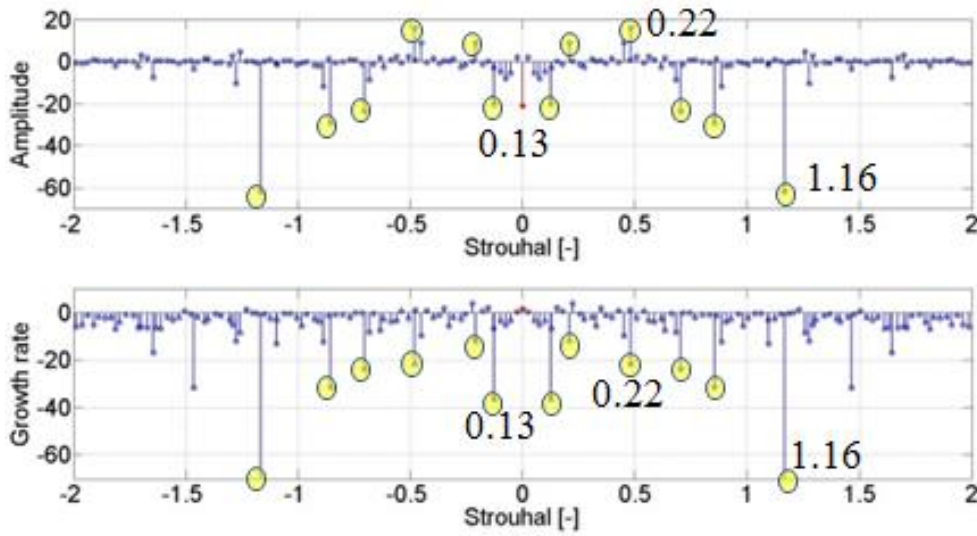


Figure III.34: DMD modes energy and growth rate.

Figure III.35 presents the residual error  $\epsilon$  between the real snapshots and the reconstructed field computed with Eq.65.

$$\epsilon = \|Cp_{rec} - Cp\| \tag{Eq.65}$$

This residual error appears to be small compared to the  $Cp$  RMS, thus convergence is reached.

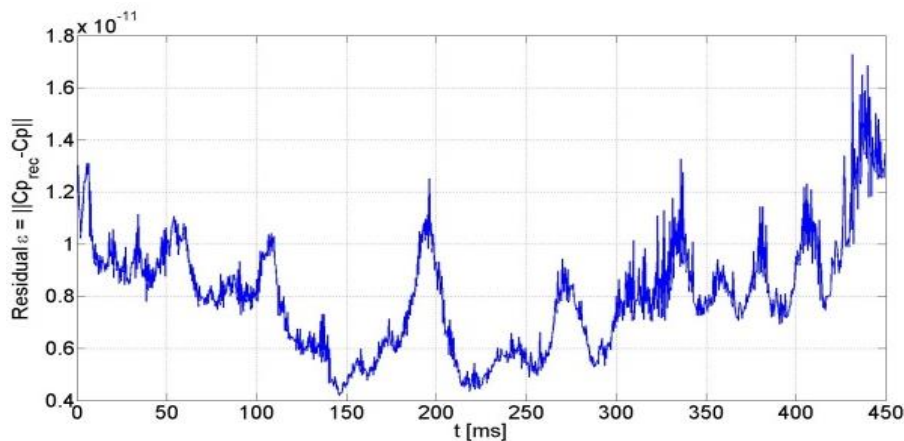


Figure III.35: Residual between reconstructed field and real snapshots.

Temporal reconstruction with the averaged field mode in Figure III.36a shows a linear pressure decrease in time due to a negative growth rate. Figure III.36b displayed same kind of reconstruction with pressure modes highlighted in Figure III.34. This second reconstruction

reveals that their positive growth rates are in opposition with the averaged mode growth rate. This can be interpreted as an energy transfer from the fluctuating part to the averaged flow.

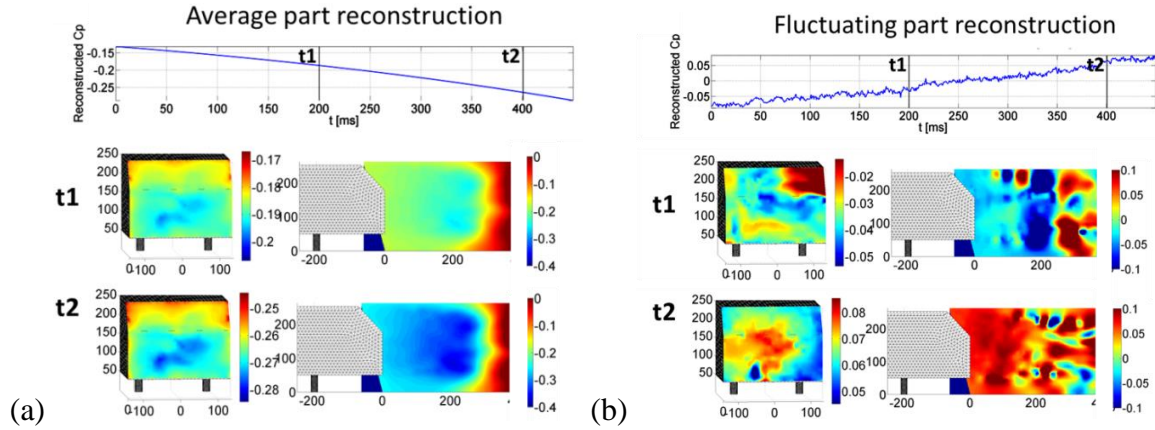


Figure III.36: (a) Reconstruction based on averaged mode with time averaged reconstructed  $C_p$  on rear of -0.200; (b) Reconstruction based on fluctuating modes highlighted in Figure III.34 with time averaged reconstructed  $C_p$  of -0.01.

It could be therefore interesting to check, if the flow control increases the energy of the modes with positive growth rate when we observed an increase of the pressure level on the rear end.

- DMD of pressure on the rear end

According to Eq.66a, contribution of each mode is estimated using the time and spatial integration leading to a modal contribution on the rear end estimated as in Eq.66b.

$$A_{Rear}^{dmd}(m) = \frac{1}{T} \int_T \int_{Rear} \alpha_m(t) \Phi(\vec{x}) dS dt \quad (a)$$

$$A_{Rear}^{dmd}(m) = \Re \left( a_m \frac{1}{N-1} \sum_{k=1}^{N-1} \mu_m^{k-1} \times \int_{Rear} \Phi_m(\vec{x}) dS \right) \quad (b) \quad \text{Eq.66}$$

Figure III.37 presents the obtained modal distribution on the rear wall pressure.

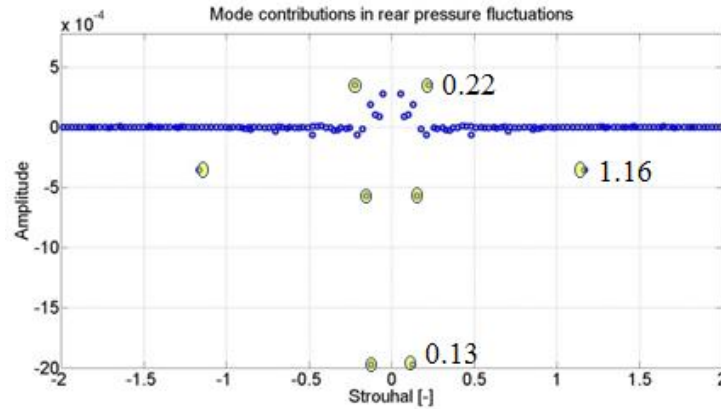


Figure III.37: Modes contributions in rear pressure fluctuations. Highlighted modes at  $St_W = [0.13; 0.15; 0.22; 1.16]$ .

If we compare the mode energy distribution on the rear end in Figure III.37 to the wake mode distribution in Figure III.34, we see that the modes at Strouhal  $St_W$  of 0.13, 0.22 and 1.16 still remain important. Mode at Strouhal  $St_W$  of 0.13 at the rear end has replaced mode at 1.16 in the wake in term of energy. This mode of  $St_W = 0.13$  has negative amplitude meaning that it greatly contributes to decrease the rear of the wall pressure.

The mode at Strouhal  $St_W$  of 0.22 is also measurable and appears to have positive amplitude so that it participates to increase the rear pressure.

The distributions of these three modes on the rear end are plotted in Figure III.38, Figure III.39 and Figure III.40. The real part is amplitude of the mode whereas the imaginary and the conjugate imaginary parts quantify the phase change of the mode during the period of the characteristic Strouhal number.

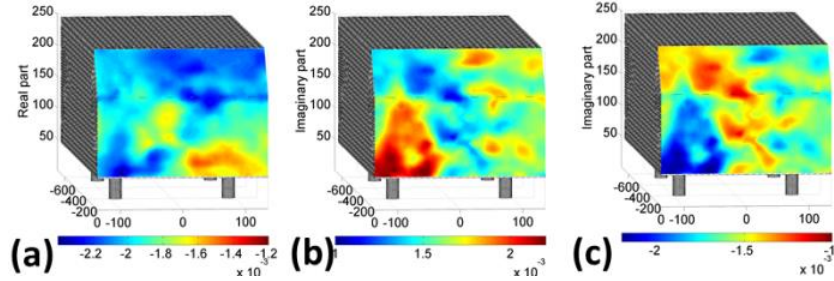


Figure III.38: Mode at Strouhal 0.13 projected on rear with time averaged  $C_p = -0.0079$ : (a) Real (b) Imaginary (c) Conjugate imaginary parts;

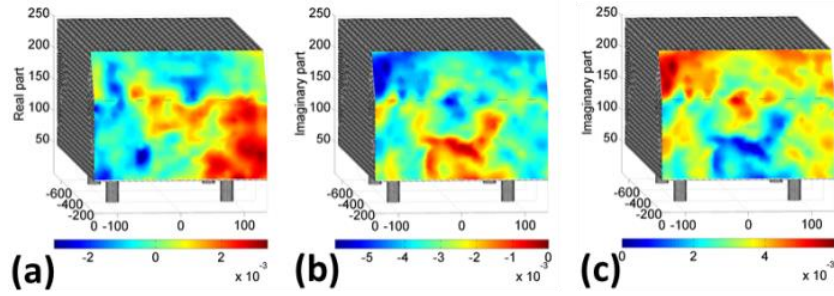


Figure III.39: Mode at Strouhal 0.22 projected on rear with time averaged  $C_p = 0.0001$ : (a) Real (b) Imaginary (c) Conjugate imaginary parts;

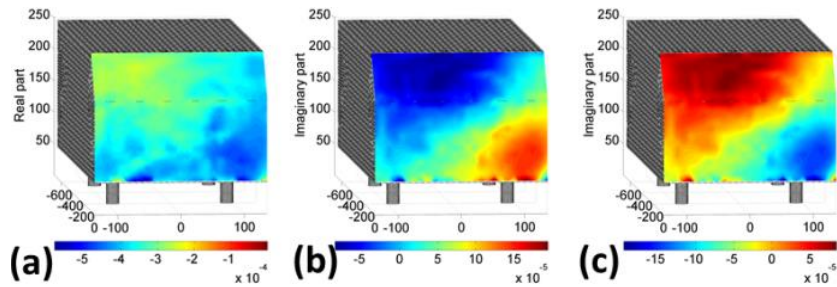


Figure III.40: Mode at Strouhal 1.16 projected on rear end with time averaged  $C_p = -0.0014$ : (a) Real (b) Imaginary (c) Conjugate imaginary parts;

We now look at the mode contribution to the rear torque in pitch  $M_{Rear}^{dmd}(m)|_y$  and in yaw  $M_{Rear}^{dmd}(m)|_z$  estimated as is Eq.67a and Eq.67b.

$$M_{Rear}^{dmd}(m)|_y = \frac{1}{T} \int_T \int_{Rear} (z - z_0) \cdot \alpha_m(t) \Phi_m(\vec{x}) dS dt \quad (a)$$

$$M_{Rear}^{dmd}(m)|_z = \frac{1}{T} \int_T \int_{Rear} (z - z_0) \cdot \alpha_m(t) \Phi_m(\vec{x}) dS dt \quad (b)$$

Eq.67

Where:

$y_0$  and  $z_0$  the coordinates rear wall centre.

From Figure III.41, we notice that the amplitude of the mode at Strouhal  $St_w$  of 0.22 is the highest one, especially on the yaw axis corresponding to an important vertical dissymmetric phase averaged on the real part of the wall pressure that could be interesting to control.

We can also notice that this dissymmetric mode at Strouhal  $St_w$  of 0.22 corresponds to a high energy level in the power spectra density displays presented in Figure III.29b. This observation confirms the interest to control the effect of this mode on the torque in yaw.

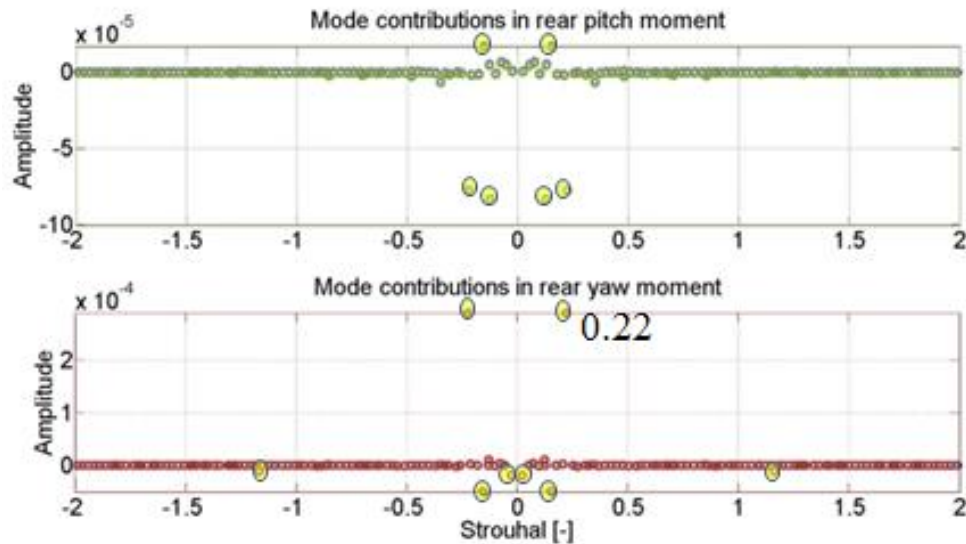


Figure III.41: modes contribution to the rear torques especially at  $St_w = 0.22$  on pitch and yaw.

- DMD of pressure in low pressure region

In addition to the PSD of the virtual torque in the wake presented in Figure III.33, contribution of each mode can be estimated by  $M_{wake}^{dmd}(m)$ ,  $M_{wake}^{dmd}(m)$ , defined in a same way as the rear torques of Eq.67a, b but spatially integrated in the  $X=250\text{mm}$  cut plane.

As shown in Figure III.42, we notice positive amplitude of the torque in the pitch direction corresponding to horizontal dissymmetric phase averaged on the imaginary part of the wall pressure shown in Figure III.43.

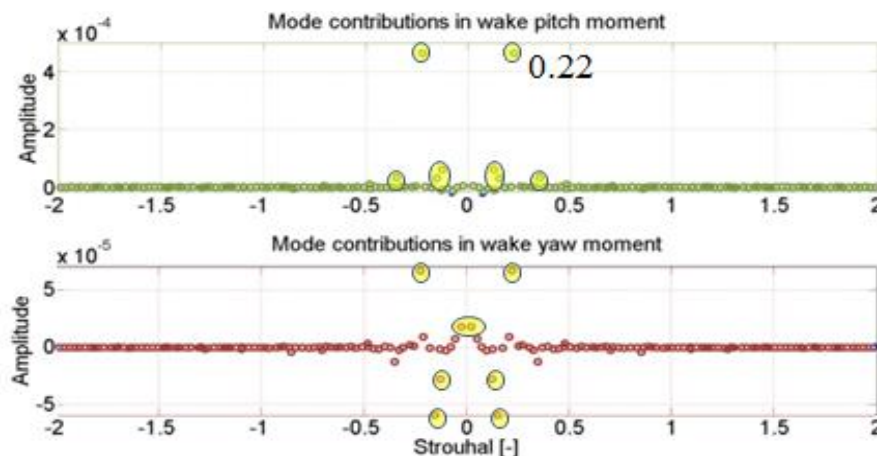


Figure III.42: Mode contribution on the virtual torques in wake flow especially at  $St_w = 0.22$  on pitch and yaw.

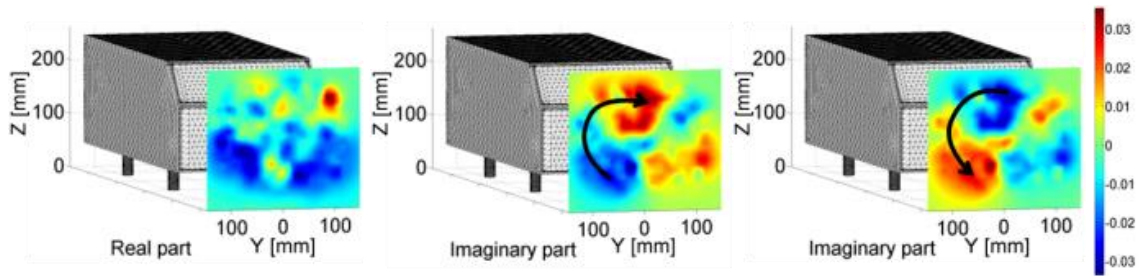


Figure III.43: Mode at Strouhal 0.22 in wake in  $Y=0$  and at  $Z=150$  mm cut sections: (a) Real (b) Imaginary (c) Conjugate imaginary parts;

### 3.3.5 Controlled flow

- Active flow control strategy

We will focus on the flow control of the strong dissymmetric mode at  $St_w=0.22$ .

The active flow control presented here is based on micro-slots illustrated in Figure III.44 located near each edge of the rear end. Jets characteristics were selected in accordance to previous work performed on a  $90^\circ$  Ahmed Body (Eulalie, 2014).

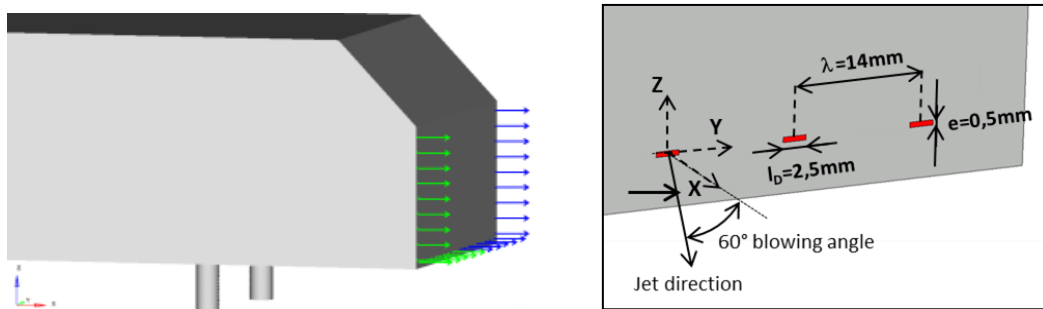


Figure III.44: Dimensions and positions of jets located on lateral and bottom edges of the basis.

As illustrated in Figure III.45, a feedback law between the transient yaw coefficient on the rear end and the injected jets momentum was implemented. The actuation strategy consists in an alternate lateral pulsed jet, blowing proportionally to the sign of the torque in yaw. The real-time closed loop control is designed in order to track the horizontal oscillation of the wake pressure drop. This technic allows the synchronization the jet boundary condition with the wake horizontal motion. This time resolved information is computed on the high pressure RMS region, located on the bottom the square back, in order to capture accurate yaw variations.

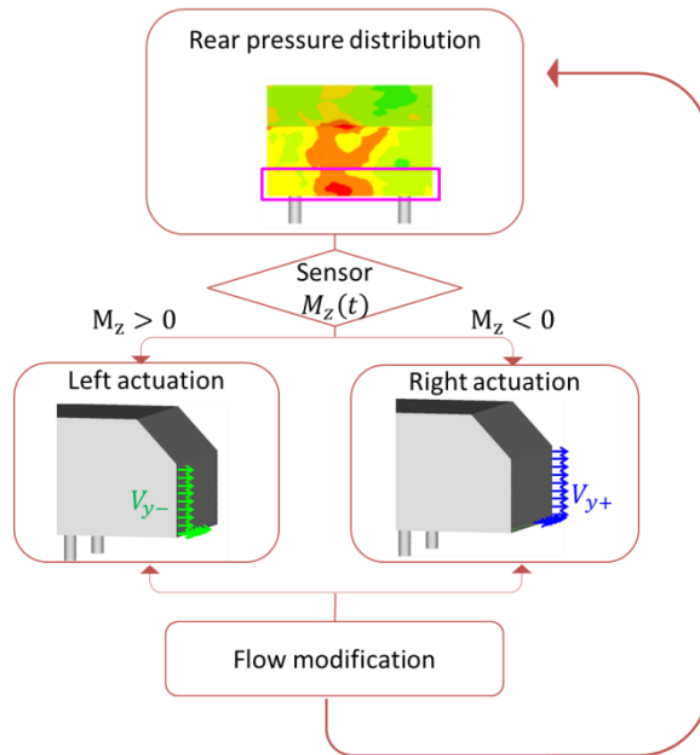


Figure III.45: Closed-loop control law.

The jet signal and sensor PSD obtained with this closed loop control are displayed in Figure III.46. Jets actuation was triggered at low Strouhal number  $St_w$  of 0.015 and around  $St_w = 0.1$ . PSD on sensor, shows a frequency emergence in yaw at  $St_w=0.15$  instead of 0.22.

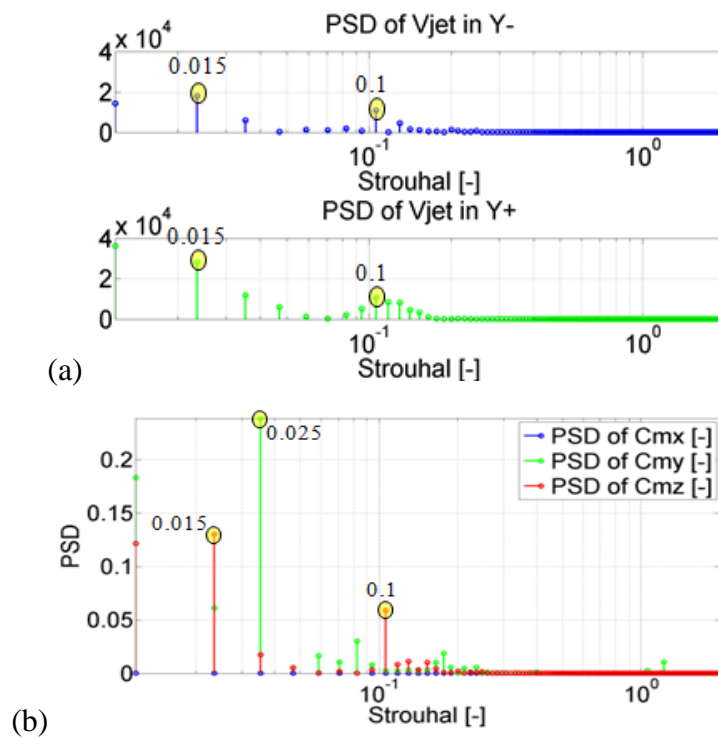


Figure III.46: (a) Jets signals PSD as a function of Strouhal  $St_w$ ; (b) Sensor PSD as a function of Strouhal  $St_w$ .

- Control effect

A drag reduction of 1.4% is obtained with this control law with an important decrease of lateral forces fluctuations (Table 4).

	Average	$\Delta F$ [%]	RMS	$\Delta RMS$ [%]
$C_x$ [-]	0.2682	-1.4%	0.0062	-1%
$C_y$ [-]	-0.0005	0%	0.0087	-33%
$C_z$ [-]	-0.0579	5.5%	0.017	+1%

Table 4: Time averaged and RMS of forces on the Ahmed Body and difference with uncontrolled flow.

Considering Figure III.47 compared to the uncontrolled results in Figure III.29, the power spectra on the rear end at Strouhal number  $St_w$  of 0.22 is completely vanished to enhance the power spectra at Strouhal number 0.03, already present in the wake fluctuations of the uncontrolled flow in Figure III. 28 and Figure III.29a.

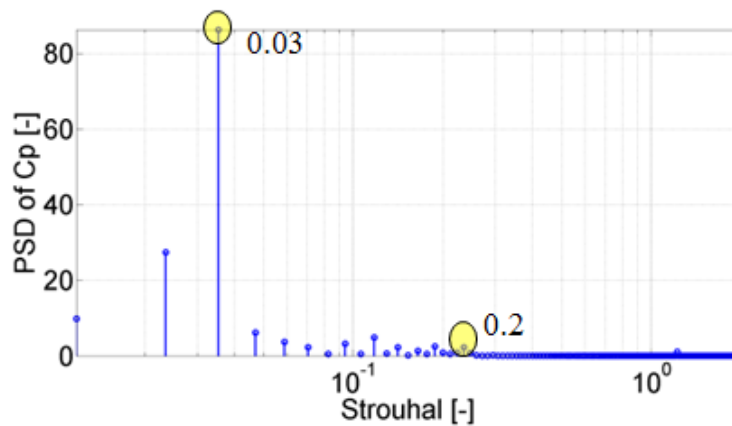


Figure III.47: PSD of pressure coefficients on rear end as a function of Strouhal  $St_w$ .

As shown in Figure III.48a, the low pressure area on the rear end is slightly increased, symmetrized and shifted close to the central edge compared to Figure III.26.

The RMS is mainly associated to power spectra frequency of  $St_w=0.03$  according to Figure III.48b.

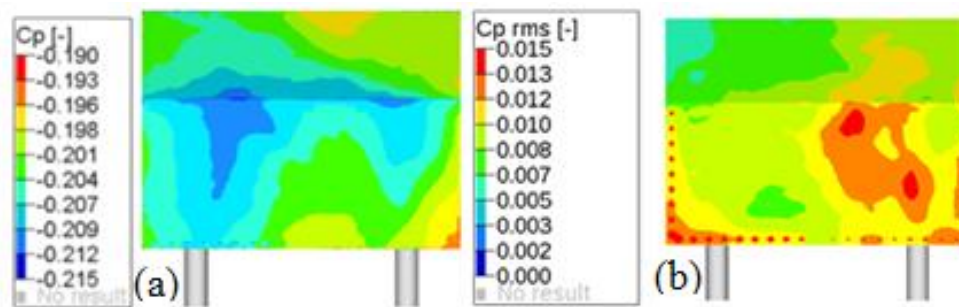


Figure III.48: Time averaged pressure (a) and RMS (b) of the controlled flow with  $C_p = -0.20$ .

### 3.3.6 Discussion

In this work the flow around a 47 degrees Ahmed body, corresponding to a simplified SUV, was analyzed. Not only classical flow analysis tools as the spectral and field quantification was used to perform the study, but also reduced order technique of Sparse Promoting Dynamic Mode Decomposition was applied to better capture the flow topology and to design an appropriate control approach. Especially, a strong dissymmetric structure dynamics was observed and a closed loop control was proposed to symmetrize this energetic mode at  $St_w = 0.22$ .

This work also revealed some capabilities of the Sparse Promoting DMD for flow topology and dynamics understanding and to identify main flow characteristics and associated Strouhal numbers. This capability is in fact very useful as it allows to design a pertinent closed loop flow control and to measure modal sensitivity of the jet actuators.

To go further, Dynamic Modal Decomposition with Control presented by (Proctor et al., 2014a) appears to be the appropriate direction to move towards the study and control of a reduced size realistic SUV geometry. Indeed, the closed loop flow control based on a reduced order model makes us able to integrate Strouhal characteristics, energy balance and actuators sensitivity.

A more sophisticated control law, dealing with several regions of interest has to be implemented in order to control this energy transfer.

## 3.4. Numerical investigation of the reduced scale generic SUV

The experimental investigations of the flow behavior around the mockup performed in chapter II define the background of the numerical study of the POSUV benchmark. The experimental characterization achieved in the context of this PhD work, provides time resolved pressure sensors distributed on the tailgate and time resolved 2D PIV measurements, the main wake flow features. This gives the foundations for the validation of the numerical simulation. This numerical study was achieved in the continuity of the preliminary simulations for an efficient implementation of the computational setup. The ramp flow increased our best practices ensuring the accurate simulation of detached flows benchmark. The in-depth examination of the shear layer control on the ramp flow improved our knowledge of the physics of an efficient actuation. This gives the premise explanations of the experimental efficiency measured on the optimal flow control. The second preliminary study of the 47° Ahmed Body were an opportunity to highlight how the 3D features drastically increase the complexity of the wake flow. This benchmark gives the first observations of the relation between the shear layer fluctuations and the wake flow dynamics and the interest of the shear layer control is emphasized.

It is within this framework that the numerical study of the flow around the POSUV is performed. The objective is to use the 3D transient results to identify the process responsible for the aerodynamic loss. After a validation of the time averaged flow topology, a comparative study of the wake dynamics is performed based on the comparison of turbulent quantities and their spectra. A more sophisticated cross-modal analysis between experimental measurements and numerical probes provides an accurate evaluation of the representativeness of the computed flow dynamic. Finally, the 3D analysis of the detachments around the body panels and the correlation with the wake flow is explored with spectral analysis and modal

decomposition. These observations will be used to corroborate the role of the boundary layer separation on the dynamics of the wake vortices. This statement will also help to understand how the control of these turbulent structures results in a pressure recovery.

Finally, the implementation of the numerical simulation of the active flow control configuration appears to be really challenging. The reduction of the pressure loss with the jet boundary condition was hardly reproduced. An investigation is proposed in order to reach an efficient active flow control boundary condition yielding similar aerodynamical gain than in experiment.

### 3.4.1 Numerical setup and convergence according to turbulent model

The previous preliminary study of the Ahmed Body in the Orleans wind tunnel shows how the external flow is reproduced with the Pitot calibration. A similar approach is used here for the numerical setup of the POSUV mockup in TU-Berlin wind tunnel. The reader may refer to the section 2.1.1 for a complete description of TU-Berlin wind tunnel characteristics. The numerical domain is reduced to the main section of the wind tunnel (Figure III.49). The definition of a probe at the same location than the Pitot tube ensures the reproduction of the experimental wind tunnel condition. The flow rate at the inflow boundary condition is enforced in order to reach a stabilized velocity value of 30m/s at the Pitot probe. The outflow boundary condition is also enforced in order to fix a zeros reference pressure at the Pitot probe.

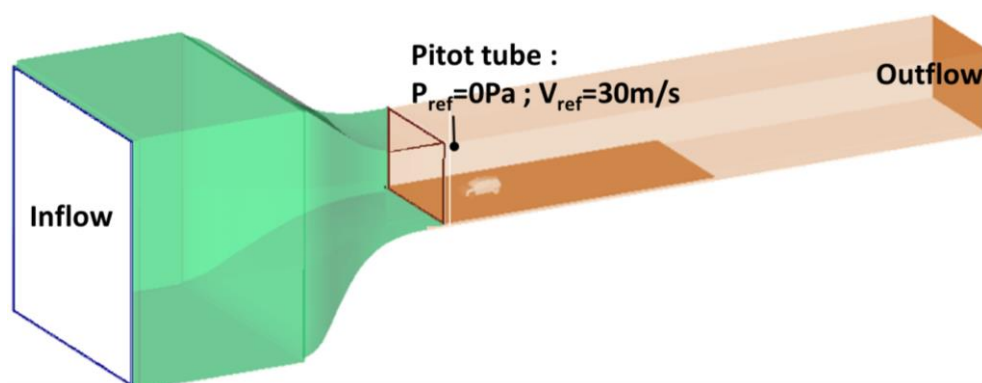


Figure III.49: Simulation domain defining the wind tunnel environment around the POSUV. A monitoring point captures the reference zero pressure and the reference velocity of 30m/s at the Pitot tube.

Similarly to what was done in the preliminary studies, the mesh cutoff frequency is chosen based on the dimensional analysis of the turbulent quantities. Based on a Reynolds number of 400 000, similitude principles inherit from the Kolmogorov theory approximate the dissipative length scales of the flow at 0.7mm associated to the cutoff frequency around 6000Hz required for Large Eddy Simulation.

Turbulent characteristics of POSUV		
Characteristic parameters	Definition	Values
H [m]		0.2
U [m/s]		30
Re [-]	$\rho HU / \mu$	400 000
Dissipation rate [m <sup>2</sup> /s]	$\epsilon = U^3 / H$	135 000
Kolmogorov length scale [m]	$L_{kolm} = H \cdot Re^{-3/4}$	1.2E-05
Dissipation length scale [m]	$L_{di} = 60 \times L_{kolm}$	7.4E-04
Dissipation velocity [m/s]	$U_{Ldi} = (\epsilon \cdot L_{di})^{1/3}$	4.6
Period of dissipation scales [s]	$T_{Ldi} = \left(\frac{\nu}{\epsilon}\right)^{0.5} = L_{di} / U_{Ldi}$	1.6E-04
Frequency of dissipation scales [Hz]	$F_{Ldi} = 1 / T_{Ldi}$	6.25E+03

Table 5: Dimensional analysis of the turbulent quantities applies to the POSUV wake flow.

As discussed on the preliminary study of the ramp flow benchmark, the choice of the Dynamic Smagorinsky subgrid scale model ensures a better management of the turbulent dissipation according to the local turbulence scale in the transient flow. This justifies the selection of a 2mm minimum mesh resolution in the highly turbulent regions associated to a cutoff frequency of 2000Hz. The resulting time step of 0.5 milliseconds is in accordance with the experimental observation showing no significant energy contribution above 1000Hz. The associated CFL number is estimated at 7.5 which suit the semi-implicit solver restriction. It should also be mentioned that a maximum number of 4 non-linear staggered iterations per time step was allowed in order to capture accurately the flow dynamic.

Figure III.50 displays the refinement boxes used for the unstructured mesh discretization of the fluid volume around the mockup. The thinner discretization level of 2mm is applied in the region of the wake flow to capture accurately the shear layers gradients and in the region of the underbody flow for the resolution of the turbulence scale from the wheels vortex shedding. The surrounding of the mockup is computed with a refinement box at 4mm. An additional refinement box at 8mm mesh resolution is used to achieve a smooth transition until the rough external mesh at 32mm. 8 tetrahedral layers ensured the mesh size continuity at the boxes interfaces.

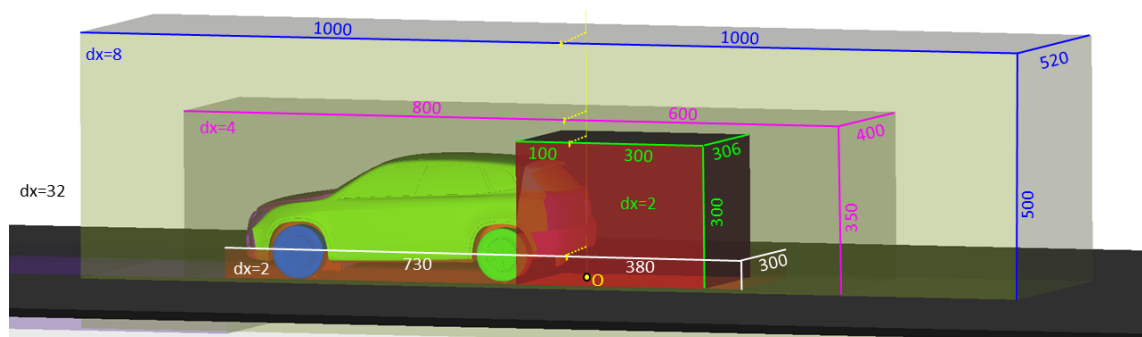


Figure III.50: Refinement boxes dimensions with the final mesh discretization.

A special care is taken for the generation of the surface mesh and the extruded boundary layer mesh. Figure III. 51 illustrates the boundary layer mesh discretization. A maximum 2D mesh size of 2mm is set on the POSUV wall surface to capture the geometric design complexity.

The first mesh layer is imposed at 0.05mm in order to compute the boundary layer gradient from  $y^+ = 5$  in accordance with the wall model constraint. The total boundary layer mesh is extruded on 4mm thickness discretized with 12 layers and a growing ratio of 1.3. These are the selected choices ensuring the accurate resolution of the wall turbulence level. They will be validated with the hot wires measurements in the boundary layer performed in experiment.

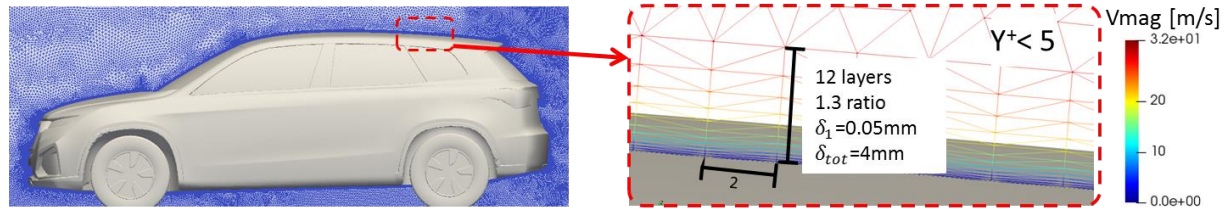


Figure III. 51: Mesh discretization in the Y0 cut plane with a focus on the boundary layer definitions.

The final converged mesh is constituted of 300 million tetrahedral elements corresponding to 53 million of nodes. Figure III.52 shows the mesh convergence result using a first coarse mesh of 15 million of nodes with 8mm minimum resolution and an intermediate mesh of 29 million of nodes with 4mm minimum resolution. The slope tendency validated the convergence with the final mesh of 53 million of nodes.

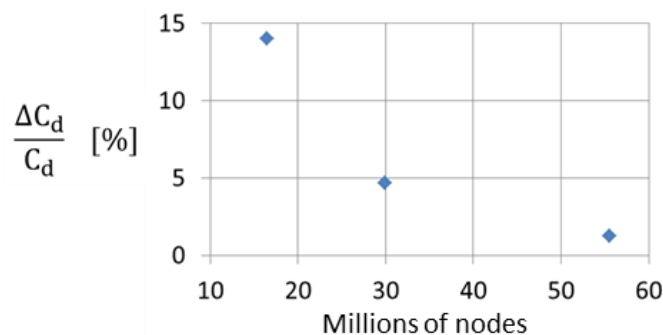


Figure III.52: Mesh convergence based on the error on the drag coefficient as a function of the number of nodes.

Finally, the converged flow analysis was performed on 1.2 seconds of simulation after 0.3 seconds of flow establishment. The simulation corresponds to a total computation time of 270 hours on a cluster of 72 CPUs using 128Gbytes of RAM, which means 19440 hCPU. According to this computational time window, we expect to capture dynamical phenomena described in chapter II.3 until above the frequency of 1.6Hz, considering the Shannon theorem. Below this frequency, the DMD will not detect the periodicity of the oscillation.

### 3.4.2 Time averaged flow topology compared with experiment

The analysis starts with an exploration of the time averaged flow features. It is based on the experimental rear end pressure (Figure III.53a), 2D PIV velocity (Figure III.53b) and force measurements.

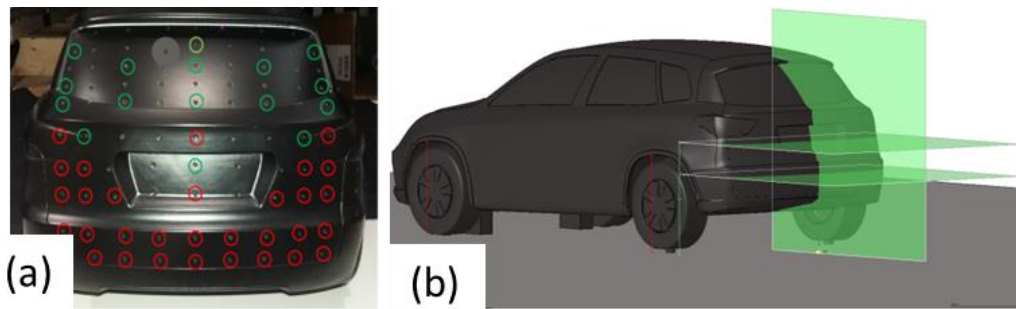


Figure III.53: Picture of experimental sensors: (a) 47 rear end pressure sensors; (b) Time resolved 2D PIV acquisitions.

- Aerodynamic loss

A time averaged drag coefficient of 0.352 is obtained in the numerical simulation instead of 0.358 in experiment. This corresponds to a numerical error of 1.2%. The force breakdown by surface is presented in Figure III.54b based on the design decomposition of Figure III.54a. The most important contribution is localized on the rear tailgate until 55% even if the front bumper and the wheels also have a strong part of the aerodynamic loss. As measured in experiment, we compute a ratio of the tailgate force compared to the overall drag coefficient in accordance with what is generally observed on the Ahmed body. However, it is significantly high compare to what is usually measured on realistic SUV. The non-moving floor and the non-rotating wheels should modify the wake and the resulting pressure loss on the tailgate.

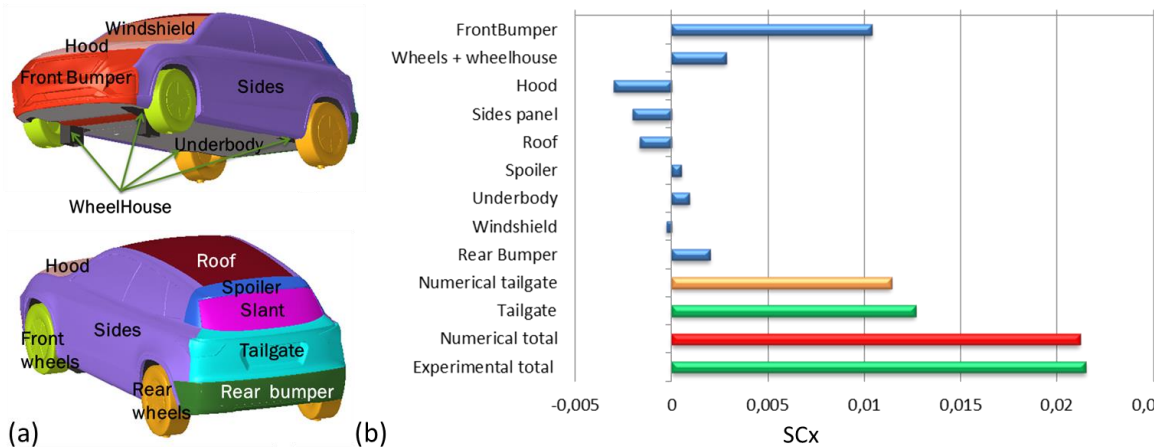


Figure III.54: (a) Breakdown of the body panels;(b) Forces breakdown per body panel. Simulated total drag force and tailgate contribution are in agreement with experiments. In both cases, the tailgate generates 55% of the total aerodynamic loss.

The aerodynamic loss due to the rear end is validated thanks to the time averaged pressure sensors measurement. Figure III.55a shows the comparison of the time averaged rear end pressure sensors measured in experiments compared to the numerical results displays in Figure III.55b. In both CFD and experiment, the same pressure distribution is observable governed by the strong pressure loss on the rear bumper and a high pressure coefficient on the rear bumper. The mean pressure coefficient integrated on the rear end surface is evaluated at -0.216 in CFD compared to the value of -0.23 in experiment. The 6% discrepancy measured on the rear end contribution indicates a slight difference in the force breakdown per body panel.

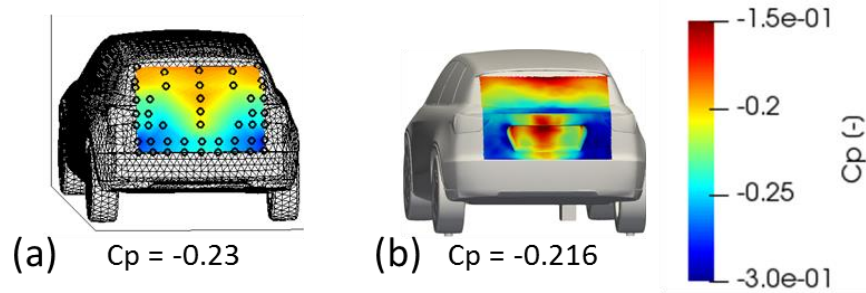


Figure III.55: Comparison of the time averaged pressure coefficient obtained in (a) experiments; (b) CFD.

The understanding of the phenomenon responsible for the rear end pressure loss required the analysis of the time averaged wake flow topology.

- Time averaged 2D wake comparison

The comparison of the time averaged velocity in the wake flow is achieved thanks to the PIV measurements. The PIV instrument was not able to capture the wake closed to the mockup and above the slant window because of the noise induced by laser reflection. Despite this limitation, quality results in the wake were obtained. Figure III. 56 displays the comparison of the time averaged velocities in the transverse vertical cut-plane Y0. The stream wise velocity (Figure III. 56a and b) illustrates a similar recirculation area between experiments and CFD. The vertical velocity component (Figure III. 56c and d) reveals the importance of the ascending flow coming from the underbody. In addition, the vortex generated in lower part of the recirculation is closer to the rear bumper than the distance of the vortex in the upper part to the slant window. This is in accordance with the low pressure distribution which is higher on the rear bumper as shown in Figure III.55.

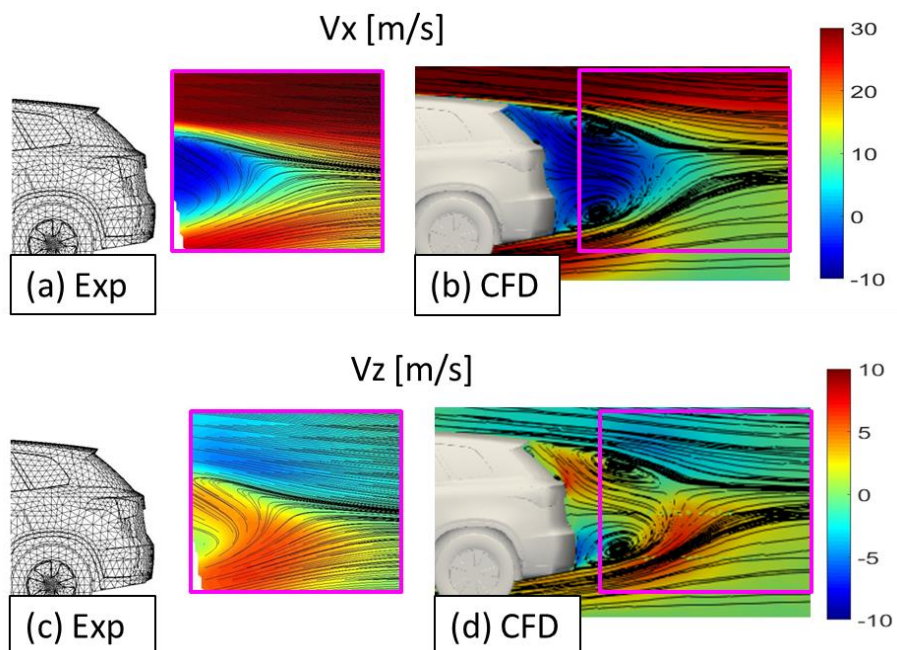


Figure III. 56: Comparison of time averaged velocity components  $V_x$  and  $V_z$  in the  $Y_0$  cut-plane: (a) and (c) experiments; (b) and (d) CFD;

Figure III. 57 shows the time averaged velocities in the horizontal cut-plane Z140. The span of the recirculation area estimated with the stream wise velocity component (Figure III. 57a

and b) is still in agreement with the experimental observation. The transverse velocity component (Figure III. 57 and d) proves the symmetry of the wake flow, which is also in agreement with the symmetrical rear end pressure distribution (Figure III.55).

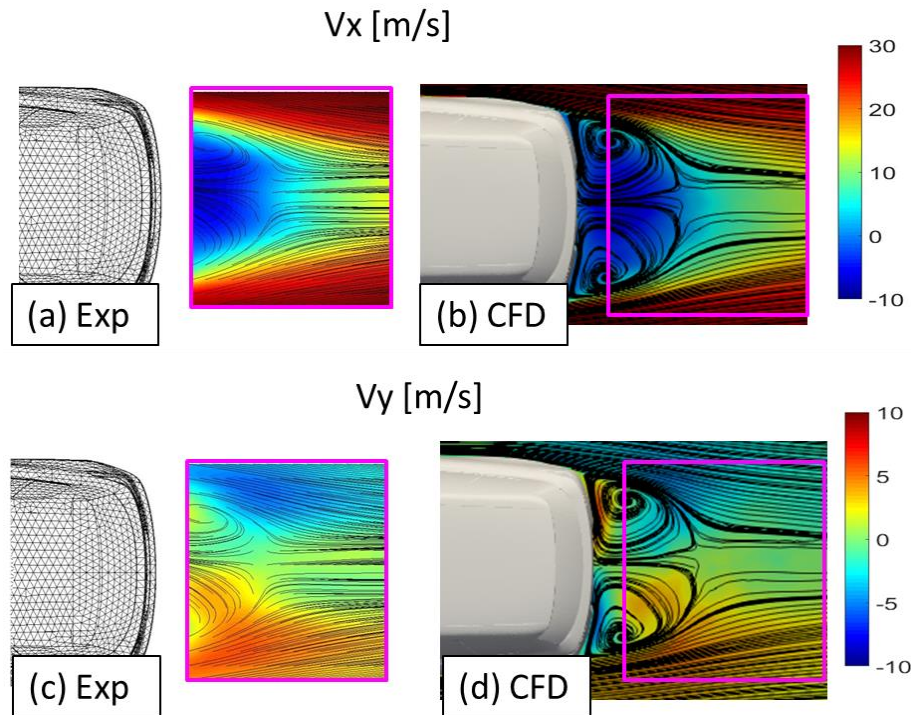


Figure III. 57: Comparison of time averaged velocity components: (a)  $V_x$  in experiment; (b)  $V_x$  in CFD, (c)  $V_y$  in experiments, (d)  $V_y$  in CFD.

These comparisons ensure our confidence in the results obtained with the numerical simulation. We can now take advantage of the 3D numerical results all around the car to go further on the analysis of the flow topology.

- Time averaged 3D wake flow

The 3D time averaged wake flow topology is described in Figure III.58a thanks to the streamlines plot. Three main structures emerged in the wake flow. The one on the bottom of the rear bumper, named  $\Omega_y$  is a horizontal structure (rotation axis orient by the Y direction) generated by the roll-up of the shear layer coming from the underbody flow.

There are also two lateral vortices  $\Omega_z^-$  and  $\Omega_z^+$  due to the roll-up of the shear layers from the rear bumper sides. They are counter-rotating large vertical structures (rotating axis close to z direction) extended from the rear bumper until the side corners of the rear window. The span of each of these vortices is approximated around  $0.5H$  along the x direction,  $0.75H$  along the z direction and  $0.4H$  along the y direction. It is interesting to point out how the typical torus pressure contour, often observed behind a bluff body, is shaped by the 3 vortices (Figure III.58a and b). Moreover, the S-shape flow path, visible in the  $Y_0$  cut-plane (Figure III. 56 a and b), is explained by the coupling between the backflow of  $\Omega_y$  with the stream wise shear layer from the roof spoiler.

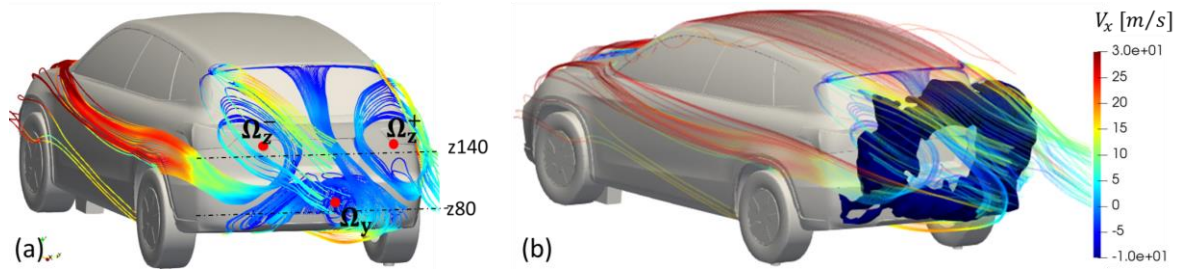


Figure III.58: (a) Time averaged velocity streamlines showing one horizontal vortex denoted by  $\Omega_y$  on the bottom of the rear bumper, and 2 lateral vortices  $\Omega_z^-$  and  $\Omega_z^+$  on each side of the tailgate; (b) Superposition of the streamlines with the iso-contour of  $C_p$  at  $-0.1$ .

The centers of the vortices are estimated thanks to the pressure minima measured in the wake. Figure III. 59a and b show the time averaged pressure coefficient field in the Y0 and Z140 cut-planes. The recirculation due to  $\Omega_y$  leads to the pressure drop visible in the Y0 cut plane and affecting the bottom rear bumper. Another pressure drop in the upper part of the wake is generated because of the S-shape structure. Two profile lines at  $z=100$  and  $z=220$  will be used to measure the pressure minima and the pressure gradient separating the centers of the wake vortices and the bumper. The recirculation due to  $\Omega_z^-$  and  $\Omega_z^+$  also leads to the pressure drop visible in the Z140 cut-plane. The profile lines at  $y=\pm 90$  will also be used for the characterization of the strength of  $\Omega_z$ .

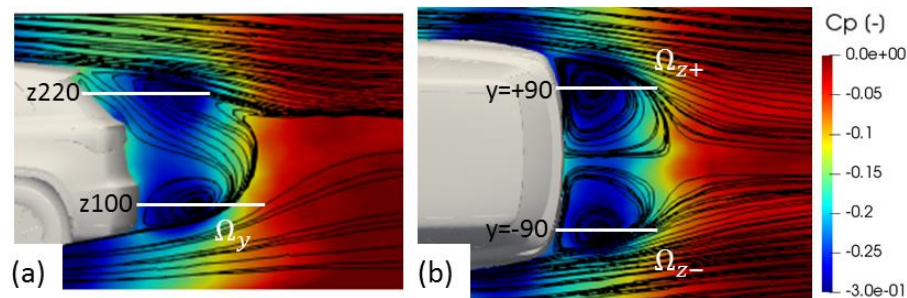


Figure III. 59: Time averaged pressure coefficient in (a) the Y0 cut plane and (b) in the Z140 cut-plane superposed with the time averaged velocity streamlines.

The stronger pressure drop induced by  $\Omega_y$  occurs at a distance of  $0.3H$  from the rear bumper and it is associated to a pressure coefficient of  $-0.3$ . The reversed flow on the upper part of the wake leads to a pressure drop at the center of the recirculation area, at a distance of  $0.4H$  from the rear window. A minimum pressure coefficient of  $-0.36$  is captured. It is stronger than in the lower part but it is further away from the rear window and the pressure is also higher. In the Z140 horizontal cut-plane, the centers of the vortices exhibit a dissymmetry between  $\Omega_z^-$  at  $0.2H$  and  $\Omega_z^+$  at  $0.12H$  from the tailgate. In addition, the pressure loss at  $\Omega_z^-$  dropped at  $-0.31$  instead of  $-0.33$  at the center of  $\Omega_z^+$ . The vortex on the driver side is weaker and further away from the tailgate than the vortex on the passenger side.

To go deeper in the understanding of the wake flow topology, it is interesting to characterize the velocity-pressure coupling occurring in this type of 3D highly turbulent flow. Three-dimensional incompressible flow are subjected to the Poisson pressure equation (Eq.69a). The vorticity and the shear stress are combined within the Q-criterion (Eq.69b), which is a source term in the pressure Poisson equation (Lesieur et al., 2005).

$$\begin{aligned} \Delta P &= 2\rho Q && \text{in } \Omega && \text{(a)} \\ Q &= \frac{1}{2}(|\vec{\omega}|^2 - |S|^2) && \text{in } \Omega && \text{(b)} \end{aligned} \quad \text{Eq.68}$$

Where:

$Q$  is the Q-criterion.

$\vec{\omega} = \vec{\nabla} \wedge \vec{u}$  is the vorticity

$S = 0.5(\vec{\nabla}\vec{u} + (\vec{\nabla}\vec{u})^T)$  is the shear stress tensor.

To go further in the discussion on the relation between velocity and pressure, we can analyze the Q-criterion in the wake. The Q-criterion can be interpreted as a source term in the pressure balance from the Poisson equation. The positive contributions of the Q-criteria are assimilated to rotating structures while the negative contributions are assimilated to shear mechanism. The Q-criterion of the time averaged field highlights the vorticity structures of the wake flow (Figure III.60a). The focus on the rear bumper detachment (Figure III.60b) shows how the shear layer coming from the underbody flow (in blue) evolves in the vortex  $\Omega_y$  in red. The impact on the tailgate is due to the shear constraint generated by the backflow of  $\Omega_y$  and resulting in a strong skin friction.

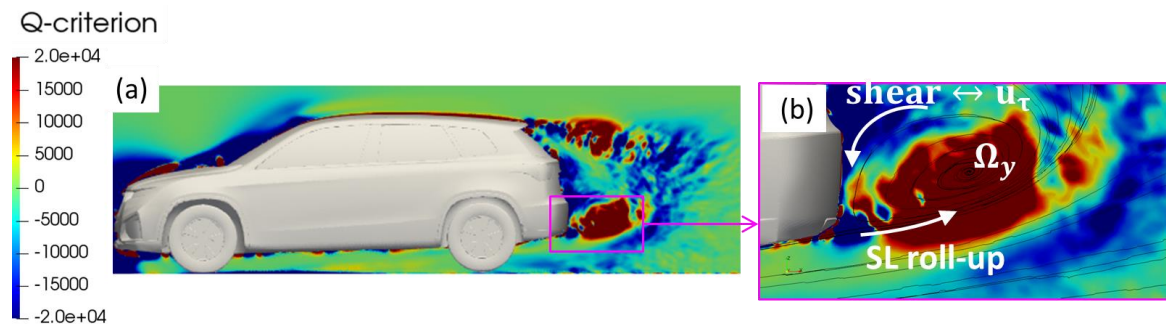


Figure III.60: Q-criterion of the time averaged field: (a) Y0 cut-plane; (b) Focus on the separation at the rear bumper.

The two lateral vortices  $\Omega_z^-$  and  $\Omega_z^+$ , are also visible on the Q-criterion field in the horizontal Z140 cut-plane (Figure III.61a). The focus on the rear bumper corner (Figure III.61b) reveals the roll-up of the shear emerging from the lateral body panel separation.

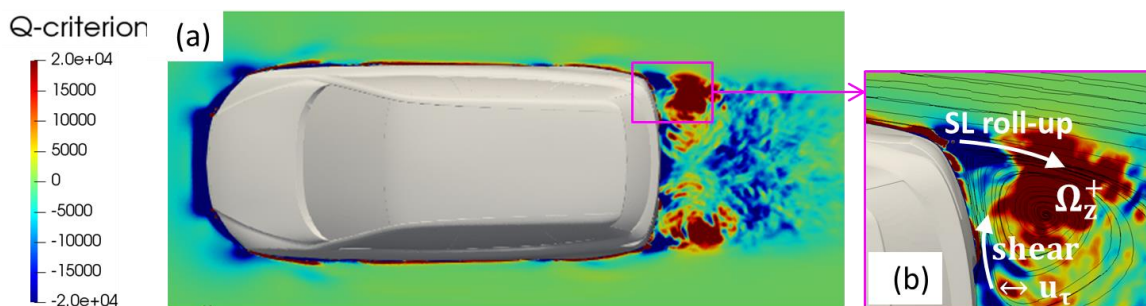


Figure III.61: Q-criterion of the time averaged field: (a) Z140 cut-plane; (b) Focus on the separation on the lateral corner of the rear bumper.

We expect to have a strong correlation between the velocity and pressure characteristics since the Q-criterion field shows the correspondence between the wake pressure minima and the vortices.

Similarly to the 2D projection on a slip wall, the projection of the Poisson equation on a fictive slice surrounding the body gives the imprint of the wake velocity on the wall pressure (Eq.69c). With this formulation, the skin friction velocity can be interpreted as the driving momentum in the viscous layer responsible for the pressure distribution.

$$\left. \frac{\partial P}{\partial \vec{\tau}} \right|_{bl} \sim \frac{1}{Re} \Delta \vec{u}_\tau - \left( \frac{\partial \vec{u}_\tau}{\partial t} + \vec{u} \cdot \nabla \vec{u}_\tau \right) \quad \text{in the fluid layer close to the wall} \quad \text{Eq.69}$$

Where:

$\vec{n}$  and  $\vec{\tau}$  are respectively the normal and tangential vectors of the wall.  
 $u_\tau$  is the skin friction.

The observation of the time averaged rear end skin friction streamlines (Figure III.62). gives the path of the backflow impacting the rear end pressure Diverging streamlines starting from zeros skin friction velocity proves the existence of 3 stagnation points on the rear end surface. Two are located in the region of the license plate cavity ( $p_1$  at  $z=117\text{mm}$  and  $p_2$  at  $z=153\text{mm}$ ) and the third one is underneath the spoiler ( $p_3$  at  $z=230\text{mm}$  displayed).

The vortex  $\Omega_y$  has presumably a strong interaction with the stagnation point  $p_1$  and has a ripple effect on the fluid flow going downward on the bottom rear bumper. There is also an interaction between  $\Omega_y$  and the stagnation points  $p_2$  and  $p_3$  meaning that the flow over the rear window is affected by the underbody flow. This is a consequence of the roof spoiler preventing the roll-up of the shear layer combined with the impact of the  $47^\circ$  slant angle, which tends to promote a fully detached flow.

There is no apparent interaction of  $\Omega_z^-$  and  $\Omega_z^+$  with the stagnation points  $p_1$  and  $p_3$  but the orientation of the streamlines emerging from  $p_2$  toward the sides of the tailgate suggests that  $\Omega_z^-$  and  $\Omega_z^+$  tends have a ripple effect pushing the fluid outward.

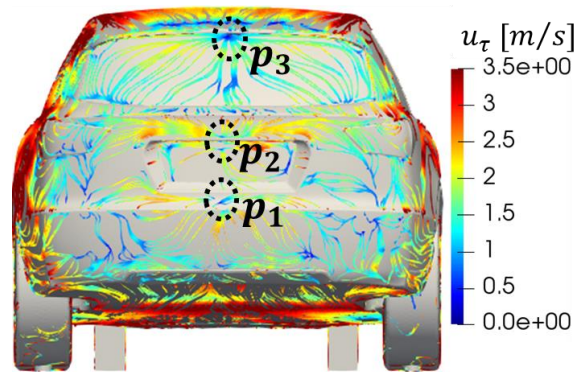


Figure III.62: (a) Time averaged skin friction velocity streamlines on the rear end wall highlighting the backflow path on the rear end. The black dot circles indicate the 3 stagnation points with low velocity and diverging streamlines.

- Discussion

The comparison of the aerodynamical features with experiments validates the representativeness of the time averaged results and ensures the simulation quality. The 3D wake characterization also confirms the choice of the 2D cut-plane Z140 to capture the behavior of  $\Omega_z^-$  and  $\Omega_z^+$  and the choice of Y0 cut-plane to capture the behavior of  $\Omega_y$  inside the S-shape structure.

It should be mentioned that, at these stage, there is no information on the hypothetical steadiness, periodicity or on the stability of  $\Omega_y$ ,  $\Omega_z^-$  and  $\Omega_z^+$ . There is also a real challenge to perform an accurate evaluation of the transient flow discrepancies between the experiments and numerical simulation. To do so, an efficient method will be proposed in the following paragraph 3.4.3 thanks to a cross-modal analysis.

Moreover, the previous observations make us suspect on the importance of the boundary layer quantity momentum in the mechanism of roll-up responsible for the wake dynamic. The interaction between the boundary layers separation around the body panels and the wake motion will be highlight in paragraph 3.4.4.

The time averaged wake flow description also brings out the interest of the active flow control in the region of the detachment on the corners of the rear bumper. Paragraph 3.4.5 will investigate on how jet quantity momentum controls this turbulent fluctuations and efficiently modify the wake flow.

### 3.4.3 Validation of the wake flow dynamics compared to experiments

Two methods will be used to compare the turbulent quantities between experiments and numerical simulation. The root mean square of the transient fields provides an evaluation of the turbulent fluctuations. The dynamics of the flow are extracted thanks to a cross-modal analysis between the experiments and CFD databases. This workflow leads to an accurate evaluation of the correlated dynamical behaviors for a validation of the transient flow.

- Comparison of the turbulent characteristics with experiment

Figure III.63 presents the comparison of the experiments and CFD pressure fluctuations on the tailgate. The intensity of the pressure coefficient RMS mainly localized on the bottom of the tailgate is higher in the numerical simulation.

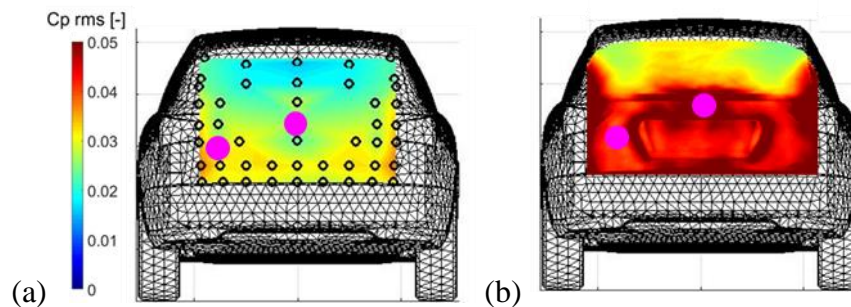


Figure III.63: RMS of pressure coefficient on the tailgate in (a) experiments and (b) CFD.

Figure III.64 displays the comparison of the power spectral density computed at the probes identified in Figure III.63. The spectral distributions show higher energy magnitude in CFD than experiments at 9Hz and at 25Hz and 30Hz.

The computation time is not able to capture the 1Hz peak observed in experiment. The feature at 30Hz will be analyzed in the modal decomposition of the tailgate pressure in order to identify the difference in the velocity cross-correlations between experiments and CFD. The discussion on the numerical flow simulation presented in section 3.4.5 will deal with the quality of the turbulent model used in our computation, which can explain this difference.

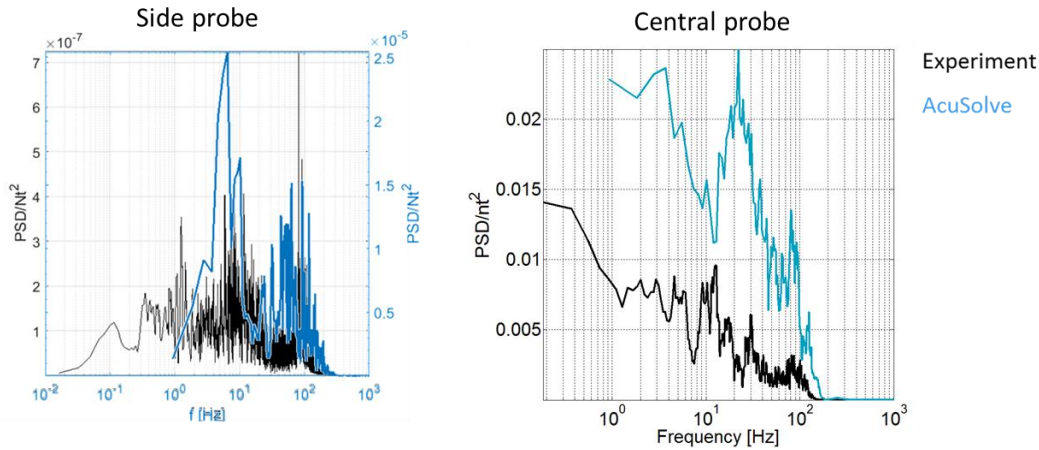


Figure III.64: Power spectra density of the pressure measured at the probe highlighted in Figure III.63. The black curve associated to experimental results is plotted on the left axis and the blue curve associated to CFD, is plotted based on the right axis.

This can be linked to the pressure fluctuations in the wake flow obtained thanks to the numerical simulations in the Y0 cut plane (Figure III.65a) and in the Z140 cut plane (Figure III.65b). We can see that the shear layers are subjected to important pressure fluctuations. If the separation on the roof spoiler generates a high RMS of pressure, it does not affect significantly the slant window. The separation on the bottom rear bumper and on the sides of the rear bumper seems to have more impact on the tailgate.

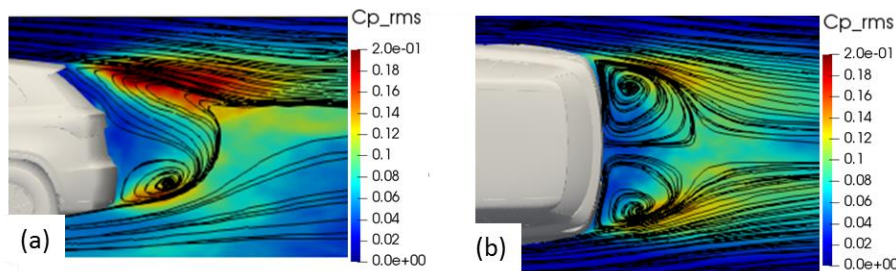


Figure III.65: RMS of pressure measured in the wake flow: (a) in the Y0 cut-plane, (b) in the Z140 cut plane.

Figure III.66 displays the comparison of the velocity fluctuations plotted in the Y0 cut-planes. The velocity RMS reveals the area of high turbulence in the wake flow generated in the region of the shear layer. In both experiments and CFD, the turbulence induces by the separation is more energetic on the top shear layer compared to the bottom shear layer. However, if a maximum velocity fluctuation of 7m/s is measured in experiment, it reaches a maximum value of 9m/s in the numerical simulation.

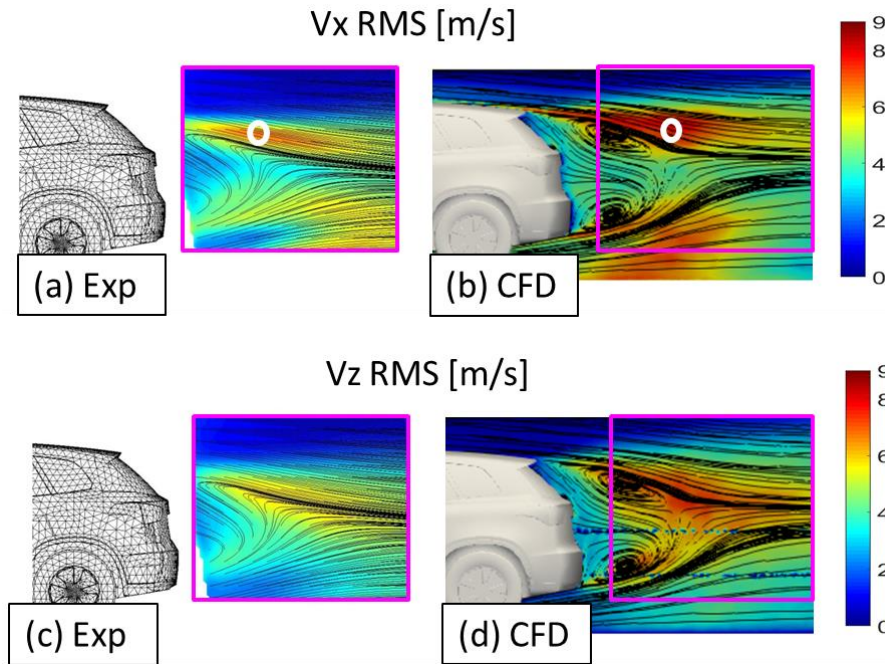


Figure III.66: Comparison of velocity fluctuations in the Y0 cut-plane: (a) stream wise velocity in experiment, (b) in CFD, (c) vertical velocity component in experiment, (d) in CFD. The white circle indicates the position of the maximum velocity fluctuation.

Figure III.67 displays the comparison of the velocity fluctuations in the horizontal Z140 cut-planes. The turbulence induced by the lateral corners of the rear bumper leads to 6m/s velocity fluctuations in experiments compared to the value of 7m/s in the numerical simulation.

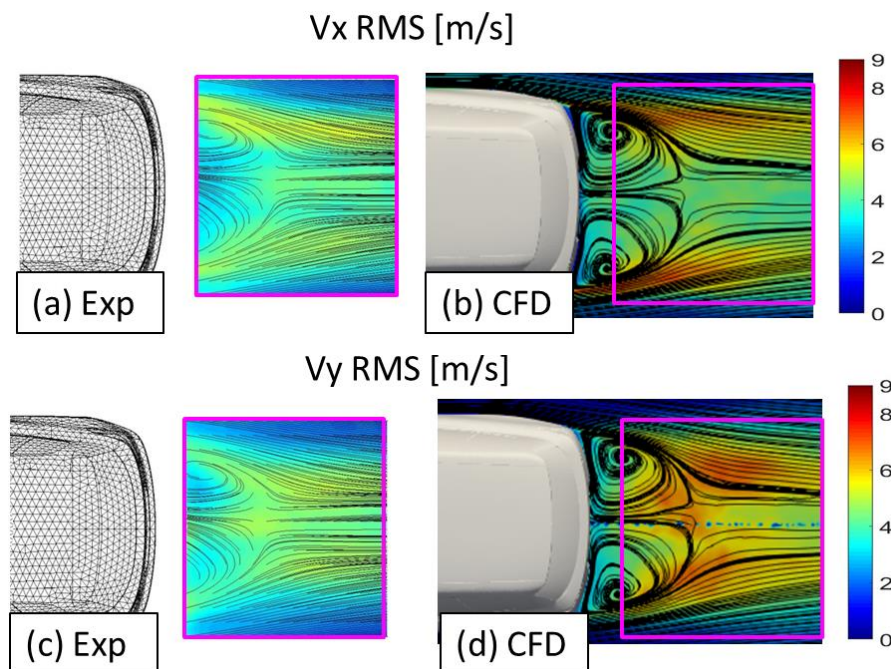


Figure III.67: Comparison of velocity fluctuations in the Z140 cut-plane: (a)  $V_x$  RMS in experiments, (b)  $V_x$  RMS in CFD, (c)  $V_y$  RMS in experiments, (d)  $V_y$  RMS in CFD.

A first identification of the turbulent scales explaining the energy difference is obtained with the analysis of the velocity spectra in the wake flow. Figure III.68b shows turbulent decay

based on the Power Spectra Density (PSD) computed at the maximum velocity RMS indicated by the white circle on Figure III.68a and b. At this local monitoring point, the experimental PSD reveals a turbulent decay driven by a dissipation rate of  $-5/3$ , which is in accordance with the literature knowledge. However, the numerical result exhibits more energy production from the low frequency eddies while the turbulent decay is governed by a more intense dissipation rate closer to  $-7/3$ .

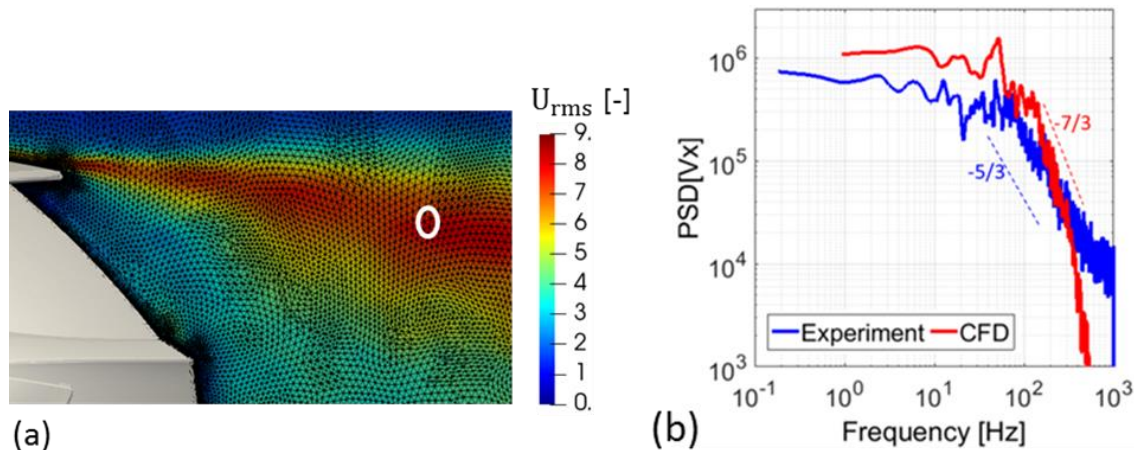


Figure III.68: (a) Focus on the velocity RMS downstream the roof spoiler superposed with the mesh grid; (b) PSD of PIV velocity magnitude and simulation velocity magnitude at the maximum turbulence intensity in Y0 vertical cut-plane.

One may recall the similitudes with the velocity spectra obtained in the preliminary ramp simulation. Similar overestimation of overestimation of the turbulent production term associated with stronger dissipation rate was observed. This energy decay suggests that there is a numerical bias, which may modify the process of dissipation in the numerical solver. The accuracy of the numerical subgrid scale model can be questioned but it should presumably affect only the end of the inertial zone. The discrepancy on the overall frequency range of the turbulent energy suggests that there is a numerical effect due to the approximation technique used to compute the resolved scales in the LES approach. One can question the influence of the regularization term of the Least-Square Galerkin operator used to enforce the weight residual constraint on the variational formulation of the LES equations. This term ensures the robustness of the simulation by a numerical smoothing of the artificial waves generated by the Galerkin constraint inside distorted elements. It is a crucial condition for the simulation of the flow around a complex design such as the POSUV.

If the Least-Square operator tends to damp the numerical instabilities generated by the Galerkin term, it also induces a numerical constraint in the region of low velocity magnitude as shown in Figure III.1 computed with a 1D simulation. In our case, Figure III.69a presents an estimation of the area subjected to high regularization term. We can see that the bound of the recirculation corresponding to a thin layer of small velocity is actually concerned by the numerical treatment produced by the Least-Square operator.

A recent simulation based on zonal mesh refinement was tested in order to validate the previous assumptions. A tetrahedral split was applied in the region subjected to the Least Square operator (Figure III.69b) and successfully managed to limit the regularization impact. However, numerical noises were generated because of the mesh interface treatment between the splitted elements and the outer mesh.

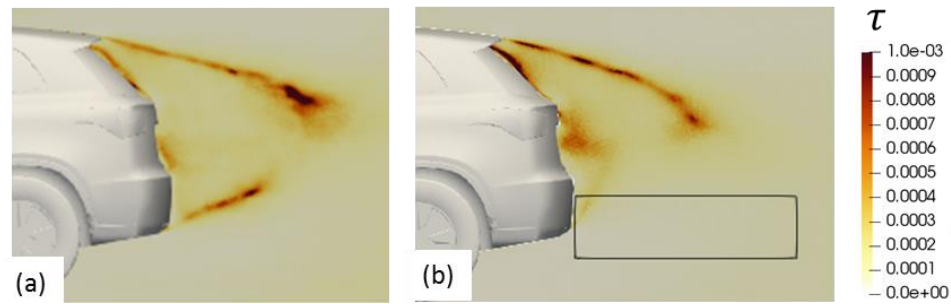


Figure III.69: Estimation of the Least-Square regularization intensity: (a) Reference mesh showing the sensitivity to the recirculation bound to the regularization term; (b) Zonal mesh refinement showing the reduction of the Least-Square matrix around the recirculation.

The turbulent energy decay solved in the bounding fluid layer of the recirculation zone is stronger due to the regularization term. This induces a lower resolved stress tensor  $L_{ij}$  in the spectral range of [500Hz-2000Hz] estimated between the numerical test filter  $\bar{\Delta}$  and the grid cutoff frequency  $\Delta$ . Thus, the dissipated energy due to the subgrid scale Dynamic Smagorinsky model is probably underestimated. This explains the establishment of an unbalanced energy between the numerical dissipation due to the approximation technique in FEM and the turbulent model estimation based on the resolved stress tensor. This numerical behavior can be related to the overestimation of the resolved low frequency scales.

We have correct time averaged values but the turbulent intensity is too high. It is then interesting to understand the origin of the fluctuations and to compare their modal magnitudes to the experimental decomposition. The numerical treatment applied in the regions of high turbulence remains of major concerns. Even if these discussions around the numerical approximations clarify the spectral behavior observed in the numerical simulations of detached flows, the overall transient flow dynamics have to be corroborated with experiment. This is achieved thanks to a cross-modal analysis with the experimental data for an accurate evaluation of the fluctuating components.

- Cross modal analysis of numerical and experimental results

The methodology presented in this paragraph was developed in order to identify the similarities and the discrepancies existing in the dynamical behavior between experiments and CFD. This method also has the advantage to output an exact estimator of the energy ratio associated to a common dynamical mechanism. Figure III.70 shows the definition of the concatenate databases used for the cross modal analysis. It is applied on the superposition of the transient databases in the pressure tailgate and the velocity data in the Y0 and Z140 cut planes. A total of 2001 snapshots, sampled at 2000Hz, from both experimental and CFD results was used.

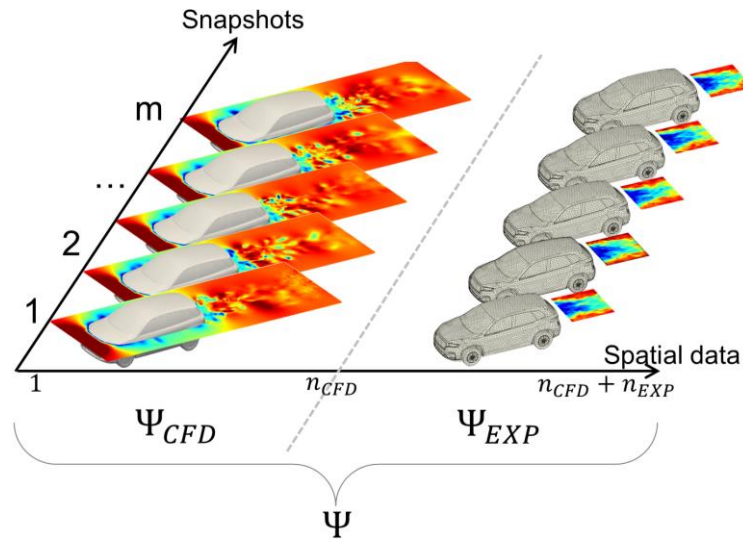


Figure III.70: Illustration of the database assembly for cross-dmd analysis between CFD results and experiments.

The DMD spectrum presented in Figure III.71, reveals the periodic characteristics commonly embedded in the concatenate database. If the energy is distributed between the low frequency until 135Hz, two major peaks stand out at 25Hz. It is associated to a Strouhal number of  $St_H = 0.167$  based on the mockup height or a Strouhal number of  $St_L = 0.2$  based on the root mean square of the frontal area ( $L = \sqrt{S_{ref}} = 0.24m$ ). This DMD mode can be related to the natural frequency of the 3D wake vortex shedding.

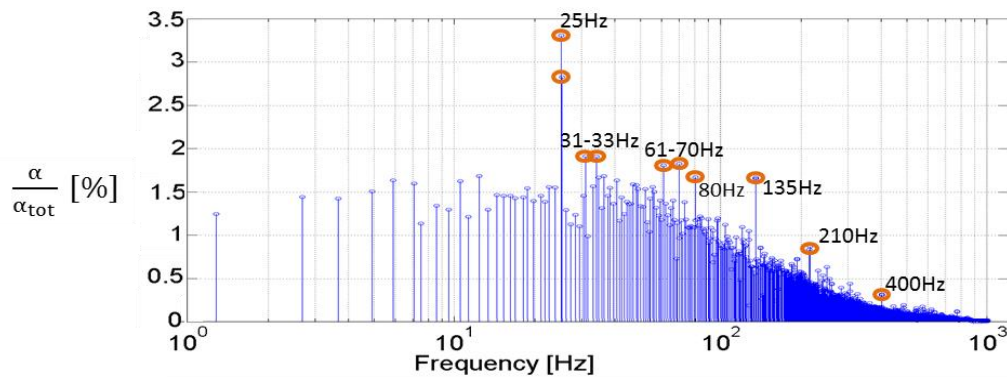


Figure III.71: DMD energy intensity as a function of the DMD frequency. In this spectrum, peaks are outlined at 25Hz, 31H, 33Hz, 61Hz, 70Hz, 80Hz, 135Hz, 210Hz and 400Hz.

The synchronized DMD spectra between the experimental and CFD of the tailgate dynamical behavior is presented in Figure III.72. We can see that the low frequency behavior is reproduced despite the additional peak due to the vortex shedding contribution at 25Hz.

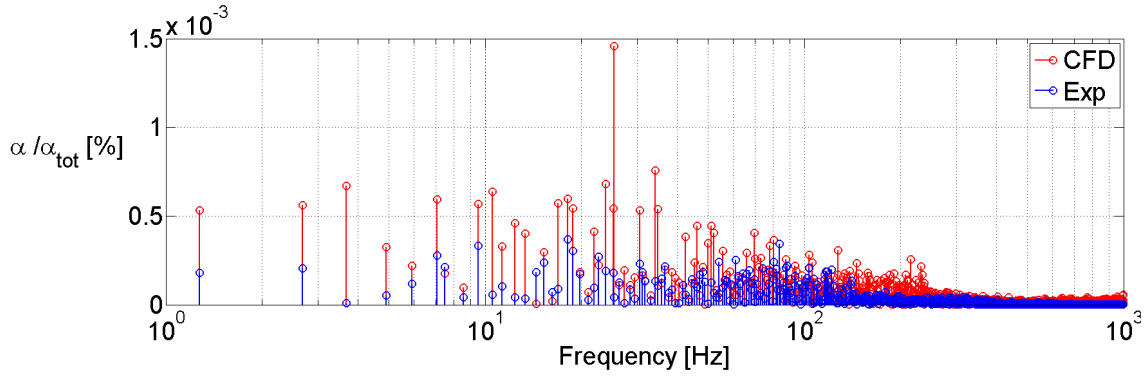


Figure III.72: Comparison of the synchronized DMD spectra on the rear tailgate between experiments and CFD.

The correlations in the database are analyzed thanks to the preliminary SVD computation performed in the DMD algorithm. The matrix  $U$  contained the correlated features between experiments and CFD. The spatial POD modes corresponding respectively to the CFD/experimental contributions are extracted using a block decomposition of the matrix  $U$  as shown in Eq.70. As  $U$  is a unit matrix, the relative energies  $E_{cf d}$  and  $E_{exp}$  respectively associated to the CFD/experimental blocks are obtained by normalization of  $U_{cf d}$  and  $U_{exp}$ .

$$U = \begin{bmatrix} U_{cf d} \\ U_{exp} \end{bmatrix} = \begin{bmatrix} E_{cf d}^{pod} & 0 \\ 0 & E_{exp}^{pod} \end{bmatrix} \times \begin{bmatrix} U_{cf d}^1 \\ U_{exp}^1 \end{bmatrix} \quad \text{Eq.70}$$

Where:

$U$  is the POD modes matrix.

$U_{cf d}$  and  $U_{exp}$  are respectively the CFD/Exp block matrices.

$U_{cf d}^1$  and  $U_{exp}^1$  are the normalized CFD/Exp modes.

$E_{cf d}^{pod}$  and  $E_{exp}^{pod}$  are  $m \times m$  diagonal matrices containing the energy contribution of respectively CFD and experimental database.

Consequently, the ratio between numerical and experimental contributions in the correlated POD modes are computed obtained with Eq.71.

$$r_{pod} = \frac{\|E_{cf d}^{pod}\|}{\|E_{exp}^{pod}\|} \quad r_{dmd} = \frac{\|E_{cf d}^{dmd}\|}{\|E_{exp}^{dmd}\|} \quad \text{Eq.71}$$

Figure III.73a shows the energy ratio per POD mode. POD modes associated to a ratio of 100% means that there is as much correlated information in the CFD block as in the experimental one. POD modes associated to a ratio above 100% means that the CFD block is too intense and below 100%, the CFD block is too weak. The POD modes are sorted by energy computed with the square of the singular values as shown in Figure III.73b. It should be noted that the SVD is applied on the transient database and not the fluctuating database (without time averaged contribution). The statistical average carrying the most energy in the flow is extracted in the first POD mode and will be denoted as the static mode. The remaining POD modes constitute a decomposition of the main fluctuation directions observable in the flow. The static mode is evaluated at 97% of the total modal energy and is associated to a ratio of 115% between CFD and experiment. The two most significant fluctuating POD modes (index 2 and 3) are about 4 times stronger in CFD than experiment. We can notice the evolution of the ratio as a function of the POD index. It is high for the first energetic POD

modes and it drops starting from the POD index 200 while the associated energy production decreases. A parallel can be drawn between above observations on the Power Spectra Density showing stronger production at low frequencies and weaker contribution of dissipative scales at high frequencies in CFD. This suggests that there is a relation between the orthogonal decomposition and the wake decaying energy.

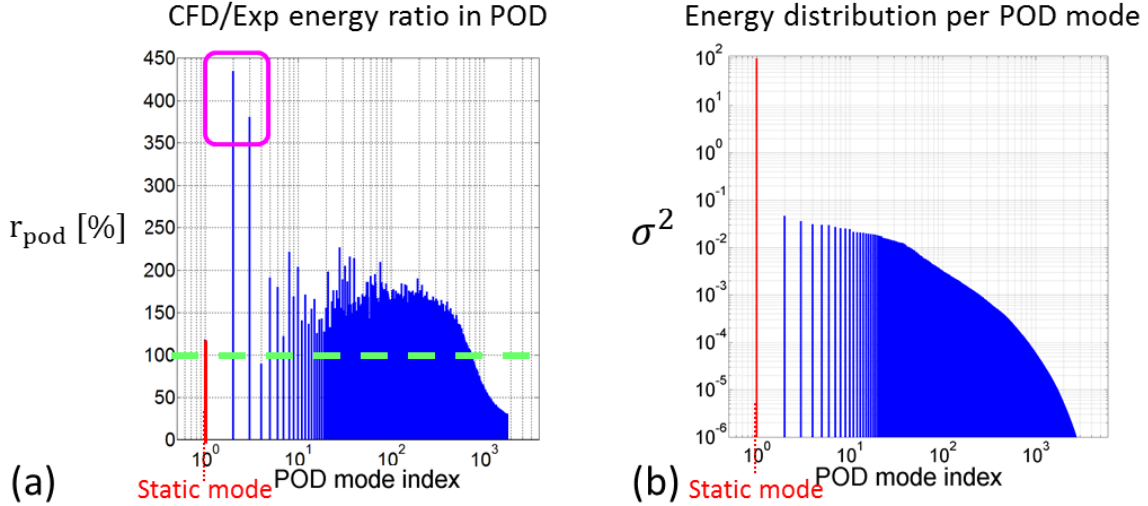


Figure III.73: (a) CFD/Exp ratio measured in POD modes. An overestimation of the energy contained in the 2<sup>nd</sup> and 3<sup>rd</sup> POD modes, is measured in the numerical simulation. (b) Energy distribution per POD mode showing the ratio of the static component in the first POD mode at 97% of the total modal energy.

The spectral information embedded in each POD mode is obtained by computation of the transfer matrix between the DMD and the POD base (Eq.72).

$$U = \Phi W \quad \begin{cases} W_{cfd} = W \cdot E_{cfd}^{pod} \\ W_{exp} = W \cdot E_{exp}^{pod} \end{cases} \quad \text{Eq.72}$$

Where:

$U$  is the matrix of the POD modes

$\Phi$  is the matrix of the DMD modes.

$W$  is the transfer matrix.

$E_{cfd}$  and  $E_{exp}$  are the relative energy per block.

$W_{cfd}$  and  $W_{exp}$  are the relative transfer matrix per block.

Figure III. 74 displays the transfer matrix  $W$  obtained between the POD and DMD bases. Each column of the matrix  $W$  gives the weight of the spectral decomposition per POD mode. Each line of the matrix  $W$  relates to one frequency and gives the list of POD mechanisms where this frequency is involved. The profile line at 0Hz gives all the POD modes correlated with in the static contribution.

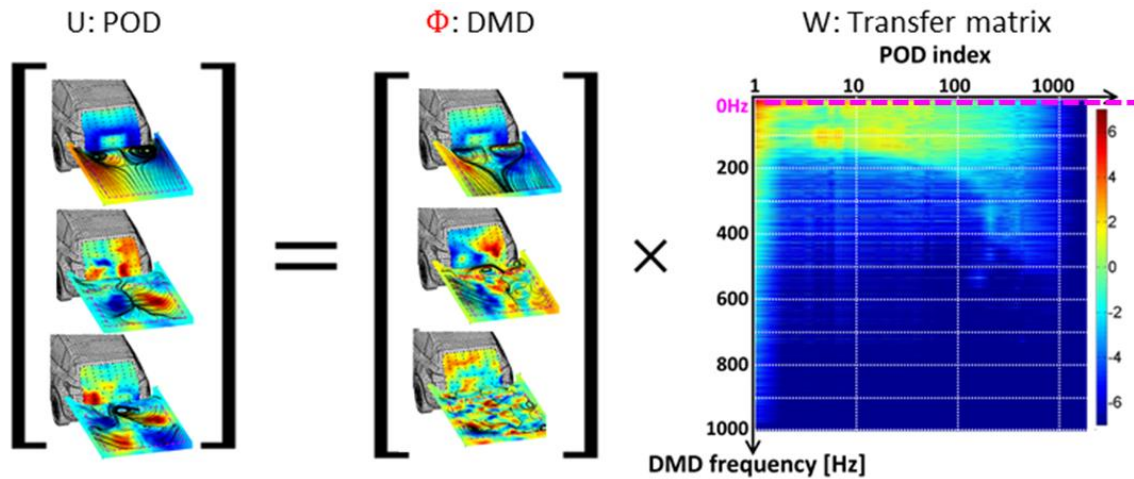


Figure III. 74: Visualization of the transfer matrix measured between DMD modes and POD modes.

Figure III.75 shows the change of spectral energy distribution per POD mode obtained thanks to the DMD projection on the POD base. The transfer matrix reveals that the first POD modes are mainly driven by low frequency dynamic modes but the frequency distribution quickly evolves depending on the POD index. The POD mode 2 (Figure III.76), associated with high energy production, is actually correlated to dynamic modes until 60Hz. The contribution of the frequency between 100Hz and 110 significantly grows in the POD modes index 100. The POD modes 1000 is correlated with the DMD modes until 400Hz. The change of spectral distribution can be interpreted as a modification of the turbulent production contributions compared to the contribution of the dissipative scales. Figure III.76 presents the spatial distribution of the 2<sup>nd</sup>, 10<sup>th</sup> and 100<sup>th</sup> POD modes. This shows the decrease of the characteristic wavelengths in the wake as a function of the POD index and consequently as a function of the coherent energy production. This methodology is particularly interesting in order to identify turbulent constitutive laws per correlated components in the wake flow.

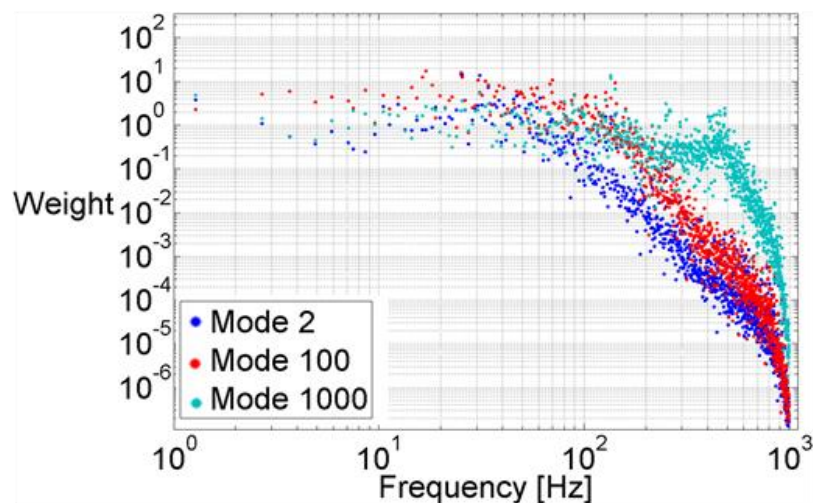


Figure III.75: DMD spectral projection per POD mode showing the change of energy distribution per frequency depending on the POD mode. The 2<sup>nd</sup> POD mode is the most energetic components and mainly driven by low frequencies. The high frequencies have more impact on the low energy POD modes such as the 100<sup>th</sup> and 1000 modes.

If the concatenation method provides an estimation of correlated signals between experiments and CFD, one can remark the differences on the spatial POD modes projected on the tailgate. Indeed, the spatial resolution of the pressure sensors limits the identification of spatial coherence. This is explained by the fact that the computation of orthogonal decomposition performed with the SVD is based on a Euclidian scalar product. The use of a  $\mathcal{L}_1$  scalar product taking into account the mesh resolution could improve the spatial definition of the POD modes. However, this does not affect the periodic features extracted in both databases.

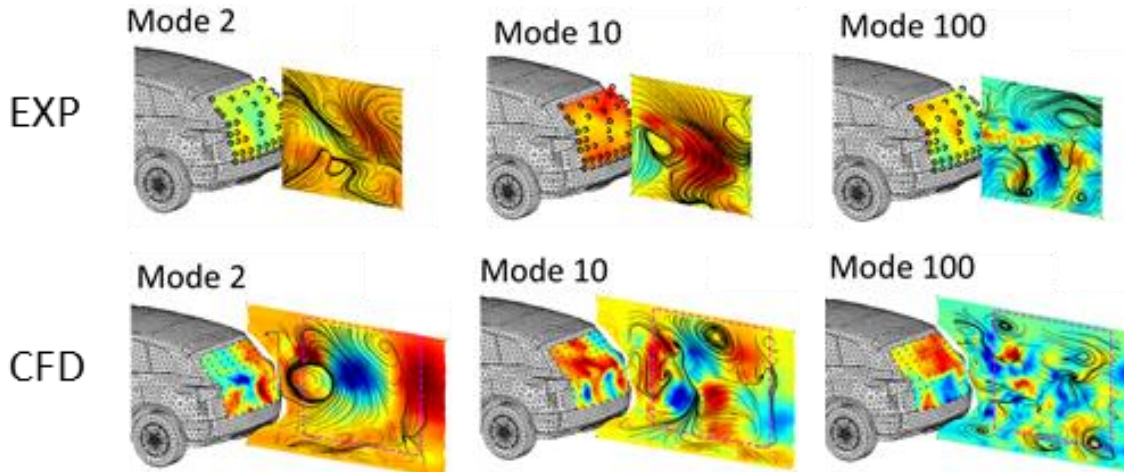


Figure III.76: Spatial correlated POD modes between CFD and experiments. If the POD mode 2 is associated to a large-scale structure, the characteristic lengths decrease as the associated POD energy decreases.

Focusing on the second POD mode, an investigation of the length scales and correlated frequencies is performed to understand this first fluctuating component of the flow. Figure III.77 presents the corresponding spatial mode in the  $Y0$  and  $Z140$  cut-planes in experiments and numerical simulation. In both cases, the spatial distributions denote a large scale structure describing a vertical recirculation combined with a horizontal oscillatory motion. This shared behavior validates the first fluctuating component measured in experiments is reproduced by the numerical simulation.

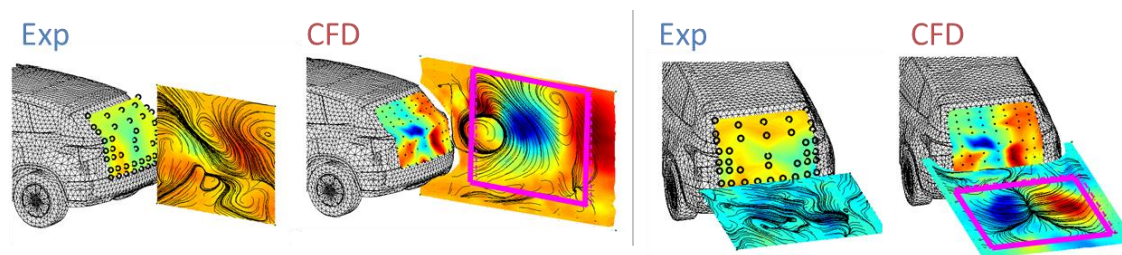


Figure III.77: Cross-POD mode 2: (a)  $Y0$  cut-plane experiment;  $Y0$  cut-plane CFD; (c)  $Z140$  cut-plane experiment;  $Z140$  cut-plane CFD.

The experimental/CFD comparison of the spectral energy ratio contained in the POD mode 2 is presented in Figure III.78. If there is a consistency in the spectral decomposition between experiments and CFD, the energy ratio showing stronger modal fluctuation in CFD is explained by the contribution of the periodic components at 25Hz and 30Hz.

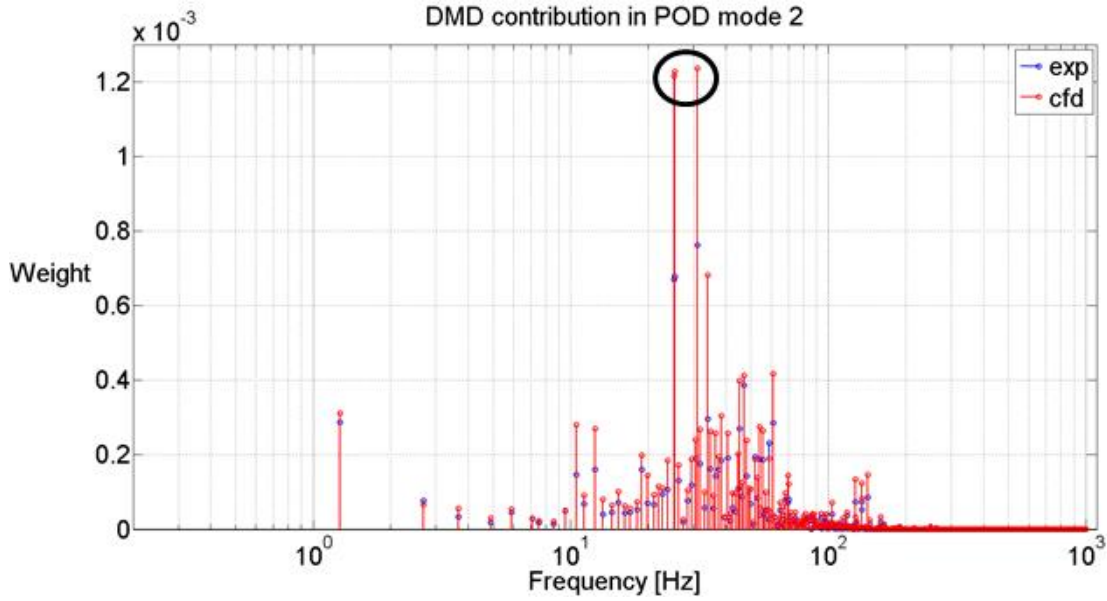


Figure III.78: DMD weights in the 2<sup>nd</sup> POD mode showing the numerical contribution compared to experiments. The frequencies at 25Hz and 30Hz appear to be too energetic in CFD.

These peaks corresponds to the vortex shedding natural frequency ( $St=0.2$  based on the square root of the frontal area).

We may refer to the previous discussion on the numerical approximation technique to explain the overestimation of these peaks. However, we should mention that the cross-correlation analysis suggests that this natural frequency due to the wake vortex shedding is captured in both CFD and experiment. The difference remains in the too high intensity associated to this mechanism in the numerical simulation.

- Modal optimization of the numerical simulation

An original algorithm is introduced here for an optimal correction of the discrepancies between the numerical simulation and the experimental results. It consists in the application of a penalty term in the reconstructed field of the modal decomposition (Eq.73).

$$\Psi_{opt} = \sum_{m=1}^M \rho_m^* \times [\alpha(\cos(2\pi f_m t) \times \Re(\Phi_m) + \sin(2\pi f_m t) \times \Im(\Phi_m))] \quad \text{Eq.73}$$

Where:

$\rho^* = (r_{pod})^{-1} W$  is the penalty term defined with correlated energy ratio between experiments and CFD ( $\rho_m$  is the  $m^{\text{th}}$  column vector of  $\rho^*$ ).

The application of this numerical optimization allows a dynamical correction of the flow behavior. Figure III.79 shows the velocity RMS in experiments compared to the numerical results before and after the cross-modal correction. The modal penalization manages an optimal adjustment of the turbulent quantities.

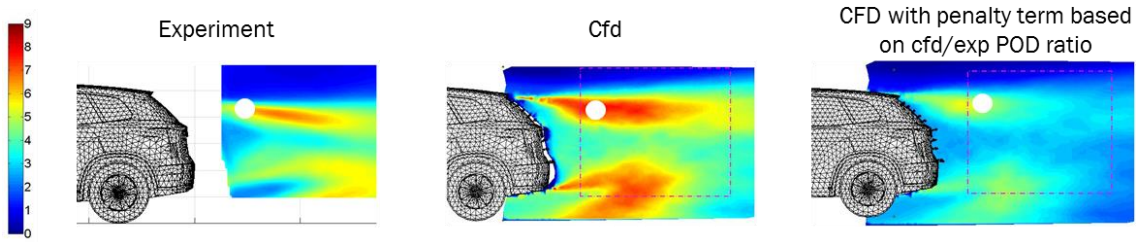


Figure III.79: Comparison of the velocity RMS: (a) in experiment, (b) in CFD, (c) in CFD after the application of the cross-modal correction. The white dot is a monitoring point used for spectral analysis

This correction has the advantage to modify the spectral signature of the transient flow. Figure III.80 outlines the comparison of the power spectra density at the monitoring point displays in Figure III.79. We can see that the low frequency contributions are damped at a similar energy level than experiments while the high frequency contributions are slightly increased. The difference of dissipation rate is reduced below 400Hz.

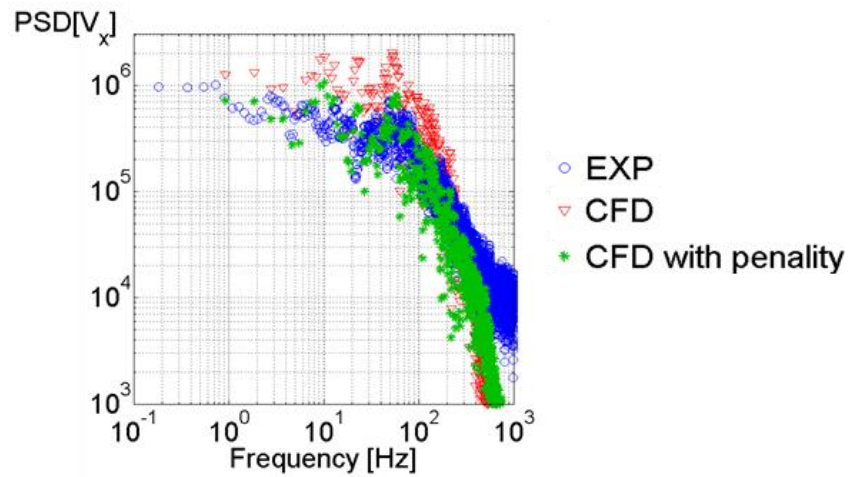


Figure III.80: Comparison of the velocity PSD computed at the white dot monitoring point of Figure III.79. The low frequencies of the CFD spectra corrected with the modal penalty term were adjusted at the level of the experimental spectrum.

It should be mentioned that this method could be extended to correct the overall 3D fluid flow by estimating a penalty factor computed with the energy ratio between sub-blocks of common spatial sensors (Eq.74). Thus, it is a powerful tool to force the convergence of the numerical simulation toward experimental results.

$$U = \begin{bmatrix} U_{cfd}^{fluid} \\ U_{cfd}^{sensors} \\ U_{exp}^{sensors} \end{bmatrix} = \begin{bmatrix} E_{cfd}^{fluid} & 0 & 0 \\ 0 & E_{cfd}^{sensors} & 0 \\ 0 & 0 & E_{exp}^{sensors} \end{bmatrix} \times \begin{bmatrix} U_{cfd}^1 \\ U_{cfd}^1 \\ U_{exp}^1 \end{bmatrix} \Rightarrow r_{pod} = \frac{\|E_{cfd}^{sensor}\|}{\|E_{exp}^{sensor}\|} \quad \text{Eq.74}$$

Where:

$U$  is the POD modes matrix.

$U_{cfd}$  and  $U_{exp}$  are respectively the CFD/Exp block matrices.

$E_{cfd}^{sensors}$  and  $E_{exp}^{sensors}$  are  $m \times m$  diagonal matrices containing the energy contribution of respectively CFD and experiments database.

To go further, it could be relevant to investigate the interest of co-simulation DMD algorithm such as “On-the-fly algorithm for DMD” proposed by (Matsumoto and Indinger, 2017) to enforce a penalty optimization as a direct mathematical constraint on the numerical solver. This underscores the interest of Reduced Order Model to improve our numerical simulation due to computational limitations.

- Discussion

In this section, the correlations with experiments corroborate the detached flow obtained in the numerical simulation. The cross-modal analysis validated coherent dynamical behavior between CFD and measurements. The energy ratio related to these coherent motions reveals too strong energy production from the numerical simulation. Based on previous investigations on the resolution of the turbulence decay performed on the ramp benchmark, a numerical bias is identified explaining the difference in the spectral and modal energy distributions.

Except for the modal magnitude, the cross analysis validates the coherence between the dynamical flow in numerical simulation and in experiment. A new numerical optimization was proposed to correct the numerical discrepancy.

We can now focus on the analysis of the mechanisms responsible for the aerodynamic loss.

### 3.4.4 Boundary layer and detachments correlations with the wake flow

The objective of this section is to understand how the development of unstable vortices around the body panel interacts with the wake flow. The interest of this analysis provides insights on how the management of these structures with flow control results in wake stabilization. After a validation of the boundary layer features around the body panels thanks to hot-wires measurements, the correlation between the flow detachments and the wake motion will be highlighted. Then the interaction with the tailgate pressure behavior will be extracted.

- Validation of the flow around the body panels

The flow around the body panel is validated thanks to hot-wires measurements achieved in experiments at a sampling frequency of 2000Hz during a period of 1 minute of acquisition. Figure III.81 describes the measured profiles lines used to characterize the transverse flow behavior along the lateral body panel. A first profile at  $x=-637\text{mm}$  captured the boundary layer on the front of the body panel before the front wheel and wheelhouse. The second profile was set on the center of the front wheel at  $x=-577\text{mm}$ . The third and fourth ones were set at  $x=-200\text{mm}$  and  $x=-100\text{mm}$  in order to define the boundary layer state feeding the shear layer. The fifth one was set at  $x=0\text{mm}$  for the shear layer description.

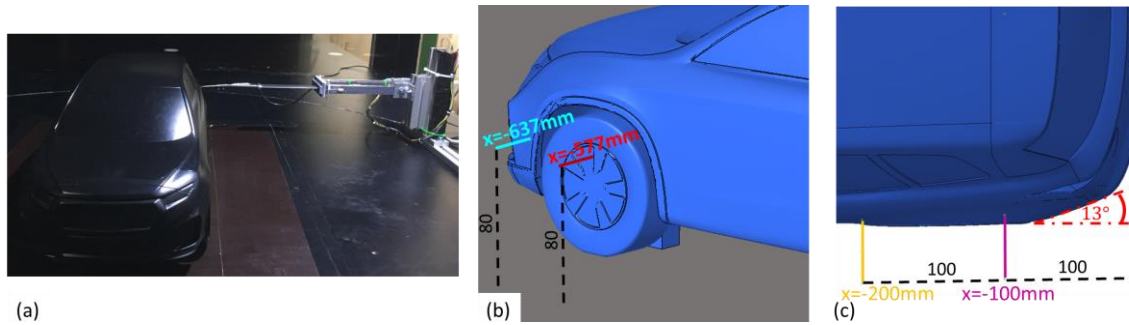


Figure III.81: (a) Picture of the hot-wires setup measured with the horizontal arm; (b) location of the measured profiles on the front fender; (c) location of the measured profiles on the rear fender.

The following analysis will focus on the lateral body panel comparison. Figure III.82 displays the normalized time averaged velocity in experiments and CFD. The time averaged boundary layer at  $x=-637\text{mm}$  is characterized by an overshoot of velocity higher than the free stream velocity. This could indicate the existence of a turbulent source generated by the front bumper curved shape. The time averaged profiles at  $x=-577\text{mm}$ ,  $x=-200$  and  $x=-100\text{mm}$  captured typical turbulent boundary layer behavior: The boundary layer thickness tends to grow through the body panel and the gradient close to the wall gets stronger.

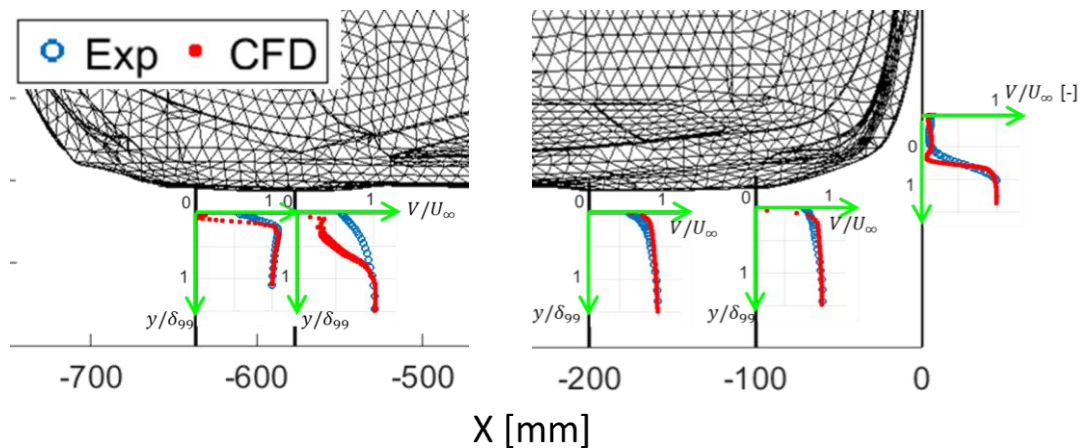


Figure III.82: Comparison of hot-wires and computed time averaged normalized boundary layer velocity magnitude profiles along the body panel in the Z80 cut-plane for the first 2 profiles and in the Z140 cut-plane for the last 3 profiles.

The velocity fluctuations, shown in Figure III.83, display several peaks around  $0.2 \times \delta_{99}$ . It appears that the numerical simulations give slightly higher energy in the vicinity of the wall than what is measured in experiment. Once again, the first boundary layer turbulent intensity profile differs from the others. The turbulent intensity is condensed close to the wall with a peaks located below  $0.1 \times \delta_{99}$  for both experiments and simulation. The fluctuations level is too strong in the numerical simulation compared to the experimental value. The penalty method proposed in the previous section could help to correct the boundary layer fluctuations intensity.

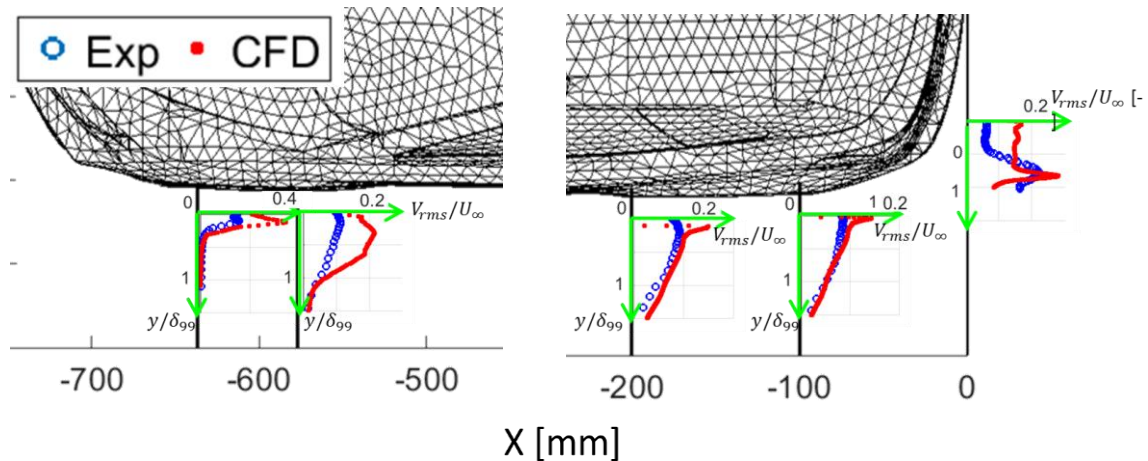


Figure III.83: Comparison of hot-wires and computed velocity fluctuations along the lateral body panel in the Z80 cut-plane for the first 2 profiles and in the Z140 cut-plane for the last 3 profiles.

Three dimensional time averaged observations from the numerical results show the existence of a vertical vortex in this region caused by the abrupt design of the front bumper (Figure III.84). The intensity of this structure is probably driven by the adverse pressure gradient surrounding the mockup.

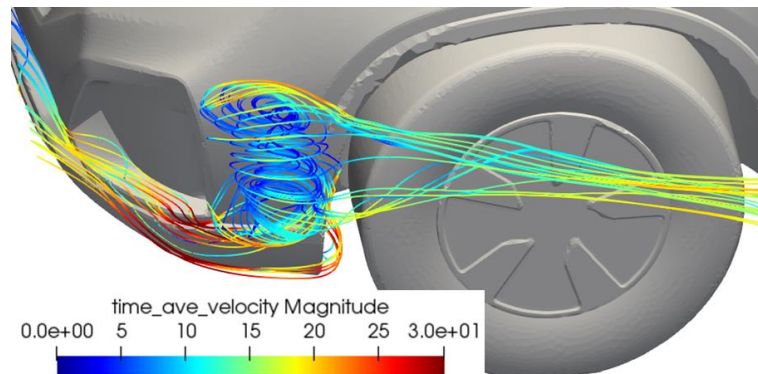


Figure III.84: Time averaged 3D structure responsible for the turbulent kinetic energy in the boundary layer of the front bumper.

- Origin of the vortex fluctuations

The experimental investigations presented in section 2.2.1, gives some insight on the relation between the wake oscillatory motion and the rear end dynamics thanks to the cross analysis of pressure sensors and velocity measurements in the Y0 and Z140 2D cut-planes. The analysis of the time averaged flow performed in section 3.4.2 on the numerical simulation, also exhibits the importance of the boundary layer separation with the wake topology. In addition, the observations of the separation mechanism in the benchmark of the 25° inclined ramp demonstrate the importance of the boundary layer quantity momentum governing the shear layer and the recirculation behavior. In the case of the POSUV benchmark, we will try to elucidate the interaction of the vortices generated on the lateral panels with the wake dynamics based on the 3D streamlines along the car (Figure III.85). We will focus on the structures coming from fender separation as the flow over the roof spoiler has a minor influence on the wake recirculation. Two pairs of monitoring points were used to identify the synchronized periodic characteristics (A1 and A2 in the Z80 cut-plane).

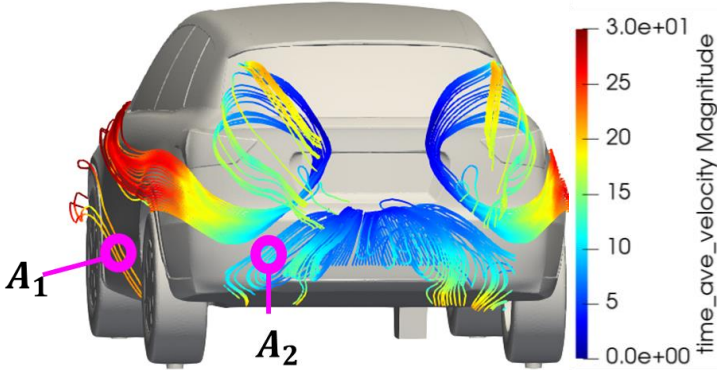


Figure III.85: Time averaged velocity streamlines of the flow around the POSUV: the circles indicate the monitoring points used to correlate the lateral detachments with the wake vortices

The cross-correlation between these sensors is displayed in Figure III.86. There is shared spectral information carried out by the frequencies of at 16Hz. Other components are also measured at 6Hz and 90Hz in the Z80 cut-planes.

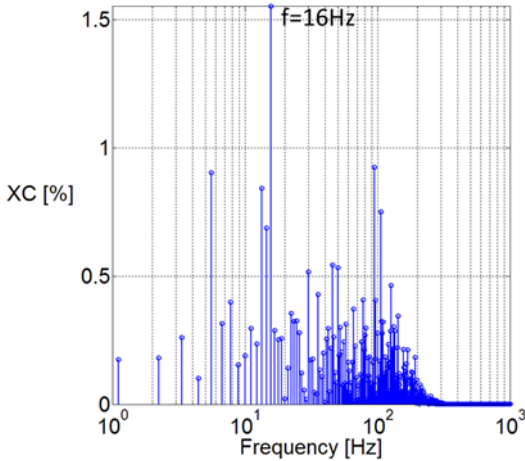


Figure III.86: Cross correlation between A1 and A2 in the Z80 cut-plane showing the synchronized characteristic at 16Hz.

The flow analysis using the numerical database with the Y0, Z80 and Z140 cut-planes extended all around the car (Figure III.87) provides more information on the sources responsible for these periodic oscillations.

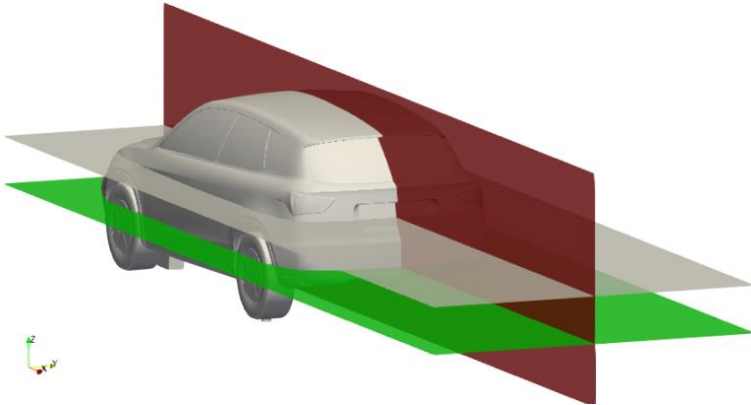


Figure III.87: Spatial data used for the 3D modal analysis.

The DMD spectra obtained with this database is analyzed in order to understand the modal behavior highlighted in experiment. Figure III.88 shows the spatial DMD modes at the frequency of 17Hz, identified in experiment, in respectively the Z140 cut-plane and the Z80 cut-plane. One can remark the periodic synchronization of the turbulent structures around the body panel with the wake motion.

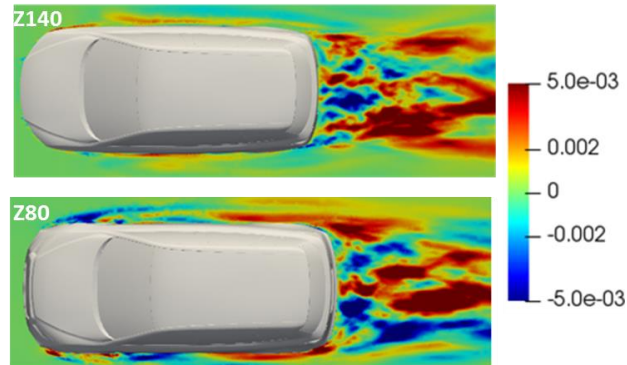


Figure III.88: DMD velocity X modes in the Z140 cut-plane at 16Hz in the Z140 and Z180 cut-planes.

The reconstruction isolates the dynamics of the component at 17Hz and shows the periodical interaction between the lateral detachments with the shear layer development. Figure III.89 displays the reconstruction in the Z140 and Z80 cut-planes, of the flow fluctuations (without the static component), induced by the periodic dynamical behavior at 17Hz. In the Z80 cut-plane, the flow exhibits a synchronized motion between the structures coming from the wheelhouse detachments and the shear layer developing from the rear bumper separation. When the body panel vortex induces an increase of the boundary layer velocity, the following shear layer tends to be weaker and when the body panel vortex reduces the boundary layer velocity, the following shear layer is get stronger. In the Z140 cut-plane, there is a strong flow fluctuation near the bumper corner, which evolves in opposition with the shear layer flapping. This is related to the feedback flow due to  $\Omega_z^-$  visible in the Z140 cut plane. In the periodic behavior at 17Hz, when the shear layer velocity increases, the backflow is constraint, while it is strengthen when the shear layer momentum decreases.

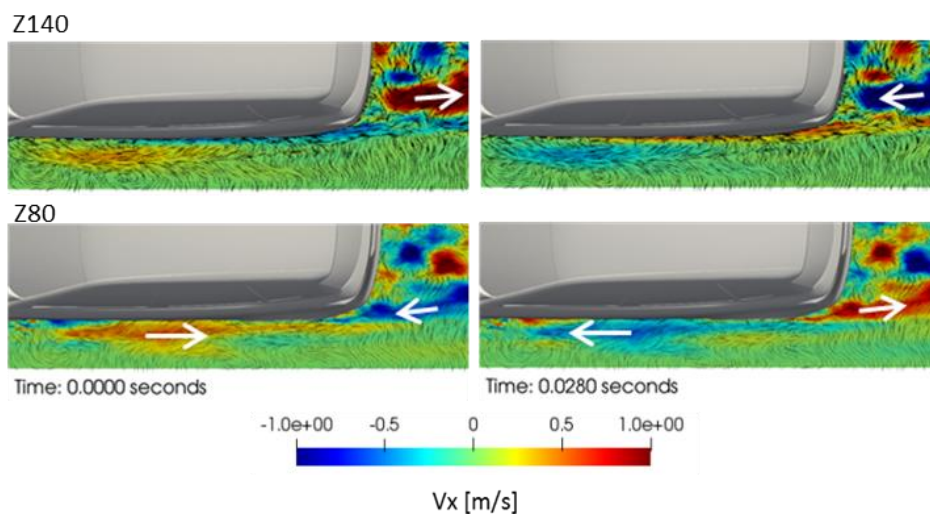


Figure III.89: Snapshots of the reconstruction in Z140 and Z80 cut-planes with the dynamic behavior of the periodic component at 17Hz during the phase ( $t=0s$ ) and the opposition ( $t=0.028s$ ).

It is difficult to conclude on the phase or opposition synchronization of the identified mechanism between the left and right hand side of the car. Indeed, the spatial DMD mode presented in Figure III.88, is not perfectly symmetric but the local velocity fluctuations in the shear layer of the Z80 cut-plane, has the same sign. This suggests a phased synchronized velocity pulsation coming from both lateral boundary layer fluctuations. However, the intensity of the pulsation is not exactly balanced. We can assume that there is a delay between the left and right hand side or there is another mode with a close frequency counter-balancing this motion.

These observations validate the assumption that the separation occurring on the rear bumper is governed by the turbulent vortices coming from the lateral boundary layer detachment. The momentum in the shear layers is increased by the recirculation emerging from the wheelhouse and fender panels. In addition, the increase of the shear layer momentum tends to compete against the circulation of the wake vortices.

We have now to understand how the wake motion drives the transient pressure loss on the rear tailgate. We previously mentioned the relation between the pressure and the velocity through the Poisson equation in 3D flow and its projection of 2D driven flow. Similar statements will be used to relate the wake motion to the pressure loss transient evolution.

- Correlation between pressure body panel fluctuations and wake dynamic

In a similar way than the correlations analysis obtained from the concatenation of two databases, the same method is used to evaluate the correlations between the velocity fluctuations in the wake and the pressure fluctuations around the SUV. The database gathered a first block matrix associated to the wake velocity data and a second block matrix associated to the SUV pressure data. The block decomposition of the modal matrices gives an estimation of the ratio of the modal fluctuations contains in the pressure or in the velocity (Eq.75).

$$\Phi = \begin{bmatrix} \Phi_{velocity} \\ \Phi_{pressure} \end{bmatrix} = \begin{bmatrix} E_{velocity}^{dmd} & 0 \\ 0 & E_{pressure}^{dmd} \end{bmatrix} \times \begin{bmatrix} \Phi_{velocity}^1 \\ \Phi_{pressure}^1 \end{bmatrix} \quad \text{Eq.75}$$

Where :

$\Phi$  is the DMD modes matrix.

$\Phi_{vel}$  and  $\Phi_{pres}$  are respectively the wake velocity and SUV pressure blocks.

$\Phi_{vel}^1$  and  $\Phi_{pres}^1$  are the normalized velocity/pressure modes.

$E_{vel}^{dmd}$  and  $E_{pres}^{dmd}$  are the diagonal matrices containing the modal energy of velocity/pressure.

The projection of the POD base into the DMD base yield the transfer matrices dimensioning the correlations between the periodic behaviors. Figure III.90 shows the transfer matrix associated to the velocity and pressure contributions. The pressure transfer matrix is unexpectedly close to the velocity weight matrix. We still have on both maps, the significant amount of energy brought by low frequency pulsations within the first POD modes.

The velocity and pressure weight matrix distribution are similar which means that these two state variables carry a common spectral information. This velocity-pressure coupling can be related to the Q-criterion definition, which can also be decompose on the same DMD mode of velocity/pressure. The extension of this statement could be done to isolate the shear and vorticity modes.

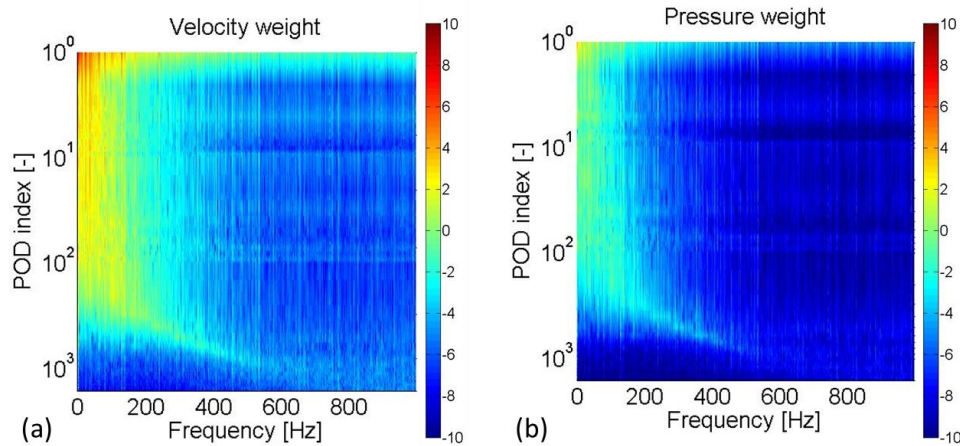


Figure III.90: Transfer matrices between POD and DMD matrices: (a) wake velocity transfer matrix; (b) SUV pressure transfer matrix.

The projection on the 0Hz static DMD modes gives the reflection of the pressure/velocity correlated fluctuations. Figure III.91a reveals the importance of the fluctuations associated to the POD index 3, 4 and 6. The associated spatial coherent fluctuations are displayed in Figure III.91b. The spatial coherent structures affecting the pressure on the body panels denote the interference between the lateral and underbody detached structures with the fluctuations generated on the rear bumper separation. We will first have a closer look on the coherent structures of the POD modes 2, 3, 4 and 6 and then we will investigate more deeply on the associated DMD periodic correlations.

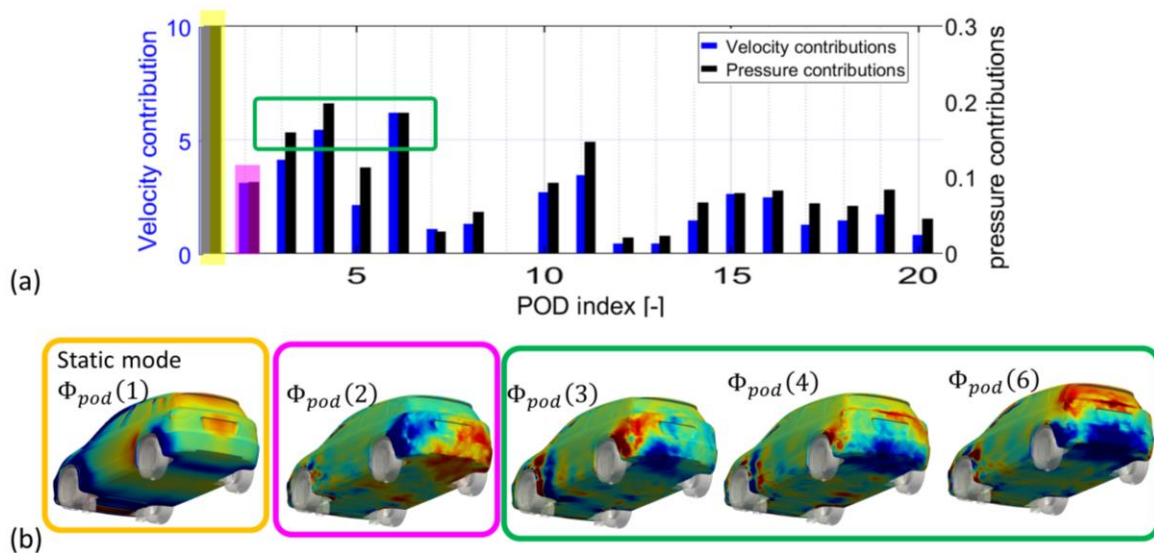


Figure III.91: (a) Projection of the velocity and pressure POD contributions into the 0Hz static component. The POD modes 3, 4 and 6, highlighted by the green box, are the main fluctuations correlated with the 0Hz static component; (b) POD modes 3, 4 and 6 correlated with the static 0Hz DMD modes.

As a first step, we will examine  $\Phi_{pod}(2)$  and  $\Phi_{pod}(6)$ , which are related to global wake oscillations. Then, we will focus on  $\Phi_{pod}(3)$  and  $\Phi_{pod}(4)$  which appear to be complementary paired modes affecting the aerodynamic loss in the static component.

Figure III.92 shows the distribution of the fluctuations due to the 2<sup>nd</sup> and 6<sup>th</sup> POD on the tailgate and in the wake cut-planes. It appears that  $\Phi_{pod}(2)$  can be associated to a horizontal oscillation of the pressure fluctuations. The associated modal velocity in the Z140 cut-plane indicates that there is a phase opposition between the flow velocity fluctuations in the wake. This validates the predominance of the wake horizontal motion. The 6<sup>th</sup> mode is related to a vertical pressure variation as shown in Figure III.92b. It is correlated with the modal wake velocity in the Y0 cut-plane. The modal intensity below the rear bumper underlines the influence of the underbody flow in the wake, which can be related to the time averaged S-shape structure observed in the wake topology (section 3.4.2). Even if the 2<sup>nd</sup> POD mode carries more energy than the 6<sup>th</sup> one, the feature highlighted in  $\Phi_{pod}(6)$  is still interesting because it indicates the existence of a pressure oscillating fluctuation varying between the slant window and the tailgate.

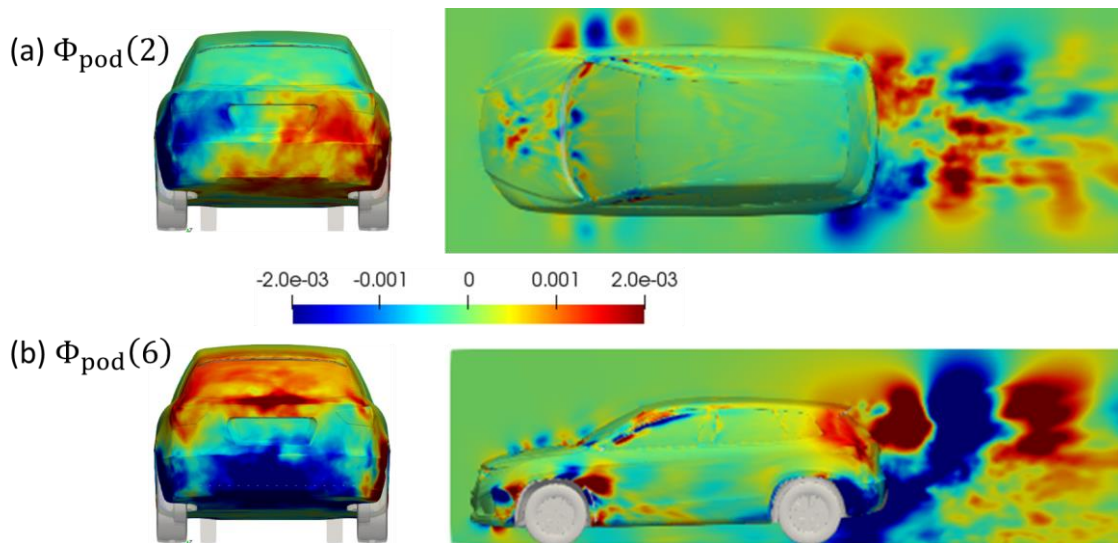


Figure III.92: 2<sup>nd</sup> and 6<sup>th</sup> POD modes of the modal pressure fluctuations on the rear tailgate and of the associated modal wake velocity.

This can be related to some observations showing a switch of the pressure minima on the slant angle depending to ground clearance, the pitch and under large yaw conditions. It was observed in the stability study of the full scale Peugeot 5008 and Renault Mégane mockups (Bonnayon and Cadot, 2018). The threshold conditions when this vertical component becomes predominant remains an important question for the control of road vehicles.

The DMD spectral projections detail the periodic motions involved in the mechanisms responsible for the 2<sup>nd</sup>, 6<sup>th</sup> POD modes. Figure III.93a, Figure III.94a, show the result of the column vectors  $W_2, W_6$  of the transfer matrix between the DMD and the coherence contained in  $\Phi_{pod}(2), \Phi_{pod}(6)$ . Concerning the 2<sup>nd</sup> POD mode, the resulting spectrum is governed by a combination of the low frequency pulsation at 6.4Hz (Figure III.93b) with the natural wake frequency of 23Hz (Figure III.93c) and 31Hz (Figure III.93d).

In  $\Phi_{pod}(6)$ , the spectral projection of (Figure III.94b) validate that this mode isolates the wake vortex shedding driving the vertical wake motion at  $St = 0.2$ . The configurations where the pressure drop is measured on the slant window, could be explained by a change of energy ratio between  $\Phi_{pod}(6)$  and  $\Phi_{pod}(2)$ . The balance between these modal components is probably governed by the flux going below the car depending on the ground clearance or the pitch.

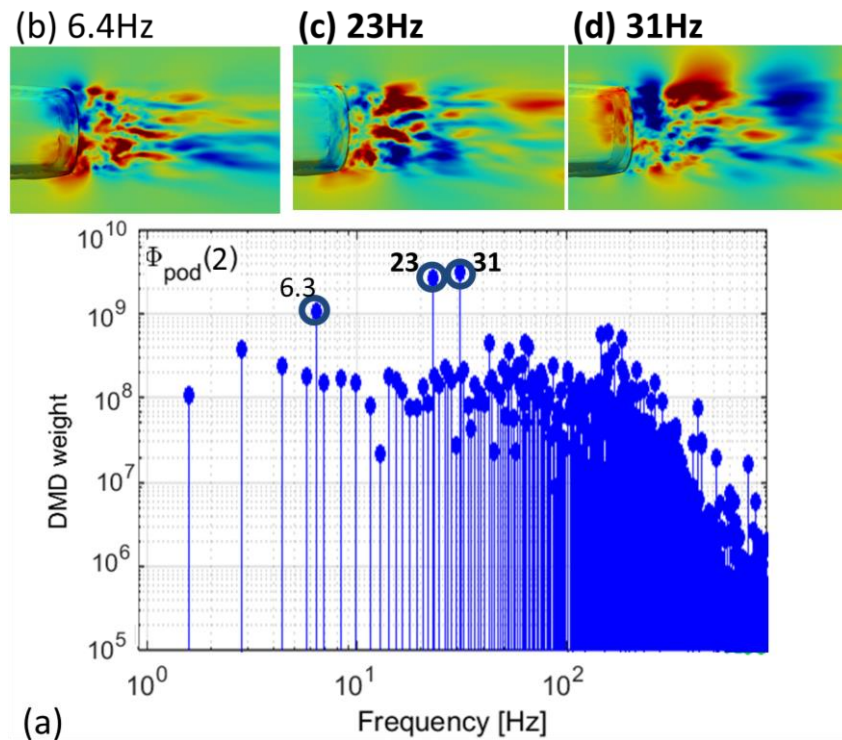


Figure III.93: (a) DMD weight corresponding to the 2<sup>nd</sup> column vector of the transfer matrix between periodic decomposition and POD. Velocity DMD modes in the Z140 cut-plane associated to the correlated mechanisms identified  $\Phi_{pod}(2)$  at (b) 6.4Hz, (c) 23Hz, (d) 31Hz. The frequencies in bold indicate common features with  $W_3$ ,  $W_4$  and  $W_6$ .

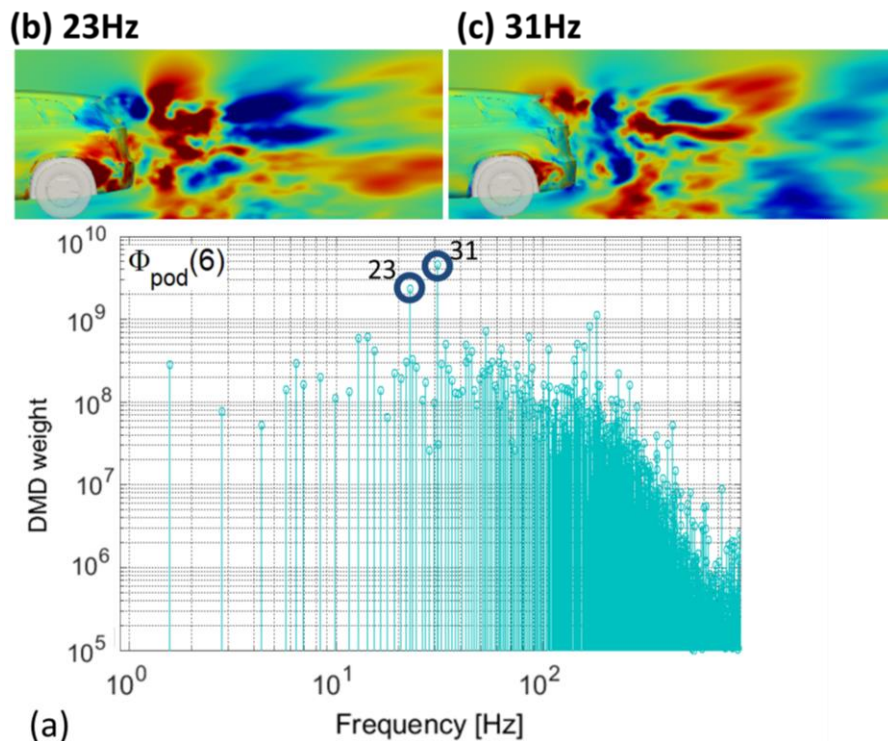


Figure III.94: (a) DMD weight corresponding to the 6<sup>th</sup> column vector of the transfer matrix between periodic decomposition and POD. Velocity DMD modes in the Y0 cut-plane associated to the correlated mechanisms identified  $\Phi_{pod}(6)$  at (b) 23Hz, (c) 31Hz. The frequencies in bold indicate common features with  $W_2$ ,  $W_3$  and  $W_4$ .

We will now focus on the complementarity of the coherent structures described by the 3<sup>rd</sup> and 4<sup>th</sup> POD modes. It is especially visible on the tailgate pressure mode presented in Figure III.95a. The tailgate pressure mode  $\Phi_{pod}(3)$  is driven by the fluctuations on the left side in opposition with the tailgate pressure mode  $\Phi_{pod}(4)$  driven by the fluctuations on the right side. Consequently, these components can be related to the large scale structures  $\Omega_z^-$  and  $\Omega_z^+$  identified in the time averaged flow topology. Figure III.95b exhibits the correlation with the velocity fluctuations contains in  $\Phi_{pod}(3)$  and  $\Phi_{pod}(4)$  in the Z140 cut-plane. Indeed, if there is a strong detachment on the right side of the SUV, the velocity fluctuations in the rear bumper shear layer increase. This is in agreement with the demonstration of the periodic synchronization of the body panel detachments with the rear bumper separation performed in the previous paragraph. With the modal wake velocity presented in Figure III.95b, we can go further and state that the increase of the shear layer momentum accentuate the recirculation intensity of the vertical structures  $\Omega_z^-$  and  $\Omega_z^+$ .

The dissociation of the fluctuations due to  $\Omega_z^-$  and  $\Omega_z^+$  in two separated orthogonal modes is unexpected. This raises once again the question of the lateral synchronization of the shear layer fluctuations. If,  $\Phi_{pod}(2)$  contains the large scale horizontal wake motion,  $\Phi_{pod}(3)$  and  $\Phi_{pod}(4)$  represent the intensity of the velocity fluctuations driving the strength of the vortices.

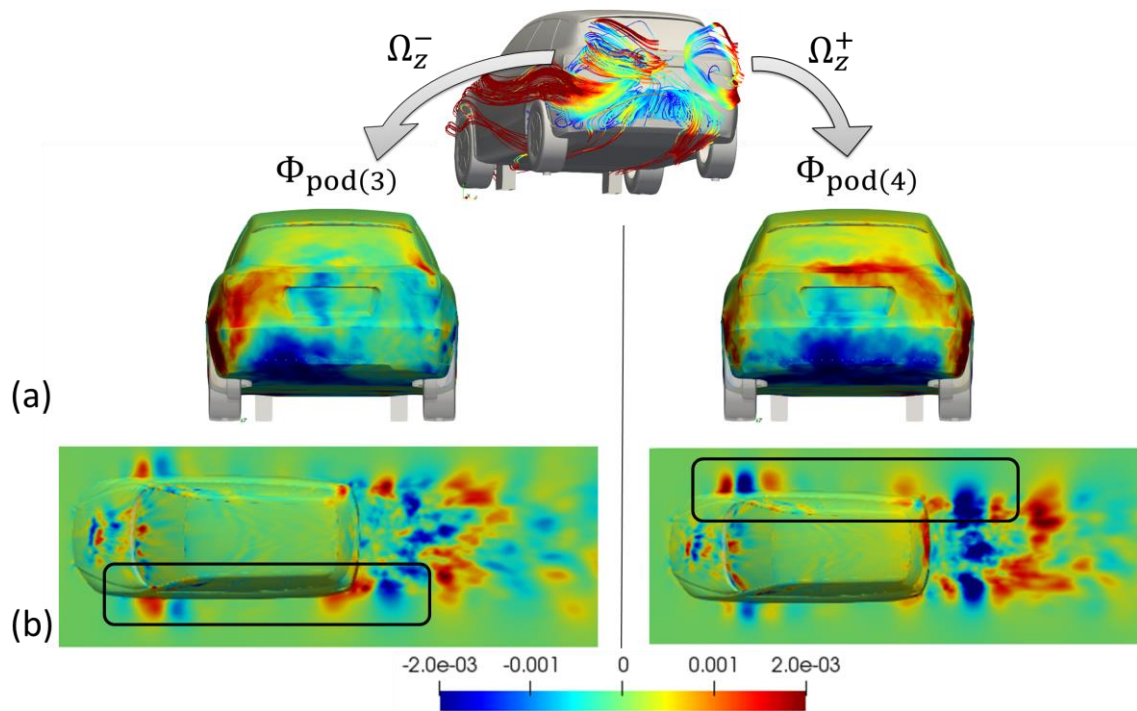


Figure III.95: 3<sup>rd</sup> and 4<sup>th</sup> POD modes showing the correlation of (a) pressure modes on the tailgate and (b) velocity modes in Z140 cut-plane.

Figure III.96a and Figure III.97a show the result of the column vectors  $W_3$  and  $W_4$  of the transfer matrix in  $\Phi_{pod}(3)$   $\Phi_{pod}(4)$ . The 3<sup>rd</sup> and 4<sup>th</sup> correlated mechanisms are more likely governed by higher frequency signals. We measure common frequencies at 63Hz, 146Hz and 168Hz. There are also some singularities with the frequencies at 106Hz emerging in  $\Phi_{pod}(3)$  and at 182Hz emerging in  $\Phi_{pod}(4)$ . The differences of the periodic DMD weights between  $\Phi_{pod}(3)$  and  $\Phi_{pod}(4)$  emphasize the spectral sensitivity to the flow disturbances. This leads to correlated mechanisms, which are significantly more complicated than the ones observed in the simplified benchmarks of the 25° ramp flow or the Ahmed Body. Therefore, in the case of

the realistic car, the process of energy transfer involved a wider range of modal components that we managed to extract thanks to the DMD/POD methodology.

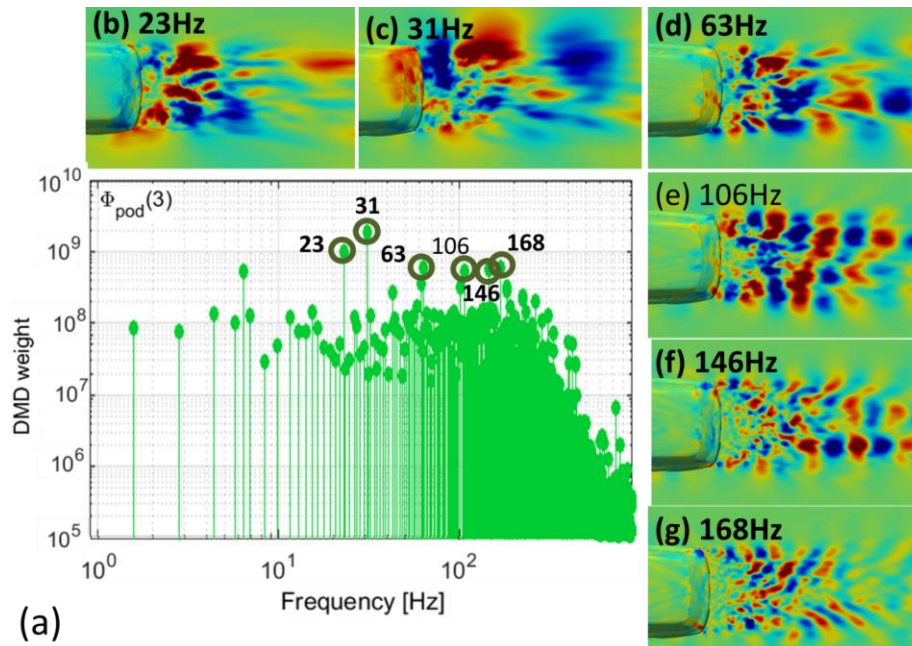


Figure III.96: (a) DMD weight corresponding to the 3<sup>th</sup> column vector of the transfer matrix between periodic decomposition and POD. Velocity DMD modes in the Z140 cut-plane associated to the correlated mechanisms identified  $\Phi_{pod}(3)$  at (b) 23Hz, (c) 31Hz, (d) 63Hz, (e) 106Hz, (f) 148Hz, (g) 168Hz. The frequencies in bold indicate common features with  $W_4$ .

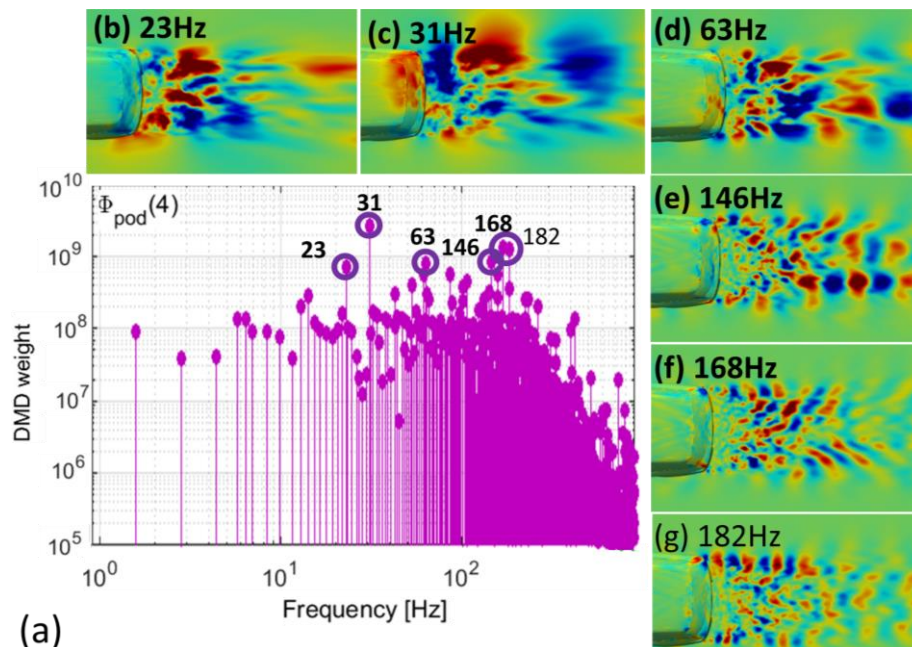


Figure III.97: (a) DMD weight corresponding to the 4<sup>th</sup> column vector of the transfer matrix between periodic decomposition and POD. Velocity DMD modes in the Z140 cut-plane associated to the correlated mechanisms identified  $\Phi_{pod}(4)$  at (b) 23Hz, (c) 31Hz, (d) 63Hz, (e) 146Hz, (f) 168Hz, (g) 182Hz. The frequencies in bold indicate common features with  $W_4$ .

Thanks to the normalized Strouhal number based on the mockup height, we can interpret origin of these features. The low frequency at 6.4Hz associated to the Strouhal number of 0.04 is assimilated to the wake horizontal oscillation. The modes at 23Hz and 31Hz are related to the wake shedding mechanisms corresponding to the Strouhal number of [0.15-0.2]. The shear layer fluctuations are described by the modes between 85Hz and 182Hz equivalent to the Strouhal number range of [0.58-0.66].

Based on the analysis of the coherence between all the periodic features, we can state that the shear layers fluctuations are source terms affecting the intensity of the wake vortices. The deviation of the computed spectral signatures around the characteristic values of  $St = 0.2$  and  $St = 0.6$  is explained by the complexity of the POSUV design. The lack of symmetry in these periodic components denotes the flow sensitivity to body panel disturbances.

- Discussion

Many structures emerged around the complex design of the POSUV. We discussed in the literature review of the importance of detachment disturbances in the excrescence drag. In the numerical simulations, similar vortices to those observed by (Hucho and Sovran, 1993) on realistic cars, were computed. Figure III.98 summarizes the detached structures observed in our numerical simulation. We can mention the hood detachments (Figure III.98a), the hood-windshield junction (Figure III.98b), the longitudinal A-pillar vortices (Figure III.98c), the detachment on the fender (Figure III.98f), and on the bottom front bumper (Figure III.98e). If the roof spoiler (Figure III.98d) prevents the impact of the structures on the roof, the separation on the rear bumper (Figure III.98g) has a major influence on the vortical structures  $\Omega_y$ ,  $\Omega_z^-$  and  $\Omega_z^+$ .

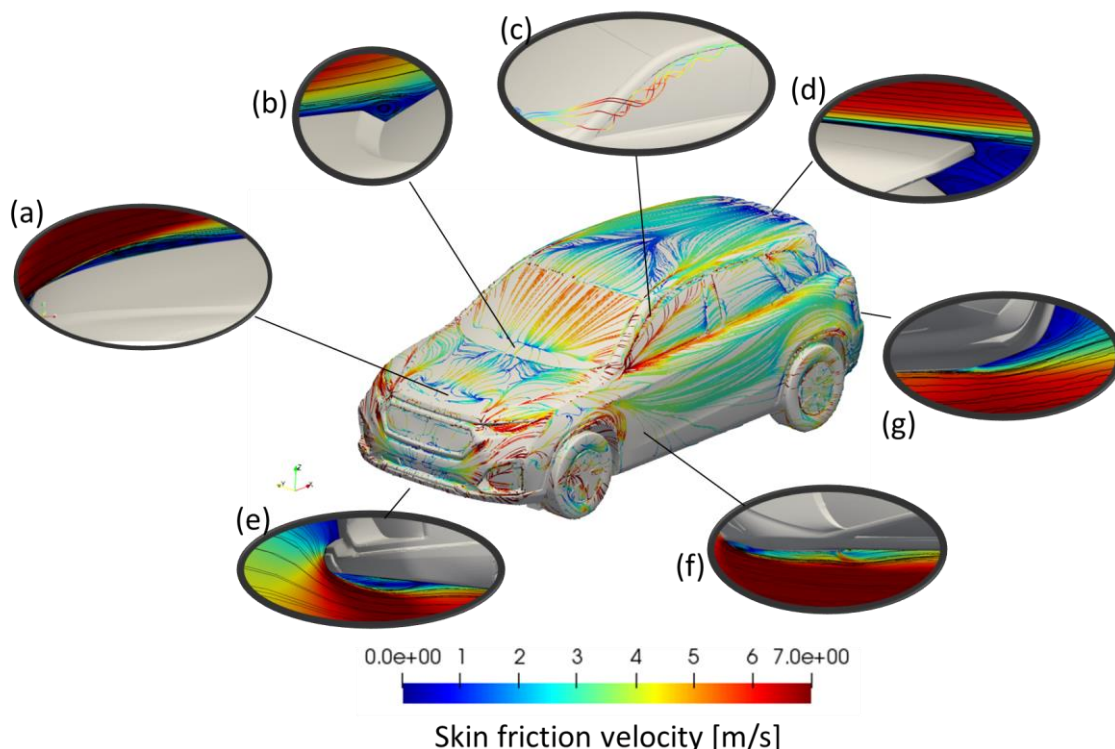


Figure III.98: Time averaged skin friction velocity computed on the generic SUV body panels with focus on separated flow vortices observed on time averaged velocity streamlines. Main detachment regions are located on (a) front end, (b) Hood-windshield junction, (c) A-pillar, (d) Spoiler, (e) Rear bumper edges, (f) Front corners, (g) Lower front bumper.

The application of the modal analysis on the overall SUV, plus the cut-planes surrounding the mockup in the numerical simulation provided a lot of information on the separation process. This completes the wake velocity analysis performed on the finite PIV cut-planes from experimental measurements. We identified the phase opposition at  $St=0.12$  between the velocity due to the detachments on the body panel and the shear layer quantity momentum on the rear bumper. Then, the modal analysis has successfully extracted the interaction between the wake horizontal motion at  $St=0.04$ , the vortex shedding at  $St=0.2$  and the turbulent source term induced by the shear layers fluctuations at  $St=0.6$ .

In addition, the spectral deviation associated with the shear layer (between 0.58 and 0.66) demonstrates the impact of the uncertainties resulting from the separation on the rear bumper.

One may recall the optimal flow control solution obtained in experiment. Indeed, free of any symmetry constraint, the optimization converged toward different forcing frequencies on the left and right jets. The uncertainties obtained in the numerical spectral decomposition helps to understand why we manage to change the pressure loss on the tailgate despite the unsynchronized shear layer control.

At this stage, two flow control strategies seem to be efficient for the reduction of the aerodynamic loss on a realistic car. On one hand, it appears pertinent to minimize the generation of detachments with shape optimization on the fender and wheelhouses surfaces. For an application on production cars, this has to be achieved preliminary to the design step. On another hand, it seems relevant to perform a regulation of the shear layer turbulent energy with active flow control on the rear bumper. In the following, we present the first result of flow control based on the experimental actuation setup.

### 3.4.5 Flow control simulations with Large Eddy Simulation

The flow control simulations are achieved according to the actuation characteristics described in 2.2.2. Figure III.99a shows the geometry of the discontinuous slots spaced each 10mm on the lateral sides and on the bottom of the rear bumper. A length of 2.5mm and a width of 0.5mm define the geometry of each slot. Then the flow rate nodal boundary condition was defined based on the optimal flow solution identified by experiments. Figure III.99b reminds the flow rates and the frequency parameters obtained at the end of the machine learning procedure. A flowrate of 15L/min was evenly distributed between the lateral slots and a flow rate of 30L/min is distributed on the bottom slots. Then, the pulsed signal is reproduced using a temporal Heaviside multiplier function.

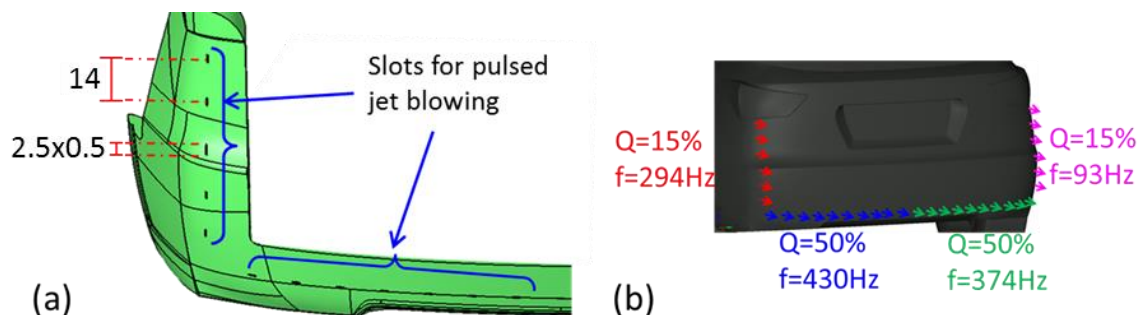


Figure III.99: (a) Geometry of the discontinuous slots in millimeter; (b) Optimal set of parameters identified in experiments with the machine-learning algorithm. A flowrate of 15L/min is distributed on the lateral boundary conditions and a flowrate of 30L/min is distributed between the bottom boundary conditions.

However, the time averaged rear end pressure achieved in simulation did not yield similar gain than in experiment. Figure III.100a shows the comparison of the baseline/AFC time averaged pressure distribution on the tailgate. Except for local pressure disturbances around the jets, the change on the tailgate is not significant. The comparison of the pressure RMS on the tailgate is presented in Figure III.101. A slight change near the bumper corners is captured.

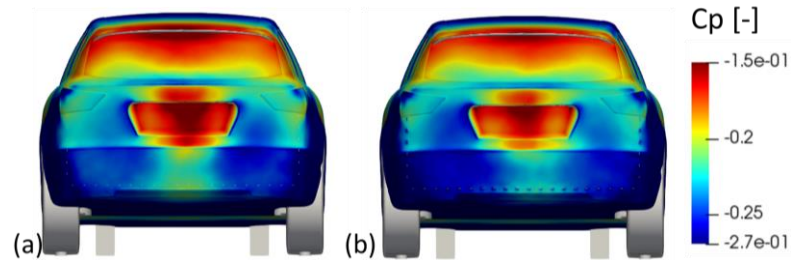


Figure III.100: Time averaged tailgate pressure coefficient in (a) baseline flow, (b) controlled flow.

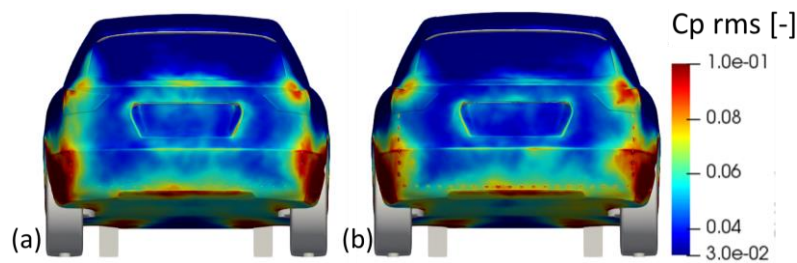


Figure III.101: Pressure coefficient RMS on the tailgate in (a) baseline flow, (b) controlled flow.

Despite the limited impact of the actuation on the time averaged pressure, a difference is observed in the wake flow topology. It is particularly visible on the position of the vortex centers in the Y0 cut-plane (Figure III. 102a and b) and Z140cut planes (Figure III. 102a and d).

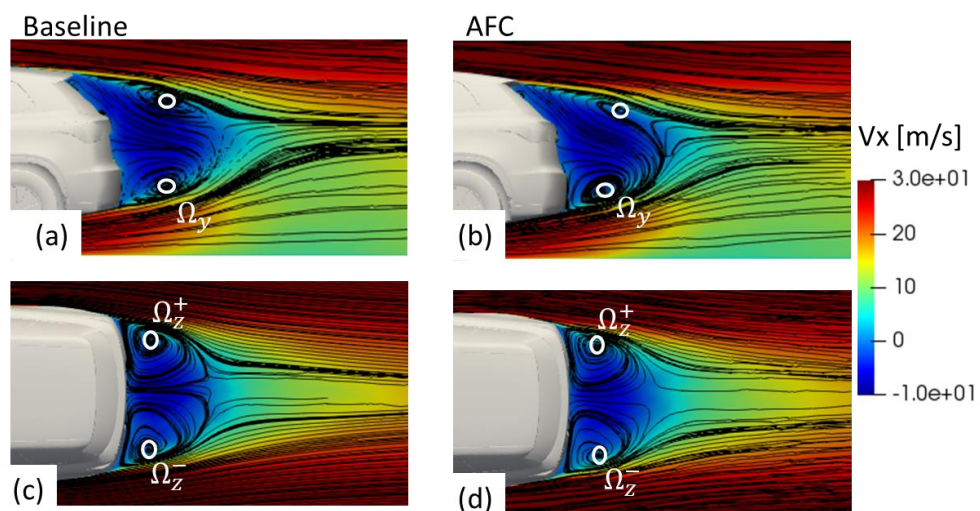


Figure III. 102: Time averaged flow showing a change of flow topology from the recirculation of  $\Omega_y$  to the S-shape structure between: (a) Y0 Baseline, (b) Y0 AFC; (c) Z140 Baseline; (d) Z140 AFC.

The examination of the time averaged jet velocity in the transverse vertical cut-planes going through the right and left slots (Figure III.103) reveals the injection of quantity momentum at 5m/s. Similarly, the velocity injected is evaluated at 4m/s in the bottom jets (Figure III.104). This is in concordance with the inlet boundary condition introduced for the control flow configuration given in chapter II.

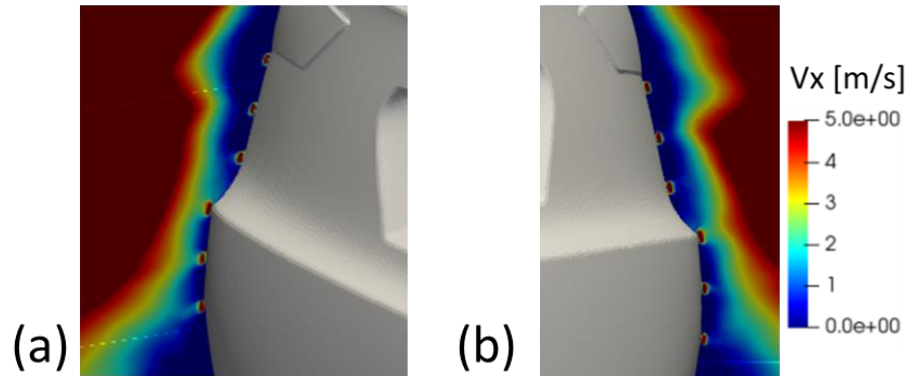


Figure III.103: Time averaged velocity field focus in the region of the pulsed jets (a) left side, (b) right side. A velocity of 5m/s is obtained near the lateral jets in accordance with the flowrate of experiments. Actuation flux is evenly distributed between all the slots.

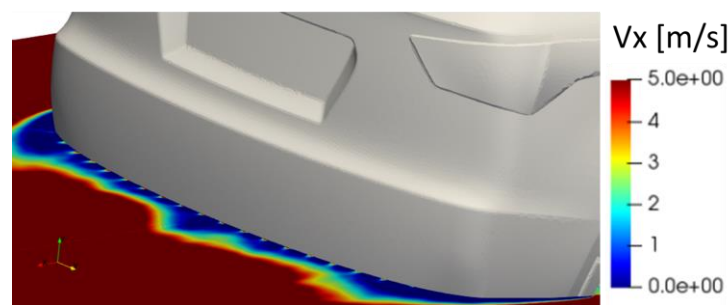


Figure III.104: Time averaged velocity field focus in the region of the bottom jets in the horizontal cut-plane going through the slots. A velocity of 4m/s is obtained near the bottom jets. Actuation flux is evenly distributed between each slot.

The comparison of the velocity fluctuations (Figure III.105) tends to confirm that the periodic jets increased the shear layer intensity. The periodic jet coming from the bottom slots leads to an increase of bottom shear layer about 2m/s compared to the baseline configuration. The impact into the S-shape structure in the Y0 cut-plane is noticeable by the reduction of the top shear layer.

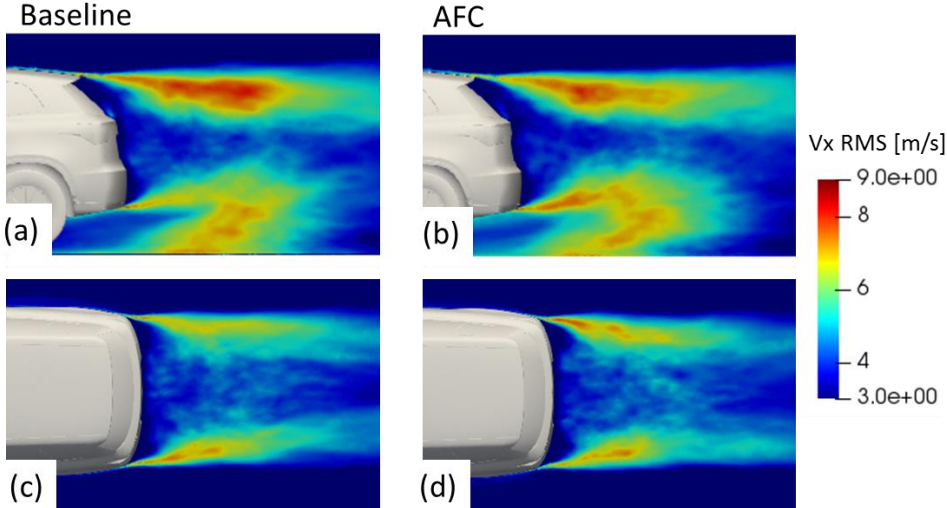


Figure III.105: Velocity RMS showing the increase of turbulent energy in the shear layers: (a) Y0 baseline; (b) Y0 AFC; (c) Z140 baseline; (d) Z140 AFC. The color map starts at 3m/s in order to capture the difference between the baseline and the controlled results.

Focusing on the region of the jet boundary conditions, we measured a velocity fluctuation of 9m/s coming from the lateral jets (Figure III.106) and a velocity fluctuations about 5m/s coming from the bottom jets (Figure III.107). This means that the high frequency actuation in the bottom jets generates less energy than the periodic forcing on the lateral jets. The high level of velocity fluctuations comes from a combination of the pulsed jet with the shear layers turbulence.

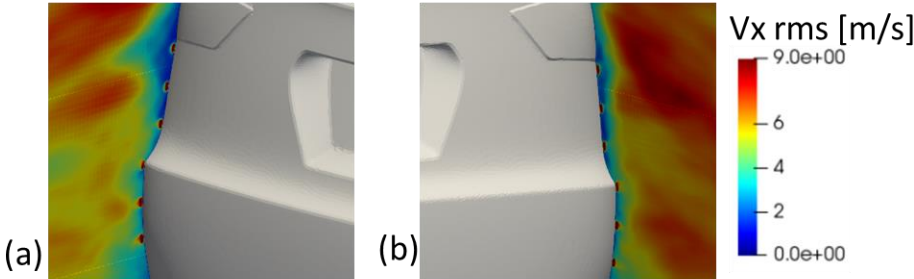


Figure III.106: Longitudinal velocity fluctuations in the vertical transverse cut-plane going through the slots: (a) right jets, (b) left jets. The inlet boundary conditions associated to the pulsed blowing jets generate 9m/s velocity RMS near the slots.

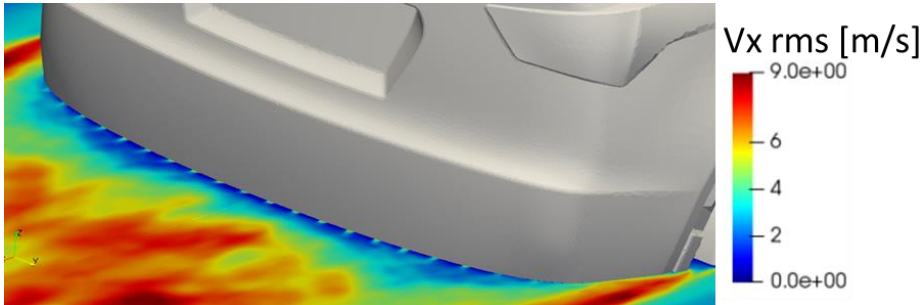


Figure III.107: Longitudinal velocity fluctuations measured in the horizontal transverse cut-plane going through the bottom slots. The inlet boundary conditions associated to the pulsed blowing jets generate 5m/s velocity RMS near the slots.

A proper estimation of the actuation efficiency is obtained thanks to the POD/DMD correlations methodology. The cross-modal analysis is performed on the concatenation of the baseline and controlled databases (1200 snapshots sampled at 2000H) using the velocity in the Y0, Z140 cut-planes and the pressure on the POSUV. Figure III.108 shows the ratio of the correlated modes between the two simulations. If the ratio associated to the static POD mode (index 1) is maintained at 1, the fluctuating modes associated to the POD indexes 2 and 3 are damped about 20% while the 5<sup>th</sup> and 6<sup>th</sup> modes are increased about 42% compared to experiments. This demonstrates the change of the flow coherent mechanisms.

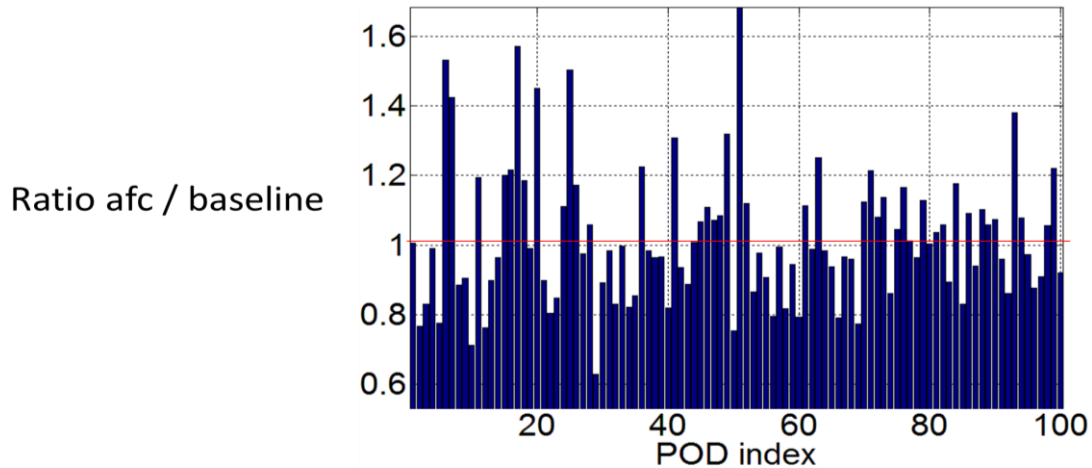


Figure III.108: POD ratio comparing the energy of the correlated mechanisms in the baseline and the controlled simulations.

It should be mentioned that the POD modes of the controlled flow are sorted depending on the energy of the coherent decomposition. The indexes can differ from the baseline results. Indeed, we managed to extract the pair of modes  $\Phi_{pod}(8)$  and  $\Phi_{pod}(9)$  (Figure III.109), which are similar to the modes  $\Phi_{pod}(3)$  and  $\Phi_{pod}(4)$  obtained in the baseline flow. We can deduce that these components are strongly decreased.

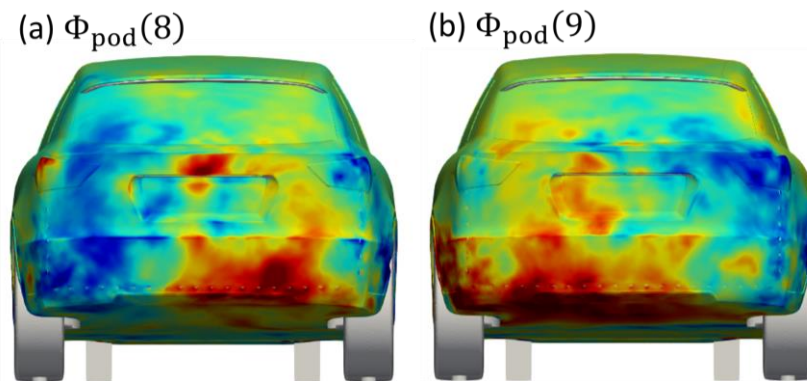


Figure III.109: Tailgate pressure POD modes obtained in the controlled simulation. The 8<sup>th</sup> and 9<sup>th</sup> POD modes can be related to the complementary paired modes  $\Phi_{pod}(3)$  and  $\Phi_{pod}(4)$  previously observed in the baseline flow.

The energy ratio measured in the synchronized DMD components is also plotted in Figure III.110. Most of the low frequency components are increased below 30Hz except for the 2Hz and 30Hz components. We can also notice that due to the simulation time, the lowest frequency begins at 2Hz. In addition, the actuation forcing frequencies at 93Hz, 294Hz, 374Hz and 430Hz do not emerge as shown in experiments even if we measure a slight

increase of the periodic components at 100Hz, 160Hz, 243Hz and 504Hz, especially in the lateral shear layers in the Z140 horizontal cut-plane (Figure III.111). One can question the accuracy of the jet resolution. A more precise experimental characterization of the pulsed blowing jet will be helpful in order to validate the boundary inlet conditions. Since energy at 25Hz and 30Hz is higher in the numerical simulations, the amount of jet momentum required for the boundary conditions should be increased compared to experiments.

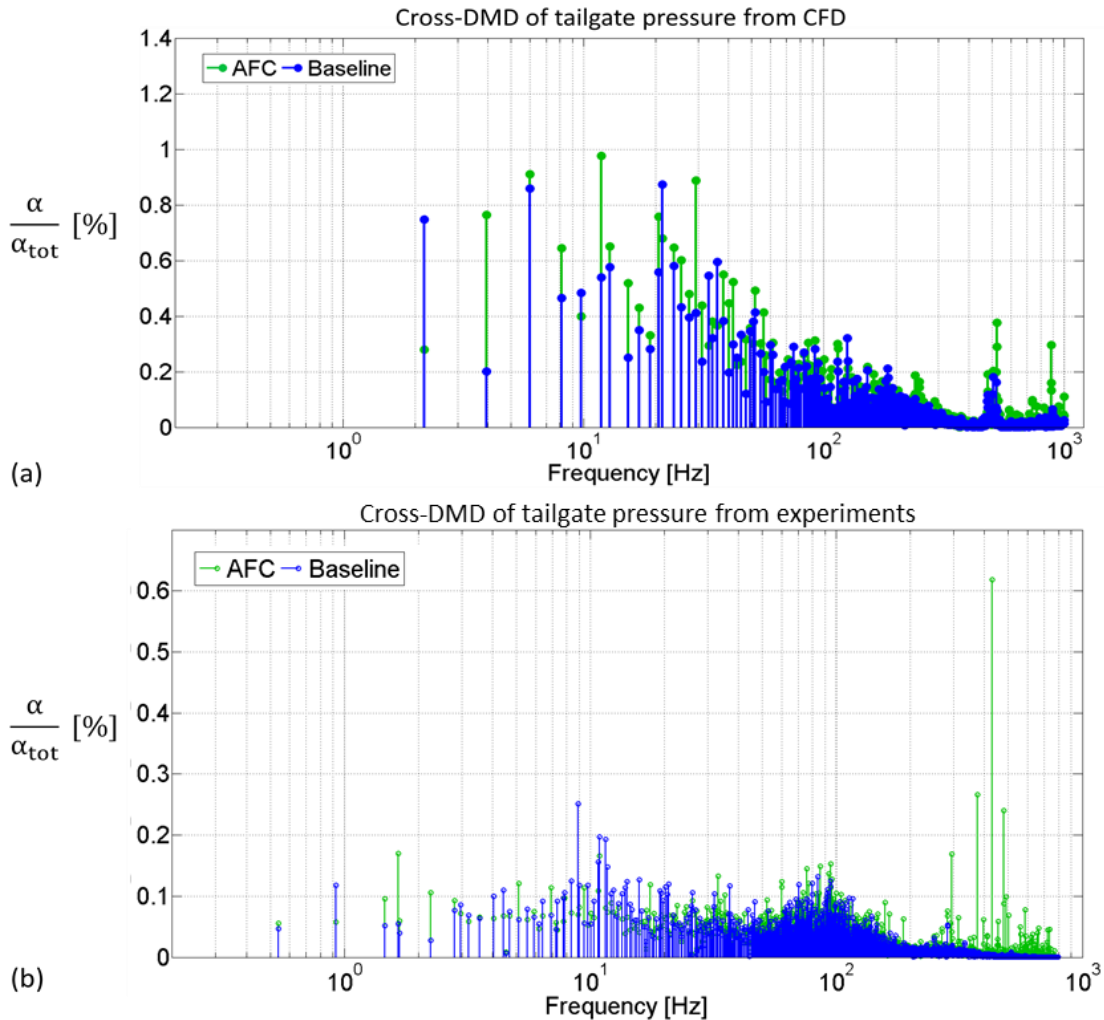


Figure III.110: DMD magnitude ratio between controlled and baseline flow in (a) CFD; (b) experiments.

The modal distributions in the horizontal cut-plane (Figure III.111) show the injected structures coming from the boundary conditions. It is especially significant in the Z140 cut-plane at 243Hz showing the turbulence injection induced by the actuation into the lateral shear layers. Similarly to what was demonstrated on the ramp simulation, we can assume that this should increase the mixing effect in order to decrease the aerodynamic loss.

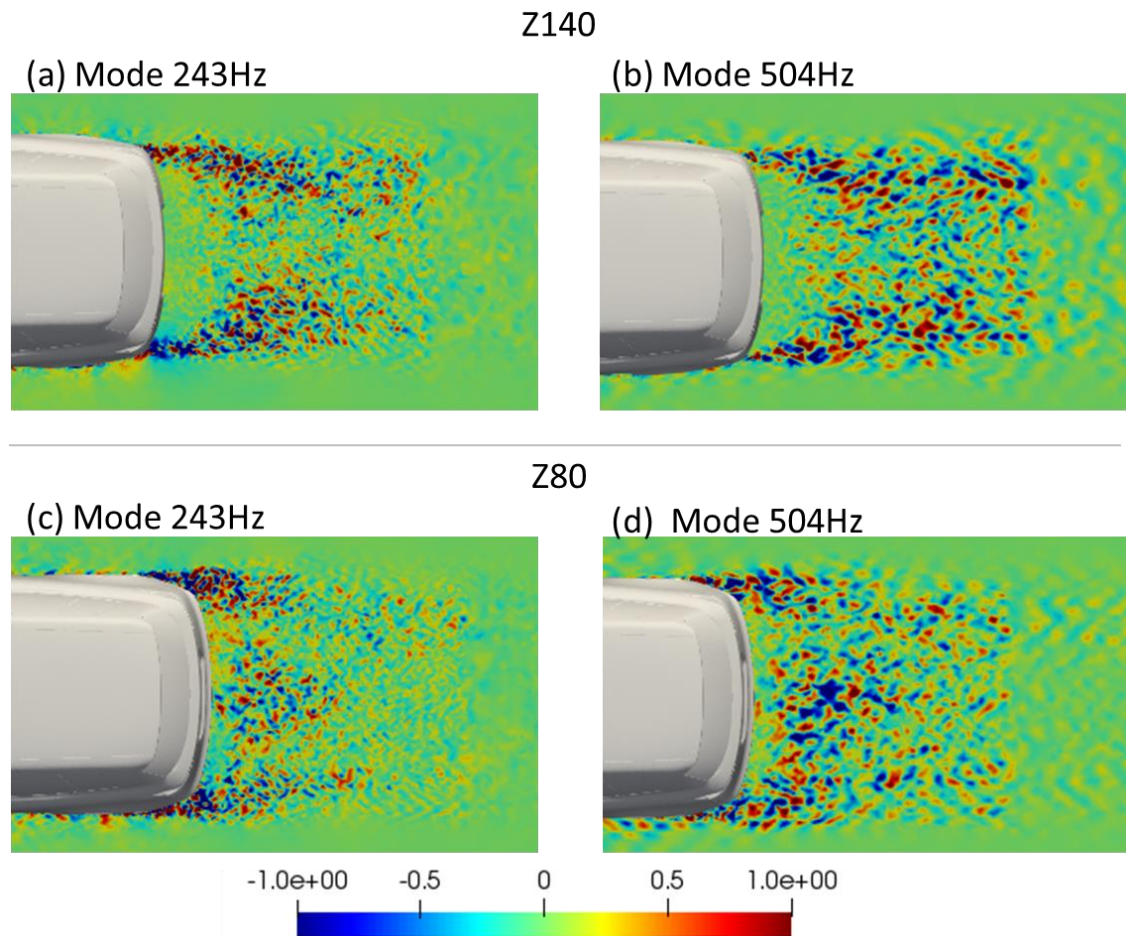


Figure III.111: DMD modes enhanced by the actuation : (a) 243Hz in Z140 cut-plane, (b) 504Hz in Z140 cut-plane, (c) 243Hz in Z80 cut-plane, (d) 504Hz in Z80 cut-plane.

To conclude, we managed to modify the flow dynamics thanks to the active flow control strategy even if the impact on the static component was not significant. The damping of low frequency components tends to confirm that we manage to take benefit of the transfer mechanisms between the shear layer and the wake dynamics. However, the fact that the periodic features of the actuation forcing frequencies do not significantly emerge in the spectra means that the jet effect is not exactly reproduced.

One may recall the numerical analysis of the high frequency control of the shear layer performed on the ramp flow. In this simplified test case, we managed to control the detachment thanks to the injection of periodic 2D structures within the turbulent mixing layer. In the case of the POSUV, the flow separation on the rear bumper generates strong 3D vortices. In addition, we have shown in the modal description of the baseline flow that a large range of modal periodic features carries the shear layer turbulent energy.

Further investigations need to be done to improve the efficiency of the active flow control in numerical simulation. However, we can already state that the uncertainties in the resolution of the shear layer make this objective highly challenging. Instead of one shot control simulation, it might be more appropriate to integrate a spectral detection of the shear layer fluctuation in order to dimension a closed loop flow control combined with an evaluation of the efficient actuation energy transfer. This could potentially yield a control strategy suitable for a large range of flow conditions in numerical simulation and in experiment. The difficulty that we can see here is the requirement of a self-updating Reduced Order Model capable to detect any

change in the shear layer behavior. In order to get a more accurate control using numerical simulations, the computations of the flow mechanisms linked to actuators should be improved. Despite the accuracy of the simulations, some vulnerability is observed in regions with high shear effects close to jets and solid boundaries.

### 3.4.6 Partial conclusions

The numerical simulation of the flow around the POSUV was successfully achieved. The time averaged results were in good agreement with the experimental measurements. The methodology of cross-modal analysis provided a comparison of the resolved dynamical features compared to what was captured during the experimental campaign. Some issues related to the approximation approach and the turbulent subgrid scale model leads to some discrepancies in the spectral behavior in the numerical simulation. A penalty method was proposed as a post-processing correction in order to constraint the dynamical features to converge toward the realistic physical behavior.

In addition, thanks to the 3D analysis of the flow behavior around the POSUV, we managed to identify the main vortex structures driving the pressure loss in the wake flow. The phase opposition at a Strouhal number of 0.12 was extracted between the body panel detachments and the shear layer quantity momentum on the rear bumper. The resulting shear layer fluctuations, around  $St=0.6$ , also has been identified as a major source term in the flow momentum of the wake vortices. The interaction with the low frequency pulsation at  $St=0.04$  on the tailgate has been proven thanks to the energy transfer evaluation. These observations will help in future research studies to extend our knowledge on correlated mechanisms to full-scale benchmarks.

The flow control simulation was also performed based on the optimal actuation solution obtained in experiment. Even if, some issues were encountered in order to reproduce the control efficiency, a significant impact on the shear layers dynamics is obtained. The complexity of the modal flow features around the POSUV can explain the change of actuation capabilities compared to the experimental results. Sensibility of the flow control results seems to be strongly related to the boundary inlet conditions. Therefore, sensibility study should be performed before to conclude on the efficiency and robustness of the numerical flow control solution. The improvement of our knowledge on the origin of the aerodynamic loss gives good prospects on further implementation of optimization solutions.

## Concluding remarks, discussion and perspectives

## Conclusions

In the context of the environmental issues brought by the automotive industry, the aerodynamic optimization of road vehicles is still a primary concern. In this framework, the purpose of this PhD work was to propose a flow control strategy for the drag reduction of road vehicles. The aim was then to apprehend the sources of aerodynamic losses on the reduced scale POSUV benchmark and to achieve a drag reduction using active flow control solutions.

As a starting point, the existing knowledge in the field of drag reduction for automotive applications was explored. After a review of fluid mechanics fundamentals, control strategies, modal analysis and numerical methods, this literature survey provided the layout and the foundations needed for the experimental and numerical analysis and control of the flow around the POSUV.

Then, the flow dynamics around the POSUV has been fully described thanks to a deep experimental investigation involving high speed PIV for the wake flow acquisition synchronized with the pressure sensors for the characterization of the tailgate pressure loss. This was successfully achieved thanks to the collaboration with TU-Berlin team. The characterization of the baseline flow gave a drag coefficient of 0.36 and a mean pressure loss on the tailgate of -0.23. The time averaged pressure distribution obtained on the tailgate demonstrated the importance of the aerodynamic loss applied on the bottom part. A methodology based on the application of the Sparsity Promoting Dynamic Modal Decomposition was implemented in order to identify the cross correlation and the main frequencies which emerged from the experimental synchronized velocity-pressure database. The low frequency oscillation of the pressure loss on the tailgate was correlated to a horizontal swiping motion of the wake combined with a vortex shedding pulsation in the symmetric vertical plan. This dynamic decomposition provided valuable insights for further numerical investigations of the flow features around the POSUV.

Active flow control was then achieved using discontinuous micro-slots distributed around the rear bumper in order to reduce the pressure loss on the tailgate. Even if, high expectation was made in real-time closed loop control, the complexity of the implementation did not ensure robustness and consistency. Therefore, adaptive closed-loop strategies appeared to be more suitable for integration on a realistic car and especially model-free techniques such as machine learning. The implemented genetic evolutionary process demonstrated really good capabilities for the identification of the optimal operating point. Based on non-symmetrical high frequency forcing with moderate flowrate magnitudes, the actuation solution led to a rear pressure profit of 20%.

The application of modal decompositions of the controlled flow provided more information on the process of the flow control. A cross-modal decomposition method was proposed in order to capture the energy transfer mechanism induced by the actuation. This methodology takes advantage of the preliminary orthogonal decomposition performed with the SVD in order to extract the energy modification between the baseline and the controlled databases. Using this modal approach, we identified high frequency mechanisms allowing to damp energetic pressure oscillations at low frequency on the tailgate. This result led to a useful insight in order to explore the mechanisms of the flow control. Based on this methodology, the amount of information needed to extract the control technique underlined the necessity to perform accurate unsteady 3D turbulent simulations.

Further investigations were performed using LES approach with Dynamic Smagorinsky subgrid scale model and a Finite Element solver. The 25° inclined ramp was introduced as a

preliminary test case for the analysis of detached flows simulations. Despite some discrepancies in the dissipation slope of the computed turbulent decay, the main flow features were in agreement with experimental literature results and the interactions between the recirculation, the shear layers and the vortex shedding was reproduced. The benefit obtained with the flow control solution, identified in experiments, was also reproduced. Further numerical investigations of the flow behavior submitted to the high frequency forcing were achieved using the methodology of the cross-correlations on the periodic DMD features. Thanks to this methodology, the mixing effect induced by the injected anisotropic vortices was demonstrated. This was correlated to an efficient damping of the turbulence coming from the shear layer which resulted in a reduction of the flapping motion at low frequency. Similar behaviors to the experimental study of the POSUV were also identified on the ramp flow control simulations.

The second test case of the 47° Ahmed Body was useful to examine the dynamics of a fully detached 3D wake flow. Dynamic Mode Decomposition was applied to better capture the flow topology and to define the most appropriate control strategy. This work revealed very useful capabilities of the Sparse Promoting DMD to measure modal sensitivity of jet actuations and to design pertinent closed loops for flow control.

The numerical LES simulation of POSUV reduced scale model was then achieved. The time averaged aerodynamical features were validated thanks to the experimental results. Thanks to the cross-modal correlation method, the computed dynamical behavior was in agreement with the experimental wake motion, despite an overestimation of the energy of the vortex shedding at the natural frequency at Strouhal number of 0.2. Further investigations on the approximation technique coupled with the Dynamic Smagorinsky subgrid scale model revealed numerical bias inherent to the numerical solver. The assumption on the influence of the regularization term was pointed out in the region of the velocity drop around the recirculation zone and submitted to high turbulence level. A post-processing numerical optimization was introduced based on a penalty correction method applied on the correlated periodic modal components. This proposed correction of the numerical solution managed to constraint the numerical results to converge toward the experimental flow behavior.

On this basis, the 3D flow features were used to improve our understanding of the wake dynamics. The description of the wake flow topology demonstrated the importance of three large vortices applying strong pressure loss on the bottom and on the lateral sides of the tailgate and the rear bumper. Thanks to the Q-criterion analysis, the strength of the recirculating flow responsible for the aerodynamic losses was related to the shear layers roll-up induced by the boundary layer separation on the rear bumper. The influence of the periodic detached structures on the fender and the wheelhouses on the boundary layers separation were evidenced based on the DMD mode at Strouhal number of 0.12. The emitted turbulent structures coming from the front of the mockup were proved to be source terms enhancing the turbulent fluctuations of the separation on the rear bumper.

The deeper analysis of the wake flow behavior showed the existence of 4 main coherent features impacting significantly the aerodynamic losses. An interaction was pointed out between the low frequency horizontal oscillation at a Strouhal number of 0.04 and the vertical vortex shedding at a Strouhal number of 0.2. In addition, two distinct coherent modes were related to the flow fluctuations of each lateral vortex governing the tailgate pressure loss. The correlation between the shear layer development at Strouhal number of 0.6 and the vortices fluctuations underscored the interest of turbulent smoothing control strategies in the region of the boundary layer separation.

Finally, the numerical simulation of the controlled flow was particularly challenging. A limited effect was computed on the time averaged pressure increase compared to experiments. However, significant change on the modal distribution was emphasized. The impact on the wake topology showed the modification of the vertical S-shape structure. Comparing with the control analysis performed on the ramp flow, the POSUV test case revealed a complex modal definition driven by a large range of periodical features. In addition, the disturbances due to the detachments on the lateral body panels appeared to be much more difficult to damp compared to the simplified upstream boundary layer of the ramp flow.

## Perspectives

This analysis performed on a reduced scaled mockup led to normalized length scale indications, which are interesting to confirm at full scale for the aerodynamic control and optimization of realistic cars. Multiple solutions can be proposed to go further in this research.

With experiments, even if we identified the importance of the pressure loss on the tailgate, the role of the pressure fluctuations on the rear bumper still should be considered in order to capture the sources of the detached flow. Additional pressure sensors distributed on the rear bumper would help to enhance our understanding of the flow separation. In addition, it is interesting to improve the experimental flow description using more PIV planes for an exhaustive wake flow analysis. This could be particularly interesting thanks to synchronization capabilities of the cross-modal method, applied in the fluid flow with and without control. In addition, the cross-modal analysis developed here can be extended for shape optimization based on modal sensitivity estimation.

This seems particularly interesting in order to optimize the detachments on the fender or the rear bumper tapered effect.

In numerical simulations, the investigations on the numerical approximation approach should to be carried on in order to set the same turbulence behavior than in experiment. On the basis of more reliable simulations, the implementation of efficient active flow control will provide the additional data required for the numerical cross-modal analysis. Also, a more precise definition of the discontinuous micro-jet actuators is required for a better implementation of the flow control boundary conditions. To go further, the computation of modal sensitivity to inlet boundary conditions or wall surface morphing appears to be an interesting option for unsteady flow optimization with reasonable simulation time. This will involve a preliminary evaluation of the consistency of the Reduced-Order-Model to the boundary conditions modifications. However, we should mention that even if the 2D modal characterization gives a significant amount of information of the flow behavior, the analysis of 3D databases should provide an exhaustive modal characterization of the flow. Sophisticated parallelization and memory management techniques for huge data processing should be implemented to reach this objective. Further developments are on the way for future implementation of the 3 dimensional DMD on numerical simulations. A short-term solution can already be achieved using thick fluid sections around the mockup in order to capture more precisely the sources of the aerodynamic losses. This could lead to an optimization of the location of the actuation boundary conditions.

Finally, the cross-modal methodology can be applied in future work on full-scale mockup. The extension of our knowledge on the sources of aerodynamic losses will require some preliminary validations in the full-scale configuration. For instance, we have to ensure if the rotating wheels tend to promote the propagation of disturbances generated by the detachments on the body panels, in the shear layers. In addition, a comparative study should be performed

in order to evaluate the contribution of turbulent structures generated by the realistic complex underbody floor existing in all vehicles except for electrical cars. Three-dimensional unsteady numerical simulations will be needed to perform these validation studies. In view of the simulation cost of the Finite Element Method with LES, other methods should be considered in order to reduce CPU time, either hybrid methods which are more permissive in the region of the boundary layer or Lattice Boltzmann Method which can perform LES simulation with efficient parallelization technique.

This gives some blueprints for future research projects on the aerodynamical optimization of realistic cars.

## Bibliography

- Adams, N., Stolz, S., 2001. Deconvolution methods for subgrid-scale approximation in large eddy simulation. *Mod Simul Strateg Turbul. Flow*.
- Ahmed, S.R., Ramm, G., Faltin, G., 1984a. Some Salient Features Of The Time-Averaged Ground Vehicle Wake (SAE Technical Paper No. 840300). SAE Technical Paper, Warrendale, PA. <https://doi.org/10.4271/840300>
- Ahmed, S.R., Ramm, G., Faltin, G., 1984b. Some Salient Features Of The Time-Averaged Ground Vehicle Wake (SAE Technical Paper). SAE Technical Paper, Warrendale, PA. <https://doi.org/10.4271/840300>
- Aider, J.-L., Beaudoin, J.-F., Wesfreid, J.E., 2010. Drag and lift reduction of a 3D bluff-body using active vortex generators. *Exp. Fluids* 48, 771–789. <https://doi.org/10.1007/s00348-009-0770-y>
- Aider, J.-L., Joseph, P., Ruiz, T., Gilotte, P., Eulalie, Y., Edouard, C., Amandolese, X., 2014. Active flow control using pulsed microjets on a full-scale production car Active flow control using pulsed micro-jets on a full-scale production car. *Int. J. Flow Control* 6. <https://doi.org/10.1260/1756-8250.6.1.1>
- Arwatz, G., Fono, I., Seifert, A., 2008. Suction and Oscillatory Blowing Actuator, in: IUTAM Symposium on Flow Control and MEMS, IUTAM Bookseries. Springer, Dordrecht, pp. 33–44. [https://doi.org/10.1007/978-1-4020-6858-4\\_4](https://doi.org/10.1007/978-1-4020-6858-4_4)
- Aubrun, S., McNally, J., Alvi, F., Kourta, A., 2011. Separation flow control on a generic ground vehicle using steady microjet arrays. *Exp. Fluids* 51, 1177–1187. <https://doi.org/10.1007/s00348-011-1132-0>
- Audi Technology Portal - Underbody [WWW Document], n.d. . Audi Technol. Portal. URL <https://www.audi-technology-portal.de/en/body/aerodynamics-aeroacoustics/underbody?c=image:1007> (accessed 11.21.18).
- Barbagallo, A., Sipp, D., Schmid, P.J., 2009. Closed-loop control of an open cavity flow using reduced-order models. *J. Fluid Mech.* 641, 1–50. <https://doi.org/10.1017/S0022112009991418>
- Bardina, J., Ferziger, J., Reynolds, W., 1980. Improved subgrid-scale models for large-eddy simulation, in: 13th Fluid and Plasma Dynamics Conference, Fluid Dynamics and Co-located Conferences. American Institute of Aeronautics and Astronautics. <https://doi.org/10.2514/6.1980-1357>
- Barnard, R.H., 2001. Road vehicle aerodynamic design - an introduction.
- Barros, D., Borée, J., Noack, B.R., Spohn, A., Ruiz, T., 2016. Bluff body drag manipulation using pulsed jets and Coanda effect. *J. Fluid Mech.* 805, 422–459. <https://doi.org/10.1017/jfm.2016.508>
- Beaudoin, J.-F., Aider, J.-L., 2008. Drag and lift reduction of a 3D bluff body using flaps. *Exp. Fluids* 44, 491. <https://doi.org/10.1007/s00348-007-0392-1>
- Bergmann, M., 2004a. Optimisation aérodynamique par réduction de modèle POD et contrôle optimal : application au sillage laminaire d'un cylindre circulaire. Vandoeuvre-les-Nancy, INPL.
- Bergmann, M., 2004b. Optimisation aérodynamique par réduction de modèle POD et contrôle optimal : application au sillage laminaire d'un cylindre circulaire. Vandoeuvre-les-Nancy, INPL.
- Bergmann, M., Cordier, L., 2008. Optimal control of the cylinder wake in the laminar regime by trust-region methods and POD reduced-order models. *J. Comput. Phys.* 227, 7813–7840. <https://doi.org/10.1016/j.jcp.2008.04.034>

- Bideaux, E., Bobillier, P., Fournier, E., Gilliéron, P., El Hajem, M., Champagne, J. y., Gilotte, P., Kourta, A., 2011. Drag reduction by pulsed jets on strongly unstructured wake: towards the square back control. *Int. J. Aerodyn.* 1, 282–298. <https://doi.org/10.1504/IJAD.2011.038846>
- Birol, F., 2017. CO2 Emissions from Fuel Combustion 2017 Highlights. International Energy Agency.
- Bonnaivon, G., 2018. Dynamics of the unstable wake modes in automotive aerodynamics : from simplified models to real vehicles (thesis). Paris Saclay.
- Bonnaivon, G., Cadot, O., 2018. Unstable wake dynamics of rectangular flat-backed bluff bodies with inclination and ground proximity. *J. Fluid Mech.* 854, 196–232. <https://doi.org/10.1017/jfm.2018.630>
- Boucinha, V., Weber, R., Kourta, A., 2010. Drag reduction of a 3D bluff body using plasma actuators. *Int. J. Aerodyn.* 1, 262.
- BouDET, J., Lévêque, E., Borgnat, P., Cahuzac, A., Jacob, M.C., 2016. A Kalman filter adapted to the estimation of mean gradients in the large-eddy simulation of unsteady turbulent flows. *Comput. Fluids* 127, 65–77. <https://doi.org/10.1016/j.compfluid.2015.12.006>
- Boussinesq, J., 1877. *Essai sur la théorie des eaux courantes*. Imprimerie Nationale, Paris.
- Bruneau, C.-H., Creusé, E., Depeyras, D., Gilliéron, P., Mortazavi, I., 2010. Coupling active and passive techniques to control the flow past the square back Ahmed body. *Comput. Fluids* 39, 1875–1892. <https://doi.org/10.1016/j.compfluid.2010.06.019>
- Bruneau, C.-H., Creusé, E., Gilliéron, P., Mortazavi, I., 2014. Effect of the vortex dynamics on the drag coefficient of a square back Ahmed body: Application to the flow control. *Eur. J. Mech. - BFluids* 45, 1–11. <https://doi.org/10.1016/j.euromechflu.2013.11.003>
- Brunet, V., Francois, C., Garnier, E., Pruvost, M., 2006. Experimental and Numerical Investigations of Vortex Generators Effects, in: 3rd AIAA Flow Control Conference, Fluid Dynamics and Co-Located Conferences. American Institute of Aeronautics and Astronautics. <https://doi.org/10.2514/6.2006-3027>
- Brunn, A., Nitsche, W., 2006. Drag Reduction of an Ahmed Car Model by Means of Active Separation Control at the Rear Vehicle Slant, in: Rath, H.-J., Holze, C., Heinemann, H.-J., Henke, R., Hönlinger, H. (Eds.), *New Results in Numerical and Experimental Fluid Mechanics V, Notes on Numerical Fluid Mechanics and Multidisciplinary Design (NNFM)*. Springer Berlin Heidelberg, pp. 249–256.
- Chollet, J.-P., Lesieur, M., 1981. Parameterization of Small Scales of Three-Dimensional Isotropic Turbulence Utilizing Spectral Closures. *J. Atmospheric Sci.* 38, 2747–2757. [https://doi.org/10.1175/1520-0469\(1981\)038<2747:POSSOT>2.0.CO;2](https://doi.org/10.1175/1520-0469(1981)038<2747:POSSOT>2.0.CO;2)
- Chovet, C., 2018. Manipulation de la turbulence en utilisant le contrôle par mode glissant et le contrôle par apprentissage : de l'écoulement sur une marche descendente à une voiture réelle.
- Cordier, L., 2008. Proper Orthogonal Decomposition: An Overview. *Lect. Ser.* 2002-04 2003-04 Post-Process. *Exp. Numer. Data*.
- Cordier, L., Bergmann, M., 2008. Proper Orthogonal Decomposition: an overview, in: *Lecture Series 2002-04, 2003-03 and 2008-01 on Post-Processing of Experimental and Numerical Data*, Von Karman Institute for Fluid Dynamics, 2008. VKI, p. 46 pages.
- Creusé, E., Giovannini, A., Mortazavi, I., 2009. Vortex simulation of active control strategies for transitional backward-facing step flows. *Comput. Fluids*, Special Issue Dedicated to Professor Alain Lerat on the Occasion of his 60th Birthday 38, 1348–1360. <https://doi.org/10.1016/j.compfluid.2008.01.036>
- Delassaux, F., Herbert, V., Mortazavi, I., Ribes, C., 2018. Comparison of Three Hybrid Turbulence Models for the Flow Around a  $\text{\$}25^{\circ}$  Ahmed Body, in:

- Notes on Numerical Fluid Mechanics and Multidisciplinary Design. pp. 265–275. [https://doi.org/10.1007/978-3-319-70031-1\\_22](https://doi.org/10.1007/978-3-319-70031-1_22)
- Dobrev, I., Massouh, F., 2014. Investigation of relationship between drag and lift coefficients for a generic car model. Presented at the BULTRANS-2014, BULTRANS -2014 Proceedings, pp. 171–174.
- Duriez, T., 2009. Application des générateurs de Vortex au contrôle d'écoulements décollés (thesis). Paris 7.
- Duriez, T., Aider, J.-L., Wesfreid, J.E., 2008. Non-Linear Modulation of a Boundary Layer Induced by Vortex Generators, in: 4th Flow Control Conference, Fluid Dynamics and Co-Located Conferences. American Institute of Aeronautics and Astronautics. <https://doi.org/10.2514/6.2008-4076>
- Edwige, S., Eulalie, Y., Gilotte, P., Mortazavi, I., 2018. Wake flow analysis and control on a 47° slant angle Ahmed body. *Int. J. Numer. Methods Heat Fluid Flow* 28, 1061–1079. <https://doi.org/10.1108/HFF-06-2017-0260>
- Ehrenstein, U., Eloy, C., 2013. Skin friction on a moving wall and its implications for swimming animals. *J. Fluid Mech.* 718, 321–346. <https://doi.org/10.1017/jfm.2012.613>
- El Shrif, A., 2008. Contrôle optimal par simulation aux grandes échelles d'un écoulement turbulent.
- Eulalie, Y., 2014. Étude aérodynamique et contrôle de la traînée sur un corps de Ahmed culot droit (PhD Thesis).
- Eulalie, Y., Fournier, E., Gilotte, P., Holst, D., Johnson, S., Nayeri, C.N., Schütz, T., Wieser, D., 2018a. Active flow control analysis at the rear of an SUV. *Int. J. Numer. Methods Heat Fluid Flow* 28, 1169–1186. <https://doi.org/10.1108/HFF-06-2017-0230>
- Eulalie, Y., Fournier, E., Gilotte, P., Holst, D., Johnson, S., Nayeri, C.N., Schütz, T., Wieser, D., 2018b. Active flow control analysis at the rear of an SUV. *Int. J. Numer. Methods Heat Fluid Flow* 28, 1169–1186. <https://doi.org/10.1108/HFF-06-2017-0230>
- Frederich, O., Luchtenburg, D., 2018. MODAL ANALYSIS OF COMPLEX TURBULENT FLOW.
- Gautier, N., Aider, J.-L., Duriez, T., Noack, B.R., Segond, M., Abel, M., 2015. Closed-loop separation control using machine learning. *J. Fluid Mech.* 770, 442–457. <https://doi.org/10.1017/jfm.2015.95>
- Germano, M., Piomelli, U., Moin, P., Cabot, W., 1991. A Dynamic Subgrid-Scale Eddy Viscosity Model. *Phys Fluids A* 3, 1760–1765.
- Germano, Massimo, Piomelli, U., Moin, P., Cabot, W.H., 1991. A dynamic subgrid-scale eddy viscosity model. *Phys. Fluids Fluid Dyn.* 3, 1760–1765. <https://doi.org/10.1063/1.857955>
- Ghosal, S., Lund, T.S., Moin, P., Akselvoll, K., 1995. A dynamic localization model for large-eddy simulation of turbulent flows. *J. Fluid Mech.* 286, 229–255. <https://doi.org/10.1017/S0022112095000711>
- Gilliéron, P., Kourta, A., 2013. Aerodynamic drag control by pulsed jets on simplified car geometry. *Exp. Fluids* 54, 14–57. <https://doi.org/10.1007/s00348-013-1457-y>
- Grandemange, M., 2013. Analysis and control of three-dimensional turbulent wakes : from axisymmetric bodies to road vehicles (thesis). Palaiseau, Ecole polytechnique.
- Grandemange, M., Mary, A., Gohlke, M., Cadot, O., 2013. Effect on drag of the flow orientation at the base separation of a simplified blunt road vehicle. *Exp. Fluids* 54, 1529.
- Heenan, A.F., Morrison, J., 1998. Passive control of backstep flow. *Exp. Therm. Fluid Sci.* 16, 122–132. [https://doi.org/10.1016/S0894-1777\(97\)10015-2](https://doi.org/10.1016/S0894-1777(97)10015-2)

- Hinterberger, C., García-Villalba, M., Rodi, W., 2004. Large eddy simulation of flow around the Ahmed body, in: McCallen, R., Browand, F., Ross, J. (Eds.), *The Aerodynamics of Heavy Vehicles: Trucks, Buses, and Trains*, Lecture Notes in Applied and Computational Mechanics. Springer Berlin Heidelberg, pp. 77–87.
- Howard, R., Pourquie, M., 2002. Large eddy simulation of an Ahmed reference model. *J. Turbul. - J TURBUL* 3. <https://doi.org/10.1088/1468-5248/3/1/012>
- Hucho, W., Sovran, G., 1993. Aerodynamics of Road Vehicles. *Annu. Rev. Fluid Mech.* 25, 485–537. <https://doi.org/10.1146/annurev.fl.25.010193.002413>
- Hucho, W.-H., 1987. Chapter 1 - Introduction to automobile aerodynamics, in: Hucho, W.-H. (Ed.), *Aerodynamics of Road Vehicles*. Butterworth-Heinemann, pp. 1–46. <https://doi.org/10.1016/B978-0-7506-1267-8.50005-1>
- Hunt, J.C.R., Morrison, J.F., 2000. Eddy structure in turbulent boundary layers. *Eur. J. Mech. - BFluids* 19, 673–694. [https://doi.org/10.1016/S0997-7546\(00\)00129-1](https://doi.org/10.1016/S0997-7546(00)00129-1)
- Hutchins, N., Marusic, I., 2007. Evidence of very long meandering features in the logarithmic region of turbulent boundary layers. *J. Fluid Mech.* 579, 1–28. <https://doi.org/10.1017/S0022112006003946>
- I. Heft, A., Indinger, T., Adams, N., 2012. Introduction of a New Realistic Generic Car Model for Aerodynamic Investigations. <https://doi.org/10.4271/2012-01-0168>
- Jovanovic, M.R., Schmid, P., Nichols, J.W., 2010. Low-rank and sparse dynamic mode decomposition 139–152.
- Jovanović, M.R., Schmid, P.J., Nichols, J.W., 2014a. Sparsity-promoting dynamic mode decomposition. *Phys. Fluids* 26, 024103. <https://doi.org/10.1063/1.4863670>
- Jovanović, M.R., Schmid, P.J., Nichols, J.W., 2014b. Sparsity-promoting dynamic mode decomposition. *Phys. Fluids* 26, 024103. <https://doi.org/10.1063/1.4863670>
- Karniadakis, G., Sherwin, S., 1999. *Spectral/hp Element Methods for CFD*.
- Karpouzas, G.K., Papoutsis-Kiachagias, E.M., Schumacher, T., de Villiers, E., Giannakoglou, K.C., Othmer, C., 2016. Adjoint Optimization for Vehicle External Aerodynamics 7.
- Kavvadias, I.S., Vezyris, C.K., Papoutsis-Kiachagias, E.M., Giannakoglou, K.C., n.d. *LOW-COST, UNSTEADY CONTINUOUS ADJOINT METHOD FOR OPTIMAL FLOW CONTROL USING JETS*.
- Khalighi, B., Ho, J., Cooney, J., Neiswander, B., Corke, T.C., Han, T., 2016. Aerodynamic Drag Reduction Investigation for a Simplified Road Vehicle Using Plasma Flow Control V01AT13A014. <https://doi.org/10.1115/FEDSM2016-7927>
- Kolmogorov, A.N., 1991. The local structure of turbulence in incompressible viscous fluid for very large Reynolds numbers. *Proc R Soc Lond A* 434, 9–13. <https://doi.org/10.1098/rspa.1991.0075>
- Kourta, A., Thacker, A., Jousot, R., 2015. Analysis and characterization of ramp flow separation. *Exp. Fluids* 56, 104.
- Krajnovic, S., Davidson, L., 2004. Large Eddy Simulation of the Flow Around an Ahmed Body. *Proc. ASME Heat Transfer/Fluids Eng. Summer Conf.* 2004 653–662.
- Krajnovic, S., Larusson, R., Basara, B., 2012. Superiority of PANS compared to LES in predicting a rudimentary landing gear flow with affordable meshes. *Int. J. Heat Fluid Flow* 37, 109–122. <https://doi.org/10.1016/j.ijheatfluidflow.2012.04.013>
- Krajnović, S., Minelli, G., Basara, B., 2016. Partially-averaged Navier-Stokes Simulations of Two Bluff Body Flows. *Appl Math Comput* 272, 692–706. <https://doi.org/10.1016/j.amc.2015.03.136>
- Le Clainche, S., Vega, J., 2017. Higher Order Dynamic Mode Decomposition. *SIAM J. Appl. Dyn. Syst.* 16, 882–925. <https://doi.org/10.1137/15M1054924>
- Leclerc, C., 2008. Réduction de la traînée d'un véhicule automobile simplifié à l'aide du contrôle actif par jet synthétique.

- Lesieur, M., Metais, O., 1996. New Trends in Large-Eddy Simulations of Turbulence. *Annu. Rev. Fluid Mech.* 28, 45–82. <https://doi.org/10.1146/annurev.fl.28.010196.000401>
- Lesieur, M., Métais, O., Comte, P., 2005. *Large-Eddy Simulations of Turbulence*. Cambridge University Press.
- Li, R., 2017a. *Aerodynamic Drag Reduction of a Square-Back Car Model Using Linear Genetic Programming and Physic-Based Control (PhD Thesis)*.
- Li, R., 2017b. *Aerodynamic Drag Reduction of a Square-Back Car Model Using Linear Genetic Programming and Physic-Based Control (PhD Thesis)*.
- Li, R., Noack, B.R., Cordier, L., Borée, J., Harambat, F., 2017a. Drag reduction of a car model by linear genetic programming control. *Exp. Fluids* 58, 103. <https://doi.org/10.1007/s00348-017-2382-2>
- Li, R., Noack, B.R., Cordier, L., Borée, J., Harambat, F., 2017b. Drag reduction of a car model by linear genetic programming control. *Exp. Fluids* 58, 103. <https://doi.org/10.1007/s00348-017-2382-2>
- Lilly, D., 1967. The representation of small scale turbulence in numerical simulation experiments. Presented at the IBM Scientific Computing Symposium on environmental sciences, pp. 195–210.
- Lumley, J.L., 1981. Coherent Structures in Turbulence, in: Meyer, R.E. (Ed.), *Transition and Turbulence*. Academic Press, pp. 215–242. <https://doi.org/10.1016/B978-0-12-493240-1.50017-X>
- Lumley, J.L., 1967. The Structure of Inhomogeneous Turbulent Flows, in: Yaglom, A.M., Tatarski, V.I. (Eds.), *Atmospheric Turbulence and Radio Propagation*. Nauka, Moscow, pp. 166–178.
- Martinat, G., Bourguet, R., Hoarau, Y., Dehaeze, F., Jorez, B., Braza, M., 2008. Numerical Simulation of the Flow in the Wake of Ahmed Body Using Detached Eddy Simulation and URANS Modeling, in: Peng, S.-H., Haase, W. (Eds.), *Advances in Hybrid RANS-LES Modelling, Notes on Numerical Fluid Mechanics and Multidisciplinary Design*. Springer Berlin Heidelberg, pp. 125–131.
- Matsumoto, D., Indinger, T., 2017. On-the-fly algorithm for Dynamic Mode Decomposition using Incremental Singular Value Decomposition and Total Least Squares. *ArXiv170311004 Phys*.
- McNally, J., Fernandez, E., Robertson, G., Kumar, R., Taira, K., Alvi, F., Yamaguchi, Y., Murayama, K., 2015. Drag reduction on a flat-back ground vehicle with active flow control. *J. Wind Eng. Ind. Aerodyn.* 145, 292–303. <https://doi.org/10.1016/j.jweia.2015.03.006>
- Metka, M., 2013. *An Examination of Active Drag Reduction Methods for Ground Vehicles (Thesis)*. The Ohio State University.
- Metka, M., Gregory, J.W., 2015. Drag Reduction on the 25-deg Ahmed Model Using Fluidic Oscillators. *J. Fluids Eng.* 137, 051108-051108–8. <https://doi.org/10.1115/1.4029535>
- Mimeau, C., Mortazavi, I., Cottet, G.-H., 2017. Passive control of the flow around a hemisphere using porous media. *Eur. J. Mech. - BFluids* 65, 213–226. <https://doi.org/10.1016/j.euromechflu.2017.03.002>
- Minelli, G., Hartono, E.A., Chernoray, V., Hjelm, L., Basara, B., Krajnovic, S., 2018. Development of Active Flow Control for Trucks. Presented at the 3rd Thermal and Fluids Engineering Conference (TFEC) Fort Lauderdale, FL, USA, 2018-03-04 - 2018-03-07, Fort Lauderdale.
- Minguez, M., Pasquetti, R., Serre, E., 2008. High-order large-eddy simulation of flow over the “Ahmed body” car model. *Phys. Fluids* 20, 095101. <https://doi.org/10.1063/1.2952595>

- Nicoud, F., Ducros, F., 1999. Subgrid-Scale Stress Modelling Based on the Square of the Velocity Gradient Tensor. *Flow Turbul. Combust.* 62, 183–200. <https://doi.org/10.1023/A:1009995426001>
- Oberleithner, K., Sieber, M., Nayeri, C.N., Paschereit, C.O., Petz, C., Hege, H.-C., Noack, B.R., Wygnanski, I., 2011. Three-dimensional coherent structures in a swirling jet undergoing vortex breakdown: stability analysis and empirical mode construction. *J. Fluid Mech.* 679, 383–414. <https://doi.org/10.1017/jfm.2011.141>
- Onorato, M., 1984. *Drag Measurement Through Wake Analysis*. Society of Automotive Engineers.
- Parezanovic, V., Laurentie, J.-C., Fourment, C., Delville, J., Bonnet, J.-P., Spohn, A., Duriez, T., Cordier, L., Noack, B., Abel, M., Segond, M., Shaqarin, T., Brunton, S., 2014. Mixing Layer Manipulation Experiment: From Open-Loop Forcing to Closed-Loop Machine Learning Control. *Flow Turbul. Combust.* Published online. <https://doi.org/10.1007/s10494-014-9581-1>
- Parkin, D.J., Thompson, M.C., Sheridan, J., 2014. Numerical analysis of bluff body wakes under periodic open-loop control. *J. Fluid Mech.* 739, 94–123. <https://doi.org/10.1017/jfm.2013.618>
- Parpais, S., 2015. *L'aérodynamique des automobiles de demain*, SIA.
- Pastoor, M., Henning, L., Noack, B.R., King, R., Tadmor, G., 2008. Feedback shear layer control for bluff body drag reduction. *J. Fluid Mech.* 608, 161–196. <https://doi.org/10.1017/S0022112008002073>
- Perry, A.-K., Pavia, G., Passmore, M., 2016. Influence of short rear end tapers on the wake of a simplified square-back vehicle: wake topology and rear drag. *Exp. Fluids* 57, 169. <https://doi.org/10.1007/s00348-016-2260-3>
- Pope, S.B., 2001a. *Turbulent Flows*. By S. B. POPE. Cambridge University Press, 2000. 771 pp. ISBN 0 521 59886 9. £29.95 or \$49.95 (paperback); ISBN 0 521 59125 2. £80.00 or \$130.00 (hardback). *J. Fluid Mech.* 427, 410–411. <https://doi.org/10.1017/S0022112000212913>
- Pope, S.B., 2001b. *Turbulent Flows*. By S. B. POPE. Cambridge University Press, 2000. 771 pp. ISBN 0 521 59886 9. £29.95 or \$49.95 (paperback); ISBN 0 521 59125 2. £80.00 or \$130.00 (hardback). *J. Fluid Mech.* 427, 410–411. <https://doi.org/10.1017/S0022112000212913>
- Proctor, J.L., Brunton, S.L., Kutz, J.N., 2014a. Dynamic mode decomposition with control. *ArXiv14096358 Math*.
- Proctor, J.L., Brunton, S.L., Kutz, J.N., 2014b. Dynamic mode decomposition with control. *ArXiv14096358 Math*.
- Sagaut, P., 2006. *Large Eddy Simulation for Incompressible Flows: An Introduction*. Springer Science & Business Media.
- Scheller, J., Jodin, G., Rizzo, K.J., Duhayon, E., Rouchon, J.-F., Triantafyllou, M.S., Braza, M., 2016. A Combined Smart-Materials Approach for Next-Generation Airfoils. *Solid State Phenom., Mechatronic Systems and Materials VII* 251, 106–112. <https://doi.org/10.4028/www.scientific.net/SSP.251.106>
- Schlatter, P., Örlü, R., 2010. Assessment of direct numerical simulation data of turbulent boundary layers. *J. Fluid Mech.* 659, 116–126. <https://doi.org/10.1017/S0022112010003113>
- Schmid, P.J., 2012. Dynamic mode decomposition of numerical and experimental data.
- Schmid, P.J., 2011. Application of the dynamic mode decomposition to experimental data. *Exp. Fluids* 50, 1123–1130. <https://doi.org/10.1007/s00348-010-0911-3>
- Serre, E.E., Minguez, M., Pasquetti, R., Guilmineau, E., Deng, G.B., Kornhaas, M., Schäfer, M., Fröhlich, J., Hinterberger, C., Rodi, W., 2013. On simulating the turbulent flow

- around the Ahmed body: a French-German collaborative evaluation of LES and DES. *Comput. Fluids* 78, 10–23. <https://doi.org/10.1016/j.compfluid.2011.05.017>
- Shadmani, S., Mojtaba Mousavi Nainiyan, S., Mirzaei, M., Ghasemiasl, R., Pouryoussefi, S., 2018. Experimental Investigation of Flow Control Over an Ahmed Body Using DBD Plasma Actuator. *J. Appl. Fluid Mech.* 11, 1267–1276. <https://doi.org/10.18869/acadpub.jafm.73.248.28600>
- Shakib, F., 1991. A new finite element formulation for computational fluid dynamics. X - The compressible Euler and Navier-Stokes equations. *Comput. Methods Appl. Mech. Eng.* 141–219. [https://doi.org/10.1016/0045-7825\(91\)90041-4](https://doi.org/10.1016/0045-7825(91)90041-4)
- Sieber, M., Oberleithner, K., Paschereit, C.O., 2016. Spectral proper orthogonal decomposition. *J. Fluid Mech.* 792, 798–828. <https://doi.org/10.1017/jfm.2016.103>
- Sirovich, L., 1987. Turbulence and the dynamics of coherent structures. I - Coherent structures. II - Symmetries and transformations. III - Dynamics and scaling. *Q. Appl. Math.* - QUART APPL MATH 45. <https://doi.org/10.1090/qam/910463>
- Smits, A.J., McKeon, B.J., Marusic, I., 2011. High-Reynolds Number Wall Turbulence. *Annu. Rev. Fluid Mech.* 43, 353–375. <https://doi.org/10.1146/annurev-fluid-122109-160753>
- Spazzini, P.G., Iuso, G., Onorato, M., Zurlo, N., Di Cicca, G.M., 2001. Unsteady behavior of back-facing step flow. *Exp. Fluids* 30, 551–561. <https://doi.org/10.1007/s003480000234>
- Spohn, A., Gilliéron, P., 2002. Flow separations generated by a simplified geometry of an automotive vehicle.
- Stella, F., Mazellier, N., Kourta, A., 2017a. Scaling of separated shear layers: an investigation of mass entrainment. *J. Fluid Mech.* 826, 851–887. <https://doi.org/10.1017/jfm.2017.455>
- Stella, F., Mazellier, N., Kourta, A., 2017b. Scaling of separated shear layers: an investigation of mass entrainment. *J. Fluid Mech.* 826, 851–887. <https://doi.org/10.1017/jfm.2017.455>
- Thacker, A., 2010. Contribution expérimentale à l'analyse stationnaire et instationnaire de l'écoulement à l'arrière d'un corps de faible allongement.
- Theissen, P., 2012. Unsteady Vehicle Aerodynamics in Gusty Crosswind. Dr. Hut.
- Tissot, G., 2018. Réduction de modèle et contrôle d'écoulements.
- Tu, J., 2013. Dynamic Mode Decomposition: Theory and Applications. Princeton University.
- Tu, J.H., Rowley, C.W., Luchtenburg, D.M., Brunton, S.L., Kutz, J.N., 2014. On Dynamic Mode Decomposition: Theory and Applications. *J. Comput. Dyn.* 1, 391–421. <https://doi.org/10.3934/jcd.2014.1.391>
- Varon, E., 2017. Closed-loop control of separated flows using real-time PIV.
- Varon, E., Eulalie, Y., Edwige, S., Gilotte, P., Aider, J.-L., 2017a. The chaotic dynamics of large-scale structures in a turbulent wake. *Phys. Rev. Fluids* 2. <https://doi.org/10.1103/PhysRevFluids.2.034604>
- Varon, E., Eulalie, Y., Edwige, S., Gilotte, P., Aider, J.-L., 2017b. The chaotic dynamics of large-scale structures in a turbulent wake. *Phys. Rev. Fluids* 2. <https://doi.org/10.1103/PhysRevFluids.2.034604>
- Varon, E., Eulalie, Y., Edwige, S., Gilotte, P., Aider, J.-L., 2017c. Control of the chaotic dynamics of a turbulent 3D wake. *ArXiv171200416 Phys.*
- Vernet, J.A., Örlü, R., Söderblom, D., Elofsson, P., Alfredsson, P.H., 2018. Plasma Streamwise Vortex Generators for Flow Separation Control on Trucks. *Flow Turbul. Combust.* 100, 1101–1109. <https://doi.org/10.1007/s10494-018-9891-9>

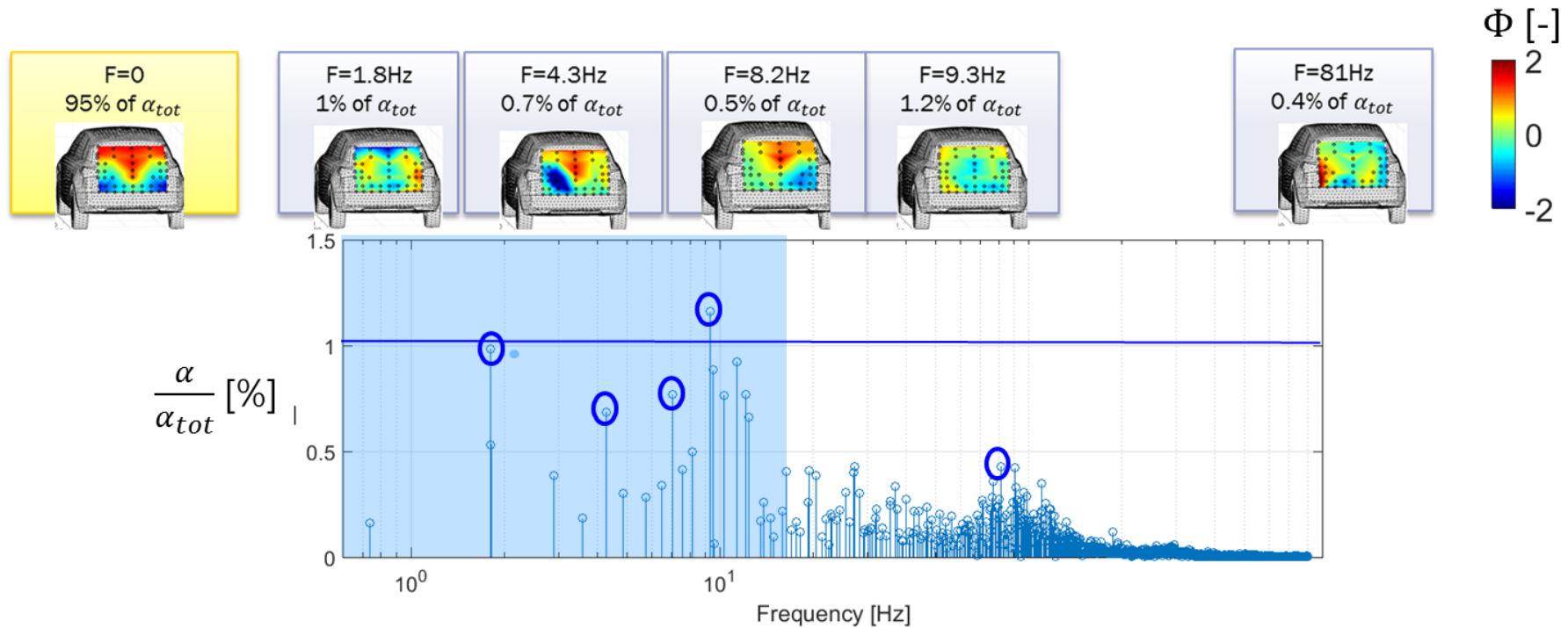
- Volpe, R., Devinant, P., Kourta, A., 2015. Experimental characterization of the unsteady natural wake of the full-scale square back Ahmed body: flow bi-stability and spectral analysis. *Exp. Fluids* 56, 99.
- von Gosen, F., Ostermann, F., Woszidlo, R., Nayeri, C., Paschereit, C.O., 2015. Experimental Investigation of Compressibility Effects in a Fluidic Oscillator, in: 53rd AIAA Aerospace Sciences Meeting, AIAA SciTech Forum. American Institute of Aeronautics and Astronautics. <https://doi.org/10.2514/6.2015-0782>
- Wassen, E., Eichinger, S., Thiele, F., 2010. Simulation of Active Drag Reduction for a Square-Back Vehicle, in: *Active Flow Control II, Notes on Numerical Fluid Mechanics and Multidisciplinary Design*. Springer, Berlin, Heidelberg, pp. 241–255. [https://doi.org/10.1007/978-3-642-11735-0\\_16](https://doi.org/10.1007/978-3-642-11735-0_16)
- Wieser, D., Schmidt, H.-J., Müller, S., Strangfeld, C., Nayeri, C., Paschereit, C., 2014. Experimental Comparison of the Aerodynamic Behavior of Fastback and Notchback DrivAer Models. *SAE Int. J. Passeng. Cars - Mech. Syst.* 7, 682–691. <https://doi.org/10.4271/2014-01-0613>
- Wojciak, J.D., 2012. Quantitative Analysis of Vehicle Aerodynamics during Crosswind Gusts 142.
- Wolf, T., 2018. Aerodynamic of the new Porsche Cayenne.
- Yuan, Z., Gu, Z., Wang, Y., Huang, X., 2018. Numerical investigation for the influence of the car underbody on aerodynamic force and flow structure evolution in crosswind. *Adv. Mech. Eng.* 10, 1687814018797506. <https://doi.org/10.1177/1687814018797506>
- Zaya, johan, 2013. Aerodynamic Optimization of Ground Vehicles with the Use of Fluent's Adjoint Solver (Master Thesis). Chalmers University of technology, Departement of Applied Mechanics, Division of Vehicle Engineering and Autonomous Systems.

## Appendices

## Appendix 1: DMD results

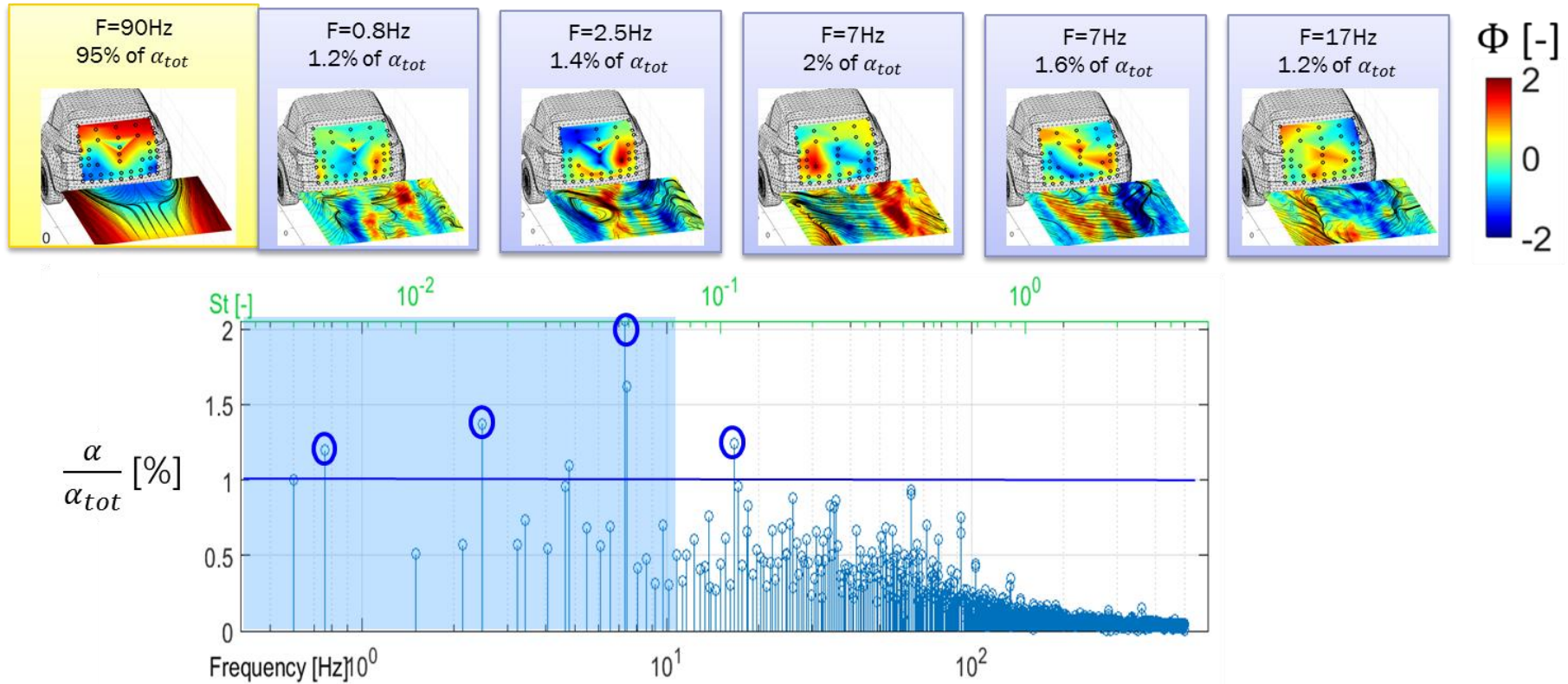
- DMD results of the pressure sensors on the uncontrolled flow.

Energy distribution as a function of the frequency obtained on the Dynamic Modal Decomposition of the rear end pressure sensors distributed on the tailgate on the database of the uncontrolled flow sampled at 2000Hz during one minute of acquisition. Main DMD components are highlighted and the associated DMD modes are plotted.



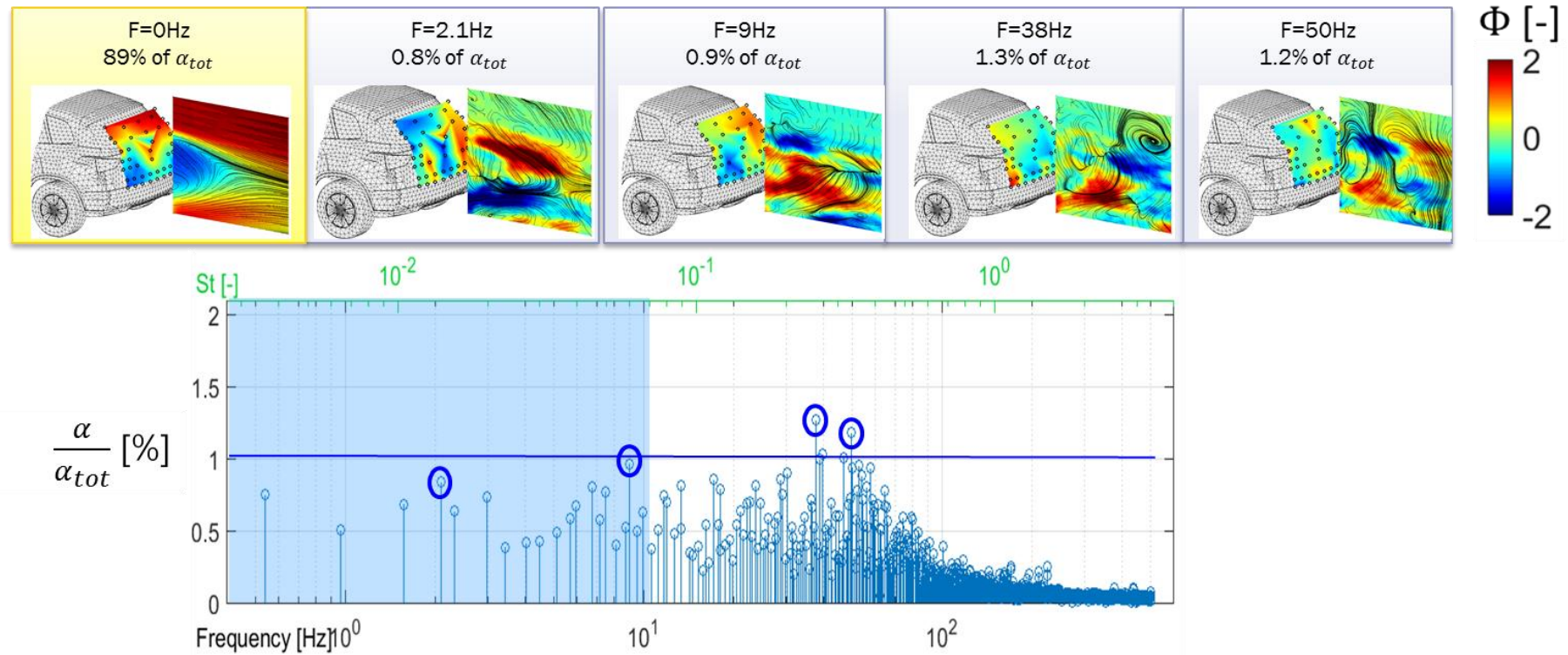
- DMD results on the synchronized pressure-velocity measurements for the uncontrolled flow in the Z140 cut-plane.

Energy distribution of the DMD applied on the synchronized pressure sensors and the wake velocity captured with PIV in the horizontal cut-plane Z140. The analysis is performed on transient data sampled at 2000Hz during an acquisition window of one minute.



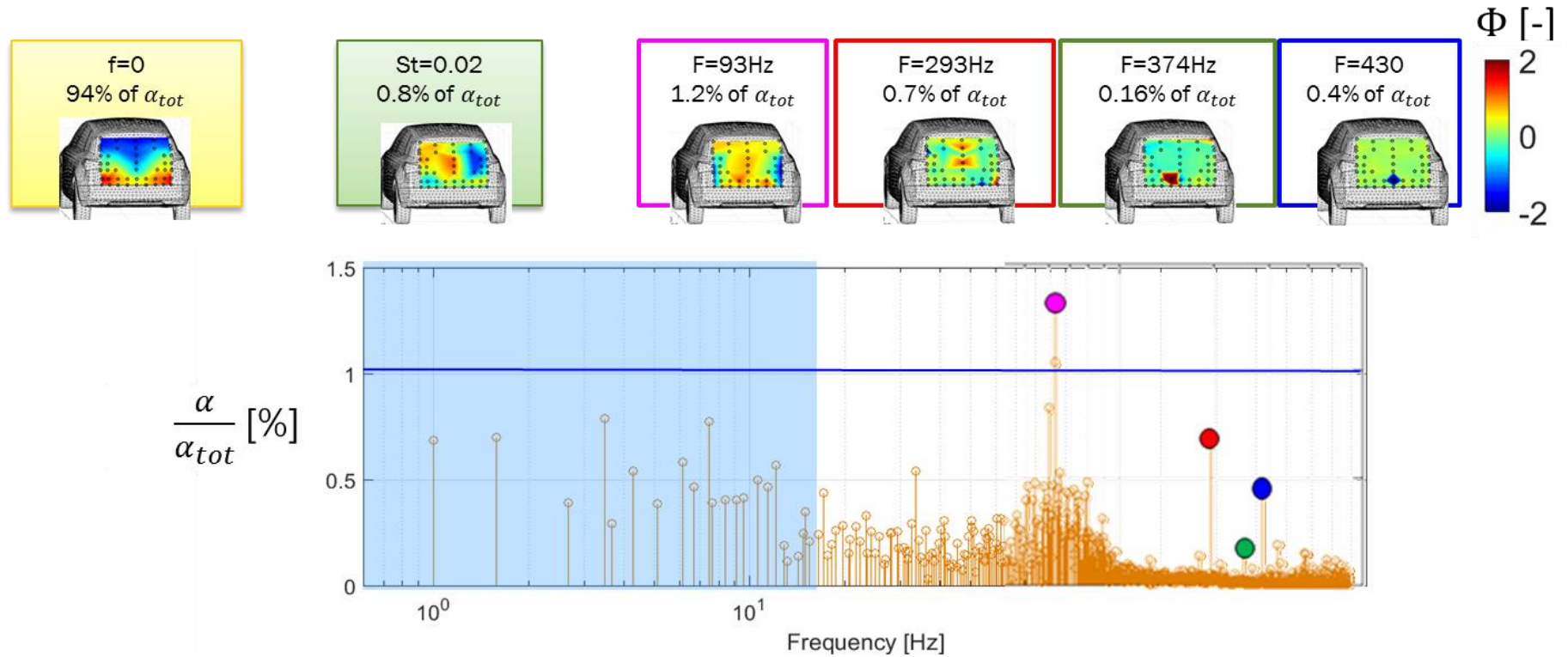
- DMD results on pressure-velocity measurements for the uncontrolled flow in the Y0 cut-plane.

Energy distribution of the DMD applied on the synchronized pressure sensors and the wake velocity captured with PIV in the horizontal cut-plane Y0. The analysis is performed on transient data sampled at 2000Hz during an acquisition window of one minute.



- DMD results of the pressure sensors on the controlled flow.

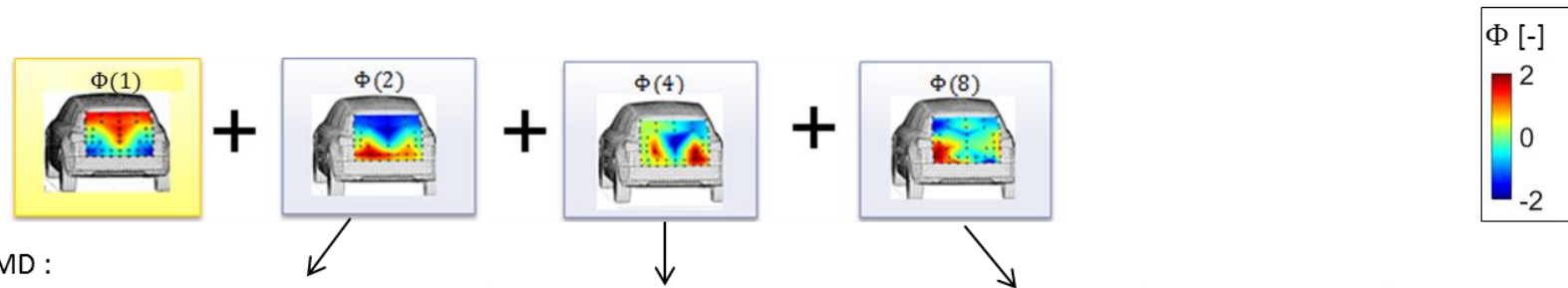
Energy distribution as a function of the frequency obtained on the Dynamic Modal Decomposition of the rear end pressure sensors distributed on the tailgate on the database of the controlled flow sampled at 2000Hz during one minute of acquisition. Main DMD components are highlighted and the associated DMD modes are plotted.



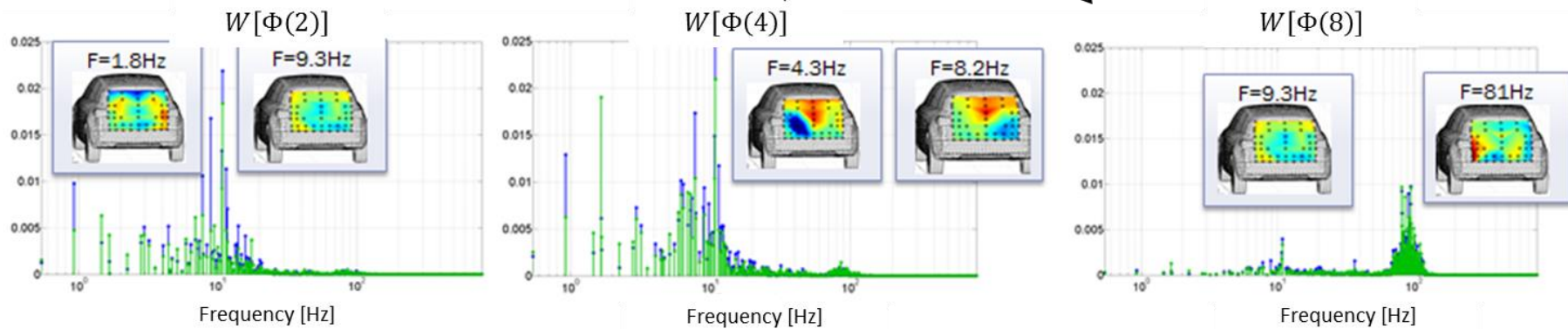
- Correlated DMD modes obtained on the concatenation of the uncontrolled and controlled pressure databases.

Spatial distribution of the POD modes affecting the 0Hz static DMD component and correlated spectra obtained with the row vectors of the transfer matrix. In green, the controlled flow contributions and in blue the baseline contributions.

(a) POD modes :



(b) Correlated DMD :



# Modal analysis and flow control for drag reduction on a Sport Utility Vehicle

## Résumé

L'industrie automobile fournit de plus en plus d'effort pour optimiser l'aérodynamique externe des véhicules afin de réduire son empreinte écologique. Dans ce cadre, l'objectif de ce projet est d'examiner les structures tourbillonnaires responsables de la dégradation de traînée et de proposer une solution de contrôle actif permettant d'améliorer l'efficacité aérodynamique d'un véhicule SUV. Après une étude expérimentale de la maquette POSUV échelle réduite, une analyse modale croisée permet d'identifier les structures périodiques corrélées de l'écoulement qui pilotent la dépression sur le hayon. Une solution de contrôle optimale par jets pulsés sur le parechoc arrière, est obtenue avec un algorithme génétique. Celle-ci permet de réduire la dépression du hayon de 20% et l'analyse croisée des résultats instationnaires avec contrôle montre un changement significatif de la distribution spectrale. Après deux études préliminaires sur la rampe inclinée à 25° et sur le Corps d'Ahmed à 47°, la simulation de POSUV à partir d'un solveur LES, en éléments finis, est validée par rapport aux résultats expérimentaux. L'approfondissement des résultats 3D permet de comprendre les pertes aérodynamiques. La simulation de l'écoulement contrôlé permet également d'identifier les mécanismes du contrôle d'écoulements.

**Mots-clés:** Aérodynamique externe, Réduction de traînée, Contrôle d'écoulement, Décomposition Modale Dynamique, Analyse modale, Simulation LES, Écoulements détachés, Sillage turbulent, algorithme génétique

## Résumé en anglais

The automotive industry dedicates a lot of effort to improve the aerodynamical performances of road vehicles in order to reduce its carbon footprint. In this context, the target of the present work is to analyze the origin of aerodynamic losses on a reduced scale generic Sport Utility Vehicle and to achieve a drag reduction using an active flow control strategy. After an experimental characterization of the flow past the POSUV, a cross-modal DMD analysis is used to identify the correlated periodical features responsible for the tailgate pressure loss. Thanks to a genetic algorithm procedure, 20% gain on the tailgate pressure is obtained with optimal pulsed blowing jets on the rear bumper. The same cross-modal methodology allows to improve our understanding of the actuation mechanism. After a preliminary study of the 25° inclined ramp and of the Ahmed Body computations, the numerical simulation of the POSUV is corroborated with experiments using the cross-modal method. Deeper investigations on the three-dimensional flow characteristics explain more accurately the wake flow behavior. Finally, the controlled flow simulations propose additional insights on the actuation mechanisms allowing to reduce the aerodynamic losses.

**Keywords:** External aerodynamic, Drag reduction, Flow control, Dynamic Modal Decomposition, Modal analysis, Large Eddy Simulation, Detached flow, Turbulent wake, Genetic algorithm